DEVELOPING A HALBACH ARRAY FOR TARGETED DRUG DELIVERY TO BRAIN TUMOURS

THESIS SUBMITTED IN PARTIAL FULFILMENT FOR THE DEGREE OF

DOCTOR OF PHILOSOPHY IN MEDICINE

AREEJ DAIFALLAH AHMAD ALGHAMDI

UNIVERSITY OF SHEFFIELD

Medical School

August 2019

Abstract

Introduction

Malignant brain tumours constitute a small proportion of annual cancer incidence; however, the death rate is almost double the rate of incidence of all cases of cancer. This is not helped by the difficulties associated with the delivery of drugs to the brain. Steering magnetic nanoparticles (MNPs) i.e. superparamagnetic iron oxide nanoparticles (SPIONs) in an area of interest has been proposed for directing magnetically labelled drugs to clinical targets. A powerful magnetic and field gradient is required to ensure that the drugs are directed to the target area. In this case, the deeper the location, the stronger the magnetic force required. External permanent magnets can provide a strong magnetic field and gradient. We **hypothesise** that an inexpensive, portable, powerful and external Halbach array of 1.1T can be designed to steer SPIONs into brain tumours for drug delivery.

Methodology

Computational model: A 2-D simulation model of a Neodymium-iron-boron (FeNdB-52) magnet was run using Finite Element Method Magnetics (FEMM) software.

In vitro model: The FEMM model was assembled and produced a Halbach array with a magnetic strength of 1.1T. The Halbach array was placed on the top of a 3D printed head in order to trap SPIONs (Fe_3O_4) in a 3D tumour, in contact with the surface of the head model. SPIONs were run through a fluid flow system using a syringe pump at 10 ml/min. The experiment was performed in two parts; the first part was to flow SPIONs with different concentrations ranging from 0.1mg/ml to 20mg/ml. The second part was to flow SPIONs, with the same concentrations, but loaded with 50 million white blood cells (WBCs) to mimic circulation. The concentration of SPIONs was quantified by inductively

coupled plasma spectrometry (ICP). Images of the tumours with trapped MNPs were also obtained by MRI (3T) using a dual gradient echo sequence (TE= 4.60ms, 20ms). The uptake of SPIONS and viability of brain cells as well as brain tumour cells was evaluated using TEM and flow cytometry.

Findings

The strength of the modelled magnetic arrays was 1.6T whereas the actual assembled one was 1.1T assessed using Gaussmeter. The concentration of trapped SPIONs in the phantom flow model was different depending on the initial concentration of SPIONs and the location of the tumours within the head phantom. As expected, the further away the tumour was from the magnet, the less SPIONs were trapped. Trapping was confirmed by both ICP and MRI. The SPIONs uptake was observed in the cytoplasm of the cells and it was also noted that increasing the concentration of MNPs resulted in increased toxicity of the brain cells and brain tumour cells. This suggests that the concentration of iron needed to guide drugs with minimal toxicity should be considered.

Conclusions

Various Halbach array designs were modelled and an optimised design assembled. The *in vitro* experiments showed that the Halbach arrays could trap SPIONs with or without WBCs inside the tumour at different distances- up to 10 cm. This suggests that Halbach arrays have the potential to trap therapeutic drugs labelled with iron particles and we believe this would be useful for targeting of anti-cancer therapies to brain tumours.

Contents

List of Figures

List of Tables

List of Abbreviations

AIDS	Acquired immune deficiency syndrome
BBB	Blood brain barrier
BMVEC	Brain microvasculature endothelial
BSA	Bovine serum albumin
CAD	Computed-aid design
CSF	Cerebrospinal fluid
CAR	Chimeric antigen receptor
CT	Computed tomography
DCs	Dendritic cells
DIPG	Diffuse intrinsic pontine glioma
DTC	Dimethyl trimethylene
FEMM	Finite Element Method Magnetics
FUS	Focused ultrasound
FUSIN	Focused ultrasound intranasal
GBM	Glioblastoma
GFP	Green fluorescent protein
hBMEC	Human brain endothelial cells
HIFU	High intensity focused ultrasound
ICP-AES	Inductively coupled plasma-atomic emission spectroscopy
IN	Intranasal
IV	Intravenously
MDT	Magnetic drug targeting
MRI	Magnetic resonance imaging
MRN	magnetic resonance navigation
MNPs	Magnetic nanoparticles
NPs	Nanoparticles
NVU	Neurovasculature unit
OV	Oncolytic virus
PBT	Protein beam therapy
PDL1	Programmed death ligand1
PDT	Photodynamic therapy
PEG	Poly-ethylene glycol
PI	Propodeum iodide
RES	Reticular endothelial system
RNAi	Ribonucleic acid interference
RIOs	Region of interests
SI	Signal intensity
SIRs	Signal intensity ratios
SPIO	Superparamagnetic iron oxide
SPIONs	Superparamagnetic iron oxide nanoparticles
TEM	Transmission electron microscopy
TMC	Trimethylene carbonate
USPION	Ultra-small superparamagnetic iron-oxide
WBCs	White blood cells
WHO	World health organisation

Dedication

To my husband, Dr Saleh Alghamdi and to my children Zeyad, Jourie, Rujin

and Zuhair who accompanied me throughout my PhD journey.

Acknowledgments

Firstly, thanks to the Almighty Allah for giving me the strength, health, wisdom and ability to carry out the doctoral studies.

Many thanks to my supervisors Dr Munitta Muthana and Professor Martyn Paley for their guidance and unwavering support during the entire course of my study at the University of Sheffield. The project could never have been without their constructive criticism and thoroughness.

I would also like to acknowledge colleagues in my group and everyone who worked closely with me in the Medical School for their advice, guidance and relentless support during my doctoral studies.

I am grateful to my sponsor; Prince Sultan Military Medical City, for giving me a scholarship to pursue the PhD degree studies.

I also want to acknowledge my parents for encouraging me to develop enthusiasm and a strong desire to pursue knowledge from my childhood and for the continued support during my doctoral journey.

A special thanks to my dear husband Dr Saleh Alghamdi for his love and never-failing support; he sacrificed his time shouldering the additional responsibilities at home to ensure that our children were cared for properly whilst I focused on my studies. I also thank my children for enduring the lack of attention during my doctoral journey.

Lastly but not least, thanks to all those behind the scenes in my academic pursuit, I really appreciate your support.

Chapter 1

Introduction

1.1 Brain structure overview

The central nervous system consists of the brain and the spinal cord. These two components are responsible for the regulation of different body functions. The brain is made up of three different parts namely the forebrain, midbrain and the hindbrain. It also consists of several lobes of the cerebral cortex which are responsible for different high order functions in an organism. The main lobes include the frontal lobe, the parietal lobe, the occipital lobe, the cerebellum lobe, the temporal lobe and the brain stem. Inside the lobes, there are different parts which perform different regulatory functions either as part of the central nervous system or the endocrine system. **Figure 1.1** shows some of the main functional regions located in the lobes.
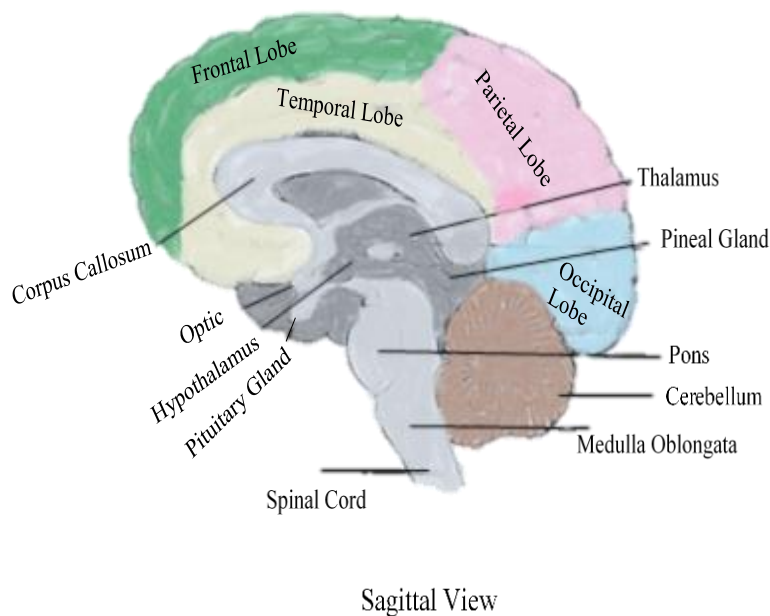
Figure 1.1: Brain structure. Sagittal view of the of the cerebral cortex showing the main brain lobes and different regions of the brain located within the main brain lobes.

The brain parenchyma consists of different cell types including the nerve cells or neurons and the glial cells. The glial cells provide support and they are located around the neurons, and they are of different types including: astrocytes, oligodendrocytes and microglia [1]. Furthermore, there are several layers that protect the brain parenchyma and these include: the skull, the dura mater, arachnoid mater and pia mater. The dura mater is the outer layer that is connected to the skull and where lymphatic vessels are located. In the subarachnoid layer located immediately before the pia mater, there is a fluid called the cerebrospinalfluid (CSF), which bathes the brain parenchyma. In addition, in the pia mater, there are the blood vessels which supply nutrients and oxygen to the parenchyma [2]. The blood brain barrier (BBB) inside the blood vessels is responsible for preventing foreign particles (which may damage the brain) from entering into the brain parenchyma. When tumours develop in the brain parenchyma region they disturb the BBB to access nutrients and oxygen from the blood vessels (**Figure 1.2**). It has also been shown that the functioning and organisation of the BBB can be affected by some pathological conditions including multiple sclerosis, epilepsy, auto-immune deficiency syndrome (AIDS), dementia and stroke [3].
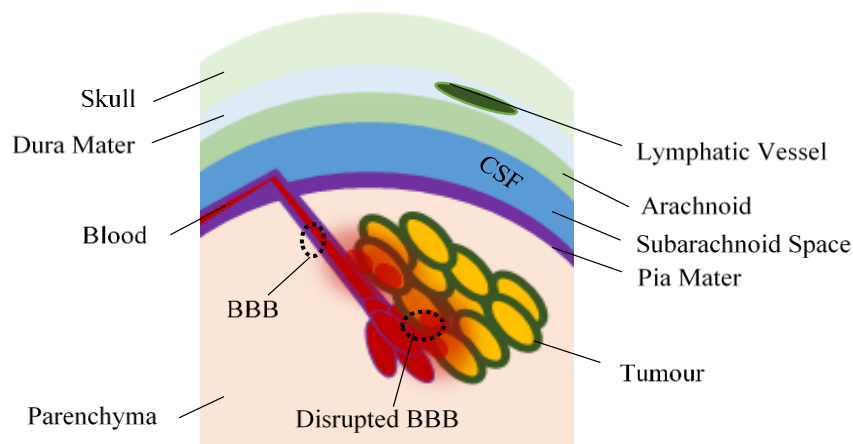
Figure 1.2: The brain parenchyma and protective layers. The brain parenchyma covered with three main layers including blood vessels, and the development of a tumour within the brain parenchyma and how it affects the BBB.

1.2   The brain and blood vessels

The central nervous system does not operate in isolation; instead, it is closely linked to other systems in the body. For instance, the brain cells are surrounded by a dense network of blood vessels whose function is two-fold. The blood vessels are useful for the transportation of nutrients and oxygen to the brain cells and they also protect the brain cells from any toxic substances that may affect their neuronal function [4]. There are three different types of blood cells: red blood cells, responsible for the transport of oxygen; white blood cells (WBCs), which are vital for the defence mechanisms; and platelets, which play a key role in blood clotting. These cells originate from the blood stem cells as illustrated in **Figure 1.3** below.

Blood Stem Cell

Myeloid stem cell

Lymphoid stem cell

Myeloblast

Lymphoblast

Red blood cells

Platelets

Granulocytes

Eosinophil

Basophil

Neutrophil

B lymphocyte

T lymphocyte

Natural killer cell
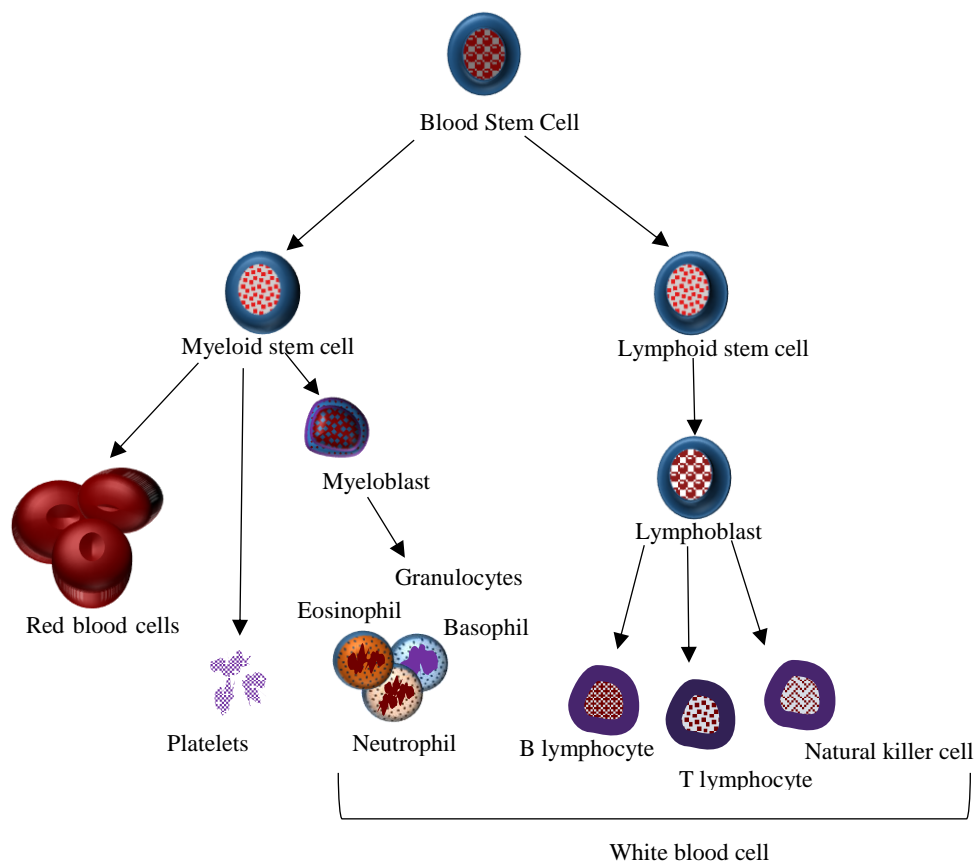
White blood cell

Figure 1.3: The cellular precursors of the components of blood leading to red blood cells, white blood cells and platelets.

As indicated above, it is important for the brain cells to be protected from any toxic neuronal substances that might be in the blood. The BBB has an endothelial cell layer that is tightly connected creating tight junctions which prevents easy entry of substances into the brain parenchyma [4]. In addition, there are some supporting cells including astrocytes, pericytes and microglia. Each cell plays an important role in the BBB. Astrocyte cells surround the basal lamina of the brain capillaries and provide the cellular connection to neurons and they play a key role in the maintenance of the barrier properties of the endothelium [5] [6]. On the other hand, pericytes cover the endothelium and contribute to the structural integrity of the BBB and the induction of barrier properties during development [7]. The following **Figure 1.4** illustrates the structure of the BBB. Despite this level of protection, the brain is not immune to cancers with tumours arising within the brain and some that metastasis from other organs to the brain.
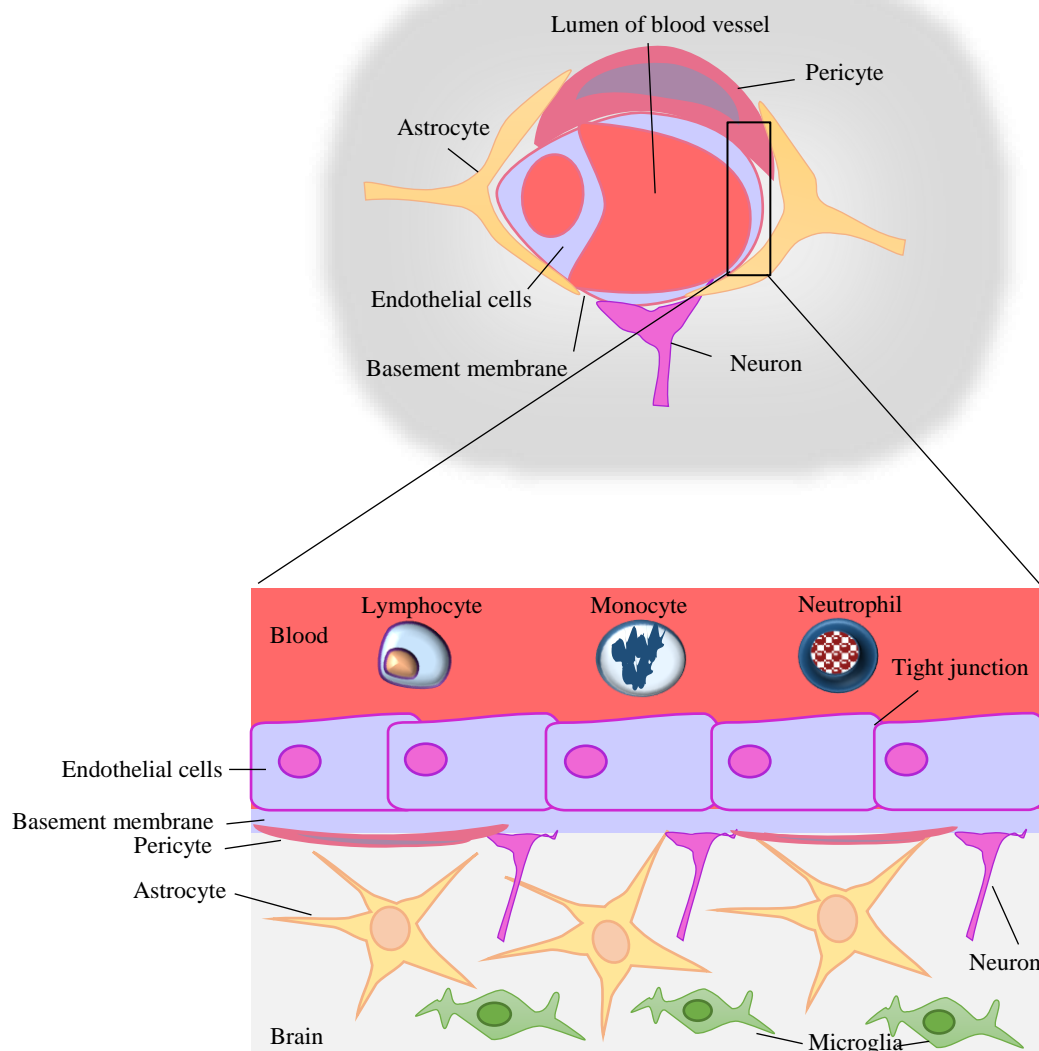
Figure 1.4: Structure of the BBB showing the endothelial cells and the supporting cells and neurones. The endothelial cells are connected tightly and supported by other cells such as the pericytes and astrocytes to protect the brain.

1.3 Brain tumours

Brain tumours are a result of uncontrolled growth of cells. They can be classified into two main categories namely: benign and malignant tumours. Benign tumours do not have any cancerous cells and can be easily treated. In contrast, malignant tumours have cancerous cells and they can spread quickly making it difficult for them to be treated.

Although these tumours occur rarely, they account for approximately 2% of all cases of cancer in adults [8]. Around 4400 people in the UK are diagnosed with a brain tumour every year and this is equivalent to a rate of 7 per every 100 000 in the total population annually (Cancer Research UK, 2019). Although malignant brain tumours constitute a small proportion of annual cancer incidence, the death rate of brain tumour patients is almost double the rate of incidence of all cases of cancer as these are extremely difficult to treat [9].

Brain tumours can occur in any region within the brain, however, 26% of brain tumours occur in the frontal lobe, as it is the largest area in the brain and covers almost two-fifths of the human brain. Tumours in the temporal lobe are considered to be 19% and 12% in the parietal lobe. Less occur in the rest of the lobes i.e. 5% cerebellum, 4% brain stem, 3% occipital lobe and 2% ventricle [10]. As can be seen from Figure 1.5 below, brain tumours occur in different places within the brain, and therefore result in different distances from the surface of the head.
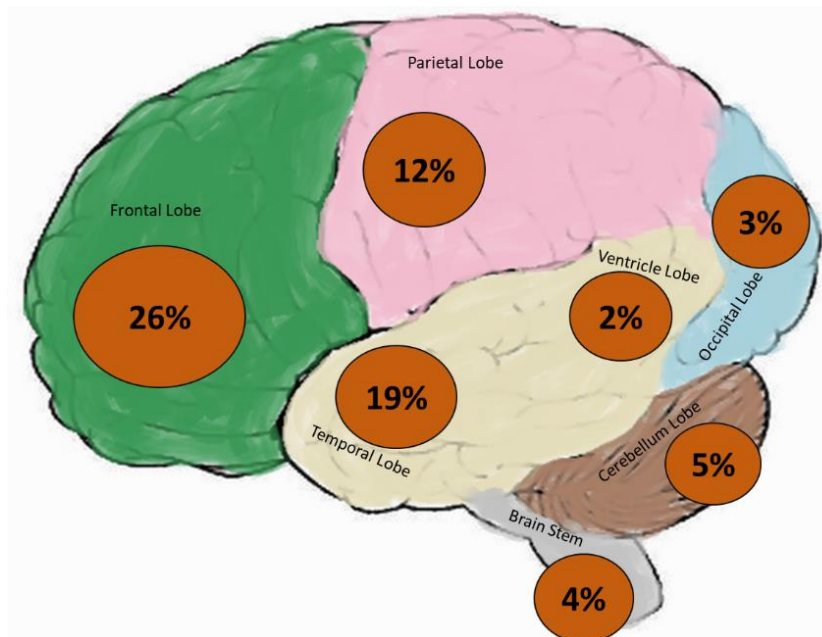
Figure 1.5: Brain tumours and the different location/distance within the brain.

As mentioned earlier, brain tumours can originate from either brain cells or are derived from metastases from other body parts. The tumours that arise from brain cells are referred to as primary tumours and in the US, for example, between 2010 and 2014, these accounted for approximately 2% of all cancers, with an overall annual incidence of 22 per 100000 population [11]. It is worth bearing in mind that these rates are age-adjusted. Crude incidence rates are calculated by dividing the total number of cases by the total population; hence, the statistics cannot be compared to crude rates from other populations (for example, UK) where the age distribution is different.

Brain metastases start from tumours located in different parts of the body such as the lungs and the breasts. These two types of cancer are among the most common brain metastases where 50% of the patients with lung tumours and 20% of patients with breast tumours develop metastatic brain tumours [12][13][14]. Brain metastases arise from the intravasation of cancer cells into the main circulation system, either directly or through the lymphatic system [15].

There are several types of primary brain tumours which can occur in both adults and children. For example, gliomas and astrocytomas are among the most common. **Figure 1.6** illustrates the most common tumours in adults and in children [16] [11].

(a)
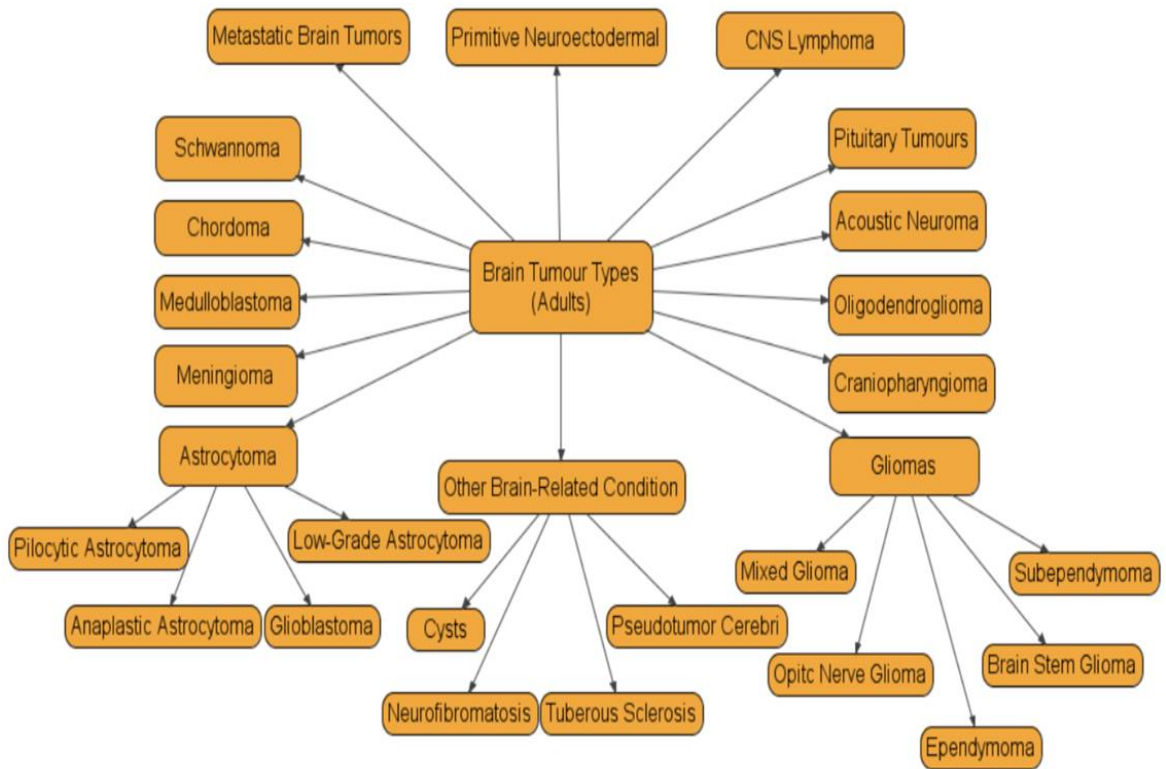
(b)
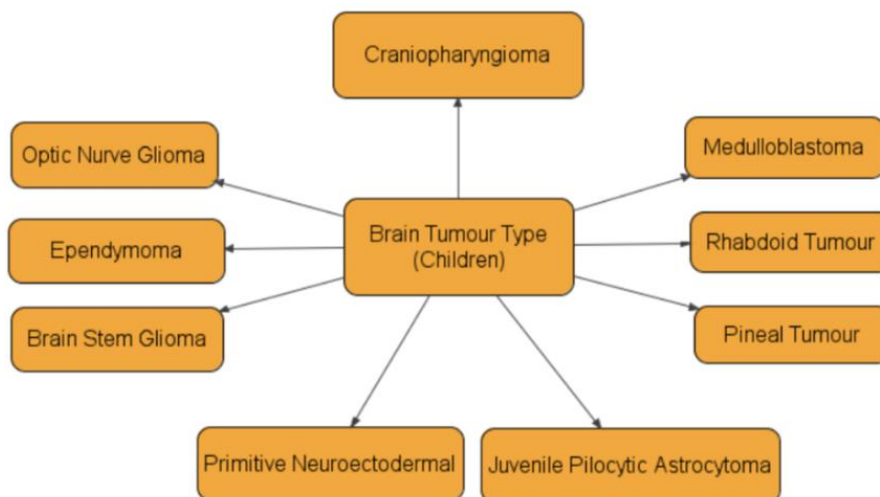
Figure 1.6: Common types of brain tumours. (a) Adults and (b) Children.

Each type of brain tumour is named according to the main type of cells present where the cancer is located. For instance, gliomas are tumours that originate from the glial cells and examples of these tumours include astrocytomas, oligodendrogliomas and ependymomas [11]. According to the World Health Organisation (WHO), gliomas constitute the most common type of brain tumours representing 80% of all malignant primary brain tumours in adults [17]. Gliomas are also classified according to their malignancy grade ranging from grade 1 to 4, where grade 4 represents the most aggressive form of brain tumour. For example, when astrocytomas reach grade 4 level, they are called glioblastomas [18]. These brain tumours are found in both adults and children [19]. However, primary glioblastomas are more prevalent in adults, where they represent more than 90% of cases in patients who are above 50 years [20].

Brain tumours can occur at any age in both genders, however, it has been found that in general brain tumour cases increase from age 30 up to 75. It appears there is a drop in the number of cases of brain tumour after the age of 75 and the reasons for this are not clear. It is argued that this might be a result of tumours of the brain being less likely to be investigated and detected among the elderly [8]. On the other hand, an increase in the incidence of other conditions such as strokes among the elderly might be an indicator of the presence of brain tumours. This is because one of the symptoms of brain tumours is stroke. It is possible that physicians may fail to detect brain tumours and just focus on the strokes. However, it has been suggested that physicians may not have the appetite to conduct thorough investigations [8]. Brain tumours are more likely to appear in males than in females with a male: female ratio of 1.5:1. Despite this general incidence ratio, in some types of cancer such as meningioma's, women are actually more likely to develop the cancer than men [8].

Recent studies indicate that brain tumours arise from genetic mutations which disrupt the existing regulatory mechanisms, making it possible for the cancerous cells to continue to multiply and spread [8]. Alterations of the genetic material can be caused by different neurocarcinogens that can be chemical, physical and/ or biological. The development of brain tumours can therefore be attributed to both genetic and environmental factors. It is possible that genetic alterations can be inherited from one generation to another, hence it becomes important to trace family histories when investigating brain tumours. An example of this phenomenon can be the predisposition to brain tumours, in particular, with genetic changes in the TP53 gene which has been found in patients with gliomas [8]. On the other hand, individuals may develop brain tumours that are a result of changes in their own internal environment. For example, changes in the cell environment may affect metabolic processes including oxidation, detoxification, DNA stability and repair and immune functioning. These changes can lead to the alteration of the structure of specific genes [8].

Apart from the main factors such as the genetic alterations and changes in the environment, there are also a number of risk factors that can contribute to the development of brain tumours. Patients exposed to ionising radiation are likely to develop brain tumours. For instance, it was observed that the use of low dose radiation as treatment for tinea capitis and skin disorders in children resulted in the development of brain tumours in adulthood [13].

1.4   Current therapeutic methods for brain tumour

Various therapeutic systems can be employed to treat brain tumour patients. These include surgery, chemotherapy, radiotherapy and more recently, immunotherapy and targeted therapy [21]. The treatment choice is decided by the physicians depending on

several factors which include the condition of the patient such as age as well as the condition of the tumour, for instance, the tumour grade, size, location and whether the tumour is in a single or multiple locations in the brain. The currently available treatment options for brain tumours are discussed in the following section.

1.4.1 Surgery

Surgical resection is one of the first options for the treatment of brain tumour patients. It involves the removal of the tumour mass from the affected part of the brain. However, as due to the type as well as the location of some brain tumours, surgical resection is not always effective [16]. This is because the malignant tumour can be located in a sensitive region of the brain where it cannot be removed completely [16]. In addition, the malignant brain tumour may not be well defined, making it difficult for the surgeon to remove the tumour without damaging some of the other brain tissue. The malignant cells can penetrate into healthy tissues surrounding the tumour, hence, it is possible for the malignant tumour to recur after the initial surgery [22]. Therefore, surgery is often followed by radiotherapy [23] and/ or chemotherapy which can be either oral Temozolomide or an implanted Carmustine wafer [24].

1.4.2 Chemotherapy

One of the primary treatments for brain tumour is Chemotherapy and it involves the use of anticancer (cytotoxic) drugs. It can be administered during the surgery to remove the tumour and this is called a Gliadel implant. Alternatively, it can be given after surgery and together with or after any other brain tumour treatment such as radiotherapy. There are different ways of administering chemotherapy into the brain including, for example, oral Temozolomide and intravenous Carmustine [24]. Although chemotherapy is designed to destroy cancer cells, it can also affect healthy cells leading to the weakening of

the body's immune system and causing some side effects, for example, increased chance of infection, easy bruising or bleeding, hair loss and fatigue among others.

1.4.3 Radiotherapy

This is also referred to as radiation therapy and is a common treatment for brain tumours which uses high energy beams, i.e. X-ray and/ or proton beam therapy (PBT), of external radiation to destroy cancer cells [25]. It can be used when the surgeon cannot remove the tumour or can be used after surgery. Similarly to chemotherapy, radiotherapy also produces side effects and this has been an area of interest to researchers in an effort to find ways of reducing the side effects and improve the quality of patient's lives [26]. In addition, radiotherapy can be combined with chemotherapy to produce significant improvements in the treatment of many tumours. A study by Komatar et al. revealed that the combination of radiotherapy and chemotherapy such as Temozolomide helps to improve the survival of brain tumour patients [27]. The study established that after 28 months of treatment, the average survival for patients who were treated with radiotherapy and Temozolomide was 14.6 months while the average was 12.1 months for those treated with radiotherapy alone. On the other hand, it is argued that the combined use of radiotherapy and chemotherapy increases the drug side effects [28], thus creating a difficult choice for patients and physicians between remaining duration and quality of life.

1.4.4 Immunotherapy

This is another form of cancer treatment where a patient's immune system is stimulated in order to fight cancerous cells. The human immune system consists of the lymph glands, spleen and white blood cells. Some cells of the immune system are able to identify cancer cells as abnormal and destroy them. However, this is not a reliable way to eliminate or kill all the cancer cells for various reasons including: 1). The immune system

cannot destroy all the cancer cells; 2). Cancer cells produce signals to protect themselves from being attacked by the immune system, 3). The cancer cells hide or escape from the immune system (Cancer Research UK, 2019).

There are several types of immunotherapy and these include: vaccines, monoclonal antibodies, adoptive cell therapy, checkpoint inhibition and virotherapy.

1.4.4.1   Vaccines

These work in the same way that vaccine's for other diseases work, where a weakened version of the pathogen is introduced into the body to stimulate the immune system. The vaccine activates the dendritic cells (DCs) to produce antigens that are transported through the lymphatic vessels to lymph nodes in order to activate T-cells. The activated T-cells help to develop immunity against cancer cells [29]. Some studies involving the use of cancer vaccines to treat brain tumours have been conducted and have shown promising results [30]–[32]. For example, the first case of brain tumour patient who had primary intracranial tumour, that was treated with DC-based immunotherapy was reported in 2000 by Lia et al. [33]. The patient underwent surgical resection first, and then injected with three immunisations of autologous DCs. The results showed that the patient responded positively to the vaccine, that is, the patient developed measurable cellular immune responses against vaccine antigens.

1.4.4.2   Adaptive Cell Therapy

This method is aimed at directly activating the T-cells to enhance immunity [34]. It involves isolation and *ex-vivo* expansion of a sample of tumour specific T-cells from the patient's blood and then transferring T-cells into the patient to develop immunity. This technique has been investigated in several *in vitro* studies and showed positive results [32], [35], [36]. Brown et al., developed a chimeric antigen receptor (CAR) T cell

immunotherapy to treat glioblastoma (GBM). GBM was derived from a patient and injected into mice. The result showed improving in anti-tumour activity which providing vital insights of translation of CAR T cells for GBM [37].

1.4.4.3 Checkpoint inhibition

Immune checkpoint therapy has recently exploded into the cancer treatment scene and involves the enhancement of T-cells by blocking certain proteins (immune checkpoints) that weaken the normal activity of cytotoxic T-cells. In this case, the T-cells are boosted to destroy the cancer cells more effectively [38]. These inhibitors have shown efficacy in certain tumours like melanoma and are currently administered to patients with this cancer [39] [40]. Currently, a number of clinical trials of checkpoint inhibitors in glioblastoma (i.e. programmed death ligand1-PDL1) are ongoing, i.e. phase III trial was established in 2014 as well as phase I and II in 2016 , hence, the outcomes of the studies are yet to be reported [41].

1.4.4.4 Virotherapy

This is one of the immunotherapy methods used to treat brain tumours by programming viruses to attack cancerous cells whilst avoiding damage to healthy tissues using the common types of oncolytic viruses [42]. Clinical trials carried out in the recent past have demonstrated that oncolytic viruses are effective in treating human tumours. Cockle et al. indicate that most clinical studies have focused on intratumoural delivery in the treatment of tumours [43]. For example, an oncolytic herpes simplex virus-1 (HSV1716), has been used in adults by injection into the brain and superficial tumours. The aim was to determine if it was safe to use HSV1716 with young cancer patients with relapsed or refractory extracranial cancers. A single dose of HSV1716 was administered to 8 patients and two doses to one patient. No dose limiting toxicities were observed. Overall,

HSV1716 was shown to be safe and effective for use in children and young adults with late stage aggressive cancer [44].

Of note, some of these therapies are still in clinical trials for brain cancer and in the next few years, it will become apparent if these are suitable for this disease type and will progress to be an approved therapy for brain cancer.

1.5 Challenges of treating brain tumours

Despite the improvements made in diagnostic imaging of brain tumours using approaches such as radio-isotope imaging, computed tomography (CT) and magnetic resonance imaging (MRI), the treatment of brain tumours remains a big challenge. This is mainly due to the difficulties associated with the delivery of drugs to the brain. Basically, 100% of large-molecule pharmaceutics including peptides, recombinant proteins, monoclonal antibodies, Ribonucleic acid interference (RNAi) based drugs and gene therapies do not cross the BBB [45] [46] [47]. This is due to the structure of the BBB, the series of closely packed endothelial cells with tight junctions in between them and supporting protective cells (**Figure 1.4**) makes it difficult to deliver drugs across the BBB into the brain tumours. The BBB functions as a barrier preventing all neurotoxins as well as drugs from invading the brain cells. The development of a brain tumour can disrupt the BBB (as shown in **Figure 1.2**) resulting in the leaking of some foreign substances into the brain cells. However, in most cases large parts of the BBB remain intact, thereby preventing drug delivery. This constitutes a big challenge in the treatment of brain tumours using traditional methods, such as intravenous injection of anti-cancer drugs, given that the drugs cannot penetrate the BBB [48]. It is also known that despite disruption of the BBB it is still difficult for anti-cancer drugs to treat brain tumours. This is due to the differences between the size of the anti-cancer drugs and the endothelial pore size in malignant tumours. In a

study by Watkins et al. (2014) it was revealed that displacement of the astrocytic end feet from an endothelial cell by a single invading tumour cell would be enough to cause local breaching of the BBB [49]. However, it is unlikely that the size of this local disruption is sufficient to allow drug penetration in meaningful quantities to reach the tumour site without direct navigation of the drug. Bearing in mind that areas with invasion do not get enhanced during contrast-enhanced MRI. In addition, it has been shown that the high metabolic demands of high-grade glioma creates hypoxic areas that trigger increased expression of Vascular Endothelial Growth Factor (VEGF) and angiogenesis which leads to the formation of abnormal vessels and a dysfunctional BBTB [50]. The invasive potential of glioma causes widespread proliferation of high-grade glioma cells outside regions of the disrupted BBTB and inside areas of otherwise normal brain, where the function of the barrier is still much more intact. In most cases, this includes the areas that do not show gadolinium enhancement on T1 weighted MRI [51]. As a result, both in low-grade and high-grade glioma, the BBB and the BBTB barrier form a major obstacle in brain tumour therapy by preventing the delivery of sufficient quantities of potentially effective therapeutic agents [50].

In addition, traditional cancer treatment methods such as radiotherapy and chemotherapy have the disadvantage of affecting other healthy cells or tissues as they are distributed throughout the body. This results in some side effects that include loss of immunity, dizziness and fatigue. Some of the techniques to improve drug delivery across the BBB and to spare the healthy cells by concentrating the anti-cancer drugs to the area of interest (tumour) are discussed in the following section.

1.6   Drug Delivery techniques for brain tumours

Drug targeting therapy is a cancer treatment that involves the delivery of drugs to specific location or area of interest in the body [52]. This technique can improve the outcome of brain tumour treatment by allowing preferential delivery of drugs to the cells of interest and ensuring that the drug molecules react exclusively with the cancer cells without affecting the other healthy cells. One of the drug targeting techniques which has already been used clinically for the treatment of brain tumours is focused ultrasound therapy [53].

1.6.1 Focused Ultrasound therapy

Focused ultrasound therapy is a non-invasive therapeutic technique, which involves focusing beams of ultrasound energy to target areas deep in the brain without affecting the surrounding tissues. It works in two different ways in the treatment of cancer including: 1) High intensity focused ultrasound (HIFU) to thermally destroy the cancer and 2) Disrupting the BBB temporarily to allow anticancer drug delivery. By temporarily disrupting the BBB using pulsed ultrasound combined with injected microbubbles it is possible to enhance the delivery of anticancer drugs to the brain in patients with recurrent brain tumours [53].

A recent *in vivo* study explored the potential of a new strategy to deliver anticancer drugs to brain tumours using this ultrasound technique [54]. This strategy involved administering radioisotopes (64Cu-AuNCs) to the brain through the nose using focused ultrasound intranasal (FUSIN). It uses focused ultrasound (FUS) to induce microbubble cavitation to enhance drug delivery to the brain tumour via the intranasal (IN) route. The aim of this study was to evaluate the effectiveness of this technique compared with the traditional treatment method which involves administering the drug intravenously (IV). In

the first group of mice, a total of 8 drops (24μL) were administered to each mouse IN and then this was followed by FUS. In the second group, 3.7 MBq/mouse were administered IV through the tail vein. The histological analysis showed that FUSIN resulted in the accumulation of most of the radioisotope in the brain with low concentrations in other organs such as lungs, spleen, kidneys and heart compared to the IV route. The histological analysis also indicated that no damage was caused to the tissues in the nose, trigeminal nerve and the brain. Therefore, it was concluded that FUSIN is a safe and promising technique to target brain tumour.

Another study confirmed the effectiveness of using FUS in combination with microbubbles under MRI guidance in the treatment of Gliomas in a rat model. This technique is called Magnetic Resonance Image-guided Focused Ultrasound (MRI-FUS). The aim of the study was to evaluate the effectiveness of MRI-FUS in the treatment of brain tumours such as Diffuse Intrinsic Pontine Glioma (DIPG). The results confirmed that MRI-FUS could open the BBB and facilitate the penetration of the chemotherapeutic agent (Doxorubicin) [55].

1.6.2 Photodynamic therapy

The interest in photodynamic therapy (PDT) came up as a result of the ineffectiveness of the other standard therapies for malignant tumours. This technique makes use of the toxicity of singlet state oxygen which is generated by irradiating a laser of 664 nm wavelength on the photosensitiser [56] [57]. Research revealed that the singlet oxygen state generated from photochemical reactions is toxic and leads to direct damage to the tumour cells (necrosis and apoptosis), the shutdown of brain tumour vascular tissues and enhancement of the body's immune system [58] [59]. This technique was used in a number of *in vitro* and *in vivo* studies and showed promising results, which could be

verified, in clinical studies [53] [54] [55] [56]. Although PDT proved to be an effective treatment method for malignant brain tumours, its downside is that it involves an operation to remove the tumour and to expose the location of the tumour to the laser.

1.6.3 Magnetic Field Technique

One of the approaches used to deliver anticancer drugs is the use of magnetic fields. This involves generating a static magnetic field and field gradient from either a permanent, resistive or superconducting magnet. The force on a magnetic particle is proportional to the product of the local field and field gradient. The magnetic field can be positioned internally using an implanted magnet [60], or externally on the surface of the patient or even completely surrounding the patient using the large volume fields found in whole body magnetic resonance imaging (MRI) systems [61] [62]. Implanted magnets involve inserting small pieces of magnetic material close to the target location in the patient's body. This approach helps to generate powerful magnetic field strength and field gradient for the attraction and concentration of drugs into the target area. A number of studies have shown the effectiveness of this technique in targeting drug delivery to the spinal cord [63], heart [64], and brain [60]. This method is not commonly used because of the need to carry out surgery to implant the magnetic material which might be a risky procedure for the patients [65].

Using an external magnetic field technique in cancer treatment is referred to as magnetic drug targeting. This approach constitutes the main focus of this study as will be discussed in the following section.

1.7   Magnetic Drug Targeting for cancer therapy

1.7.1 Overview

Efforts to find efficient ways to deliver drugs to tumour locations have continued and recent research has seen the development of another promising technique called magnetic drug targeting (MDT). This technique can be applied in the delivery of drugs for the treatment of many different types of tumours [66]. MDT involves the delivery of anticancer drugs loaded with MNPs to the targeted area, i.e. tumours. These MNPs are controlled using external magnetic fields focused on the tumour [67]. This type of target directed drug injection attempts to concentrate the anticancer drug at the tumour site by enhancing its effectiveness and at the same time reducing unwanted side effects by preventing the targeting of healthy tissues and organs [68] [52] [69]. Unlike traditional methods such as chemotherapy, in this case, the anticancer drug is concentrated at the target cells away from the reticular endothelial system (RES) (**Figure 1.7**). The RES is known to sequester drugs from circulation preventing them from reaching their target location.

(a)   (b)

Magnetic Anti-cancer

Body Circulation

Target Tissue   RES Phagocytosis

Magnet

Magnetic Anti-cancer Drugs

Body Circulation

Target Tissue   RES Phagocytosis
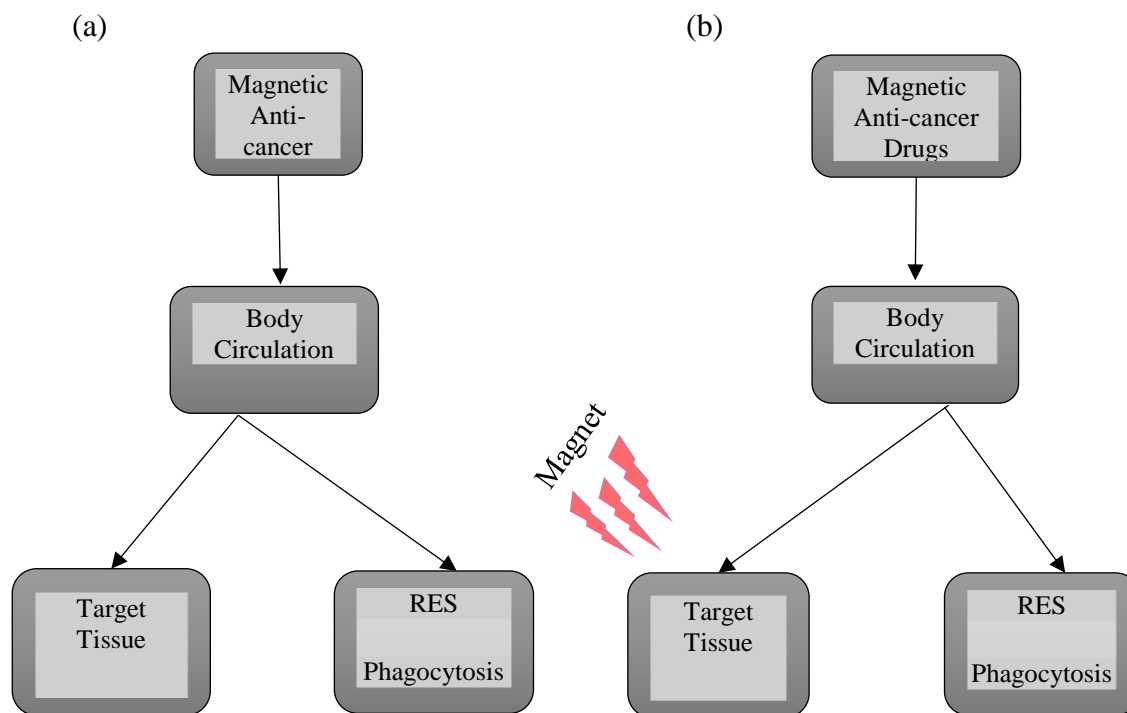
Figure 1.7: Comparison of traditional and MDT in the treatment of cancer

(a) Traditional approach: anticancer drugs are injected into the bloodstream and most go to the RES organs, (b) MDT approach: most of the injected anticancer drugs reach the tumour.

In MDT, an anticancer drug is attached to MNPs and injected intravenously into the patient, i.e. through the artery or vein [70]–[72]. These MNPs will circulate in the bloodstream, and once the external magnet is placed on the target area the MNPs will be directed towards the tumour. MDT can take place either before the MNPs pass through the liver (this is referred to as the first pass method) [67] [68] or after the MNPs have passed through the liver (commonly used approach) [63] [69] [70] depending on whether the MNPs have been injected through the vein or artery. The MNPs will accumulate in the tumour and then release the anticancer drugs to destroy the tumour cells. In some cases the MNPs can be administered outside the blood flow; for example, in the treatment of inner

ear tumours, a small amount of gel containing MNPs loaded with anticancer drugs is placed either on the round window membrane [77] or intranasally [78].

Research interest in the area of MDT started in the middle of the 20th Century. In 1956 Gilchrist and others published a seminal paper focusing on the study of selective radiofrequency inductive heating of the lymph nodes after 20.100 nm sized MNPs were injected into the lymph nodes close to the location of the tumour, following surgical removal [79]. After that, Turner et al., combined this radiofrequency heating method with embolization therapy [80]. In 1965, Meyers found that these MNPs could be driven to the desired location by using an external magnetic device. From this, he came up with the idea of using this approach to target lymph nodes as well as using these small particles as a contrast agent. Therefore, MDT was first explored in 1965 when Meyers showed that small iron particles accumulated in the veins in the legs of a dog following intravenous injection, via application of an external magnet (horse shoe-shape) [81]. After that Hilal and others described how magnetic catheters could be used to deposit and selectively embolise arterio-venous malformations with small magnets [82]. In the 1970s and for the first time, spherical magnetic microspheres were made and worked well in an *in vivo* study using an animal model for tumour treatment as well as for magnetic resonance contrast agents [83][84]. They developed a technique of targeted hyperthermia to target rabbit kidneys. The heat was produced by magnetic hysteresis produced in small ferromagnetic microspheres subjected to a time-varying magnetic field. The results showed that by using such a technique, the 42 ⁰C therapeutic temperature threshold and above, could be reached in the target tissue [84]. Further research has continued to demonstrate that MDT is an efficient approach in the delivery of anticancer drugs to the target area. For instance, in a recent study by Price et al., it was demonstrated that MDT successfully delivered a chemotherapeutic drug loaded with iron oxide nanoparticles into the lungs in a mouse

model [85]. Of note, this was carried out in a healthy mouse model and the authors did not demonstrate any therapeutic effect of the chemotherapy in a tumour model.

1.7.2 The application of MDT in cancer treatment

A number of research studies conducted to date have revealed that MDT has several applications in the treatment of cancer. Several anticancer drugs have been delivered using MDT as shown in **Table 1.1**.

Drug	Application	Reference
Mitomycin C (trimethylene carbonate (TMC) and 5,5-dimethyl trimethylene carbonate (DTC))	Potential hepatic carcinoma therapeutics	[86]
Yttrium-90 (Human serum albumin)	Bimodal radionuclide-hyperthermia cancer therapy	[87]
Doxorubicin (albumin)	Cancer therapy	[88]
Oxantrazole (chitosan)	Cancer therapy (i.e. mouse hepatoma)	[89]
5-FLUOROURACIL (bovine serum albumin (BSA))	Tumour of hepatoma	[90]
Adriamycin (albumin)	Cytotoxic effect on tumour cells (i.e. melanoma cells)	[90]
Vancomycin (starch)	cytotoxic effect on tumour cells	[91]

Table 1.1: Examples of some drugs and their applications in MDT

White blood cells (WBC) called 'monocytes' have also been used to magnetically target gene therapies and viruses to tissues including tumours [92] [93] [94]. In 2008, Muthana et al. showed that monocytes transfected with green fluorescent protein (GFP) successfully take up superparamagnetic iron oxide (SPIO) [92] and can be guided from circulation to superficial prostate tumours grown in the flanks of mice using an external

magnet placed above the tumour. They demonstrated a 3-fold increase in the number of tumour-infiltrating monocytes compared to in the absence of a magnetic field [93].

A further study by Muthana et al., reported that monocytes differentiated into macrophages and loaded with super paramagnetic iron oxide nanoparticles (SPIONs) were able to carry a cancer killing oncolytic virus (OV) to tumours located in the prostate of mice using pulsed magnetic field gradients in the direction of the tumour using a preclinical 7T MRI scanner [93]. The study reported that, by using such an approach, the number of OV-loaded macrophages increased in the target i.e. in primary and metastatic tumours in mice and tumour growth significantly decreased.

MRI is used in clinics for diagnostic purposes, and recent *in vitro* studies show the success of MRI in targeting, this is known as Magnetic Resonance Targeting (MRT) [93][65]. This technique is used to magnetically steer the magnetised drug to the area of interest. In *in silico* models, researchers called this technique magnetic resonance navigation (MRN) where this is based on variation of a field gradient to steer/navigate MNPs in real-time to a target [95].

In an *in vitro* study, it was shown that MRI which produced a magnetic field gradient (12 T/m), was used successfully to manipulate and track agglomerates of superparamagnetic nanoparticles (micron sized) in real time. In this study 132 μl samples having 48 mg/ml MNPs in MilliQ H_2O were used in a glass tube of 4.1 mm (ID) located at the iso-centre of the MRI magnet [96].

In an *in vivo* study aimed at targeting a tumour (Leukemia cells) using MDT, 0.2 mL of Gemcitabine loaded with Fe_3O_4 /Chitosan was injected intravenously into each mouse [97]. An external magnet with magnetic strength of 1.1 T was used to direct the MNPs to the tumour site. The tumour (leukaemia cells) was first introduced into the mice

and left to grow in the upper part of right flank of the mice for six days after which the drug loaded with MNPs was injected into the mice. After 2 hours, an external magnet was placed on the tumour site and it showed that in treated mice the MNPs accumulated on the periphery of the tumour while no significant accumulation of MNPs was observed in the control mice. It was interesting to observe that when the magnet was placed on the tumour, the MNPs were trapped on the periphery of the tumour and when the magnet was removed, the MNPs diffused into the tumour. It could have been interesting if more details were provided about the magnetic device, i.e. the structure and the size as well as the time that the magnet was placed on the tumour site. However, the results from this study helped to confirm the efficiency of using a magnetic gradient to direct the MNPs into the target area, hence, the potential for using MDT in cancer treatment [94].

The first clinical trials in patients involving MDT were conducted by Lübbe et. al. using MNPs attached to epirubicin with patients who had facial tumours that could not be surgically removed [98]. They conducted a Phase I clinical trial using MDT in patients with advanced and unsuccessfully pre-treated cancers or sarcomas. It was concluded that the MNPs were successfully directed to the tumours in about one-half of the patients. In addition, no toxicity was reported to the organ tissues which means MDT is a safe technique to be used for cancer treatment. Although the reason why treatment did not work in the other half of the patients was not provided, the study made important conclusions that it appears that the effectiveness of the MDT treatment is still dependent on individual patients' conditions and disease-related problems. The need to conduct a further study design aimed at comparing conventional treatments with the new treatment within one patient was cited as of crucial importance in order to get rid of the interindividual differences observed in the study.

Following the success of the Lübbe trials, more researchers have been motivated to explore further applications of MDT. For example, Pankhurst et al. has been investigating the use of MDT to deliver mesenchymal stem cells to sites of vascular injury in mouse models [99]. In the same vein, Häfeli et al. made use of implanted magnets located behind the cornea to collect stem cells for retinal regeneration [100]. Using MNPs combined with ultrasound, it has been possible to deliver therapeutics across the BBB [101]. Similarly, there has been a growing interest in the application of SPIONs in the delivery of thermal energy to tissues [99] [100]. This same technique has been used to generate targeted hyperthermia in prostate cancers [102]. In this thesis, focus will be placed on exploring the use of MDT in cancer treatment.

1.8   Magnetic Nanoparticles for Drug Delivery

MNPs have been utilised in different ways in the medical field. They are used for diagnostic purposes, i.e. as a contrast agent for MRI [104]. In addition, MNPs are used for therapeutic purposes, for example, drug delivery. The use of MNPs in drug delivery started in the late 1970s [105]. The structure and properties of the MNPs make them useful in biomedical applications and their use in drug targeting has been made possible by their magnetic properties which enable them to be directed to target areas using an external magnetic field. The materials that are commonly used for drug delivery contain metal or metal oxide nanoparticles (NPs) such as SPIONs. The SPIONs used for MDT should be coated with organic materials such as fatty acids, polymers or polysaccharides and this helps the attachment of the therapeutic agent or anticancer drugs [106].

There are many different magnetic materials that are commercially available, however, not all of them can be used for drug delivery *in vivo* because some of them are highly toxic, for example, cobalt and chromium. Iron oxides are relatively safe and are

currently being used as MRI contrast agents in the clinic [107]. The common iron-oxides include hematite (α-Fe_2O_3), magnetite (Fe_3O_4) and maghemite (γ-Fe_2O_3). They are different in their structure and this confers them different chemical and physical properties. Magnetite and maghemite are the commonly used magnetic materials in MDT because of their chemical and physical properties which include their high permeability and high resistance to corrosion as well as their stability under ambient conditions [108].

MNPs are materials of micron size [109] and many are available commercially including ferromagnetic (super-paramagnetic) nanoparticles (NPs), paramagnetic NPs and diamagnetic NPs. Ferromagnetic NPs are more preferable in biomedical applications because of their biocompatibility, low toxicity, affordability, high magnetic moment, availability and tunable cellular uptake [110] [65]. Unlike paramagnetic and diamagnetic NPs, ferromagnetic NPs show response to a magnetic force even after immediately removing the applied magnetic field [111] [112]. Ferromagnetic (super-paramagnetic) NPs can be classified into two types; Superparamagnetic Iron Oxide (SPIOs) or (Fe_3O_4) which are greater than 50nm in diameter and Ultra-small Superparamagnetic Iron Oxide (USPIOs) which are smaller than 50nm [113]. The most popular MNPs used in biomedical application are Fe_3O_4 SPIOs [112].

Different sized MNPs have been documented for both *in vitro* and *in vivo* studies; 100 nm MNPs are typically used in human studies, including drug & gene delivery, and hyperthermia [112] and MNPs from 500 nm – 5 µm in size have been documented in animal studies [61]. The size of MNPs is a crucial parameter for reaching the target location without causing occlusion of blood vessels [114]. Large MNPs are useful as they resist the velocity of the bloodstream and hydrodynamic force that can be controlled by an external magnetic field. However, large MNPs can lead to aggregates forming in capillaries and other blood vessels, which can result in obstruction of the vessel and

occlusion of blood to tissues [114]. In contrast, it is difficult for MNPs in the micron size range to be controlled by a high magnetic field, as the velocity of the bloodstream is very high, enough to release the particle from the magnetic force and push them away [115]. In turn, a low gradient field can contribute to MNP aggregation even in case of small MNPs, due to the attractive forces between them. MNP aggregation can result in blood clot formation. Thus the size of MNPs is a crucial parameter that should be considered in MDT applications [116].

Coating of the MNPs is important for addressing the aggregation challenge, protection against corrosion and reduction of toxicity. MNPs are generally known to be highly reactive due to their high surface to volume ratio, hence the need to apply a coating to prevent corrosion. MNP materials should be coated to avoid the leaching of substances that can be potentially harmful to cells *in vivo* applications. In addition, coating is essential for the conjugation of the therapeutic agent to the MNPs. Different biocompatible materials are used to coat MNPs. These include polymers, activated carbon, silica or gold in order to prevent toxicity as well as reduce particle aggregation [112]. Apart from gold, because of its high cost [117], [118], different materials can be used for coating depending on the purpose or application. For example, for drug delivery: some polymers can be used for coating such as carbohydrates (dextran) [118], polyvinyl alcohol [119], for tumour targeting and MR imaging, starch [69] and proteins (e.g. albumin) [120] can be used and for immunoassay, lipids can be used [121]. It is important to take into account the application and the hydrophobic properties of the polymers, i.e. solubility in water and mechanical strength when selecting a suitable coating for the MNPs [107] [119] [122].

In order to enhance the attachment of the therapeutic agents to MNPs, organic linkers can be used. They also play an important role in controlling the release of the therapeutic agents. Examples of organic linkers include amine (-NH2), carboxylic acid (-

COOH), aldehyde (-CHO) and thiol (-SH) [107]. The typical structure of a MNP is shown in **Figure 1.8** below.
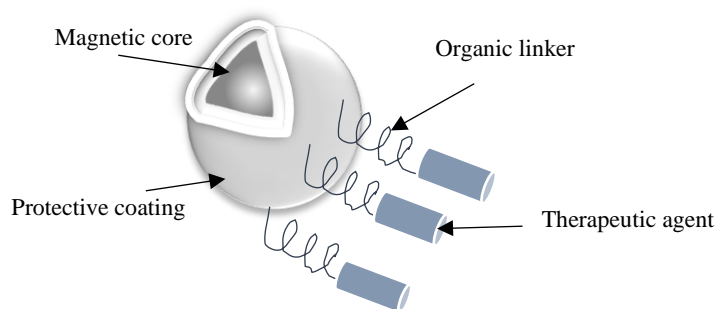
Figure 1.8: The general structure of a MNP consisting of magnetic core, protective coating and the organic linkers which are attached to the therapeutic agent.

Research into drug delivery has also revealed the potential of using other carriers such as naturally existing blood platelets and other biomolecules such as liposomes in delivering drugs in cancer treatment. For example, the body's natural platelets have been shown to be carriers in the delivery of drugs to the targeted tumour due to their size and ability to penetrate the BBB [123]. For instance, studies revealed that a chemotherapeutic drug called doxorubicin was successfully attached to the natural platelets without disrupting the structure of the platelets, hence, the potential to deliver drugs without being destroyed by the body's defence system [124] [125]. In addition, biomolecules called liposomes have been shown to have an ability to combine with several compounds including MNPs and therapeutic agents. As a result, liposomes can also be used as effective carriers in drug delivery for cancer treatment [126]. There are various studies focusing on the effectiveness of liposomes in drug delivery and the use of platelets, however, this is beyond the scope of the current study.

1.8.1 Application of MNPs

MNPs have several biomedical applications and their use depends on biocompatibility and their level of toxicity. In turn, these features are determined by the nature of the magnetic materials used, the size of the composite nanoparticles including the core and the coating component. It is evident from the literature that MNPs' application can be divided into two broad areas which include diagnosis and therapy. For example, it is well known that in diagnostic procedures, MNPs are used as contrast agents to enhance the quality of MRI images [127]. Apart from their role in the imaging of tissues and cells, the MNPs are also used for labelling and tracking individual cells [128]. In addition, MNPs play an important role in the delivery of therapeutic agents including drugs, genes, viruses and radionuclides, among others. The MNPs are able to combine and form complexes with the different therapeutic agents thereby facilitating their delivery into different sites. On the other hand, the delivery of the MNPs loaded with therapeutic agents can be driven by the use of an external magnetic field, i.e. MDT. Several examples of using MNPs in MDT applications have been widely discussed in literature. For example, MNPs can be conjugated with therapeutic viruses for gene delivery systems in cancer treatment [129]. In this case, the attachment of adenoviral particles to MNPs using an external magnetic field facilitates the protection of the virus from inactivation by the body's immune system and delivery to the target area [130]. MNPs attached with therapeutic viruses have a transfection rate *in vivo* (of NIG-3T3 cells) that is 3-4 times higher than therapeutic viruses lacking MNP functionalisation [131]. This result, therefore provides the basis for the potential use of therapeutic viruses in clinical treatments [132]. Another example for the application of MNPs in drug delivery for cancer therapy was demonstrated *in vivo* by using iron oxide NPs loaded with a chemotherapeutic agent (DOX) which was delivered into the lungs using an external magnetic field. The results

indicated that the MNPs were effective carriers for the delivery of chemotherapeutic agents in cancer treatment [85].

Magnetic hyperthermia is one of the applications of MNPs in cancer treatment. This involves the generation of heat by exposing the MNPs to an external alternating magnetic field [133]. This technique has been used since 1957 by [79] who was able to heat several tissues using γ -Fe_2O_3 ranging between 20-100nm exposed to a 1.2 MHz magnetic field. The positive outcome of this study led to the development of other models by other researchers which are being used up to the present day [134]–[136]. In general, this technique involves introducing the MNPs in the target area followed by the heating of these particles by applying an alternating current magnetic field. Heat is generated at a temperature of 42˚C (above the therapeutic threshold) and should be kept in place for at least 30 minutes to ensure the destruction of cancerous cells. Magnetic hyperthermia has the advantage of ensuring that the generated heat is focused on the targeted cells, hence, does not cause the damage of healthy cells. **Figure 1.9** below provides a summary of the biomedical applications of the MNPs.
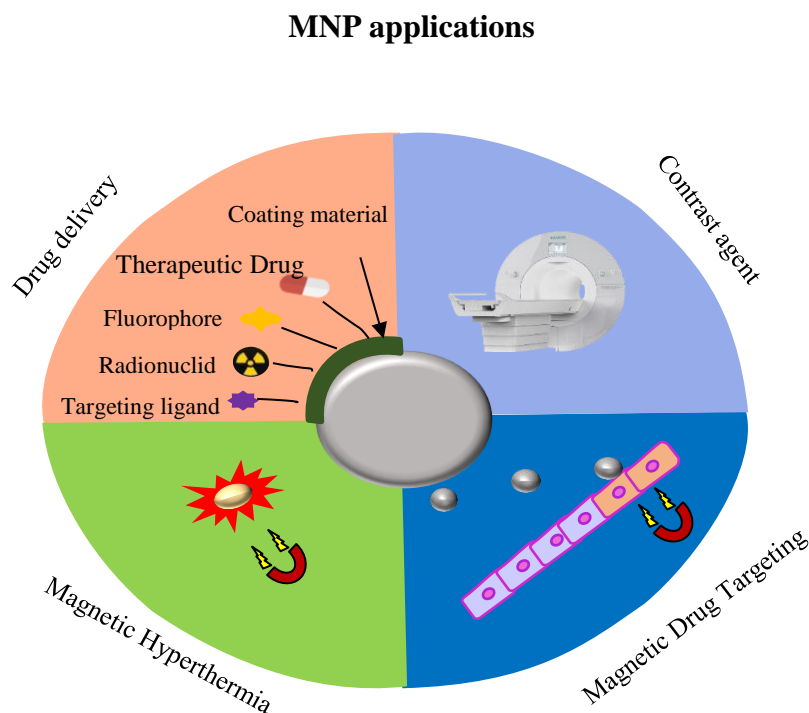
MNP applications

Figure 1.9: The main applications of MNPs

1.9 General Physics principles of applying external magnetic field on MNPs.

An applied external magnetic force on MNPs with a hydrodynamic fluid flow is considered in this scenario.

Three main forces are considered when a magnetic force is applied, these include; blood advection forces induced by blood plasma convection, magnetic drift induced by the applied magnetic field and diffusion forces induced both by Brownian diffusion [137] and the scattering effect that colliding and shearing red blood cells have on MNPs.

Before describing the three main forces, it is worth mentioning the magnetic field first.

1.9.1 Magnetic field

A magnetostatic field is described best by Maxwell's equations as follows [137]; (Bold letters indicate vector quantities).

$$\nabla \times \boldsymbol{H} = \boldsymbol{J}$$

$$\nabla . \boldsymbol{B} = 0$$

$$\boldsymbol{B} = \mu_\circ(\boldsymbol{H} + \boldsymbol{M}) = \mu_\circ(\boldsymbol{H} + x\boldsymbol{H})$$

Where,:

∇ : gradient operator [units/m]

$\vec{B}$: magnetic field [T]

$\vec{H}$: magnetic intensity [A/m]

$\vec{J}$: current density [A/m2]

$\vec{M}$: material magnetization [A/m]

x: magnetic susceptibility

$\mu_\circ$: permeability of a vacuum $4\pi \times 10^{-7}$ N/A2.

However, in this thesis only the magnetostatic field was considered as a permanent magnet was used. Hence, the magnetic field was calculated and plotted using FEMM software which is useful for magnetostatic problems.

1.9.2 Magnetic forces on MNPs

A ferrofluid consists of many magnetisable MNPs, which are mainly superparamagnetic. This means that MNPs are strongly magnetised in the presence of an

external magnetic field and then lose their magnetisation once the magnet is removed. Neglecting particle-to-particle interactions, which are small due to particle reorientations and anti-aggregation coatings, the magnetic force acting on each MNP under the effect of external magnet is given by

$$\boldsymbol{Fm} = (\boldsymbol{m} \cdot \nabla)\, \boldsymbol{B}$$
<div align="right">Equation 1.4</div>

Where (m) is the magnetic dipole moment of a MNP.

By assuming that the applied magnetic field is only acting in the y-axis, Eq 1.4 can be written as;

$$\boldsymbol{F_{m,y}} = \boldsymbol{m}\, \frac{dB}{dy} = V_m\, \varDelta x\, \boldsymbol{B}\, \frac{dB}{dy}$$

$$\boldsymbol{F_{m,y}} = \frac{V_m\, \varDelta\chi}{\mu_\circ}\, (\boldsymbol{B}.\nabla)\, \boldsymbol{B}$$
<div align="right">Equation 1.5</div>

Vm is the volume of the magnetic particle. In cases where a cell or anticancer drug is loaded with multiple MNPs and an aggregation of MNPs exists, the particles will generally behave as a single MNP.

$\Delta\chi$ is the relative magnetic susceptibility of the particle. This can be interpreted as a relationship between the induced magnetisation and the strength of the inducing field and this unique characteristic can be calculated for each type of MNPs in a given configuration. In MDT procedures, the amount of force that can be applied on the MNP is directly proportional to $\Delta\chi$, and this is the difference between the magnetic susceptibility of the particle and that of the external medium. Given that the normal biological tissue and fluids such as the blood have magnetic susceptibility that is usually negligible in comparison to the MNP, $\Delta\chi$ is equivalent to the magnetic susceptibility χ of the particle.

The external magnetic field and its spatial variation (magnetic field gradient) is expressed by the vector product with the gradient operator, (B·∇) B. The amount of force

that can be applied to a magnetic particle is proportional to the field strength, and this is true up to field strengths that approach the saturation magnetisation for a given particle (typically 0.5 <B< 1.0 T). The field strength depends on the strength of the magnetic device as well as the distance between the magnetic device and the MNPs.

It is worth mentioning that the magnetic force unit that was used in this study is T^2/m. This is for two main reason; 1) magnetic field strength was measured in Tesla, hence, field gradient was measured in T/m. Therefore, it was more convenient to measure magnetic force in T^2/m. 2) to convert from T^2/m to Newton it is required to know the actual volume of MNPs where this was not the main interest of this study. In the simulated Halbach models (using FEMM) the main interest was to measure the strength of the magnet at different distances where no MNPs was included, so the unit of the magnetic force that was used is T^2/m. For the rest of the experiments, the major interest for this study was to see trapping of MNPs at different distances, thus, the volume of MNPs was not calculated and is difficult to predict. Thus, using T^2/m as a unit of magnetic force was more convenient for this study and used for consistency throughout the thesis. However, we showed the relationship between MNPs size and magnetic force in Figures 1.9 and 3.3.

In the case of applying an external magnet to the MNPs flowing inside a single vessel, the following forces were considered;

1.9.3 Magnetic drift velocity (Stokes drag force)

When MNPs flow in the blood stream, the magnetic force described in Eq 1.5 is applied. MNPs will accelerate in the direction of this force until an equilibrium velocity (VR) is reached. The opposing force on a spherical MNP, which is called the Stokes drag force [138], is given by

$$F_D = 6\pi a\mu\eta V_R \qquad\qquad \text{Equation 1.6}$$

Where

  α: radius of the particle [nm]

  η : the dynamic fluid viscosity [kg m/s].

  V_R: equilibrium velocities [m/s]

  When both forces, F_m and F_D are equal, then the MNP has reached its equilibrium relative velocity;

$$Fm + F_D = 0 \qquad\qquad \text{Equation 1.7}$$

MNP size plays a major role in MDT, Figure 1.10 the relationship between F_m , F_D and MNPs size under the effect on magnet.
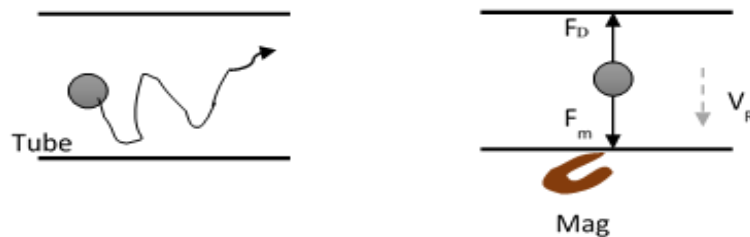
Figure 1.10: The behaviour of MNP; no magnet –left, side and under magnetic force (Fm) and drag force (FD)- right side.

1.9.4   Advection force

In any fluid flow, the fluid velocity profile in a tube or channel is curved. The highest value of the fluid velocity is at the centreline while zero value is found at the walls. This is because of a no-slip boundary condition. An example of this is water, where the curved shape is parabolic (Newtonian fluids). On the other hand, blood is a non-Newtonian fluid which is described as having plug flow. This is due to the clotting protein fibrinogen [137]. The fluid velocity of such flow can be expressed as;

$$\overrightarrow{v_B} = \ v_{Bmax}\ \left(1 - \frac{r}{R}\right) \qquad\qquad \text{Equation 1.8}$$

Where

$\overrightarrow{v_B}$: the blood velocity in [m/s]

v_{Bmax} : the maximum centerline velocity [m/s]

r: the radial location [m]

R: the radius of the vessel [m]

1.9.5   Diffusion forces

There are two main types of diffusion that occur for MNPs within a blood vessel, including Brownian thermal motion and particle scattering due to collisions with blood cells.

Brownian thermal motion refers to the random motion of MNPs under the action of thermal fluctuations and is calculated by a diffusion coefficient

$$D_B = \ \frac{K_B T}{6\pi\mu a} \qquad\qquad \text{Equation 1.9}$$

Here, K_B is the Boltzmann constant and T is the absolute temperature.

When blood cells collide with MNPs this causes particles to scatter, which can be considered as further diffusion. The coefficient of scattering for diffusion (D_S) is in the range $10^{-11} - 10^{-10}$m^2/s [137].

The overall MNP diffusion is thus described as the sum of Brownian and scattering diffusion;

$$D_{Total} = D_B + D_S \qquad \text{Equation 1.10}$$

Particle size and vessel radii affect the diffusion of nanoparticles. The largest diffusion coefficients occur in large vessels (arterioles and arteries) whereas cell scattering effects are high for small particles where Brownian diffusion is large. The smallest diffusion coefficients occur in small vessels (capillaries) where scattering effects are negligible and with large particles where Brownian diffusion is low. The typical range of total particle diffusion coefficients in humans is between 1×10^{-14} and 6×10^{-10}m^2 /s [137].

1.10 Challenge of using MDT in brain tumour treatment

There are several advantages associated with the use of MDT in biomedical applications. This includes the high level of precision in terms of delivering drugs to the target region resulting in the destruction of cancerous cells only without affecting the surrounding healthy cells [139]. However, the use of MDT is limited by a number of factors including lack of thorough understanding of how the MNPs interact with cells as well as their overall transportation in the human body [140] and the fact that the MNPs will be left permanently in the target tissues constituting the threat of causing long term side effects [141]. Although MRI is a powerful tool that can be used in MDT, its downside

is that it is large in size, meaning that there can be problems surrounding its portability and cost feasibility/effectiveness of the device is a major concern. In an effort to address the challenges associated with the use of MRI, the use of single permanent external magnet has been considered as an alternative. However, their weak magnetic field (range between 0.1-0.5T) makes it difficult to target deep tumours, i.e. brain tumours.

To address the cited limitations of single permanent external magnets, developing such magnets using the Halbach array technique has become an interesting area for many researchers. The following section discusses the development of Halbach array techniques for MDT and this is the focus of this thesis.

1.11 Halbach

As mentioned earlier, permanent magnets have been used in the design of MDT devices, however, they are limited in terms of treating deep tumours due to their weak magnetic strength. As a result, researchers have been exploring how the permanent magnets can be developed to produce stronger magnetic field to enable the treatment of deep cancers. Klaus Halbach discovered a way of arranging the permanent magnets to produce a strong magnetic field and his design became known as the Halbach array [142].

A Halbach array refers to a specific arrangement of permanent magnets which are equal in size, shape and magnetic flux property [143]. The array has a spatially rotating magnetisation pattern, which results in weakening the magnetic field on one side of the array, while boosting it on the other side, by at least a factor of 1.2 compared to other conventional permanent magnet arrays. The strong magnetic field is due to the superposition of field lines generated by the individual magnets. Figure 1.11 illustrates an example of a Halbach array model that shows the magnetisation orientation pattern which induces a strong magnetic field on one side. Due to the Halbach array properties, that is a

magnetic field on one side, lightweight, portable and inexpensive, makes Halbach arrays the best choice for this project (MDT).
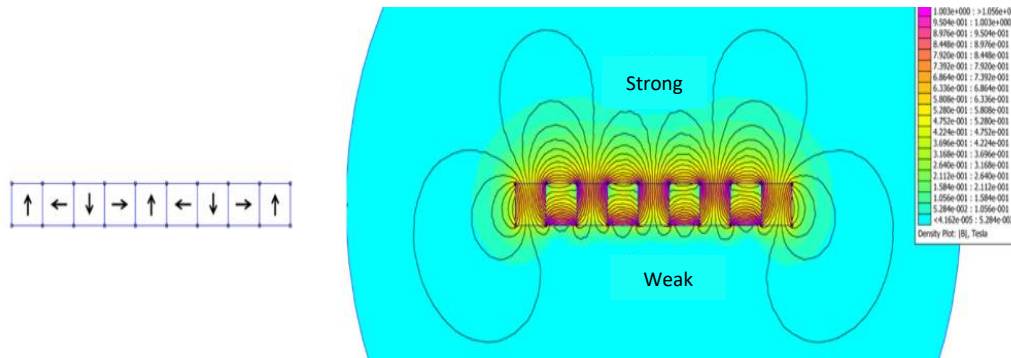
Figure 1.11: Halbach array pattern-left side and generated magnetic field-right side.

Halbach array design has been used extensively in industrial applications and researchers have also explored its use in biomedical applications. This thesis focuses on the development of Halbach arrays for cancer treatment. In this section, reference will be made to the historical development of Halbach array models and designs and specific studies involving the application of Halbach arrays in MDT.

The development of Halbach array magnetic devices has led to various studies including *in silico, in vivo* and *in vitro*. In general, most of the studies have been conducted *in silico* as a basic step towards the development of Halbach arrays to be used in MDT [144] [145] [146] [116].

In silico

A study conducted by Baun and Blumler aimed at the development of a Halbach array design to be used for guiding SPIONs [147]. They modelled Halbach arrays in

FEMM to generate a magnetic field of 0.5T. Their model consists of two layers of magnets in a Halbach cylinder shape ($Nd_2Fe_{14}B$), the inner layer had 16 magnets, in a dipole configuration and these were surrounded by 8 magnets in a quadrupole configuration. The whole model with an overall mass of 9kg was assembled and tested in the lab to steer SPIONs by mechanical rotation. It was considered that the model developed in this particular study was unsuitable for the present study because of the large size and low magnetic field which cannot adequately steer MNPs to deep target areas.

Barnsley et al. compared the effectiveness of Halbach arrays and other permanent magnet designs in steering SPIONs to target areas. This was achieved by developing a mathematical model in order to simulate the trajectory of the SPIONs as well as the effect of Halbach arrays and other permanent magnets on the trajectory of the particles. The study results indicated that Halbach arrays were more effective in directing SPIONs to the target areas compared to other permanent magnet designs [148].

The Halbach array design should produce a strong magnetic field and field gradient in order to trap MNPs in MDT. In a study conducted by Odenbach, this was demonstrated using a flow phantom with a half-Y branched tube design. The main tube represented the artery from which a tumour supplying artery was simulated by side branches[149]. The behaviour of the MNPs was affected by the viscosity of the magnetic suspension, and on the other hand, the viscosity was affected by the magnetic field strength. When the magnetic field was stronger, more MNPs were trapped by the magnet in the side branch closer to the magnet.

In vitro

Researchers have been exploiting Halbach array designs to develop portable magnets that can be used in MDT at relatively deep positions in the body. In a study by

Kopcansky et al., a Halbach array magnet consisting of 36 pyramidal shaped magnets was constructed with a magnetic field strength of 0.38T which reached between 1.5 to 2cm deeper than the simple classical prism permanent magnet (where no different magnetic orientations are set) [150].

In another study by He et al. a portable Halbach array magnet was developed using three permanent blocks, each measuring 5cm $\times$ 4cm $\times$ 4cm [151]. The orientation of the magnets was as follows, the magnetisation of the middle magnet was directed at 90^0 while the magnetisation of the two magnets on the sides was directed at 0^0 and 180^0 respectively. As a result, the magnetic strength generated in the middle of the magnet was 1.26T at 0 cm and 0.28T at 3cm away from the magnet. Although the design generated a relatively good magnetic field strength, its downside was the overall large volume making it difficult to be applied to patients for MDT. Also, its configuration requires use of other materials, for example, the use of screws to keep the magnets in place which can be a challenge when assembling the device.

In vivo

A few studies have been conducted *in vivo* to evaluate the effectiveness of Halbach arrays in MDT. One of the studies demonstrated the use of an external Halbach array magnet helps to facilitate the movement of MNPs to the target site [152]. In their study, magnetoliposomes were administered intravenously into a rat-tail and an external magnet with magnetic field strength of 0.35T was placed on the right kidney of the rat. For comparison purposes, no magnet was placed on the left kidney. The results showed that magnetoliposomes were retained in the right kidney and this provided evidence that use of a Halbach array external magnetic field was effective in terms of guiding the MNPs to the target site.

1.12 Project Hypotheses

Brain tumours constitute one of the major medical challenges in today's world. They can affect people of any age including children; however, they are more common in older adults.

Survival rates are higher in young people compared to old adults. Different treatment methods including chemotherapy and radiotherapy have been explored, however, it has been shown that brain tumour treatment using these traditional methods is not always effective. The use of external magnets to guide the MNPs loaded with drugs is a promising alternative treatment method, however, studies have shown that it is difficult to target brain tumours at a further depth. There is, therefore, a need to explore alternative ways of increasing the magnetic field strength to ensure that magnetised chemotherapeutic agents can be directed to deeper brain tumours.

In this thesis, we **hypothesise** that an inexpensive, portable, powerful and external Halbach array could be designed, modelled and simulated to be used for MDT with the purpose of targeting tumours, such as brain tumours at depths of between 5cm or greater.

1.13 Research aims and objectives

We used *in silico* and *in vitro* modelling to design, build and evaluate Halbach arrays for generating magnetic field gradients and forces to target brain tumours. The ultimate goal is to generate a personalised magnetic treatment plan based on MRI scans for patients with deep tumours. Figure 1.12 below illustrates the general goal of using a HA in MDT.
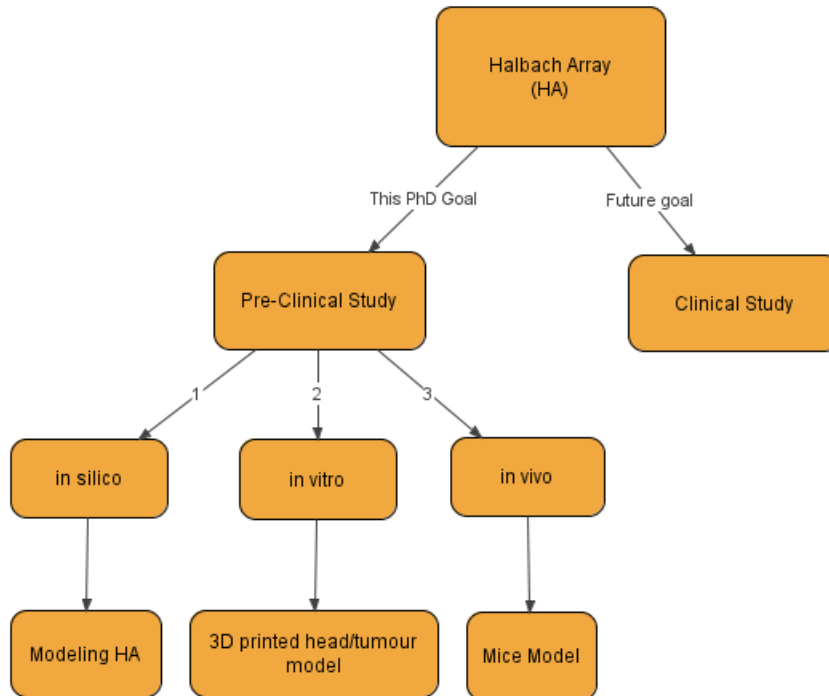
Figure 1.12: Sketch of general aim of Halbach array.

This project is pre-clinical, so in line with the stated goal, a number of steps and procedures were followed as highlighted in the four experimental chapters indicated below:

<u>Chapter 3</u>

The aim was to develop Halbach arrays models using FEMM software with a view to identifying the most effective model for brain tumour treatment. The following objectives were formulated:

- To calculate the magnetic force required to trap MNPs with different sizes using Lua scripting.

- To develop and optimise Halbach array models in order to obtain the highest magnetic field/field gradients to reach a maximum target depth.

Chapter 4

The aim was to assemble Halbach array models which were simulated in FEMM in chapter 3 and to evaluate their potential effectiveness for MDT in brain tumours treatment by measuring their magnetic field strength, field gradient and magnetic force at different distances. The following objectives were formulated:

- To assemble Halbach array magnets based on the FEMM models.

- To measure the strength of magnetic field using a Gaussmeter (GM 08, HIRST, Magnetic instruments Ltd), as well as to calculate the field gradient and magnetic force for each layer of each model at different distances.

- To optimise the selected Halbach array magnet for the MNP trapping experiment with a 3D tumour/head phantom model.

- To determine the maximum depth where the tumour could be located within the brain using the 3D head/tumour phantom model.

Chapter 5

The aim of this chapter was to demonstrate the ability of the Halbach array of model 2 to trap different concentrations of SPIONs (Fe_3O_4) at different distances. The following objectives were formulated:

- To use a 3D printed phantom flow model with plastic and bio-phantom tumours to assess the trapping ability of SPIONs at different distances

- To use a custom-made vasculature model to investigate the amount of time required for the SPIONS to be trapped within the vasculature tubing and how long the SPIONS remain trapped in the target area after removing the Halbach array magnet.

- To apply different techniques including magnetic resonance image (MRI), inductively coupled plasma microscopy (ICP) and nuclear magnetic resonance (NMR) to assess iron trapping within the models.

Chapter 6

The aim of this chapter was to evaluate the uptake of SPIONs and the viability of the brain cells and brain tumour cells following uptake. In line with this, the formulated objectives were:

- To use transmission electron microscopy (TEM) to assess the SPION size and evaluate the intracellular uptake of SPIONs in the cells.

- To assess cell viability following incubation of the different cell types with SPIONs for 24h. Flow cytometry was used to measure cell death using Propidium iodide (PI).

The above section summarises the aims and objectives of all the experimental chapters. The other chapters, for example, chapter 2 focuses on the discussion of the materials and methods employed in the study, and **chapter 7** presents the summary of the key findings and highlights the potential areas for further studies.

Chapter 2

Materials and Methods

2.1 Materials

List of reagents

Reagent	Company
Absolute Ethanol	Thermo Fisher Scientific
Acetone	Thermo Fisher Scientific
Astrocyte Growth Supplement	ScienCell
Basal medium	ScienCell
Collagen IV	Thermo Fisher Scientific
DAPI staining solution	Lonza BioWhittaker Ltd
Dimethyl Sulfoxide (DMSO)	Sigma Aldrich
DPX Mounting medium	Sigma Aldrich
Dulbecco's Modified Eagle's Medium (DMEM) Ultraglutamine, 4.5g/L glucose Lonza DMEM medium	Lonzo BioWhittaker Ltd
Eosin	Sigma-Aldrich
Eosin Y	Thermo Fisher Scientific
FACS buffer	Lonza BioWhittaker Ltd
Ficoll-Paque	Sigma-Aldrich
Human AB serum	Lonza BioWhittaker Ltd., Wokingham, UK
Hydrochloric acid	Sigma Aldrich
Immune-mount	Sigma-Aldrich
Iscove's Modified Dulbecco's Medium (IMDM)	Lonza BioWhittaker Ltd
L-Glutamine (4mM)	Lonzo BioWhittaker Ltd
Nitric acid	Sigma Aldrich
Nuclease free water	Qiagen
Paraformaldehyde	Sigma Aldrich
phosphate buffered saline (PBS)	Thermo Fisher Scientific
Phosphate Buffered Saline (PBs)	Lonzo BioWhittaker Ltd
Propidium iodide (PI)	Thermo Fisher
ProLong Gold Antifade mountant	Invitrogen
Potassium Ferranocyanide	Sigma Aldrich
Super PAP pen	Thermo Fisher Scientific
Trypan blue	Sigma-Aldrich
Trypsin/EDTA	Lonzo BioWhittaker Ltd
TO-PRO-3	Thermo Fisher

List of materials

Material	Supplier
Bio tumour phantom	PureImagingPhantom

Block of steel	Magnet Expert Company, UK
Coverslips	Scientific Laboratory Supplie
Cytospin slide champers	Thermo Fisher Scientific
Falcon tube	Thermo Fisher Scientific
IRON (III) OXIDE	Sigma-Aldrich
Loctite Control Super Glue Adhesive	First4Magnets
Masterflex® L/S® Series Peristaltic Pumps	Cole-Parmer
Neodymium Iron Boron (NdFeB)-grade N52	Magnet Expert Company, UK
Silicon tubing	Fisher Scientific UK Ltd
Superflex clear sealant	Fisher Scientific UK Ltd
Superfrost Plus Microscope Slides	Thermo Fisher Scientifi
Steel sheet of 30	Magnet Expert Company, UK
Syringe pump	Master Dual Pump,WPI
Tissue culture flasks (Nunc EasYFlask) $25cm^2$; $75cm^2$; $125cm^2$	Thermo Fisher Scientific
Vials, Bijou; Polypropylene	Fisher Scientific UK Ltd
3D tumour/head phantom	Advanced Manufacturing Research Centre (AMRC), Sheffield, UK

List of equipment and Apparatus

Equipment and apparatus	Company
Automated Cell Counter	BIO-RAD
Bench centrifuge	SANYO
Compound light microscope	Olympus
Cytocentrifuge	Thermo Fisher Scientific
FACSCalibur	Becton Dickinson
Gaussmeter (GM 08)	HIRST Magnetic instruments Ltd
Inductively coupled plasma atomic emission spectroscopy (ICP-AES)	SPECTRO
Incubator	SANYO
Laminar airflow hood	Heraeus
Light microscopy	Leica DM1000
Micropipette	Eppendorf
Nikon A1 Confocal	Nikon
Pipetboy	Integra
Refrigerator	BioCold
Sensitive balance	Sartorius
Transmission Electron Microscopy (TEM)	FEI Tecnai Biotwin
Water bath	Grant
3T MRI	GE Healthcare, Milwaukee, USA
9.4T NMR	Bruker BioSpin, Coventry, UK

List of cell lines

Name	Provided by	Original resource
Human astrocyte cells (HA)	Dr.Claire Garwood, SITraN, The University of Sheffield	ScienCll
Human Brain Microvascular Endothelial (hBMVEC/D3)	Dr. Julie Simpson, SITraN, The University of Sheffield	Cedarlane, Canada
Human brain tumour cells (U138MG)	Dr.Spencer Collis, Oncology and Metabolism, The University of Sheffield.	ATCC

List of commercial kits

Kit	Company
AM kit	ScienCll
EGM-2 MV bulletkit	Lonzo BioWhittaker Ltd

List of software

Software	Supplier
Excel	Microsoft office 2018
Fiji	https://imagej.net/Fiji [184]
Finite Element Method Magnetics (FEMM)	http://www.femm.info/wiki/HomePage
GraphPad Prism 7	Graph Pad Inc.

2.2 Methods

2.2.1 FEMM modelling

Finite Element Method Magnetics (FEMM) is a finite element software bundle used for solving 2D planar in low frequency magnetics and electrostatics problems (http://www.femm.info/wiki/HomePage). The bundle consists of an interactive shell encompassing graphical pre- and post-processing and includes a mesh generator and various solvers. In addition, a scripting language, Lua 4.0, is integrated with the

programme. Lua was used to create batch runs of SPIONs. In this project, FEMM was used to model Halbach array magnets of 1 cm^3 with different magnetisation orientations and Lua scripting was used to run the simulation of SPIONs movement under the effect of magnetic force.

To create a FEMM model; firstly, the magnetic problem option was selected. Then, the type of problem was selected as axisymmetric. In order to draw the model graphically, the nodes mode was also selected to start drawing the model at a desired size, e.g. 1×1cm. Then each node was connected using segment lines. After that, the material type of the magnet was defined, for this study - a Neodymium-Iron-Boron-N50 magnet. It was important to draw the model within a defined boundary to create magnet flux density plots. In this model, "air" was selected as the material type of the boundary. Once the model was completed "mesh" was run to ensure that each magnet in the model was included in the simulation. Finally, the simulation of the model was run and the model was then ready for analysis by plotting the flux density. The details of each model are discussed in chapter 3.

2.2.2 Halbach array assembly

Next the Halbach array was assembled based on the FEMM models. Each magnet was placed on a steel sheet of 30×30 cm, which was used to hold and keep the magnets in place. An adhesive super glue (Loctite Control Super Glue Adhesive), was used to stick the magnets together. After gluing two magnets, a block of steel was placed on top of the glued magnet faces to hold them together for several hours (between 7 and 24h). After that, the steel block was removed and the next magnet placed in position. This process was repeated until the assembly was complete. The strength of the magnetic field was measured using a Gaussmeter (GM 08). The Halbach arrays were then used to assess their ability to trap SPIONs at different distances.

2.2.3 Trapping SPIONs in a flow fluid system using Halbach arrays

2.2.3.1 Flow model of 3D tumour/head phantom

To test the ability of the Halbach arrays to trap SPIONS, a 3D phantom flow model was made by Advanced Manufacturing Research Centre (AMRC), University of Sheffield, UK. A 3D head was printed based on optical and MR scan data, which geometrically mimics the surface of the head of a patient. Tumours were also printed, these were made of a plastic synthetic polymer and were approximately 3 cm in diameter (typical of a human brain tumour) [153]. The tumours had a complex network on the inside and had an inlet and outlet for connecting to a flow system using plastic tubing of 1 mm diameter. A peristaltic pump, infusion rate of 10ml/min (Master Dual Pump, WPI) was used to pump SPIONs (Fe_3O_4) through the tumour. The SPIONs were pumped through silicon tubing of 1mm internal diameter, which was connected to the tumour using a Superflex clear sealant. The tumour was designed so that it could be placed at different distances underneath the 3D printed head i.e. 0, 5 and 10cm away from the head to mimic the potential locations of the tumour within the brain. A Halbach array was then placed on top of the 3D printed head in order to trap SPIONs in the tumour. A range of SPION concentrations was used including 0.1, 1, 5, 10, 20 mg/ml. The experiments were performed in two parts; the first part was to flow SPIONs with different concentrations. Additional techniques were used to validate the trapping of SPIONs such as 3T MRI, T2* and ICP. See **Figure 2.1** for a schematic.

Magnet

3D printed tumour with holder

3D printed head

Flow direction

Flow direction

Tube

Tube

Collected SPIONs

Matrix grid

Pump

SPIONs in a tube
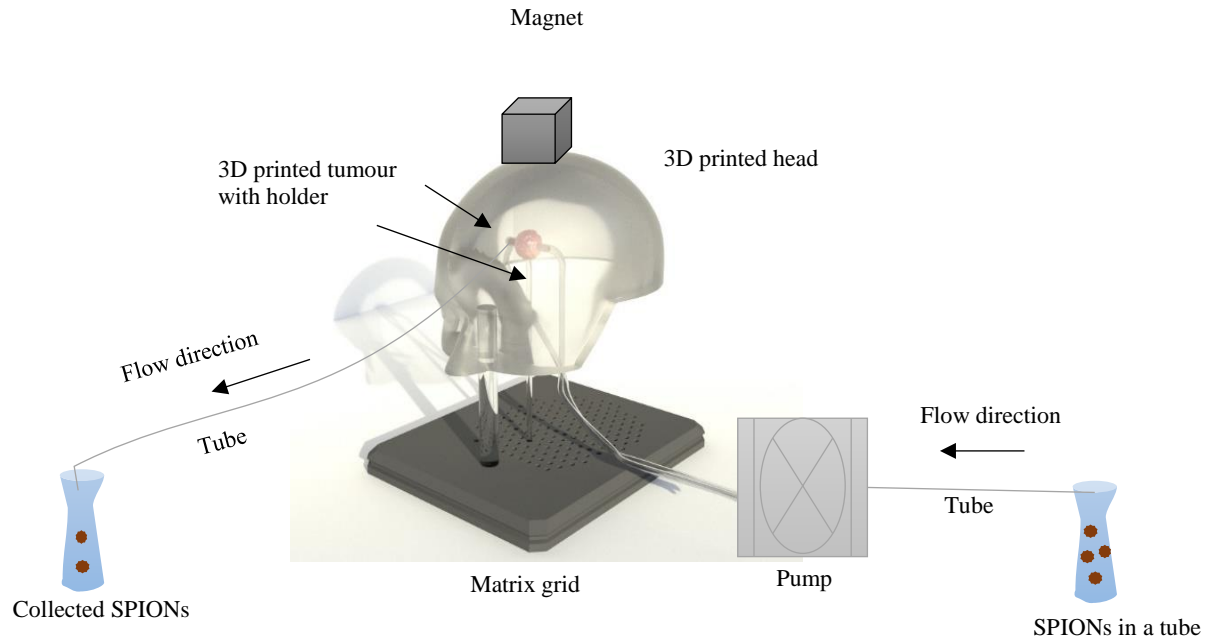
Figure 2. 1: 3D phantom flow model- Plastic tumour model

2.2.3.2 Flow model 3D Bio-phantom tumour

A Bio-phantom model was used to mimic a brain tumour where the tumour tissue was made from a unique composition of an ultra-soft urethane based rubber developed by Pure Imaging Phantoms (UK). The material is realistic in terms of ultrasound and mechanical properties and suitable for medical imaging such as ultrasound, MRI and CT. The components of the tumour phantom were designed using a computer-aided design software (CAD) based on real anatomical models extracted from MRI scans of actual patients. The models were then used to 3D print moulds which were later used to cast the tumour and the entire phantom. The advantage of this model is that it is suitable for MRI scans where the T1 and T2 values were mimicked. This was achieved by applying a solid homogeneous piece of material that had MR properties close to the average properties of human brain tissue. The tumour used also had a complex network from inside and had two inlets to be connected to the flow tubes.

To create a flow model, the tumour was connected to plastic tubing of 1 mm diameter which was the size of the tumour inlets, and then it was attached to the main tubing model - U shaped plastic tubing of 3 mm diameter creating a complex vasculature model using a Superflex clear sealant (**Figure 2.2**). This model was connected to an advanced peristaltic pump from Cole-Parmer (Masterflex® L/S® Series Peristaltic Pumps, model # 77200-62). This pump was able to infuse the flow at 150 ml/min to mimic the blood flow rate in human vessels. A Halbach array was placed on top centre of the complex tubing model, which had 3mm internal diameter. The tumour was located 5 cm away from the magnet. SPIONs of 5mg/ml were pumped through the model using a pump at 150 ml/min speed of rate. The aim of this experiment was to assess the MNP trapping ability of our Halbach array and to image the trapped SPIONs using a 9.4T MRI.
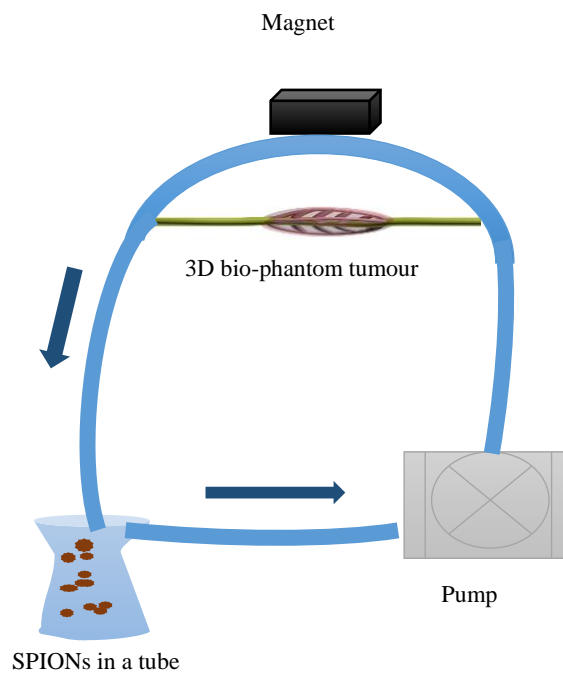
Figure 2. 2: 3D phantom flow model- Bio-phantom tumour model

2.2.3.3 3T MRI

The trapped SPIONs in the 3D printed plastic tumour phantom was visualized using a dedicated 3T neonatal MRI, located in the Neonatal Intensive Care Unit, Jessop Wing, Sheffield. The images were scanned using a dual gradient echo sequence (TE= 4.60ms, 20ms) to measure T2* as described below.

2.2.4 MNP quantification

2.2.4.1   MRI

The trapped SPIONs in the bio-phantom tumours were visualized using a 9.4T (400MHz) NMR, which was operated by a Research Fellow Dr. Steven Reynolds.

2.2.4.2   T2*

In MR images, T2* relaxation time refers to the decay of transverse magnetisation caused by spin-spin relaxation due to magnetic field inhomogeneity. Accurate measurements of $T2^*$ in the presence of macroscopic magnetic field inhomogeneity is problematic due to signal decay resulting from through-slice dephasing. The two-point method used here, that is, the in-phase and opposed-phase MR imaging allows reliable measurements of $T2^*$. This approach allows the signal decay due to through-slice dephasing to be characterised and removed from the data thereby facilitating an accurate measurement of $T2^*$ even at very high magnetic field. However, it is worth bearing in mind that the method has got its limitations. For instance, other factors such as large voxel size and increased field strengths can increase the $T2^*$ sensitivity of the sequence. Both of these factors cause more dephasing that is due to susceptibility effects. When compared to the three-dimensional GRE sequences, two-dimensional GRE sequences are more sensitive to the deleterious $T2^*$ effects from air-tissue interfaces or implants because of the thicker sections (and generally larger voxel sizes) used in two-dimensional imaging. In addition, change in oxygen

saturation during specific tasks changes the local T2* which leads to the blood oxygen level-dependent effect seen at functional MR imaging [154].

Iron (SPIONs) in tumours were quantified by measuring the ratio of the signal intensity (SI) in images acquired with different echo times. In order to calculate T2* of SPIONs in the 3D plastic tumour model, a contour was drawn over the tumour on one image and copied to the other echo. The mean value of both region of interests (ROIs) were taken to do the calculation [155]. The signal intensity ratios (SIRs)-pixel values were extracted from the same region of interest from each tumour for scans with two different echo times i.e. TE 4.60 ms and TE 20 ms. This was applied for each tumour with the different SPIONs concentration. The following equation was applied to calculate T2*;

$$T2^* = \frac{-\Delta TE}{\ln(^{I_{TE2}}/_{I_{TE1}})}$$

Where $^{I_{TE2}}/_{I_{TE1}}$ is SIRs of TE_2 20 ms and TE_1 4.60 ms respectively.

2.2.4.3 Inductively coupled plasma Atomic Emission Spectrometer (ICP-AES)

Inductively coupled plasma atomic emission spectroscopy (ICP-AES) was used to measure the concentration of trapped SPIONs. The technique was carried out by Mr Neil Bramall in the Faculty of Science Mass Spectrometry Centre in the Department of Chemistry. In general, ICP is an analytical method for chemical analysis of elements. When the element is ionised in the ICP process, electromagnetic radiation is created at specific wavelengths. Therefore, the concentration of each element can be measured by measuring the strength of the emission. A Spectro-Ciros-Vision Inductively Coupled Plasma Atomic Emission Spectrometer ICP-AES was utilized to calculate the quantity of Fe as a ratio of metal ions for the SPIONs used in this project. Different MNP

concentrations were dissolved in Aqua Regia (King's water a mixture of concentrated nitric and hydrochloric acids (HCL) at a molar ratio of 1:1 of nitric acid and HCL. 1ml of the SPION sample was added to 1ml of Aqua Regia solution and diluted in 8 ml of dH_2O. The samples were kept for 24 hours before ICP. Fe content (mg/l) was determined from atomic absorption [156].

2.2.5 White blood cell isolation

The Sheffield Blood Transfusion Service supplied human platelet-depleted waste buffy coats, this was under the ethics of Dr Munitta Muthana (SMBRER 139). In these experiments we wanted to mimic SPIONs as though they were in circulation. Red blood cells were not used as these coagulate, however white blood cells (WBCs) survive better in culture [157].

In order to isolate WBC, Ficoll density gradient centrifugation was carried out. To do this, 20ml of blood was diluted with 30ml of PBS in a 50 ml falcon tube. Then, 30 ml of diluted blood was carefully pipetted onto 20 ml of Ficoll-Paque. The mixture was centrifuged at 1400 rpm with the brake off for 40 minutes. As a result, 4 layers were formed including Plasma, WBCs "creamy layer", Ficoll and red blood cells. After that, WBCs that were isolated by pipette and washed twice in PBS. After the centrifugation, complete medium consisting of IMDM medium supplemented with 2% human AB serum and 4mM L-Glutamine was used to re-suspend the cell pellet. To count the cells, a haemocytometer cell count machine (Bio-Rad) was used. This eliminates any contaminated red blood cells from the cell count. Finally, 300,000 cells were seeded with 2ml of complete medium into a 6 well-plate and incubated for 24 hours at 37∘C, 5% CO2 [157]. After 24 hour incubation time, SPIONs of required concentrations i.e. 0.1, 1, 5, 10, 20 mg/ml were added to WBCs in each well and kept in the incubator for 24 hour prior

use. WBC-loaded SPIONs were used in trapping experiment in the presence of the Halbach array in the 3D head and tumour model. They also were used to evaluate SPION uptake, distribution and cell viability.

2.2.6 Cell culture

2.2.6.1 Human astrocyte cells-HA

Astrocyte cells were originally isolated from human brain (cerebral cortex). They were provided by Dr.Claire Garwood, SITraN. The University of Sheffield. They were received in a 6 well-plate at passage one and cultured in astrocyte medium (AM) that consisted of 500 ml of basal medium, 10 ml of fetal bovine serum (FBS), 5 ml of Astrocyte Growth Supplement (AGS) and 5 ml of penicillin/streptomycin solution [158]. The cultured cells together with the medium of 9 ml were kept in a T75 flask and incubated at 37°C with 5% CO_2 in an incubator. Because the components of AM are light-labile, the medium was kept in dark bottles and not exposed to light for extended periods. After using, the medium was stored at 4°C for no longer than a month.

2.2.6.2 Human brain tumour cells -U138MG

Human brain tumour cells (U138MG) were received in a frozen vial at passage number (3), provided by Dr. Spencer Collis, Oncology and Metabolism, The University of Sheffield. The cells were thawed and cultured in Dulbecco's Modified Eagles Medium (DMEM) with 10% FBS and 5% Non-essential Amino Acids (NEAA). The cultured cells with 9 ml medium of were kept in T75 flask and incubated at 37°C with 5% CO_2 in an incubator [159]. It is recommended that the medium should be stored at 4°C for no longer than a month. The tumour cells stored as for the astrocyte cells.

2.2.6.3 Human Brain Microvascular Endothelial Cells

(Hbmvec/D3)

The Human Brain Microvascular Endothelial (Hbmvec/D3) are adult human brain microvascular endothelial cells. They were provided by Dr Julie Simpson, SITraN, The University of Sheffield. The cells were cultured in complete EBM-2 medium that consisted of 500 ml EBM-2 media, 200 µl of Hydrocortisone, 500 µl Ascorbic Acid, 12.5 ml FBS, 5 ml Penicillin Streptomycin (Pen/Strep). All the growth factors including 125 µl human epidermal growth factor (hEGF), 125 µl Insulin-like growth factor (IGF), 125 µl Vascular endothelial growth factor (VEGF) and 500 µl human Fibroblastic Growth Factor (hFGF) were pooled together and divided into 10 aliquots of 87 µl each. Each aliquot was then added to 50 ml of EBM-2 medium (endothelial basal medium) each time before use, as GFs have a short life span [158]. The cultured cells together with the medium were kept in a coated T75 flask and incubated at 37°C with 5% CO_2 in an incubator.

To make the collagen coat; the collagen was diluted with distilled water to make a final concentration of 150 µg/ml. Before transferring the cultured cells to the flask, the flask was coated with 5 ml collagen IV and left in the incubator for at least an hour. After one hour, the collagen was removed and the flask was washed with 4 ml PBS once and then left in the hood to dry [158]. The collagen was stored at 4°C, should not be kept for more than a month.

2.2.7 Cell harvesting

This procedure was applied to all types of cells. When the cells were confluent at 70-80%, the medium was carefully removed and the flask was washed with 4 ml PBS once and the PBS was then removed. In order to detach the cells from the flask, 3ml of trypsin-Ethylenediaminetetraacetic acid (EDTA) (170,000 U Trypsin/L and 200 mg/L EDTA) was added to the cultured cells, and then the flask was kept in the incubator for 5 min. After

that, the flask was removed from the incubator and to ensure complete detachment, a gentle tapping on the side of the flask with the palm of the hand was applied. The cells were then observed under the microscope. The contents of the flask were then transferred into a falcon tube. Trypsin/EDTA was neutralised in an equal volume of culture medium in preparation for centrifugation (Sanyo® Harrier 18/80). The speed of the centrifuge varied depending on cell type and their sensitivity, for example;

- o 650 g for 6 minutes for endothelial cells.
- o 600 g for 5 minutes for astrocyte and brain tumour cells.

The supernatant was discarded and the cells were resuspended in culture medium and counted in trypan blue (Sigma-Aldrich®) to determine cell viability using a TC20 Automated Cell Counter (Bio-Rad®). Live cells were trypan blue negative.

2.2.7.1   Seeding densities

The cells were seeded as described below:

1. For flow cytometry experiments, cells were seeded onto 6 well plates at 300,000 cells/well in 2ml of culture medium.
2. For Prussian blue assays, cells were seeded on to 6 well plates with 13mm coverslips (BDH Cover glass), using a seeding density of 500,000 cells/well in a final volume of 1ml of culture medium.

For the TEM assays, cells were plated at a seeding density of 1000 cells/well in a final volume of 200 μl of culture medium in 6 well plates.

2.2.7.2   Incubation of SPIONs with the cultured cells

When the cells were 60%-70% confluent, the culture medium was removed from the 6 well plates and then washed with 2mL PBS then 2mL of fresh pre-warmed medium

was added to each well. After that, SPIONs of different concentrations i.e. 0.1, 1 and 5 mg/ml were added to the cells and kept in an incubator for 24 hours. Endothelial cells, astrocyte cells and brain tumour cells were seeded at a density of 300,000 cells/well in 2ml of medium.

2.2.8 Flow cytometry to assess cell viability

Flow cytometry was used to assess cell viability after adding SPIONs to the cells and incubating them for 24 hours. After that, cells were harvested as described above. 400μl of the cells were transferred from the falcon tube into and 2μl of Propidium Iodide (PI) was added to each tube to assess cell death. Propidium iodide is a membrane impermeant dye that is generally excluded from viable cells. It binds to double stranded DNA by intercalating between base pairs of dead cells [160]. Cell death was measured on a FACS Calibur system where 10,000 events were measured from each sample (equivalent to 10,000 cells). FlowJo® software was used to analyse cell death by generating a fluorescent dot plot based on changes in forward scatter (FSC-H) and side scatter (SSC-H).

2.2.9 Prussian blue staining to visualise MNP uptake

Prussian blue staining was used to visualise SPION uptake by cells. After incubation with SPIONs cells were harvested and 5×10^5 cells/ resuspended in 1 ml of PBS in preparation for a cytospin on glass slides [161]. 1 ml of each this cell suspension was added to a slide chamber and centrifuged at 800 rpm for 5 min. The slides were carefully removed from cytocentrifuge and left to dry prior to staining.

To fix the cells on the slide, each slide was dipped into;

o   95% of ethanol for 5 min, then;

o   70% of ethanol for 5 min then placed under running water for 5 min.

2% of a 1:1 dilution of 1M Hydrochloric acid (1 M HCL) and 2% Potassium Ferranocyanide was mixed in a glass bottle inside the fume hood and then the mixture was added to the slides and left for 30 min. The slides were washed again by immersing them in PBS three times for few seconds and then the slides into 1% eosin for 5 min, then 70% ethanol followed by 95% of ethanol. This was followed with acrylonitrile butadiene styrene (ABS2) for a few seconds and then left in ABS1 prior to mounting. The slides were transferred to the fume hood to mount them by attaching them to coverslips using immune-mount. Light microscopy (Leica DM1000) was used to assess MNP uptake by viewing the slides at 40x magnification. Mitotic Images plus 2.0 Software was used to take the images.

2.2.10   Transmission Electron Microscopy (TEM)

TEM was used in the Department of Biomedical Sciences (FEI Tecnai Biotwin) operated at 120kV with an Orius 1000 camera. TEM studies were carried out with the support of Mr Chris Hill in the Department of Biomedical Science at The University of Sheffield.

2.2.10.1   TEM sample preparation

After cell harvesting, cells were transferred into 1ml Eppendorf tubes and resuspended in PBS. A droplet of this buffer was added onto a carbon-coated copper grid for one minute and excess fluid was removed using tissues to leave a thin layer of sample over the TEM grid. This was also applied to the samples containing SPIONs only.

2.2.10.2   Preparation of cells for TEM

The cells were fixed in fresh 2.5%-3% Glutaradehyde[NB] in 0.1M Phosphate buffer overnight at 4^0C. 0.1M phosphate buffer was used to wash the specimens two times with 30 min intervals at 4^0C. Post fixation; 2% aqueous osmium tetroxide was added for 1 hour

at room temperature and washed in the buffer as above. The following procedure was then applied at room temperature;

o Dehydration was performed through a graded series of ethanol concentrations:

o 75% ethanol for 15 min.

o 95% ethanol for 15 min.

o 100% ethanol for 15 min.

o 100% ethanol for 15 min.

o 100% x2 ethanol dried over anhydrous Copper sulphate for 15 min.

The specimens were deposited in propylene oxide, which is an intermediate solvent, for two changes of 15 min duration. For infiltration, the specimens were placed in a 50/50 mixture of Propylene oxide/Araldite resin at room temperature overnight. After this, the specimens were placed in full strength Araldite resin at room temperature for 6-8 hours. Then they were placed in fresh Araldite resin for 48-72 hours at 60°C. Semi thin sections about 0.5um thick were cut on a Reichert Ultracut E ultramicrotome and stained with 1% Toluidine blue in 1% Borax. Ultrathin sections, about 70-90 nm thick, were cut on a Reichert Ultracut E ultramicrotome and stained for 25 min with 3% of Uranyl Acetate followed by staining with Reynold's Lead Citrate for 5 min. The sections were observed using a FEI Tecnai TEM at an accelerating voltage of 80Kv. A Gatan digital camera was used to take electron micrograph images.

2.2.10.3   SPION size determination by TEM

TEM was carried out to measure the size of SPIONs; this was taken arbitrarily from prepared samples. SPIONs were measured by analysing TEM-SPIONs randomly at 100 and 200 nm magnification scales. ImageJ was used to measure the length of selected particles manually.

2.3   Statistical analysis

All statistical analysis was achieved utilising GraphPad Prism (GraphPad Inc, San Diego, CA, USA). Statistics were analysed utilising suitable statistical tests and post tests as described in the figure legends. Microsoft Excel was also used to prepare data.

Chapter 3

Developing Halbach arrays for Magnetic Drug Targeting (MDT):

Modelling Halbach Magnet Arrays.

3.1   Introduction

The current challenge when using external magnets in MDT is the distance between the magnet and the target organ [61]. The magnetic field/field gradient, and hence the magnetic force, is inversely proportional to the distance, meaning that increasing the distance between the magnet and the target leads to a decrease in the strength of the magnetic field. Several studies have proposed various Halbach array models in order to maximize the magnetic field strength and thus enable it to reach increased depths [116] [162] [61].

A successful therapeutic depth of 5 cm has already been achieved in human clinical trials with a magnetic strength of between 0.2 T and 0.8 T (3 T/m and 100 T/m) [98] and a depth of 12 cm and 0.5 T magnetic strength in animal models (i.e. a swine model) [163]. MDT was first applied in human clinical trials to treat shallow tumours which were inoperable [98]. In this treatment, the chemotherapy drug, in this case epidoxorubicin, was magnetised using 100nm coated SPIONs and then administered systemically to 14 patients with advanced and unsuccessfully pre-treated malignant tumours or sarcomas. An external magnet of 0.8 T was placed for between one to two hours on the target in order to concentrate the chemotherapy to the target. The results revealed that the drug was directed successfully to the tumours in about 50% of the patients. As explained previously, the difference observed in the way patients responded to the treatment was attributed to individual differences of the patients' condition. The study concluded that the treatment was still dependent on patients' conditions and/ or disease related problems in each patient.

In addition, the results showed that MDT is safe, that is, no organ toxicity was observed.

MDT was also applied in an animal study to target regions of interest (liver and lung) in a swine model where iron oxides (Fe_2O_3) were used at a concentration of 20

mg/ml and a range of sizes (between 0.5 µm and 5 µm). In order to monitor MNP retention, iron oxides were labelled with 1 mg/ml of the gamma-emitting isotope Technetium 99 (^{99m}Tc) [164]. The external magnetic field was generated by a permanent neodymium magnet of 250 to 1000 G, which was placed on the target site for about 15—30 min in order to concentrate the drug (doxorubicin), which was infused at 2 ml/min concentration intra-arterially. It was found that the magnet helped to concentrate the drug by 40% to 43% compared to the controls.

There are many studies that have performed *in silico* modelling of their magnets with a potential for MDT. For example, in a study by Kang et al., a 30 mm depth was reached when a Halbach array (NdFeB) was simulated using FEMM to produce a magnetic field strength of 1.5 T. This study used a rectangular bar magnet consisting of five-magnet elements with dimensions of 6.35 mm width x 6.35 mm height x 50.8 mm length, and polarisation angles varying clockwise by 90° between successive magnets [165]. A Halbach array was also simulated by Barnsley et al., to reach a 5 mm depth. This model was further optimised to reach 20 mm and then post optimised to reach 50 mm with magnetic field strengths of 0.85T, 0.81T and 0.78T, respectively [166].

In 2007 a computational study was conducted to simulate a flat magnetic bandage using Finite Element Method Magnetics (FEMM) software with the intention to use this to target a superficial area including diseased tissues such as non-healing wounds and skin tumours [167]. The study compared different models including a single square magnet (3.75 cm^2 and 0.2 cm thickness) and four button magnets (1.5 cm diameter and 0.4 cm thickness). The single magnet had a normal magnet polarisation with the N (north-pole) pointed up and S (south-pole) pointed down. The four-magnet model was simulated with different arrangements of dipoles (NNNN, NNSS, NSNS). These models were compared with a flat magnet Halbach array, which consisted of eight elements with different

magnetisation orientations, to see which had the highest magnetic force. It was found that the magnet, with a single N, four NNNN, NNSS and NSNS models generated magnetic forces of 32, 51, 76 and 90 N, respectively, at 1 cm away from the centre of the magnet, while the Halbach array model generated a magnetic force of 100 N at the same distance; these figures were calculated numerically using the equation $\vec{F} = m\nabla|\vec{B}|$. This result confirmed that Halbach array magnets represent a promising technique for MDT.

The size/volume of Halbach arrays is a crucial parameter that should be considered when using Halbach arrays in medicine. In order to achieve a higher magnetic gradient, and hence force, a Halbach array with a large volume is required. Exploring this, Sarwar et al. reached a depth of 10 cm by using semi-definite quadratic programming to simulate a Halbach array model consisting of 36 magnet elements, 2000 cm^3 in six layers. This model generated a magnetic force nine times greater than one with the same magnetic orientation but with only two elements, i.e. a smaller size [61].

An interesting study investigated the relationship between the magnetic field/force, the size of the magnet, as well as the magnetisation orientation, and the ability to capture ferromagnetic beads in a microchannel (100 µm high and 1 mm long). The simulation procedure was performed using FEMM. A 2D Cartesian static case with no flow was considered. Two permanent magnets set up as a uniform field created a zero force zone in the middle of the microchannel gap and MNPs were instead trapped at the edges of the magnet [168]. It was found that a square bar magnet (200 µm) trapped more MNPs. This study showed that it is possible to use FEMM software to predict the force zone and thus to indicate where MNPs will be trapped.

Building on the above work, in this PhD study, FEMM software was employed to model Halbach arrays. This software is open source, freeware which is simple to use and popular in science and engineering. It is used mainly to solve and analyse electromagnetic

problems, including 2D planar, magnetostatic and linear electrostatic problems [169]. This software has been used in several areas of science including medicine [170], robotics [171], materials science [172], and experimental and particle physics [173].

FEMM is a group of programmes geared to solve low frequency electromagnetic problems on 2D planar axisymmetric domains. FEMM is divided into three parts, including the interactive shell, a pre-processor and a post-processor to solve several types of problems including magnetics, electromagnetics, heat flow and current flow [174]. FEMM also includes the Lua scripting language, which is integrated in the interactive shell. The purpose of the Lua scripting language is to run "batch" dynamic simulations and it is activated by adding code through the Open Lua Script icon on the File menu [175]. Overall, FEMM is useful for modelling both Halbach arrays and the movement of MNPs under the effect of a magnetic field and it will therefore be utilised for this study.

This study was conducted with the primary aim of designing appropriate Halbach arrays for the delivery of drugs loaded with MNPs to tumours in the brain. This chapter focuses on discussing the computer-based simulations that were conducted to design appropriate Halbach arrays.

3.2   Aims and objectives

Hypothesis

We hypothesise that an inexpensive, portable, powerful and external Halbach array magnet can be designed, modelled and simulated to be used for MDT with the purpose of targeting brain tumours, at depths between 5 and greater, i.e. 10 cm.

Aims

To achieve this, two different Halbach array magnets were designed and simulated using FEMM software (v4.2).

Specific objectives

- To calculate the magnetic force required to trap SPIONs with different sizes using Lua scripting.

- To develop Halbach array models in order to obtain the highest magnetic field/field gradients to reach a maximum target depth.

- To optimize the Halbach arrays model in order to generate higher magnetic field strength at further depths. We will assume that the Maximum Penetration Depth (MPD) of the magnetic field is 1% of its original magnetic field strength value (close to zero), and will use MPD throughout the thesis.

3.3 Movement of SPIONs under the influence of a magnetic field

From the Equation 1.2 mentioned earlier, it was found that large volumes of SPIONs require large values of magnetic force. This equation was used in FEMM-Lua scripting in order to calculate the magnetic forces that effect the movement of SPION.

In order to model and simulate the movement of SPIONs under the effect of a magnetic field, a specific magnet design and SPIONs with diameters of 24 nm, 50 nm and 70 nm were modelled using FEMM v 4.2. Then, to simulate movement of SPIONs, Lua scripting was applied.

For simplicity, a simple magnet array of two opposed blocks of NdFeB-52 that had dimensions of 5.5 cm width, 10.8 cm length, 5.5 cm height, was modelled. The magnets were separated by 2.5 cm gap and an attractive force was created in the gap. This simple model generated a magnetic field strength of 0.6 T, **Figure 3.1.** The blue arrows in the graphs (in this chapter) indicate the locations where the magnetic field strength was measured (perpendicular to the simulated model).
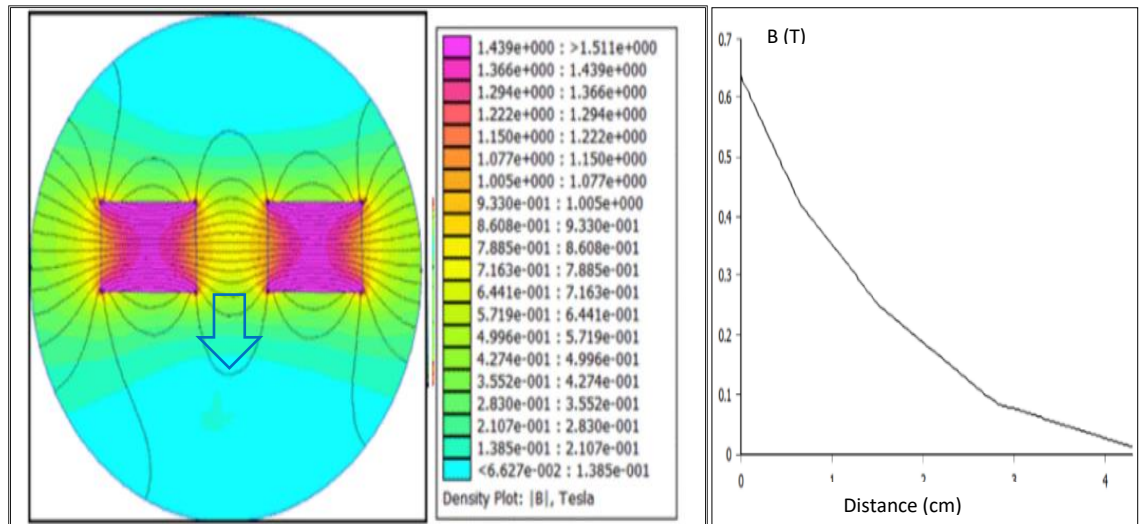
Figure 3.1: FEMM simulation of a two-block magnet. This model created a magnetic field of 0.6T, which was measured as the blue arrow indicates from the surface up to 4 cm away from the magnet. The maximum magnetic field that was created in the model was 1.1 T in the middle of the magnet in between the blocks.

After modelling the magnet and SPIONs , the simulation of SPION movement was run (**Figure 3.2**). To simulate the movement of SPIONs under the effect of the magnetic field, the code was set up to include the distance to be travelled and whether single or groups of particles were moved. The magnetic force on single and multiple SPIONs of different volume was then calculated as a function of position. The calculations were saved and then exported to Excel to plot the relationship between magnetic force and distance, based on the size of SPION, as shown in **Figure 3.3**.
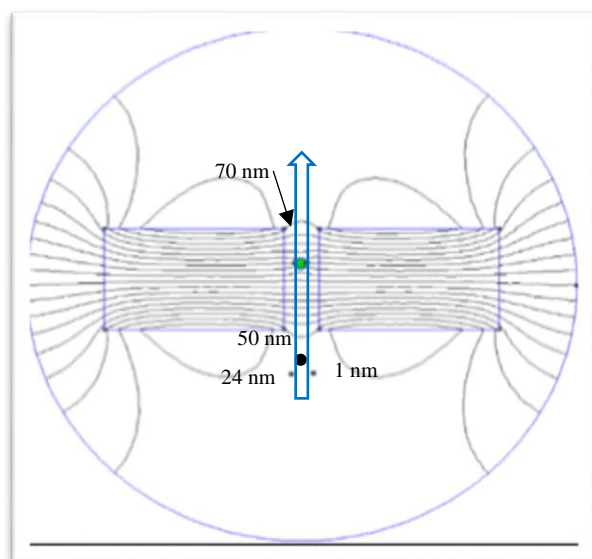
Figure 3.2: FEMM simulation and movement of the magnet and SPIONs of different sizes. Blue arrow indicates the direction of MNP movement where magnetic forces were calculated.
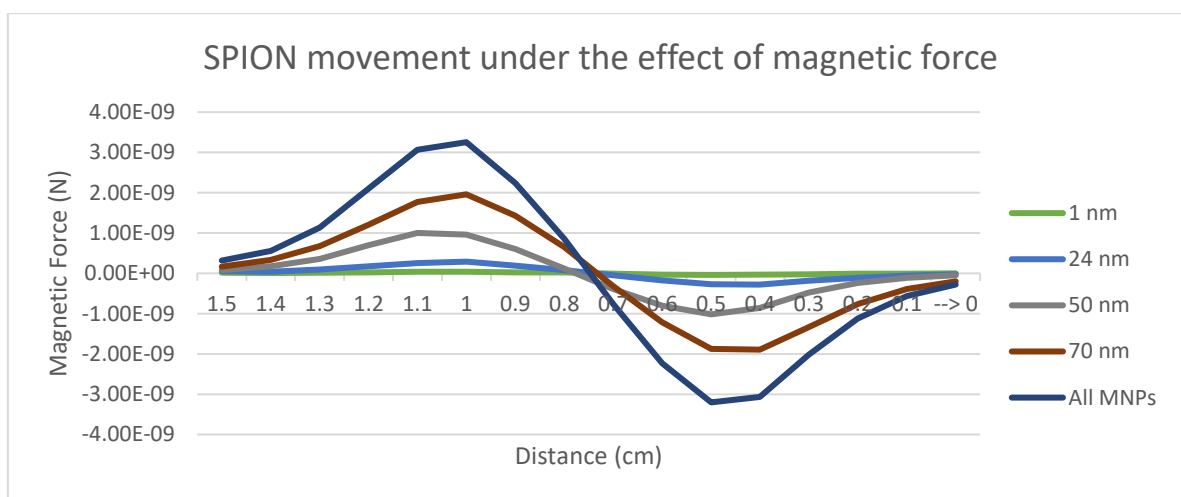
Figure 3.3: Calculated magnetic force for MNPs vs. distance. Green line represents the movement of 1 nm SPION, light blue line represents the movement of 24 nm SPION, grey line represents the movement of 50 SPION s brown line represents the movement of 70 SPION s, and dark blue line represents group simulation. This graph shows the increased magnetic force required with increasing size of SPIONs.

It was found that the large SPIONs of 70 nm (brown line) required more magnetic force, $2 \times 10^{-9}\ N$, than smaller i.e. 24 nm particles (light blue line) that required less than $1 \times 10^{-9}\ N$ to transport them. When all the different sized SPIONs were grouped to be moved at the same time (dark blue line) more magnetic force was required to transport them i.e. $3 \times 10^{-9}\ N$. The magnetic force that is required to move or transport the

SPIONs is therefore strongly dependent on the volume of the SPIONs. These observations helped to guide the development of the Halbach arrays models.

3.4   Development of Halbach array models

This section presents a discussion of how 2-D simulation models were run using FEMM software for different designs of Halbach arrays.

The magnetic material and the magnetisation direction were defined for each magnet element. The magnetisation direction was set up to create either an attractive or a repulsive force to create the highest magnetic field and field gradient at a point of interest (POI). A finite element mesh was then created for the geometrical model and the magnetic problem solved using FEMM. The calculated flux density of the magnet was then displayed. To measure the magnetic field at a POI in the model, two points were selected and connected to plot a profile and to measure the local magnetic field. **Figure 3.4** shows the modelling and optimisation procedure used in these studies.
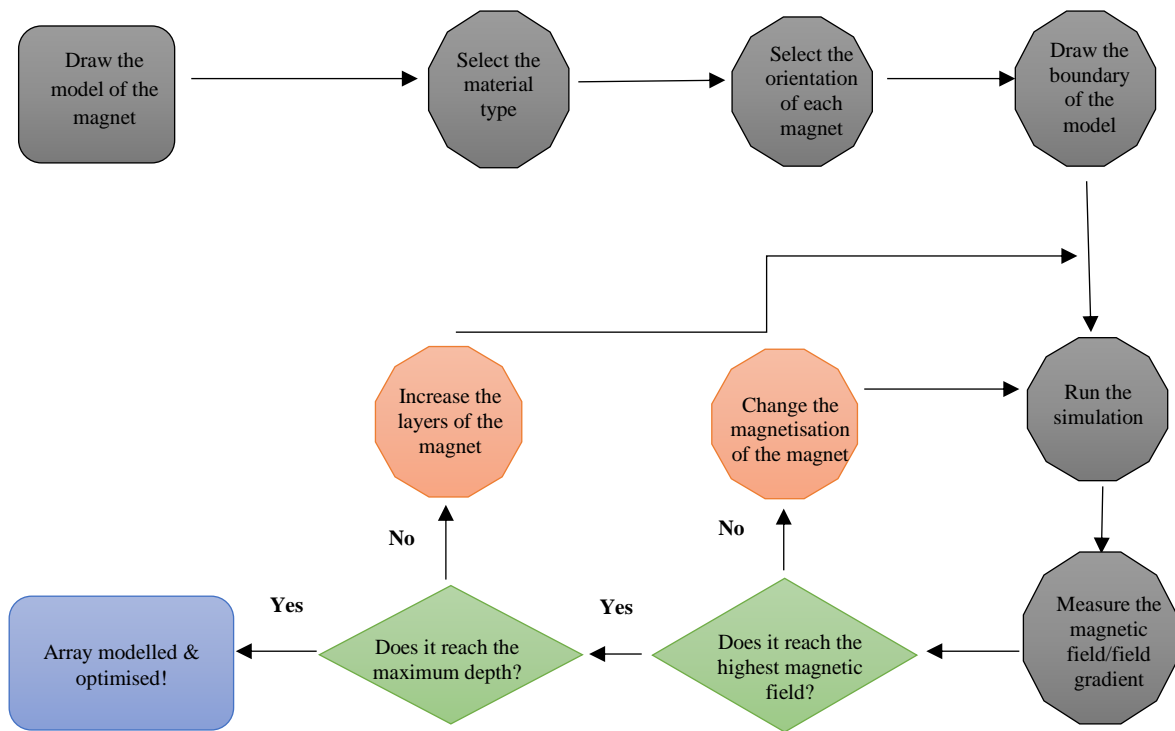
Figure 3.4: Schematic diagram of modelling and optimisation routine. The 2-D simulation and development process was conducted using FEMM software.

In this modelling, Neodymium-Iron-Boron (FeNdB-52) magnetic material was used, since this material is the strongest permanent magnetic material available to date.

The two different designs both had the same magnetic orientations but with different polarisation configurations. Model 1 consisted of one layer of three cubic magnets, in which the magnetisation of the two magnets at the edges pointed to the one in the middle, while the magnetisation orientation of the middle one pointed down, as illustrated in **Figure 3.5**. In the same Figure, Model 2 is also shown which consisted of one layer of four cubic magnets that had the same magnetisation orientation as Model 1 but with a doubling of the middle magnet; i.e. there were two magnets in the middle and two at the edges. For optimisation purposes, both models were simulated in multiple layers.

Model 1

Model 2

a

d

b

e

c

f
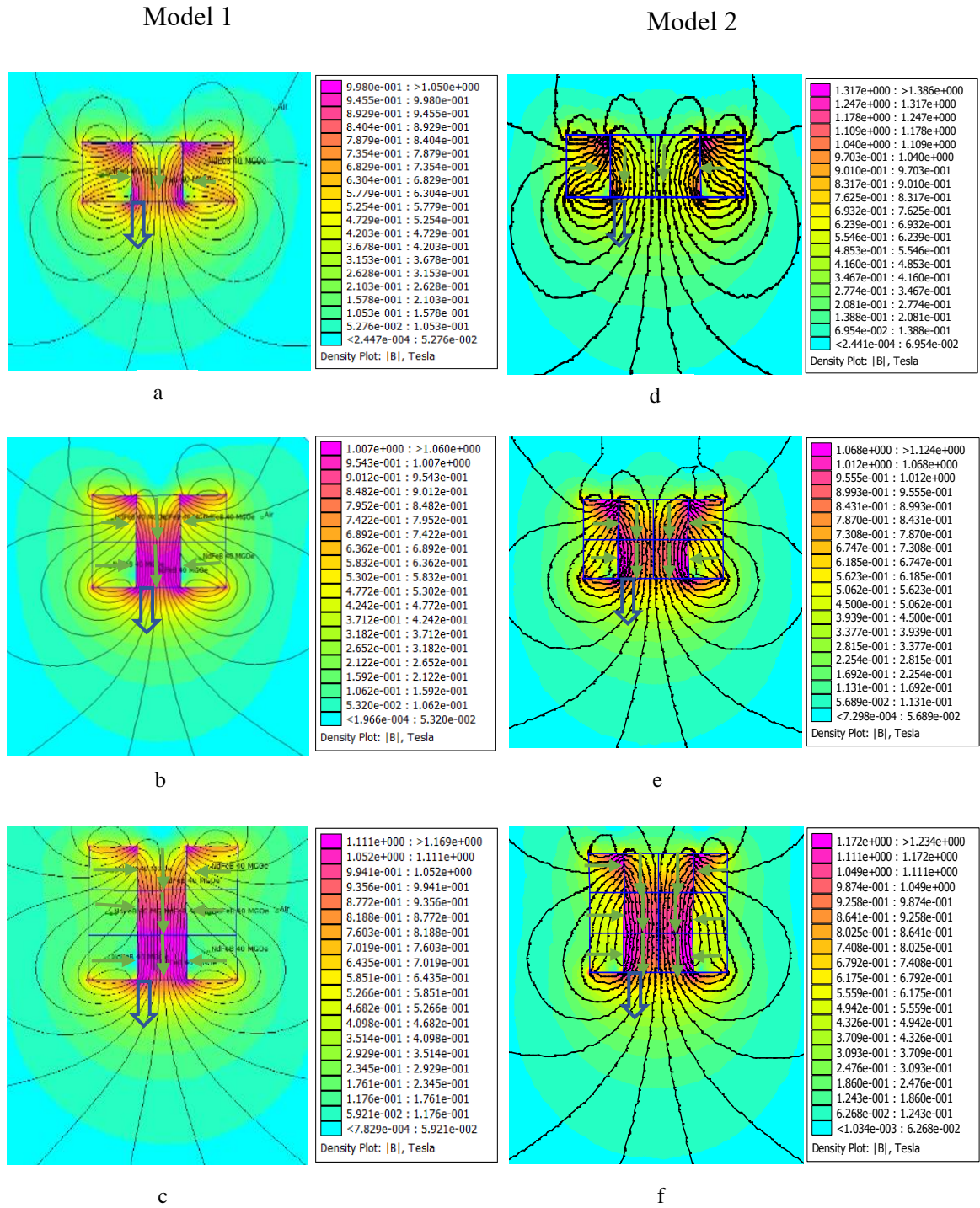
Figure 3.5: 2D distribution of magnetic field strength of Halbach array Model 1 and 2. a, b, and c represent Model 1 with one two and three layers respectively. d, e, and f represent one, two and three layers respectively of Model 2. The pink and turquoise blue colours represent the maximum and minimum magnetic field strength respectively. Blue arrows refer to position where magnetic field strength was plotted. These models were produced using the FEMM software.

3.4.1 Magnetic field strength based on Halbach array models

The marked difference between the models introduced in the previous subsection is the distribution as well as the strength of magnetic field that were obtained. The "pink" regions in **Figure 3.5** indicate the maximum magnetic field strength, which gradually decreases with distance from the magnet, reaching the lowest magnetic field strength shown in "turquoise". The magnetic field strength in Model 1 is very focused in the middle of the magnet and starts to emerge from the surface of the magnet and enlarge when the number of layers is increased (**Figure 3.5** b & c). This model therefore created a strong magnetic field on the surface of the magnet but was more focused in the middle of the Halbach array. Unlike Model 1, Model 2 generated less magnetic field strength "pink" in the middle of the magnet but was stronger at the edge of the magnet with increasing number of layers, see **Figure 3.5**, d & e. Setting up the magnetisation orientations — green arrows in the models — resulted in different magnetic field profiles. **Figure 3.6** below demonstrates how the magnetic field vectors for both models depended on the magnetisation orientation.
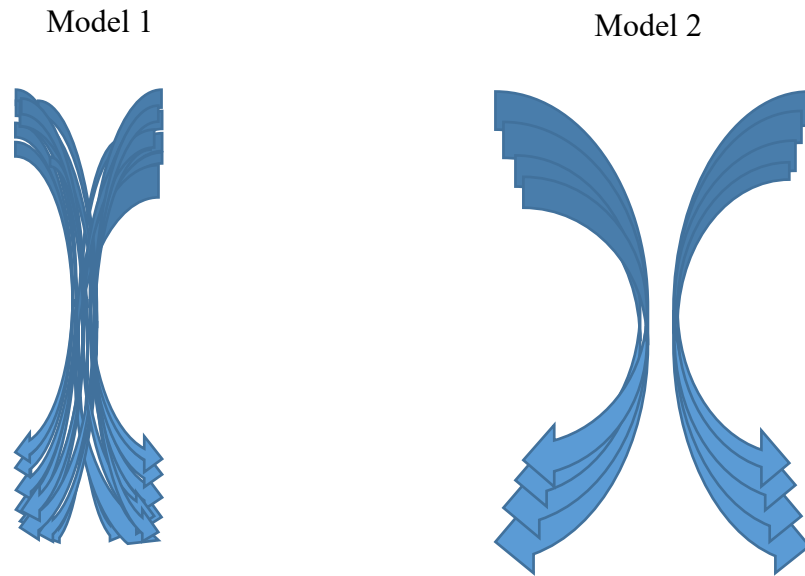
Model 1   Model 2

Figure 3.6: Demonstration of magnetic field vectors for Model 1-LHS and Model 2-RHS. They show the focused magnetic field distribution for model 1 and a larger distribution for model 2.

It was observed that increasing the number of layers and hence the volume of the magnet resulted in an increase in the strength of magnetic field and hence the field gradient and force. **Figure 3.7** below demonstrates the differences in magnetic field strength of each layer for both models. For example, the first layer of Model 1 (a) generated a maximum magnetic field of 1 T with a total of three magnets, whereas b and c, using a total of six and nine magnets respectively, generated maximum magnetic fields of 1.1 T and 1.2 T, respectively. On the other hand, Model 2 (d) generated a maximum magnetic field of 0.95 T using a total of four magnets, whereas (e) and (f), generated maximum magnetic fields of 1.2 T and 1.3 T, respectively, using a total of eight and twelve magnets, respectively.

(a)

(b)
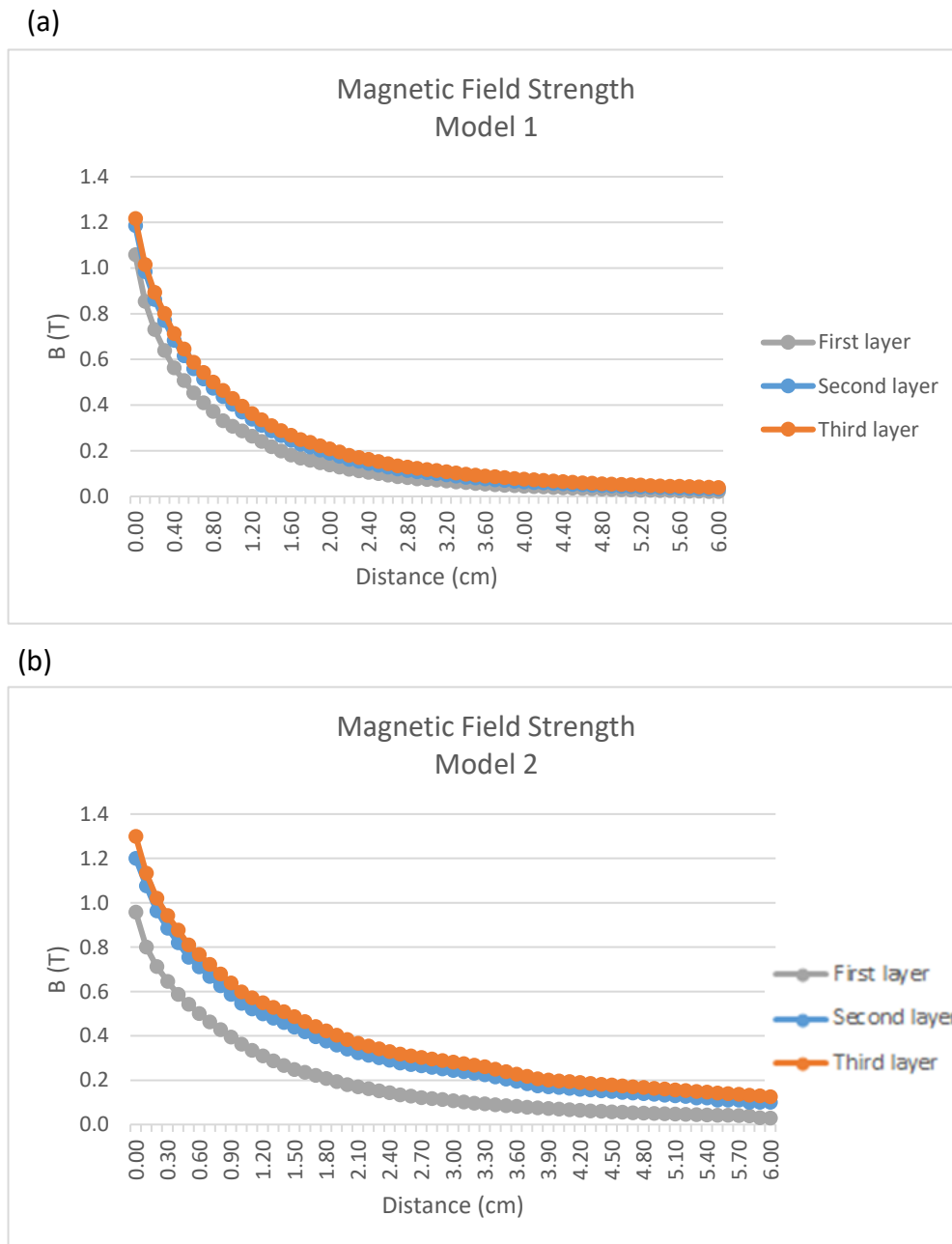
Figure 3.7: The maximum magnetic field strength (B) of multiple layers of Model 1(a) and Model 2 (b). Larger sizes of magnet produced the highest magnetic field in both models. Magnetic field strength seemed to be better in Model 1, whereas magnetic field and penetration depth were slightly increased in Model 2.

It can be seen from **Figure 3.7** that adding a third layer to both models generated

the highest magnetic field. There was a noticeable improvement in the magnetic field

strength for Model 2 with a third layer (1.3 T) compared to the first layer of the same model (0.95 T).

To compare both models, it is obvious from **Figure 3.7** above that the magnetic field strength of the first layer for Model 1 was slightly higher than the magnetic field strength of Model 2. However, at greater distances from the magnet surface, i.e. 2.4 cm, Model 2 (0.38T) seems to be more powerful than Model 1(0.28T) of three layers. Maximum magnetic field strengths for three layers were 1.3 T and 1.4 T for Models 1 and 2 respectively. In order to visualise clearly the strength of the magnetic field (shape of the curve) of the two models with three layers, 10cm was selected and illustrated in **Figure 3.8** below.
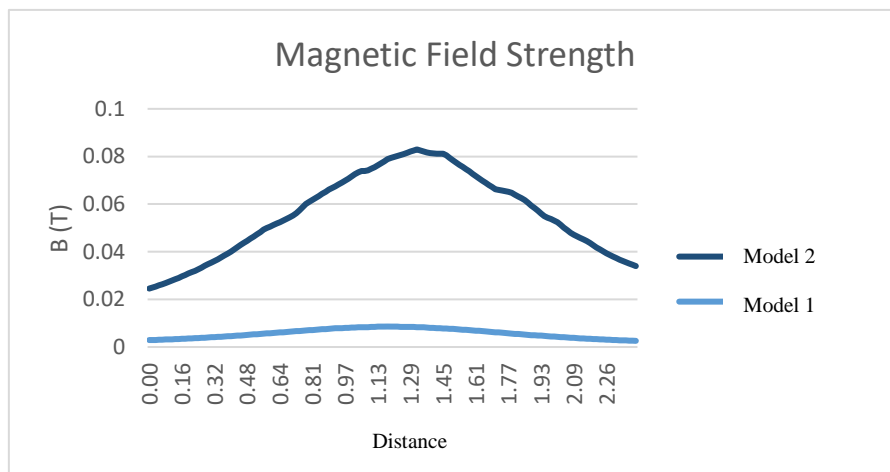
Figure 3.8: Magnetic field strength and shape of Model 1 and 2 at 10cm away from the magnet. Magnetic field of Model 2 was higher than Model 1 and had a curved peak.

It is clear that Model 2 is more powerful in terms of magnetic field strength, hence, field gradient and force, than Model 1 at depth, e.g. at 10 cm away from the magnet. Model 1 produced 0.01 T, 1 T/m and 2.35 T^2/m of magnetic field, field gradient and magnetic force respectively. While Model 2 produced 0.08 T, 8 T/m and 18 T^2/m magnetic field, field gradient and magnetic force at the same distance, respectively. In addition, the magnetic force generated from Model 2 is promising in terms of treatment as the focused

force at the peak should be able to hold SPIONs loaded with anti-cancer drugs. The Table below summarises the main differences in the models.

(a)

	Model 1	**Model 2**
Magnetization orientation	180°, 90°, 0°	180°, 90°, 90°, 0°
Total number of magnet element	3 elements	4 elements
Magnetic field strength (B)	1 T	0.95 T
Magnetic field gradient (G)	10T/m	9.5 T/m
Magnetic field force (F)	10 T^2/m	9 T^2/m

(b)

	Model 1	**Model 2**
Magnetization orientation	180°, 90°, 0°	180°, 90°, 90°, 0°
Total number of magnet element	9 elements	12 elements
Magnetic field strength (B)	1.2 T	1.3 T
Magnetic field gradient (G)	12 T/m	13 T/m
Magnetic field force (F)	14.4 T^2/m	16.9 T^2/m

Table 3.1: Magnetic properties of Model 1 and 2 as simulated (a) summarises the magnetic properties of Model 1 and Model 2 with (a) first layer and (b) three layers-up to 10 cm.

Since the main aim of this research was to model an external magnet, which has a strong magnetic field at depth, Model 2 appears to be the best configuration for the application of MDT for brain tumours. Further optimisation was required, however, to focus the array on the area of interest and to reach greater depths. Efforts were therefore made to improve the basic model design.

3.5 Optimisation of the FEMM model

In order to ensure that the magnetic arrays were focused on the area of interest, the effect of iron loaded epoxy resin was modelled. Epoxy resin is commonly used as a strong adhesive due to its chemical properties, however, if iron powder is loaded into the epoxy resin it can be considered as a magnetically soft material [176] [177]. The reason for using iron-loaded epoxy resin is that when a square-shaped magnet array is placed on top of a curved head a gap would be created at the edges of the magnet, as shown in **Figure 3.9** below. The iron-loaded epoxy can be used to fill the gap and further steer the magnetic field.
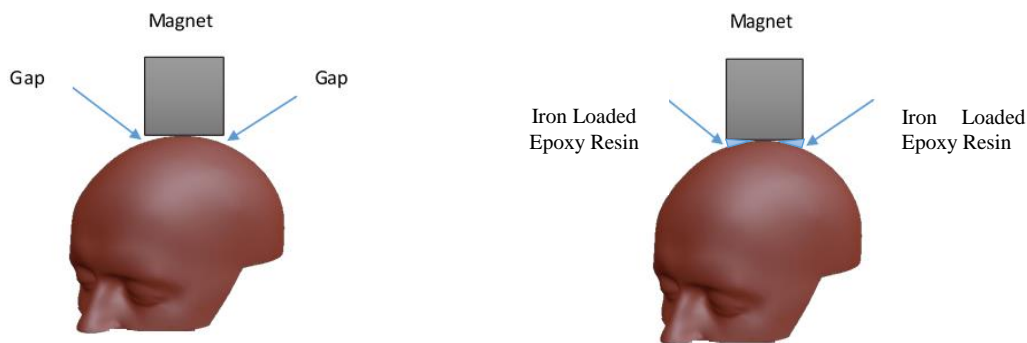
Figure 3.9: Adding iron-loaded epoxy resin to fill the gaps when the magnet is on top of the head. LHS shows that when the magnet is attached to the head gaps are created. RHS shows the gaps filled with iron-loaded epoxy resin.

In the FEMM model, a triangular shape was modelled to fill the gap with iron-loaded epoxy resin, as illustrated in **Figure 3.10;** where the left-hand side picture shows Model 2 without optimisation, while the picture on the right-hand side shows the iron-loaded epoxy resin modelled using pure iron material. It is well known that iron can be used to shape magnetic fields [177] [176].
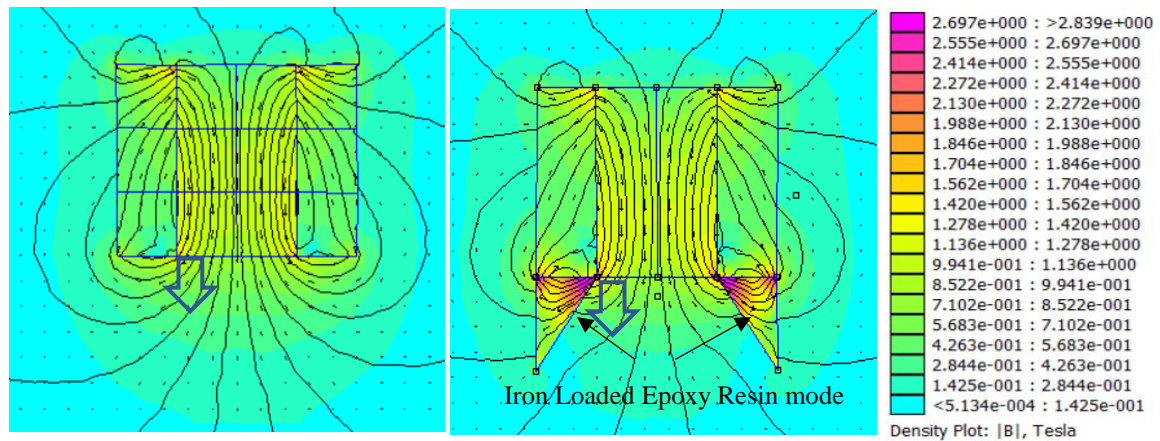
Figure 3.10: a 2D distribution of magnetic field using FEEM Software. LHS no iron-loaded epoxy resin, RHS with the iron-loaded epoxy resin, showing the creation of a focused magnetic field. Blue arrows refer to position where magnetic field strength was measured (perpendicular to the simulated model).

The iron-loaded epoxy resin shown in the **Figure 3.10**-RHS above helped to shape the magnetic field and produced a more focused magnetic field in the middle compared with the one without the epoxy resin-LHS, although there was no changes in the strength of the magnetic field that was generated with and without the iron-loaded epoxy resin. These results can be seen clearly in **Figure 3.11** below where both models generated a magnetic field strength of approximately 0.8 T.
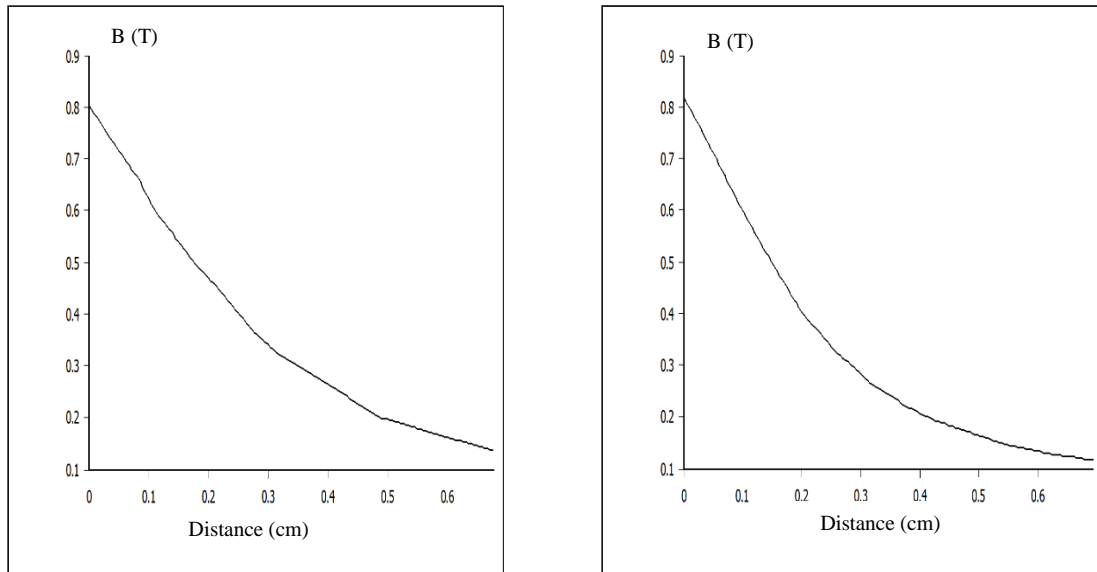
Figure 3. 11: The maximum magnetic field of the magnet with and without the epoxy resin produced using FEEM Software. Graph on left without the epoxy resin and on the right with the epoxy resin, showing no significant difference.

3.6 Discussion

This chapter focused on providing a detailed description of the processes and procedures followed in identifying an appropriate Halbach arrays for the therapeutic MDT purposes under investigation. Prior to developing the Halbach array models, an investigation into the relationship between the volume/size of SPIONs and the magnetic force was conducted. It was confirmed through FEMM modelling of SPION movement under the effect of magnetic force, that the amount of magnetic force required to move SPIONS to the desired site was directly proportional to the volume of the SPIONs, which agreed with theoretical predictions [168]. Smaller sized SPIONs require less magnetic force while large volumes of SPIONs require higher magnetic force to move the SPIONs to the desired depth, **Figure 3.3**. This implies that the choice of the correct size of SPIONs prior to treatment is a vital parameter that should be considered in designing optimal

Halbach magnet arrays to produce the required force to steer/trap SPIONs in a desired location.

Having established the relationship between the size of the MNPs and the magnetic force required to move the particles, the next step involved modelling the Halbach arrays. This helped to identify a good design for our application by determining the maximum magnetic field strength and depth of penetration associated with each model.

In order to obtain high magnetic force, two crucial parameters should be considered; the size of the magnet and the magnetisation orientation of each element [61]. It was shown in **Figure 3.7** that increasing the number of layers of magnets, that is, having a larger volume of magnet, increased the total magnetic field strength, magnetic gradient and magnetic force. A Halbach array model that consisted of six layers, including 36 magnet elements, giving a total magnet size of 2000 cm^3 was simulated by Sarwar et al. [61]. This Halbach array model reached a high penetration depth of 10 cm away from the magnet. Although this penetration depth is quite promising for MDT, the size of the magnet is quite massive and heavy and therefore would not be convenient for brain tumour patients.

The configuration of the magnetisation orientations plays a major role in altering the magnetic field strength, field gradient and hence magnetic force. Zhu et al., simulated two Halbach array models with the same volume and seven magnet elements but different magnetisation angles [178]. One model had the following magnetisation angles: 180°, 90°, 0°, -90°, 180°, 90°, 0° while the second model used -90°, 90°, -90°, 90° and so on. Both models generated magnetic flux differently in terms of the strength and the distribution, i.e. Model 1 produced a higher magnetic field strength than Model 2 and the magnetic field flux was weak on one side and strong on the other side, whereas in Model 2 this was distributed equally on both sides [178]. A Halbach array with a high maximum magnetic

field strength, however, does not necessarily have high field gradients and hence force. For instance, Model 2 in **Figure 3.7** showed less magnetic strength than Model 1 but had a higher field gradient and hence force, **Figure 3.8.**

Predicting a magnetic force zone is important prior to MDT treatment and this is achievable via modelling. Gassner et al., simulated the force distributions that were produced by rectangular permanent magnets in a static microchannel using different magnetisation orientations. This was to determine where in the channel MNP beads were more likely to be trapped. It was found that two permanent magnets set up to create a uniform field in attractive mode yielded one force zone in the middle of the magnet gap where MNPs were trapped whereas permanent magnets set up in repulsive mode to create a field gradient yielded two force zones at the edges of the magnet where the MNPs were trapped [168].

Soft iron materials have been used in MRI scanners to help increase and focus magnetic field flux, known as shimming [179]. In this study, iron-loaded epoxy resin was included in the FEMM model- **Figure 3.10,** aiming to produce more homogenous and focused magnetic field flux. The data did not show significant results in terms of increasing magnetic field strength, but it did show that the magnetic field flux became more focused, with increased trapping force at the POI. This is worth considering when applying magnet arrays to patients for the MDT therapeutic process. Although using iron-loaded epoxy resin has several applications, this has not been performed for MDT purposes yet. A device was patented that demonstrated the effect of iron powered on the utilization of permanent magnet materials in advanced motors [180]. It was used in an electrical motor to eliminate the unwanted thrust force by fitting the iron powder wedges between adjacent coil sides in the armature.

In order to validate the Halbach array models that were simulated, physical assembly of the magnet arrays was required. The following chapter thus describes how these Halbach arrays were assembled and how measurements of field, gradient and force performed. These measurements were then compared with the simulations from the FEMM models presented in this chapter.

Limitations:

In this study, Halbach arrays models were simulated using 2D software, which thus precluded forming the 3D shape that we were ultimately aiming to model. With 2D modelling it is only possible to model the cross section of the 3D shape and then simulate the magnetic field strength. This may produce a result that is not very precise due to the difference between the simulated magnet shape and the actual 3D magnet. This software was easy to use and free of charge, however. The alternative 3D software that could be used to model the Halbach array magnets is COMSOL [181]. This is more precise, however, it difficult to use and very costly.

The other limitation that exists in any magnetostatic computer model is the boundary conditions of the model. The function of the boundary is to shield the intensity flux and keep it surrounded with magnet. The value of the intensity flux will vary as the position of the magnet varies, however, for example, if the boundary was drawn close to the magnet, the magnetic field will be higher than if the boundary was drawn a bit further than the magnet. This is an important issue that should be considered in future work.

Chapter 4

Constructing Halbach arrays for Magnetic Drug Targeting (MDT)

4.1   Introduction

A key challenge in the assembly of Halbach arrays is the presence of the forces that are generated from the different polarisation angles between each magnet. These forces, mainly repulsive forces, should be overcome in order to attach and stick each magnet element together to complete the construction indicated through the FEMM models. The forces between two magnets (NdFeB-N52), of a 0.5 inch cube were numerically calculated for a set of magnetisation orientation configurations by Barnsley [116]. For example, the forces were 165 N, 124 N, and 58.5 N for two magnets that had the same magnetisation orientation of 90⁰, for a magnet which has a 90⁰ magnetisation angle connected with a block with a 30⁰ magnetisation angle and for a magnet which had a 90⁰ orientation connected with a magnet with a 180⁰ magnetisation angle, respectively. The magnetisation configuration of the two magnets shared either a face or an edge. The maximum calculated force was 330 N, which came from two magnets that shared a surface and were connected so the positive pole of one magnet attracted the negative pole of the other magnet [116].

A Halbach magnet array with two layers of a 5×5 array of magnets, 50 magnets in total, was assembled using an aluminium brace [182]. Removable rods contained the arrays to prevent them from movement. The magnet was assembled layer by layer and in each layer the assembly was row by row. When the assembly of each layer was completed, a sheet of aluminium was used as a sliding lid to cover the layer and then each rod was removed column by column from the base of the brace. After which, the base, from the bottom, and the lid, from the top, were pushed to align the layers together. The magnetic field obtained was around 0.3 T and reached up to 20 mm, and this increased as the layers of the magnet were increased to reach 1.3 T at up to 50 mm. The total weight of the magnet, including the base and lid, was 1.3 kg. The magnet was intended for use in MDT applications, therefore, *in vitro* experiments were conducted to demonstrate the magnet's

ability to separate and retain microbubbles loaded with MNPs against a constant flow. Although the magnetic field strength was considered to be promising for MDT, it would not be suitable for brain tumour patents due to its large weight (1.3kg).

Another technique that has been used to help in constructing Halbach arrays is where two 3D plastic printed holders are used to hold five bar magnets of 6.35 mm width, 6.35 mm height, 50.8 mm length. The magnetisation orientation of these magnets varied clockwise by 90° between successive magnets. While the magnets were kept still by the holders, a metal plate bonded to the epoxy adhesive was applied from the rear (weaker side) of the magnet to secure the magnet [165].

Assembling a Halbach magnet array can require specialized equipment to avoid the hazard that may occur when using high strength magnets such as N52 grade, due to large and sometimes unpredictable forces between the magnets [182]. Tools including a band saw; a lathe, a milling machine and simple hand-finishing are sometimes used for high performance assembly. Long cylindrical Halbach arrays were constructed by Tayler et al., using permanent magnets for NMR applications i.e. pre-polarisation and subsequent detection that occur at different locations [182]. In this model a group of magnets with different material types were used (i.e. NdFeB- N52 and N48SH) to build a multiple layer magnet with a total of 38 magnets. The dimensions of each magnet were 2, 0.5, 0.5 inch^3 and each was magnetized through the side with 0.5 inch thickness. Aluminium casings were fabricated to assemble 2, 4, 8 and 24 block magnet arrays. These Halbach magnet arrays generated a high magnetic field but were not suitable for our research due to their high weight, which was unsuitable for brain tumour patients. The final assembled magnets weighed a total of 1.3 kg (8-block) plus 3.0 kg (24-block) and external dimensions were 4 inch width and depth and 3 inch height.

Assembling Halbach arrays using tens or hundreds of small separate magnets offers many advantages rather than using a few large magnets. For example, small magnets allow different patterns of magnetisation orientations, which can help to strengthen the magnetic field on a magnet side. Also it helps to control the overall magnet size to fit for personal treatment [183].

4.2　Aims and Objectives

Hypothesis

The FEMM Halbach array magnets modelled in chapter 3 have a strong magnetic field gradient that can trap SPIONs within a brain model at depths of around 5 to 10 cm. We also hypothesise that large volume Halbach array magnets generate both high magnetic field strength and field gradients.

Aims

To test this, both Halbach array Model 1 and 2 were assembled and measurements were made to validate the FEMM models in terms of maximum magnetic field, field gradient and hence magnetic force as well as maximum penetration depth using a Gaussmeter (GM 08, HIRST, Magnetic instruments Ltd).

Specific objectives

- To assemble both Halbach array magnets based on the FEMM model.
- To measure the strength of magnetic field, field gradient and magnetic field of each layer of each model at different distances.
- To optimise the Halbach array for the SPION trapping experiment with the tumour/head phantom model.

- To determine the maximum depth at which the tumour could be located within the brain using the 3D head/tumour phantom model.

4.3 Assembly of Halbach array magnets based on FEMM model

Chapter 3 demonstrated the simulation of two Halbach array models in terms of magnetic field strength, field gradient and magnetic force. To validate the FEMM model, both Halbach array models were physically assembled. Based on the FEMM models, a cubic magnet element of 1 cm^3 and Neodymium Iron Boron (NdFeB)-grade N52 were chosen for the assembly of the magnets. Both magnets had the same magnetisation orientation but with different configurations. The magnetisation orientations of the magnets were adjusted based on the FEMM models. In the centre of the magnet array, the magnetisation orientation angle was set to be $\theta = 90°$ with the positive pole pointing out of the paper. For all the other magnets in the array, the magnetisation orientation angles were set to be $\theta = 180°$, orthogonally magnetized towards the array centre, as illustrated in **Figure 4.1.** Black circles in the magnet refer to the position where the magnetic field strength measurements were taken, perpendicular to the magnet's surface.

Each magnet was placed on a ferritic stainless steel sheet with an area of 30 cm^2, which was used to keep the magnets in place. In addition, a cyanoacrylate adhesive was used to stick the magnets together. After gluing two magnets, a block of ferritic stainless steel was placed on top of the glued magnet faces to ensure that they remained held together for several hours (between 7 and 24 h). After that, the block was removed and the next magnet put into place and this process was repeated until the assembly was complete.
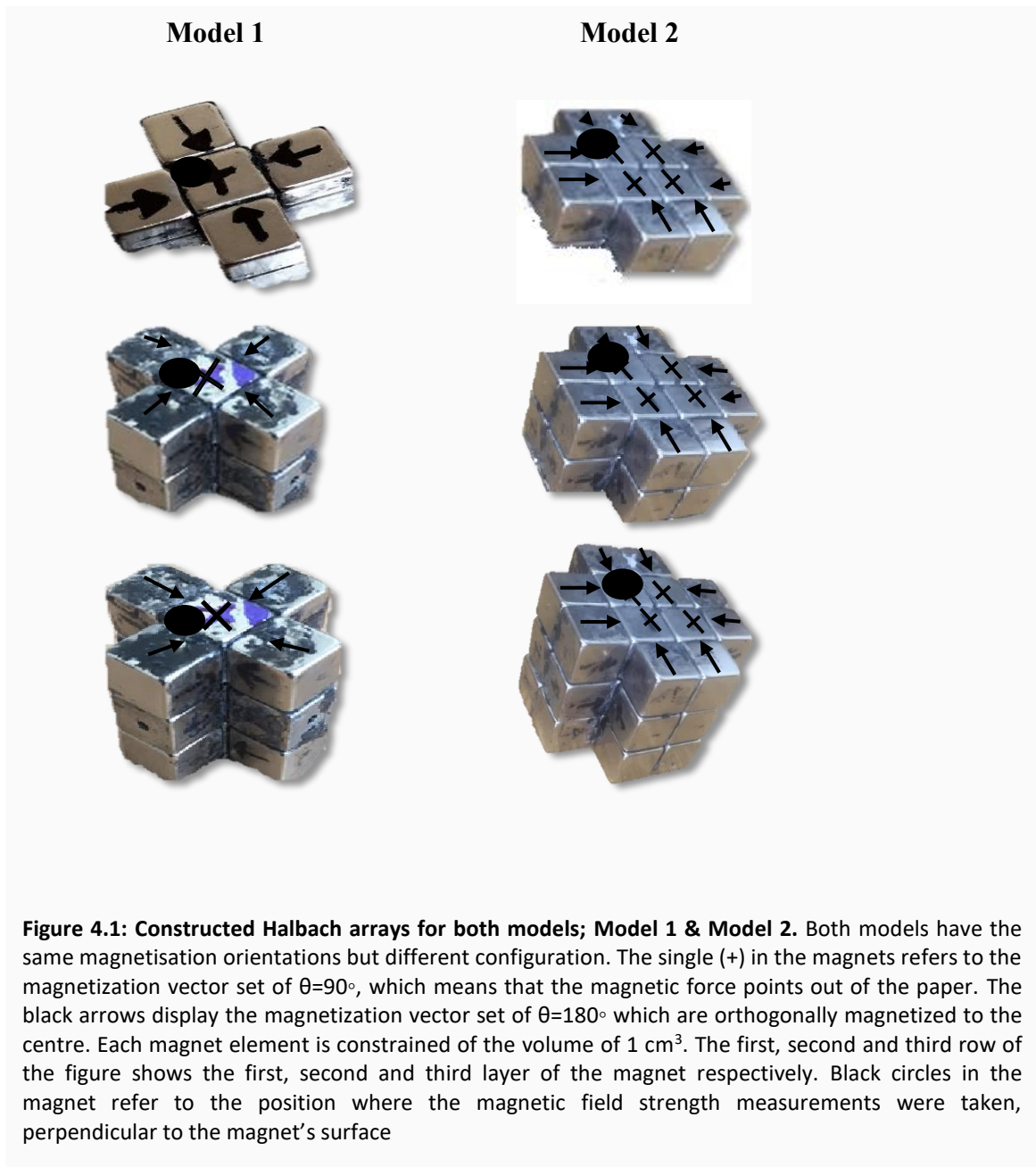
Figure 4.1: Constructed Halbach arrays for both models; Model 1 & Model 2. Both models have the same magnetisation orientations but different configuration. The single (+) in the magnets refers to the magnetization vector set of θ=90◦, which means that the magnetic force points out of the paper. The black arrows display the magnetization vector set of θ=180◦ which are orthogonally magnetized to the centre. Each magnet element is constrained of the volume of 1 cm^3. The first, second and third row of the figure shows the first, second and third layer of the magnet respectively. Black circles in the magnet refer to the position where the magnetic field strength measurements were taken, perpendicular to the magnet's surface

Model 1 started with five magnets, one in the centre and four surrounding the centre, making a cross shape, the polarisation of the central magnet pointed up, forming the positive pole, whereas the surrounding magnets pointed towards the centre of the magnet. A total of 15 magnets were used to create all three layers. Similarly, for Model 2, the same shape and magnetisation orientations were applied, but with four magnets in the centre and eight surrounding magnets for the first layer and 24 and 36 magnets for the second and third layers, respectively.

The main challenge faced during the assembly procedure was management of the repulsive forces that arise between neighbouring permanent magnet elements. This issue was made more difficult with increasing magnet array size. The challenge of attaching the additional layers was overcome by segmenting the configuration into smaller groups (two magnet elements in each group). Using steel blocks to surround each group of magnets while keeping the base of the magnet array attached to the steel sheet, helped to reduce the repulsive dipole forces.

4.4   Measurements of the Halbach arrays

Based on the FEMM model simulations in chapter 3, Model 2 demonstrated superiority over Model 1 in terms of magnetic field strength, field gradient and magnetic force. It was also shown that when the volume of the magnet increases, the magnetic field strength, and hence both the field gradient and the magnetic force increase. In order to validate the simulations, measurements of the magnetic field strength of the assembled Halbach arrays were taken for each layer and for both models using a Gaussmeter (GM 08, HIRST, Magnetic instruments Ltd). The field strength was measured over a range of distances from the magnet surface. The field gradient and magnetic force were then calculated based on the magnetic field strength measurements.

Figure 4.2 (a-f) demonstrates the magnetic field, field gradient and magnetic force measurements for each layer and for both magnets.

(a)

Magnatic Field Strength
Model 1

(b)

Magnetic Field Strength
Model 2

(c)

Magnetic Field Gradient
Model 1

(d)

Magnetic Field Gradient
Model 2

(e)

Magnetic Force
Model 1

(f)

Magnetic Force
Model 2
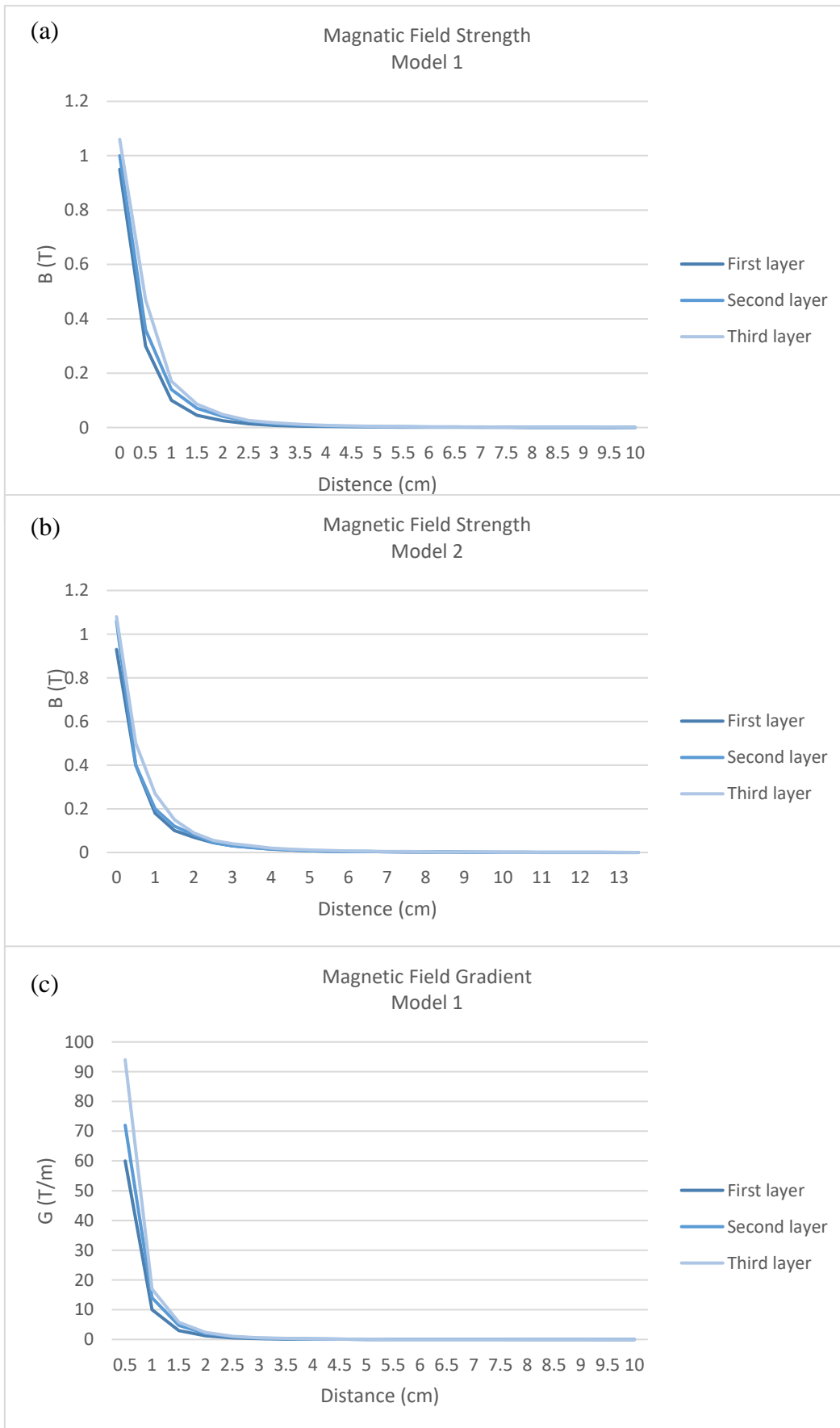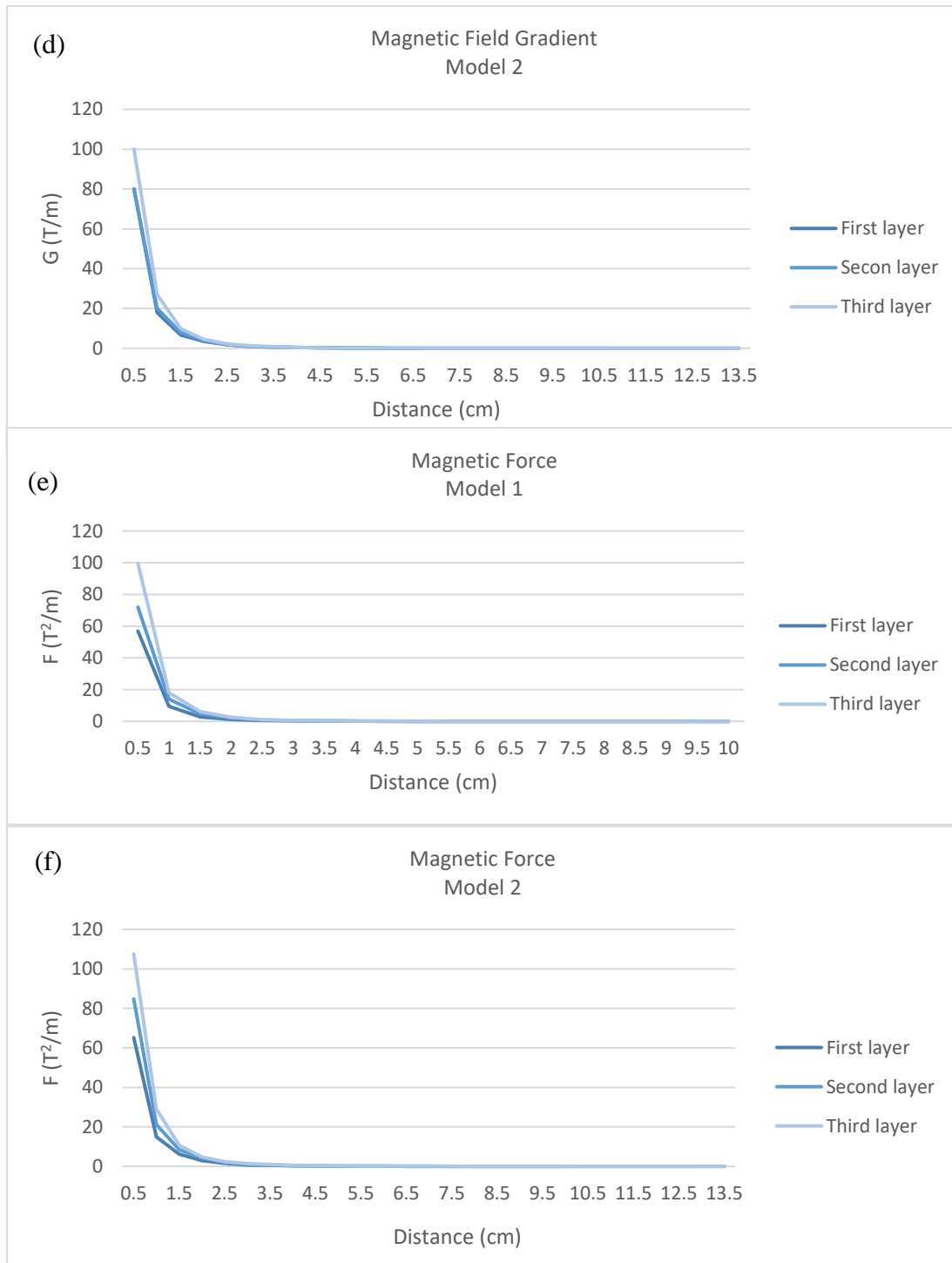
Figure 4.2: Measurement of magnetic field strength and magnetic force for model 1 and 2. (a-f) show the measured magnetic field (B), field gradient (G) and magnetic force (F) of each layer for both models, 1 & 2, at a range of distances until the magnetic field strength reached zero (integral).

As can be observed from **Figure 4.2**, the maximum magnetic field generated from the first layer of Halbach array Model 1 was 0.95 T at the surface of the magnet. This value increased with increasing number of layers i.e. 1 T and 1.06 T after adding the second and third layers, respectively. The field values dropped off sharply at 0.5 cm away from the magnet i.e. 0.3 T, 0.36 T and 0.47 T for the first, second and third layers respectively. Beyond this distance, the magnetic field strength decreased more gradually.

For Halbach array Model 2, (**Figure 4.2**), it can be observed that the maximum magnetic field generated by the first layer was 0.93 T at the surface of the magnet. This value increased as the number of layers of magnet increased to 1.06 T and 1.08 T for the second and third layers respectively, again dropping off sharply at 0.5 cm away from the magnet, i.e. 0.3 T, 0.4 T and 0.5 T for the first, second and third layers, respectively.

It is worth mentioning that the maximum magnetic depth penetration of Model 1 of each layer was 7.5 cm, 9 cm and 9.5 cm for magnets made up of one, two and three layers, respectively, where the magnetic field strength at these points for all layers was 0.001 T. The maximum field gradient and magnetic force for the first layer of Model 1 were 12.7 T/m and 12.0 T^2/m respectively (up to 7.5 cm). When the second layer was added, the total field gradient and magnetic force were 11.1 T/m and 11.1 T^2/m respectively (up to 9 cm). For the third layer, the total field gradient and magnetic force were 11.1 T/m and 11.81 T^2/m respectively (up to 9.5 cm). The magnetic force values increased as the number of layers of the magnet increased, as predicted from the FEMM values.

Although the magnetic field strength reached up to 13 cm for Model 2, it was so weak at that depth that it would be unlikely to be able to trap SPIONs. For example, the maximum magnetic depth penetration for Model 2 for each layer, was 10 cm, 12.5 cm and 13 cm when the magnet contained one, two and three layers, respectively, but the magnetic

field strength at these points for all layers was 0.001 T. The maximum field gradients as each layer was added were 8.8 T/m, 8.3 T/m and 8.53 T/m, respectively. The magnetic force was 8.2 T^2/m (up to 10 cm) when there was one layer, 9 T^2/m (up to 12.5 cm) when there were two layers and 9.3 T^2/m (up to 13 cm) when there were three layers. These depth points cannot be considered useful for MDT, therefore, due to the weak magnetic field strength, field gradient and force values.

Figure 4.3 shows that Model 2 has a slight increase in terms of magnetic force compared to Model 1.
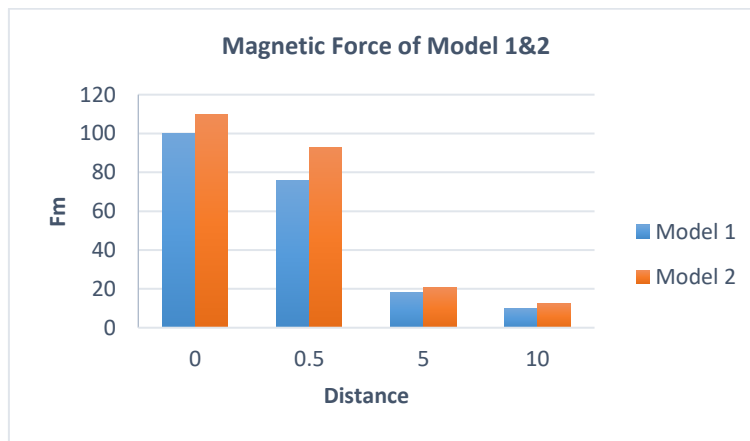
Figure 4.3: Magnetic force of the constructed Halbach array of Model 1 & 2.

As mentioned earlier, these magnets were developed to deliver magnetised drugs to brain tumours. The size/volume of the device should therefore be suitable and convenient for patients. All the magnets were weighed in the lab using an accurate weighing scale. It was found out that the weight of Model 1 with one, two and three layers was 36.6, 55, and 110 g, respectively. For Model 2 the weight of the first, second and third layers was 88.5, 177.1, 265.7 g respectively. Adding the third layer generated a strong repulsive force as explained previously on page 91, hence, its configuration required use of more adhesive. This explains why the volume/weight of the magnet is the largest in the presence of three

layers. Overall, it seems that Model 2 with three layers was the heaviest at 265.7 g but this can still be considered to be low enough for MDT use. **Figure 4.4** below demonstrates the differences in weight for each layer and for both magnets.

(a)   (b)
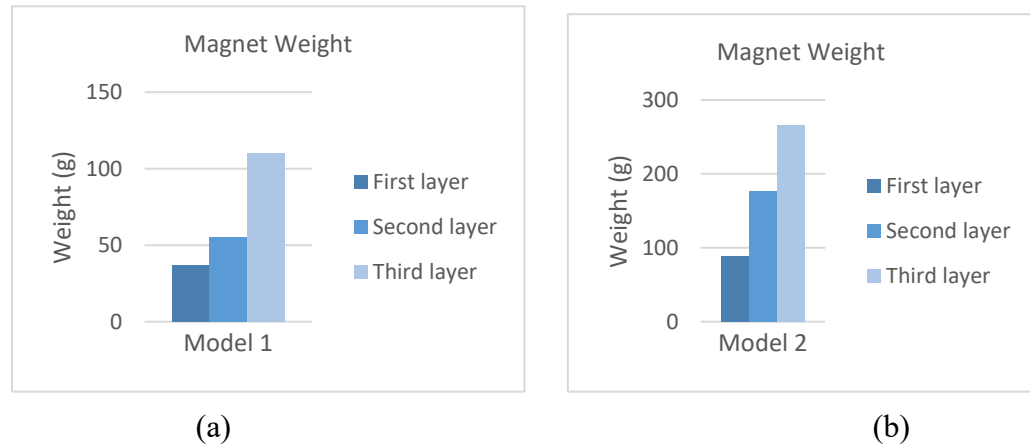
Figure 4.4*: The weight of both magnets (a) Model 1 and (b) Model 2. Magnet 2 was heaviest but was still considered reasonable for MDT.

As alluded to earlier, it was necessary to identify the model that works most effectively in terms of directing drugs that are loaded with SPIONs to the desired depth. Model 2 produced a slightly higher magnetic field strength at the surface of the magnet (0 cm) compared to Model 1. As the distance from the magnet increased, for example to 2.5 cm, Model 1 produced a slightly higher magnetic field in comparison to Model 2. In terms of magnetic force, there is no major difference between the models, Figure 4.3. Overall, it can be concluded that Model 1 is better for small, superficial brain tumours because this model produced very focused magnetic fields, as can also be seen in the FEMM model in chapter 3. On the other hand, Model 2 should be better for large, deep brain tumours as it produced a larger, more extended magnetic field.

In terms of comparing between the simulated and constructed Halbach array, Figure 4.5 below illustrates the comparison of the main properties between the simulated and constructed Halbach array (as a whole) of Model 2.

(a)
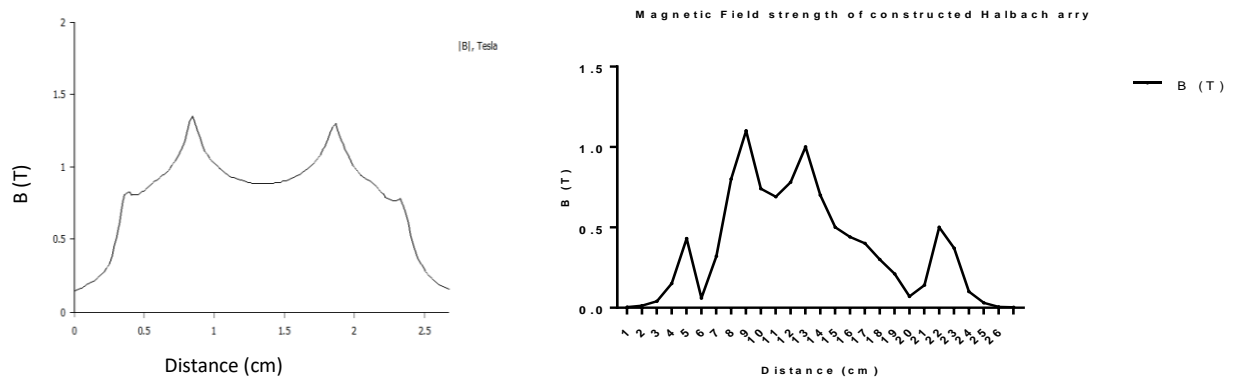
(b)
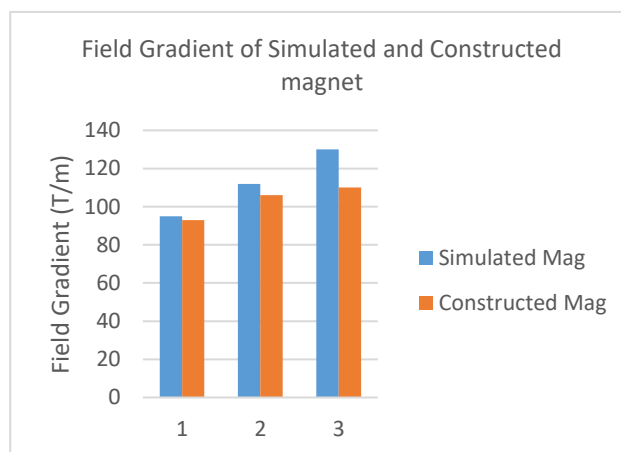
Figure 4.1: Comparison between the simulated and constructed Halbach array for Model 2. a) The magnetic field strength profile, b) Field gradient of 1st 2nd and 3rd layer.

The reason of the differences between both versions of the model was already discussed in 3.6 (limitation).

The primary objective of this research project was to build a Halbach array with a high magnetic field strength that has the capacity to reach deep within tissue in order to

steer the drugs that are loaded with SPIONs to brain tumours. It was concluded that Model 2 has a more effective configuration to produce extended trapping forces.

4.5   Optimisation of Model 2 for improved magnetic targeting

Several strategies to improve Model 2 are now described. The first strategy to optimise the magnetic field strength was to ensure that no magnetic field could escape from the corners of the model (**Figure 4.1**). In order to close the gaps (convert the shape from a cross to a square) a magnetic element of the same magnet grade-N52, with a magnetisation orientation of 45°, was attached in each corner, as illustrated in **Figure 4.6** (a). The magnetic field strength was measured using the Gaussmeter and the values were plotted in **Figure 4.6** (b). For the sake of demonstration of the principle this optimisation was applied for only one layer.

The maximum magnetic field for the optimised model was 1.16 T compared with 0.93 T for the non-optimised Model 2. The maximum penetration depth was improved from 10 cm to 12.5 cm for the optimised model. At 2.5 cm the magnetic field gradient and magnetic force were 44.16 T/m and 51.22 T^2/m respectively compared with 36 T/m and 33 T^2/m respectively for the non-optimised model.

(a)   (b)
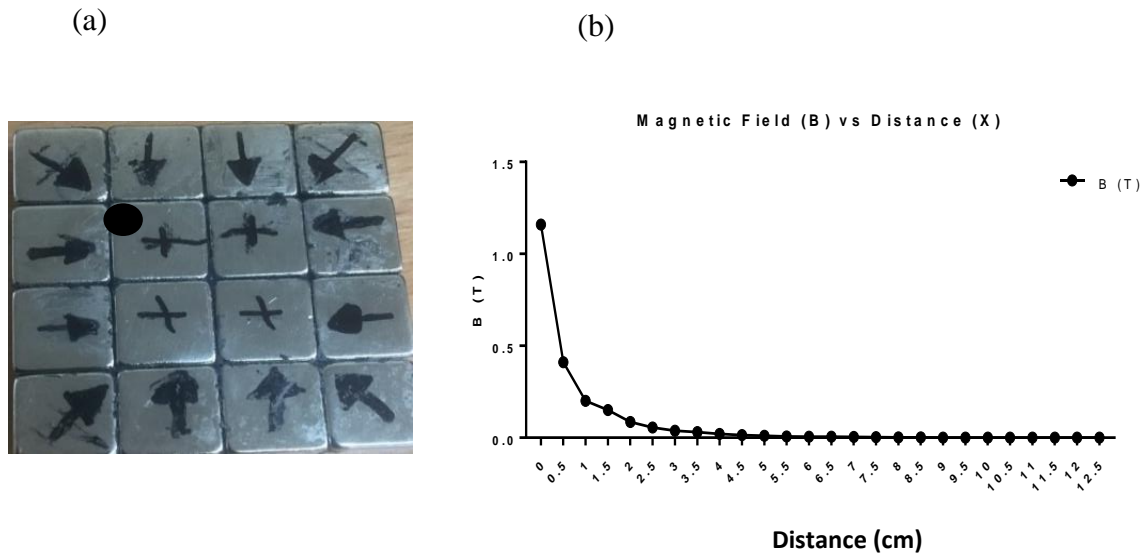
Figure 4.6: Optimised Halbach array of Model 2: (a) Constructed Model 2 Halbach array with one layer after optimisation by closing the corners. The sign (+) on the magnets refers to the magnetization orientation sets with θ=90°, which means that the magnetic force points out of the paper. The black arrows display the magnetization orientation set with θ=180°, 0°, which are orthogonally magnetised towards the centre as well as 45 degrees from the corners. Each magnet element had a volume of 1 cm^3. (b) Magnetic field strength of the optimised Halbach array versus distance. The magnetic field strength and magnetic penetration depth were slightly increased. Black circles in the magnet refer to the position where the magnetic field strength measurements were taken, perpendicular to the magnet's surface.

The second strategy for optimising the magnet involved housing the magnet within a stainless steel case as illustrated in **Figure 4.7** (a) below. This was applied for the first layer only as this provided enough evidence for the subsequent configurations. The magnetic field strength was measured and the average magnetic field and force were calculated and plotted in **Figure 4.7** (b, c, d). The maximum magnetic field for the model with a steel case was 1.17 T, compared with 1.16 T for the non-cased model at the surface of the magnet. The difference in the magnetic field strength between the models with and without the steel case is not noticeable, however, its effect is observed in MDP where 12.5 cm of the model without steel case compare to 14 cm with steel case. This suggests that cover the magnet with steel case can help to improve MDP in MDT.

(a)

(b)
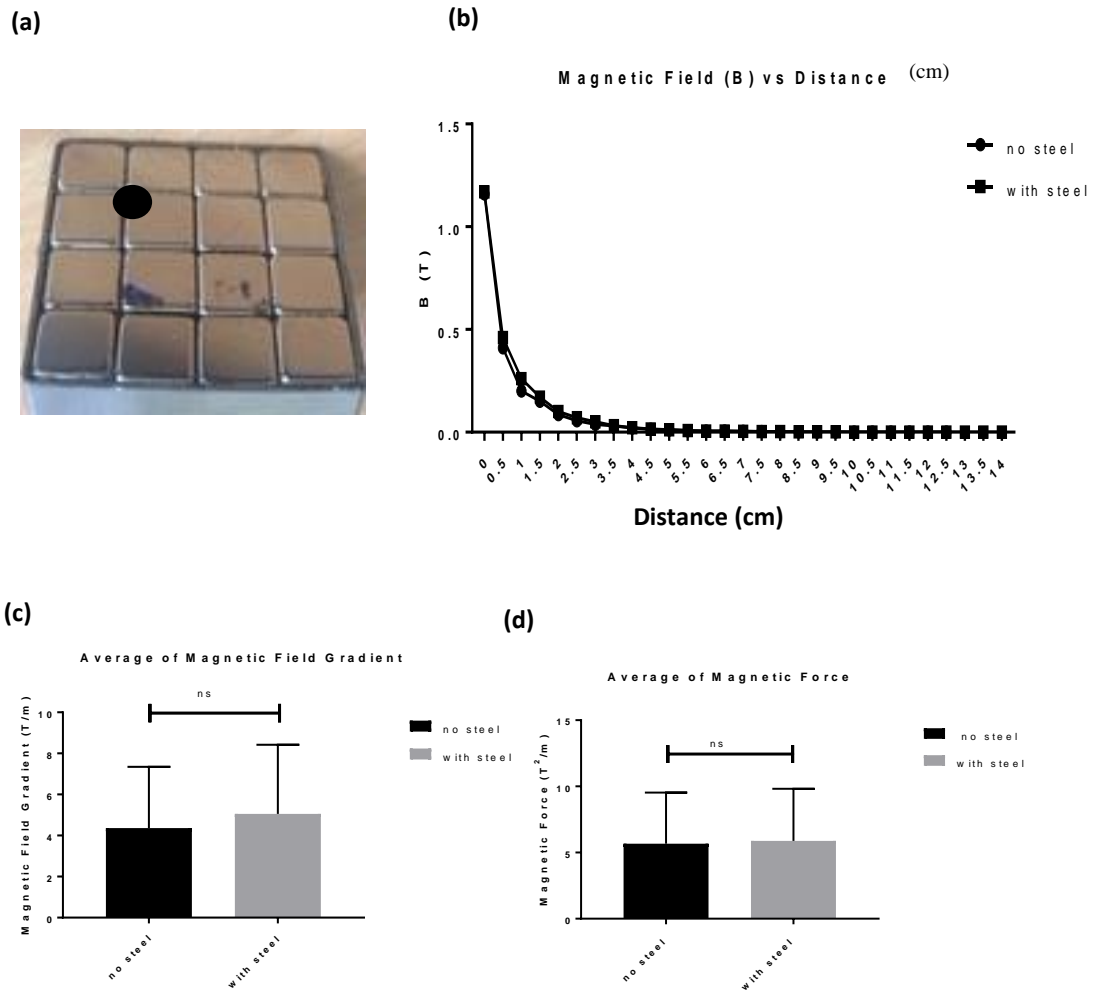
Figure 4.7: Optimised Halbach array of Model 2: (a) optimized Model 2 Halbach one layer array with closed corners and a steel case. (b) Magnetic field strength of the magnet with and without the steel case which showed slightly increased magnetic field strength at 0.5 cm and further penetration depth with the steel case. (c & d) show that there was no significant difference in magnetic field gradient and magnetic force for Halbach array magnets with/without a steel case. Black circles in the magnet refer to the position where the magnetic field strength measurements were taken, perpendicular to the magnet's surface.

After the promising data obtained from the optimization of one layer of the Halbach array, it was decided to assembly a three layer optimized Halbach array magnet, which thus had 48 magnet elements compared to 36 in the original version. With increased magnet numbers, the strength of both the attractive and repulsive magnetic forces were increased, which made it very difficult to safely build in the lab. As a result, expert help was sought (from the Magnet Expert Company, UK). A confidentiality agreement was

signed by the company to protect any IP resulting from the magnetic arrays. After this the magnet design and requirements were sent to the company.

Interesting results were found when the magnetic field strength was measured away from the surface of the magnet. It is noteworthy that the magnetic strength at the magnet surface varies depending on the orientation of each magnet. **Figure 4.6** (a) shows two main areas where the magnetic field strength was different; blue areas which involved a meeting point with four different magnetisation orientations and yellow areas which also involved a meeting point of four magnetisation orientations, but all with the same angle, i.e. 90°. The difference in the magnetic field strength at these areas were measured and plotted, as illustrated in **Figure 4.8** (b). The magnetic strength of the areas indicated with blue squares was higher than the magnetic strength of the middle area marked by the yellow square. With increasing distance, however, it was found that the magnetic strength and penetration depth of the middle area (yellow) were higher than the corners (blue) as illustrated in **Figure 4.8** (c-d). The average values of the field gradient and magnetic force were calculated from both areas and the results plotted in **Figure 4.8** (e-f). These finding are worth considering when applying MDT for deep brain tumour targeting. It is commonly assumed that the area having the highest magnetic field at the magnet surface is the best region to be located directly above the tumour. This is true for superficial treatment but for deeper treatment, the weaker magnetic field strength region seemed to be the best as it had a higher magnetic field gradient at further depth.

(a)

(b)

(c)

(d)

(e)

(f)
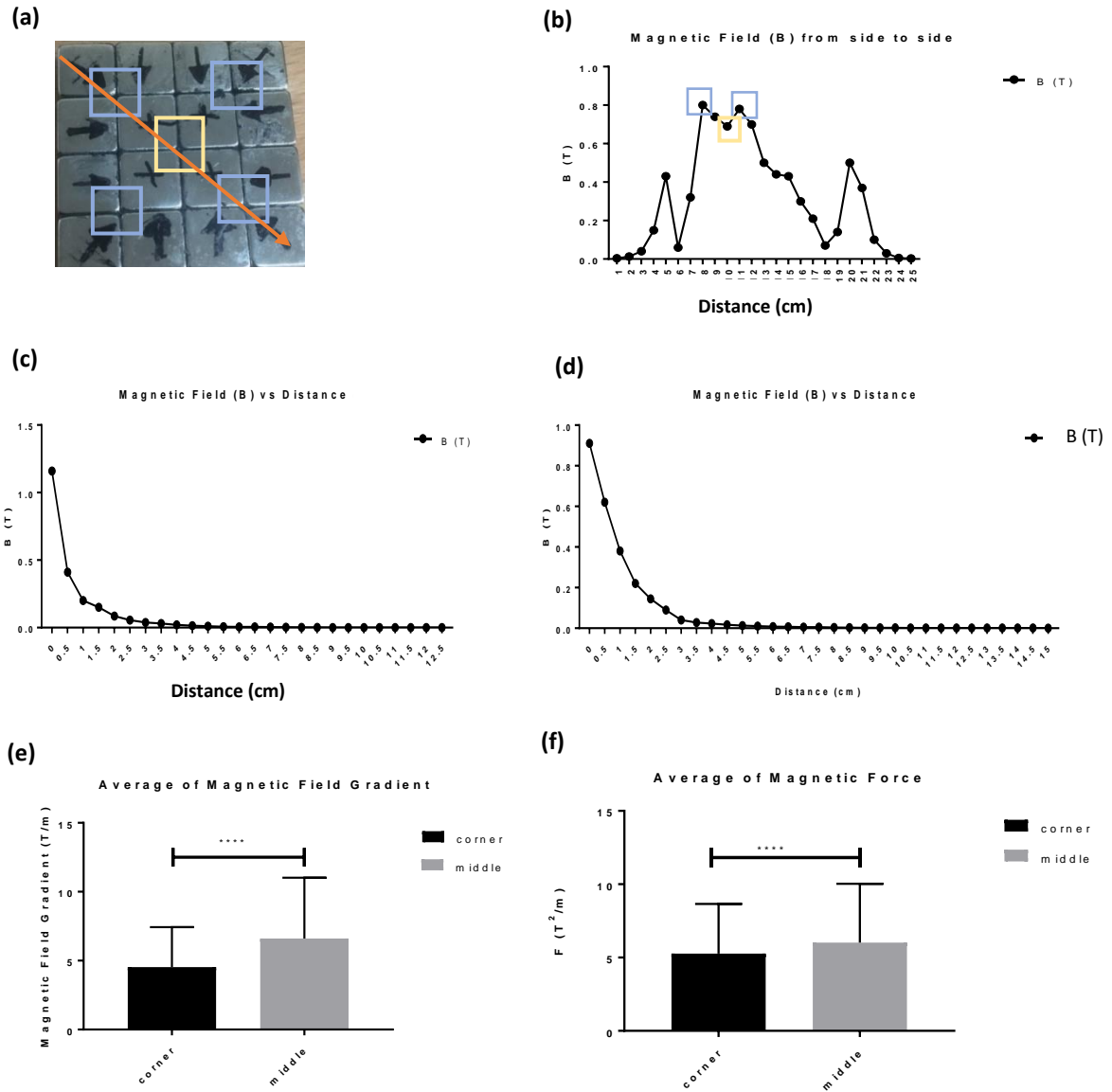
Figure 4.8: Optimised Halbach array of Model 2: (a) blue (corners) and yellow (middle) (b) Strength of magnetic field for both areas. The yellow areas (middle) showed the weakest magnetic field strength. (c-d) Magnetic field strength increased at further depth for the yellow areas. (e-f) Calculated average values of field gradient and magnetic force for both areas clearly indicate that the weakest surface magnetic field strength area (middle) has the highest field strength as well as magnetic force at depth. The orange arrow refers to the direction of the magnetic field measurement which was parallel to the magnet. Data was analysed using two way ANOVA-PRISM. ****$p < 0.0001$.

4.5.1 Development of a phantom model to assess SPION trapping

An MRI scan of a brain tumour as well as a head of a patient was taken (provided by Professor Martyn Paley). The data was extracted and transferred to 3-D software in order to print a 3-D tumour phantom from clear photopolymer resin, using a Formlabs Form2 printer. The internal structure of the original prototype was created using a careful exploitation of the printing process, where the lattice infill of the printed component represented the internal flow structure of the tumour. For the head model, it was first attempted to extract surface/dimensional data from MRI data sets. Although it was possible to gather data from these data sets, the quality of the model was severely lacking. A compromised solution was therefore applied, where a downloaded photogrammetry head model was transformed to fit the size and shape of the low quality MRI extracted model. This head model was then modified to provide access, a mounting point, and a 'skull thickness' was added. The head model was printed on a 3D Systems ProJet 6000SD in clear photopolymer resin. A base plate with mounting points was created from a piece of acrylic on a CNC router.

All the 3D modelling was done using Blender, a 3D surface modelling software, which is excellent at creating organic surfaces and complex models, which would be very difficult to achieve using traditional parametric CAD modelling techniques. The DICOM data surface extraction was done using 3D Slicer. This was carried out at the medical Advanced Manufacturing Research Centre (mAMRC) by Mr Marcus Crossley.

Figure 4.9 represents the 3D head model, which geometrically mimicked the surface of the head of a patient. An x,y,z Cartesian coordinate framework (3-D) was used, where x represented the distance from the top to the bottom of the head, y represented the distance from the front of the head (forehead) to the back of the head and z represented the distance from the left ear to the right ear.

Figure 4.9: 3-D simulated head phantom with the tumour held on a stand on the grid matrix. The tumour was located at the maximum depth within the head for measurements; 16.5 cm from side to side, 20 cm from forehead to the back and 15 cm from top head to down (nose level). The target depth was (8.25, 10, 7.5 cm).

With the magnetic device placed on top of the head, the distance to the tumour was 7.5 cm. On the other hand, if the magnetic device was placed on the front or back of the head, the maximum distance to the tumour was 10 cm. Last but not least, if the magnetic device was placed on the left or right side of the head, the maximum distance to the tumour would be 8.25 cm. Therefore, the maximum tumour depth would be ($X = 8.25$cm, $Y = 10$cm, $Z = 7.5$ cm).

A simulated brain tumour, approximately 3 cm in diameter, was printed, using a synthetic polymer, with a positioning matrix allowing the tumour to be relocated anywhere within the printed head (**Figure 4.10**). The inside of the tumours were designed so that they had a complex flow network and had an inlet and outlet for connecting to a flow system.
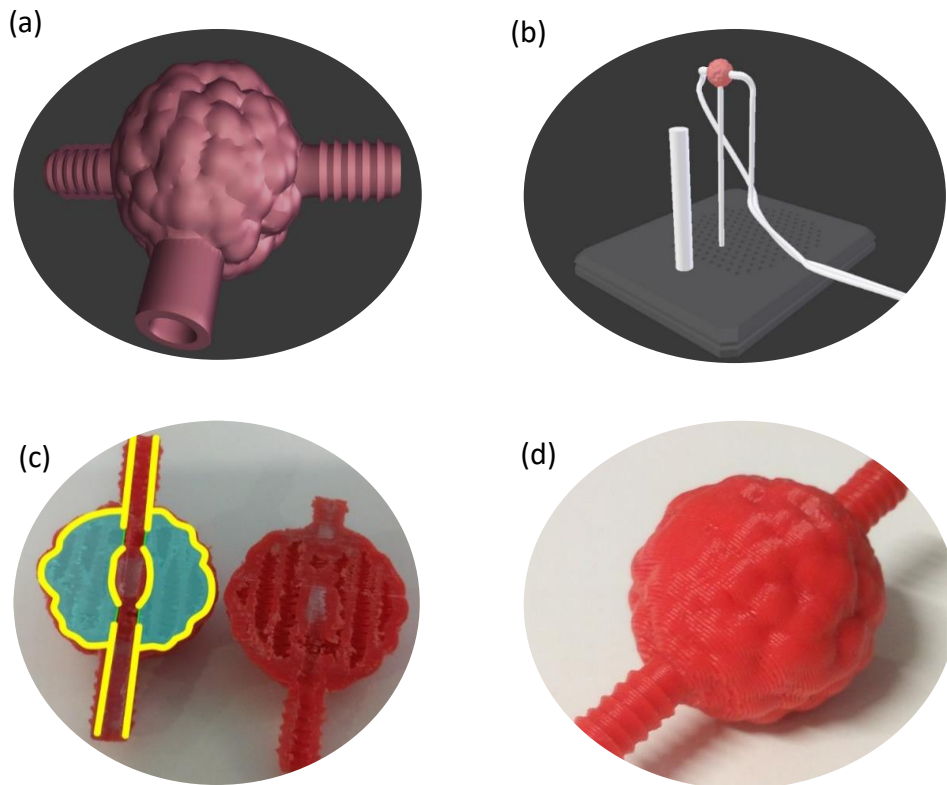
Figure 4.10: 3D printed tumour: (a & b) show the simulated tumour with a stand on a grid matrix. (c & d) show the printed tumour where (c) shows the complex flow network inside the tumour, (d) shows the tumour from outside with the inlet and outlet connectors.

4.6   Discussion

Two Halbach arrays were assembled physically based on the FEMM model design configurations in chapter 3. The main challenge in the assembly procedure was to overcome the forces generated from using two different magnetisation angles for two magnet elements i.e. repulsive forces. NdFeB-N52 magnetic blocks create very strong magnetise fields ~1T [183]. It was therefore necessary to restrain the magnet blocks during the assembly procedure.

In general, the data generated from FEMM models were slightly higher than those obtained from the assembled Halbach magnets. For example, from the FEMM model, the

magnetic field strength was 1 T while the magnetic field strength from the physical model was 0.93 T. This discrepancy could be a result of technical errors in the way the magnets were simulated including the boundary conditions of the model. It is also possible that the difference could be due to the way the models were assembled, for example, due to high repulsive forces, gaps emerged between magnets with similar positive polarities. Also using glue to stick the magnets resulted in slight gaps. This discrepancy between simulated and assembled magnets was also noted by Bashyam et al. when a Halbach array magnet was designed, modelled and assembled for single-sided magnetic resonance [183]. In their study, the magnetic field strength of the assembled magnet was 0.17T while that of the simulated magnet was 0.174T. Similarly to our observations they attributed the discrepancy to variations between magnets and imperfections (gaps) in magnet assembly. In general, gaps between the magnets within the assembly are often inevitable, but using an adhesive with iron particles loaded into the glue the magnet may help to overcome this issue. Iron-loaded epoxy may also help focus and shape the magnetic field [168].

Assembling both models with multiple layers allowed assessment of the effect of the magnet volume on magnetic field strength, field gradient and hence magnetic force, as well as the penetration depth. **Figure 4.1** provided clear information on the impact of adding more magnet layers to both models. It was noticed that the magnetic field strength for both models with three layers was slightly higher than those with one or two layers. There was a significant change in field gradient and magnetic force for both models with a third layer, however. It can be confirmed that increasing the volume/size of the magnet helps to increase the magnetic field strength, field gradient and force which agrees with results found in the literature [183][184][162]. Both models showed a sharp drop off in magnetic field strength, field gradient and magnetic force between 0 cm and 0.5 cm but after this, the drop off was more gradual.

In a comparison between models, it was found that Model 2 produced slightly higher magnetic field, field gradient and magnetic force than Model 1 for all numbers of layers. In terms of penetration depth, however, Model 2 had a significantly deeper penetration depth compared with Model 1. Some studies have reported a maximum penetration depth from Halbach arrays of between 5 mm and 50 mm [184] while our Halbach model ranged between 50 mm to 100 mm.

It is worth mentioning that MPD for models 1 and 2 was 7.5cm and 9cm, 9.5 cm and 10cm, 12.5 cm and 13 cm for first, second and third layers, respectively. Although the field gradient is weak at those distances (~ 8 - 10 T/m), preliminary theoretical studies carried out by Voltairas and Ruuge proved that the required field gradients to trap MNPs should be 8-100 T/m (Ref), which confirm the ability of Halbach array to trap MNPs at those distances [185] [186]. In dynamic conditions, MNP trapping will occur if Fm in Eq 1.5 of MNPs exceeds F_D in Eq 1.6. This will be investigated experimentally in the next chapter.

Model 2 was superior to Model 1 in terms of magnetic field strength, field gradient and magnetic force. Given that the primary objective of the study was to identify a model that produces higher magnetic field strength as well as penetration depth, Model 2 was therefore selected as the best Halbach array to use for further investigation.

According to measurements from the 3D head/tumour phantom, the maximum depth of a tumour located within the head would be 10 cm. It was noted from the Gaussmeter measurements that the strength of the magnetic field is weak at 10cm. Therefore, further efforts were also made in order to further optimise the value of the magnetic field strength, field gradient and hence magnetic force of Model 2 at 10 cm. The

optimisation strategies that were considered for Model 2 included closing the corners with 45° magnetisation orientation pointing towards the middle of the magnet array, as well as covering the magnet with a steel case to help shield and redirect the magnetic field.

Interestingly, it was found out that the area that had less magnetic field strength at the surface of the magnet demonstrated the highest magnetic field gradient and force as well as magnetic penetration depth. In this case, therefore, to get an effective delivery of drugs to deep locations will require pointing the centre of the magnet towards the location of the brain tumour. The ability of the **Model 2** Halbach array to steer SPIONs to the desired location of a simulated brain tumour will be discussed in the following chapter 5.

<u>Limitations</u>

One of the challenges associated with the assembling of Halbach arrays magnets was the magnetic forces that acted between each element, which made it difficult to assemble the multiple layers. To overcome this limitation, it was necessary to find an expert company to construct multiple layer magnet, but this can be costly and required that a confidentiality agreement was put in place.

The other limitation is that only uniform shape magnets, i.e. square, can be assembled but such a shape would create a gap from the magnet edges when placed on a patient's head. A curved shape would overcome this limitation, but a special machine would be needed to bend the magnet, this was not available for the current study.

Chapter 5

Halbach Array trapping of SPIONs

5.1 Introduction

The success of magnetic drug targeting (MDT) depends strongly on the ability of the magnet to steer and trap SPIONs that are loaded with drugs to the desired location. When the desired location is far from the external magnet, a strong magnetic field gradient is required, as it has been proved that magnetic field gradients drop off sharply with increasing distance between the magnet and the target [165]. As a result, the higher the magnetic field gradient, the higher the chances of trapping the SPIONs [187] [170]. In addition, the vascularisation of the target area is a crucial parameter in MDT and steering the SPIONs to a target with a complex vasculature is challenging [188] [189].

Previous studies have been conducted to investigate the movement of SPIONs under the effect of magnetic fields in blood vessels in two models, namely *in silico* and *in vitro* [190] [191] [192]. Together, these studies show that movement of magnetised SPIONs under the effect of a magnetic field provokes interactions between the magnetised SPIONs leading to the creation of aggregates in the direction of the homogeneous field. Furthermore, the magnetic gradients are capable of steering the aggregates, as a whole, to the target.

Kang et al., tested the ability of a Halbach permanent magnet array to separate living cells magnetically (*Staphylococcus aureus*-bacterial cells) over distances of up to 30 mm. Magnetic micro-particles were bound to the cells and then placed in a 50 ml tube before exposing them to the magnet. In this study they used both a Halbach array (0.8 T) made with rectangular bar magnets and compared this to a conventional alternating magnet. The Halbach array was more effective and removed more than 95% of the bacterial cells compared to only 70% when they used the alternating array [165]. This

suggests that Halbach arrays could be used in high-throughput magnetic devices for separation of cells, molecules and toxins.

Additional evidence that indicates the ability of the Halbach array to capture SPIONs in a desired location was shown in a study by Gitter& Odenbach in which they modelled a blood vessel supplying a tumour using a half Y-shaped glass tube and steered the SPIONs (7.5 nm) to a specific location [193]. The fluid flow was run for 10 min. The tube had a diameter of 1.6 mm and the flow rate was 12.3 mm/s, which was constant for the whole experiment. The magnetic field was generated by an axially magnetised cylindrical Halbach array with a diameter of 10 mm, a height of 5 mm and a magnetic flux density at the centre of the surface of 310 mT. It was claimed that injecting SPIONs towards and closer to the target area would result in the trapping of a higher SPIONs concentration in that area. In this case, it was observed that the targeting efficiency reached up to 97% of the SPIONs in the chosen branch [193]. Although they used an artificial system, the aim was to achieve MDT for tumour treatment.

Magnetic fields can be used effectively to manipulate the movement of MNPs in a flow model with varied flow rates. This was confirmed by Munir et al.[194], where a microfluidic model containing 75 mm long and 800 µm diameter tangential microfluidic channels was used to switch MNPs from lesser to greater flow rates. The channel was set up to form an X-shaped where the lower rate flowed with MNPs and the upper flow rate flowed with water only. The flow rate was varied from 0.6–11 µl/s and was pumped using a peristaltic micro-pump. The MNPs consisted of an inner core made up of magnetite (Fe_3O_4) crystals of about 12 nm diameter, to form an overall size of 200 nm diameter at a concentration of 1 mg/ml. A permanent neodymium magnet (N52) was placed at the centre of the X-shaped channel. The magnet had dimensions of 1×1 inch 3/8-inch thickness with a flux density of 14 800 Gauss. It was found that negligible switching of MNPs takes place

in the absence of a magnetic field, whereas 90% of switching was observed when the magnetic field was employed.

5.2   Aims and Objectives

Hypothesis

We hypothesise that our Halbach array can trap SPIONs in a 3D printed phantom (head/tumour) flow model at distances between 0 to 10 cm.

Aim

This chapter sought to demonstrate the ability of the Halbach array of Model 2 to trap different concentrations of SPIONs (Fe_3O_4) at different distances.

The main challenge that has been focused on in this project is estimating the distance between a brain tumour (pg7) and the external magnet which allows trapping. For this reason, it was decided to use the technique of a 3D printer in order to print a model of a head and tumour based on that of a patient. By doing so, it would be possible to change and control the tumour location. Therefore, a physical head (not the brain/tumour) was modelled in order to place (fix) the magnet on the surface and control the magnet to tumour distances. The 3D printed tumours were not hollow from inside but consisted of a mimicry vessel network, typical of that seen in tumours. For this reason, the printed tumour is considered to have a complex vessel network inside. Evaluating HA using an *in vitro* model has an advantage over *in vivo* models e.g. a mouse model, where the head size is not comparable with a human head, and hence, the distance between the tumour and the magnet is too small.

The following objectives were chosen based on the above conditions.

Specific objectives

- To use a 3D printed phantom flow model with plastic and bio-phantom tumours to assess the trapping ability of SPIONs at different distances

- To use a custom-made vasculature model to investigate the amount of time required for the SPIONs to be trapped within the vasculature tubing and how long the SPIONs remain trapped in the target area after removing the Halbach array.

- To apply different techniques including magnetic resonance image (MRI), inductively coupled plasma microscopy (ICP) and nuclear magnetic resonance (NMR) to assess iron trapping within the models.

This project is a preclinical study designed to use a lightweight, inexpensive and powerful permanent magnet (HA) for MDT. With the hope of eventually using this for clinical studies (see pg7). Therefore, in this preclinical study, three main objectives were defined;

1. Use of in silico methods to design the required HA.

2. Evaluation of the constructed HA in the lab using an *in vitro* method. This was to evaluate the trapping ability of HA for SPIONs.

3. Evaluate the constructed HA using an in vivo model. This work was done in collaboration with a postdoctoral researcher (Dr Priya Patel) in mice. The results of these experiments were highly promising, see pg164.

5.3 Halbach array based on Model 2 traps SPIONs in a phantom flow model

In this experiment, a head and tumour phantom model were used to evaluate the ability of Halbach array to trap SPIONs (**Figure 5.1**). From optical and MR scan data, a 3D head model was printed which geometrically mimics the surface of the head of a patient as described in Chapter 4 **Figure 5.1 a**. Also, a brain tumour was printed using transparent material (synthetic polymer), with a positioning matrix allowing the tumour to be relocated anywhere within the printed head (**Figure 5.1 b**). The inside of the tumours were designed so that when printed they had a complex network and had an inlet and outlet for connecting to a flow system (**Figure 5.1 c**). The structure of the tumour model has been explained in more detail in section 2.2.3.2. A Halbach array magnet was placed on top of the head in order to trap SPIONs in the tumour whilst under flow conditions. The surface of the head was 0.8 cm in thickness, and the magnet was in direct contact with this. Ferrofluids with a range of SPION concentrations, i.e. from 1 mg/ml to 10 mg/ml were placed in 50 ml tubes and the fluid was run in an open loop through a fluid flow system using a syringe pump at a flow rate of 10 ml/min.

(a)

(b)

(C)
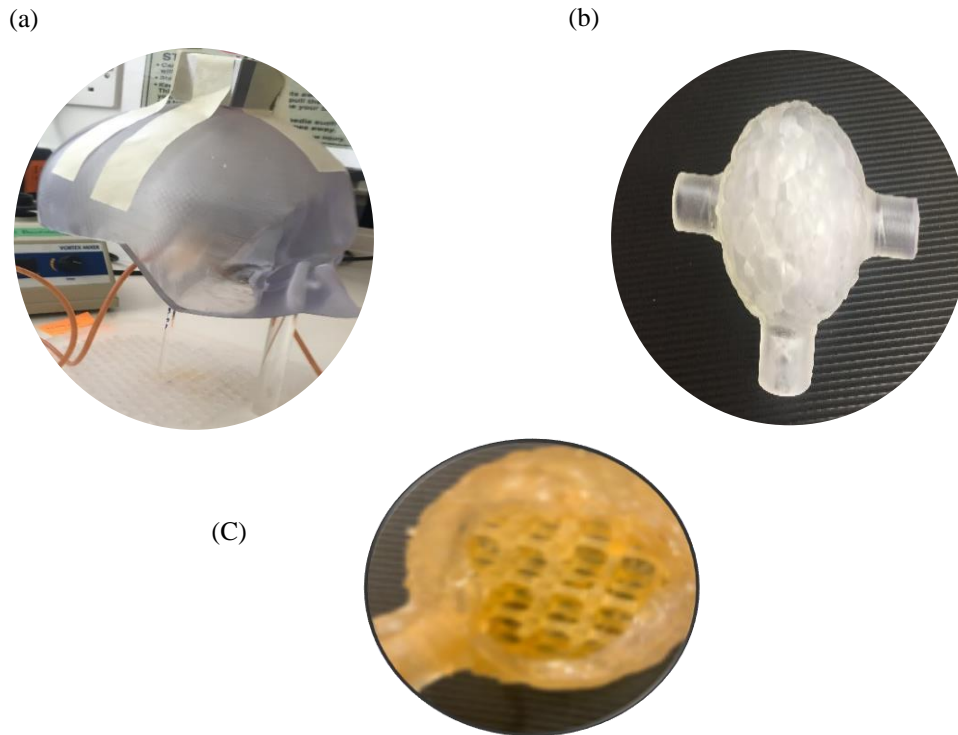
Figure 5.1: A 3D printed phantom model to assess SPION trapping. (a) 3D printed adult head based on a patient MRI scan. (b) A transparent 3D printed tumour. (c) Interior structure of the tumour. SPIONs are pumped in an open loop through a flow system using a syringe pump at a rate of 10 ml/min. The magnet was placed in the centre of the head, in contact with the head (0 cm) and 8 mm way from the tumour (skull thickness). The flow was run until the fluid in the tube of 50 ml finished, for about 5 min.

In these experiments, the tumour was placed directly below the head (from inside).

SPIONs flowed at 10 ml/min were instantly held within the tumour and could be seen by

eye. **Figure 5.2a** shows very little trapping of SPIONs in the control experiment in which

no magnet was in place. On the other hand, the iron was instantly trapped after placing the

magnet above the head **Figure 5.2b**. Once the iron was trapped there was a change in the

colour of the collected fluid (Dark brown - SPIONs are concentrated) and after trapping of

SPIONs (light brown - fewer SPIONs present) (**Figure 5.2c**).

(a)   (b)   (c)
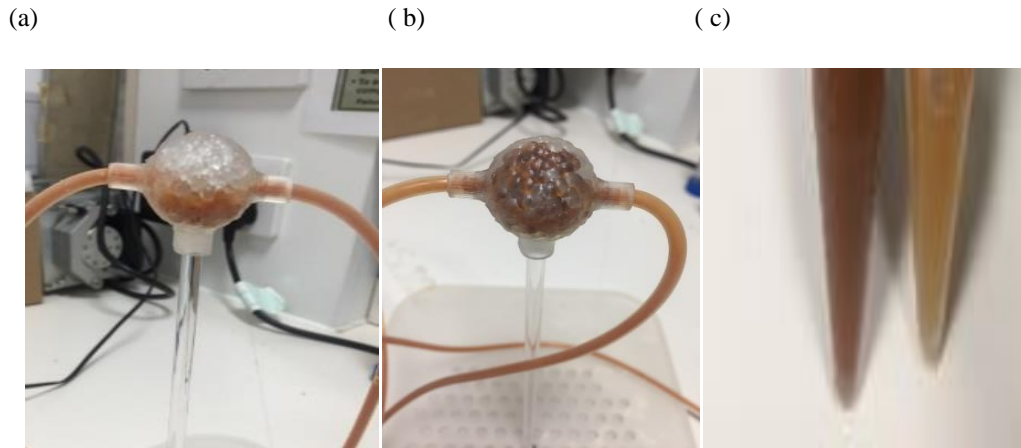
Figure 5.2: Halbach array traps SPIONS undergoing flow. SPIONs at 5 mg/ml in a 3D tumour phantom in an open loop through a flow system using a syringe pump at a rate of 10 ml/min. The magnet was placed in the centre of the head, in contact with the head (0 cm) and 8 mm way from the tumour (skull thickness). The flow was run until the fluid in the tube of 50 ml was finished, for about 5 min.

a. Shows the control tumour where the magnet was not applied where all SPIONs are the bottom of the tumour.

b. Shows the tumour where most of SPIONs were trapped because the Halbach array magnet was placed on top of the head while the tumour was contained within the head.

c. Shows collected SPIONs in the control tumour, before placing the magnet (dark brown) as all SPIONs came through the tumour, the collected SPIONs in the light brown tube shows that SPIONs were released from the fluid due to the presence of the magnet.

Once the trapping of iron was complete, both the inlet and outlet of the 3D tumour phantom models were sealed with a silicone sealant to prevent the particles from leaking out and keep them inside the tumour. The tumours were then scanned via MRI in order to confirm SPION trapping.

Figure 5.3 confirms the trapping of iron inside the tumour in the presence of the Halbach array. For the MRI scans, tumours were imaged following trapping of SPIONs at different concentrations of ferrofluid. MRI scans showed that the number of SPIONs trapped in the tumours increased with increasing concentration of the particles. This can be seen by the differences in the intensity of the colour in the samples where the control (with

no magnet and trapped SPIONs) was the clearest. The more concentrated the SPIONs the more iron was present within the tumour.
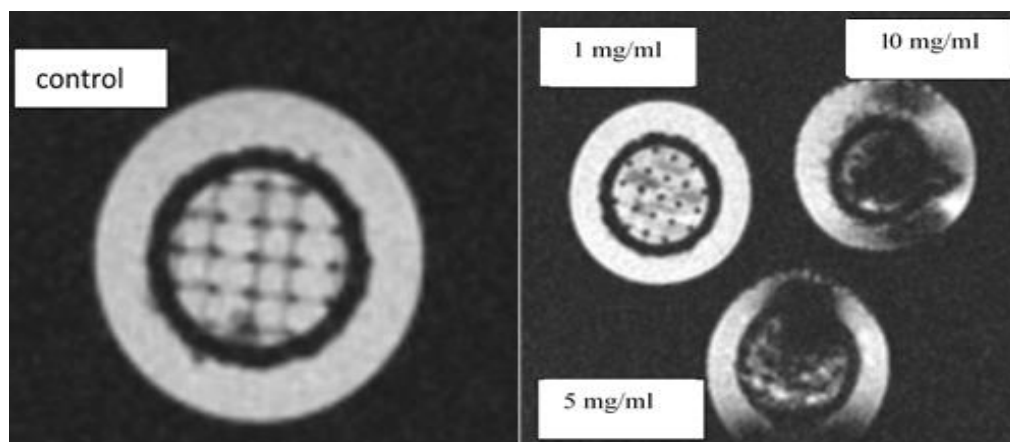

Figure 5.3: T2* weighted MR images of four tumour models with different SPION concentrations. The MRI scan shows the SPIONs trapped within the tumours in the presence of the magnet. The darker the colour, the more SPIONs were trapped. In the control sample no magnet was present. The tumours were placed underneath the head (0.8 cm away from the magnet). The scans were obtained using a 3T neonatal MRI system with a dual gradient echo sequence, TE=4.60ms and 20ms.

In addition, pixel values were extracted from the same region of interest from each tumour for scans with two different echo times i.e. TE 4.60s and TE 20s. The natural logarithm of the signal, Ln (signal) was calculated and plotted against time (**Figure 5.4**). The slope of the graph provides a measure of the T2* relaxation time.

SPIONs in the tumour scan can be quantified by measuring the ratio of the signal intensity (SI) where pixel values were extracted from the same region of interest from each tumour with two different echo times, i.e. TE 4.60s and TE 20s, then signal intensity ratios (SIRs) in both TE was measured. The equation that was used to calculate T2* was described in chapter 2. **Figure 5.4** below illustrates the values of T2* for each SPION concentration which show that the higher the level of iron concentration, the less the T2* value, as expected. These experimental results confirmed that iron particles with different

concentrations were trapped adequately using the Halbach array magnet for the flow rate used.

SPIONs vs T2*
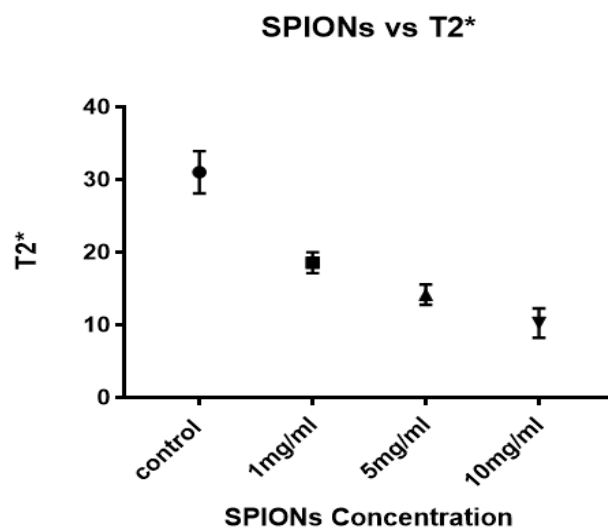
Figure 5.4: T2* decreases with increasing SPION concentrations. T2* values were calculated after SIRs were measured from 3T MRI scans at two different TE values; 4.60s and TE 20s.

5.3.1 Ability of the Halbach magnet array to trap SPIONs at a range of distances

Here, the iron trapping experiment was conducted in two parts. The first part involved trapping the iron alone, while the second part entailed trapping white blood cells (WBCs) loaded with iron. All the WBCs were incubated with SPIONs at a different range of concentrations for 24 hours. WBCs were seeded at 300,000 and incubated with 0.1, 1, 5, 10 and 20 mg/ml. WBCs were harvested from healthy blood donors (n = 3). All the

procedures were explained in 2.2.12. Then the fluid was flowed using the same model as above.

Both parts aimed to trap the iron at different distances, such as at 0.8 cm and 5 cm away from the magnet. The previous procedure was applied, to explore the effectiveness of the technique at different tumour depths within the head. When the fluid flow was run until the experiment was completed, the fluid iron inside the tumour was flushed out into a small tube in order to be prepared for ICP. This was another technique that was used to confirm the ability of the Halbach array to trap the iron particles with different concentrations at different distances. Interestingly, the trapping ability can be confirmed via the naked eye, as can be seen in **Figure 5.5** below, where the attracted SPIONs decreased with increasing distance from the magnet.


Figure 5.5: the SPIONs at an initial concentration of 5 mg/ml flushed from the tumour after trapping at different distances.

From right to left, control, at the internal head surface (0.8 cm away from the magnet), at 5 cm and 10 cm away from the magnet. Halbach array magnet was used to trap SPIONs at a concentration of 5 mg/ml in a 3D tumour phantom in an open loop through a flow system using a syringe pump at a rate of 10 ml/min. When the trapping procedure was completed, the SPIONs trapped within the tumour were flushed out into a 15ml falcon tube to visualize the trapped SPIONs at different distances.

After the flow process was completed, the fluid in the tumour containing iron was flushed out into a small tube in preparation for ICP. The results obtained are shown in **Figures 5.6** and **5.7** below. The results demonstrate the trapping ability of the Halbach array magnet at 0 cm (plus 0.8 cm which is the skull thickness) and 5 cm (plus 0.8 cm)

away from the magnet without WBCs as well as with WBCs. The results showed that the Halbach array trapped SPIONs at both distances but that the trapping efficacy decreased as the distance increased, i.e. 5 cm.

SPIONs of 1 mg/ml

SPIONs of 5mg/ml

SPIONs of 10 mg/ml
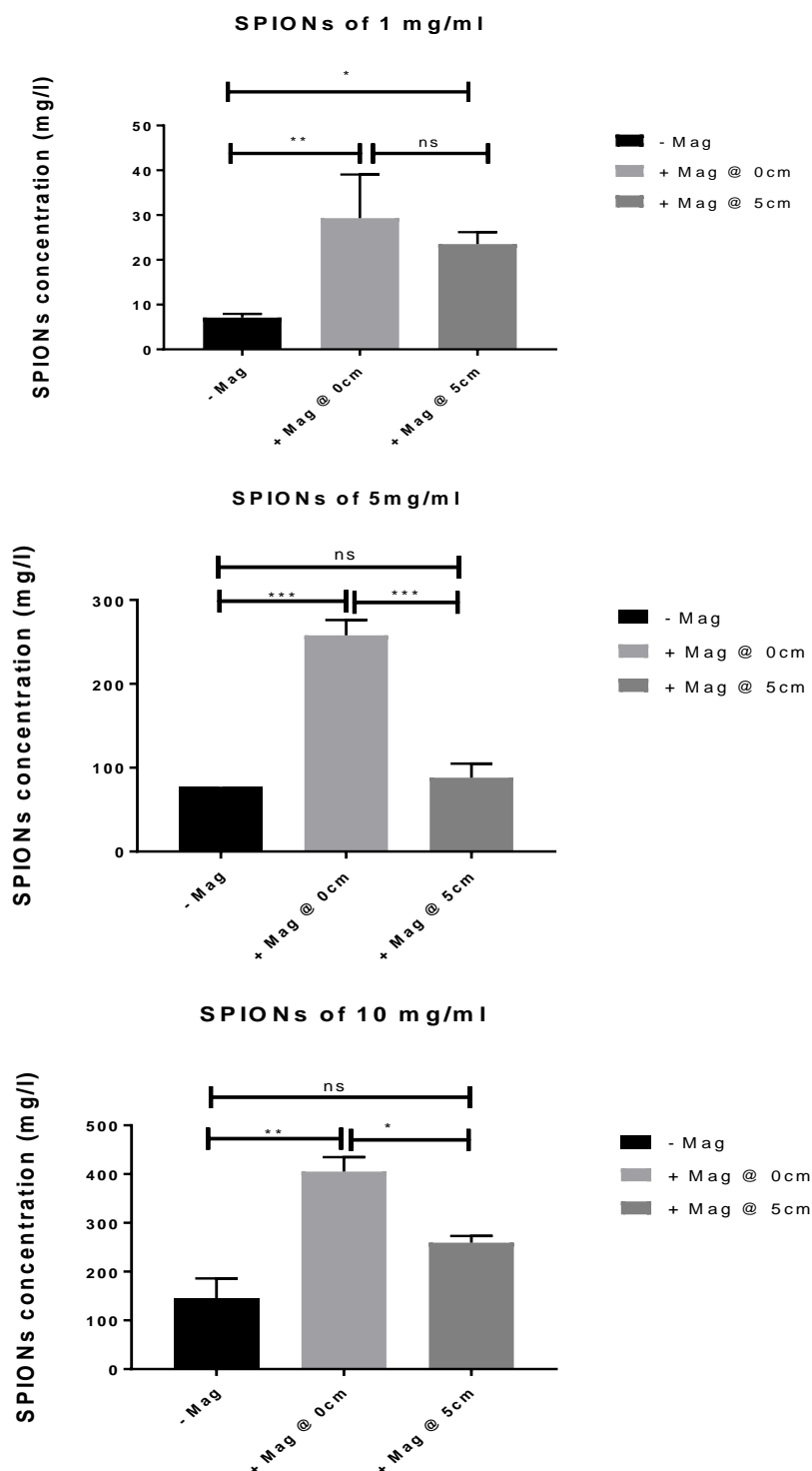
Figure 5.6: ICP data demonstrate the trapped SPIONs that were flushed out from the tumour phantom after applying a Halbach array magnet with one layer. The tumours were located at two different distances; (a) 0 cm away from the magnet and (b) 5 cm away from the magnet. When the trapping procedure was completed, the trapped SPIONs of different concentration, i.e. 1, 10, 15 mg/ml within the tumour were flushed out into a 15 ml falcon tube to be ready to detect SPIONs using ICP. Data are the mean and SD of N=3 experiments. All data was analysed using one way anova-prism.*p <0.01, **p =0.001 and ***p <0.001.
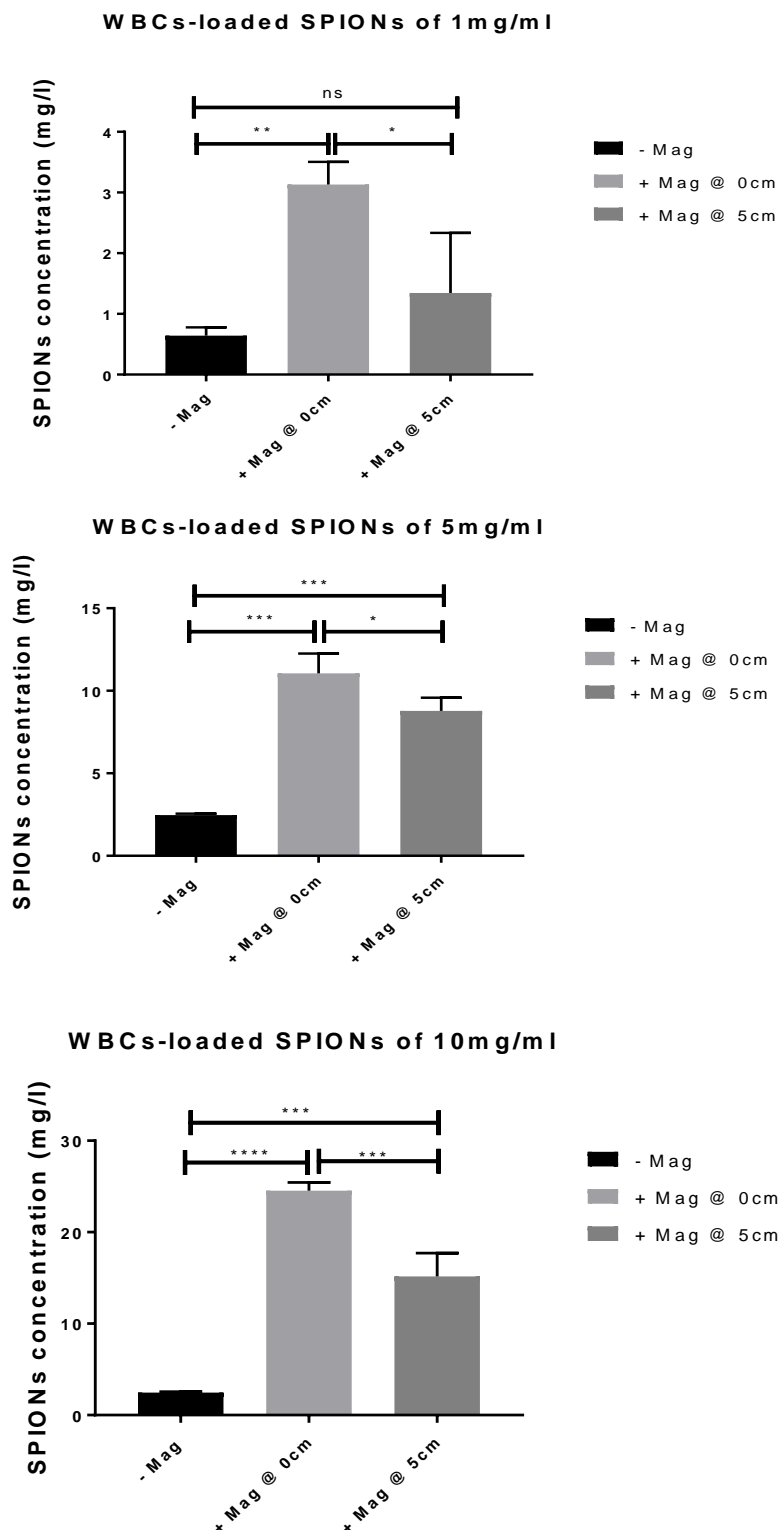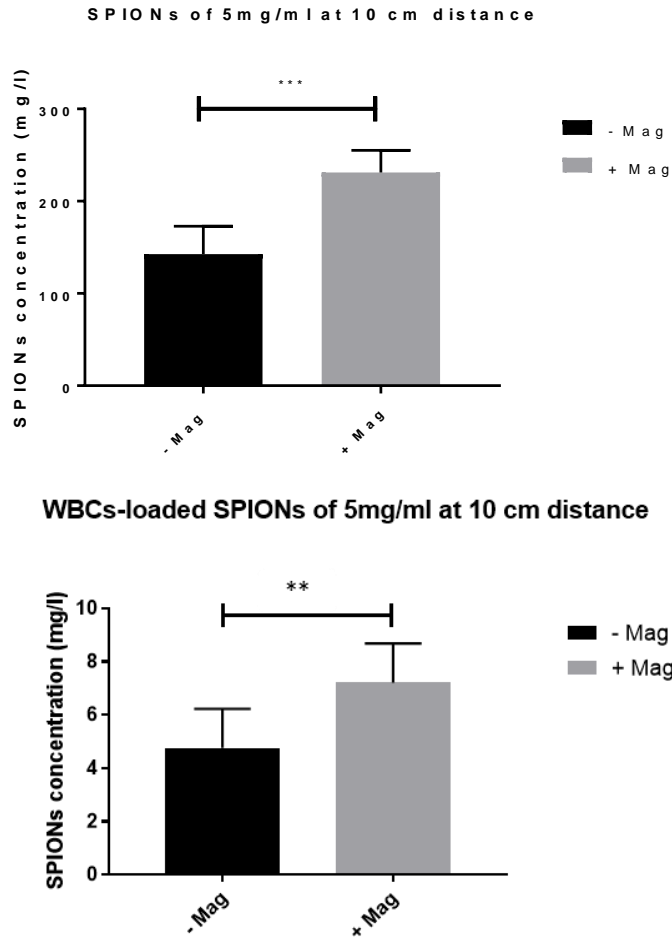
Figure 5.7: ICP data demonstrate the trapped SPIONs-WBCs that were flushed out from the tumour phantom after applying Halbach array magnet of one layer. The tumours were located at two different distances; (a) 0 cm away from the magnet and (b) 5 cm away from the magnet. When the trapping procedure was completed, the trapped SPIONs of different concentrations, i.e. 1, 10, 15 mg/ml within the tumour were flushed out into a 15 ml falcon tube to be ready to detect SPIONs using ICP. Data are the mean and SD of N=3 experiments. All data was analysed using one way anova-prism.*p <0.01, **p =0.001 and ***p <0.001.

The previous data were sufficiently encouraging to consider trapping SPIONs at a greater distance, therefore, it was attempted to trap SPIONs at 10 cm. For simplicity, only one SPION concentration, i.e. 5 mg/ml, was used in the flow model with the Halbach array of three layers.

Interestingly, although the magnetic field strength which was obtained both theoretically from the simulated FEMM and measured from the assembled Halbach models was very weak, i.e. 0.001 T at 10 cm, nonetheless SPIONs were still trapped at such a distance. ICP data in **Figure 5.8** below showed a slight difference between the control and trapped sample but a significant difference between both samples where WBCs were loaded with SPIONs.

This can confirm that our Halbach array was able to trap the iron at this depth (10 cm) even with a weak magnetic field.

Figure 5.8: ICP data demonstrates the trapped (a) SPIONs and (b) WBCs loaded with SPIONs of 5 ml/mg at 10 cm away from the Halbach array magnet of three layers. The control demonstrated the SPION concentration when no magnet was applied, while SPIONs+Mag demonstrates the trapped SPIONs where the magnet was applied. When the trapping procedure was completed, the fluid that was inside the tumour was flushed out and transferred into a 15 ml falcon tube to be ready for detecting SPIONs using ICP. All data was analysed using t-test-PRISM.**p =0.702 and ***p =0.0824.

In general, the concentration of trapped SPIONs in the phantom flow model was different depending on the initial concentration of SPIONs and the location of the tumours within the head phantom. As expected, the further away the tumour was from the magnet, the fewer SPIONs were trapped. For example, at 5 cm depth, the concentration of SPIONs was 241 mg/l whereas at 10 cm, the concentration of SPIONs was 183 mg/l.

It was proved from the FEMM model that the Halbach magnet array is able to reach a depth of 10 cm with B = 0.001 T. Although the magnetic intensity is weak, it was interesting to confirm the trapping ability around that distance.

In summary, it can be confirmed that our Halbach array magnet was able to trap iron particles with and without WBCs with different iron concentrations at different distances in a tumour model with a simple vasculature, i.e. a 3D printed tumour model with flow in a simple supply tube simulating a vessel.

5.3.2 WBCs ability to take up SPIONS with minimal cell toxicity

Next, the uptake of SPIONs by WBC and cell viability was confirmed. When SPIONs of different concentrations were incubated with WBCs for 24 hours, Prussian blue staining was used to confirm the distribution of SPIONs within the WBCs (**Figure 5.9**).
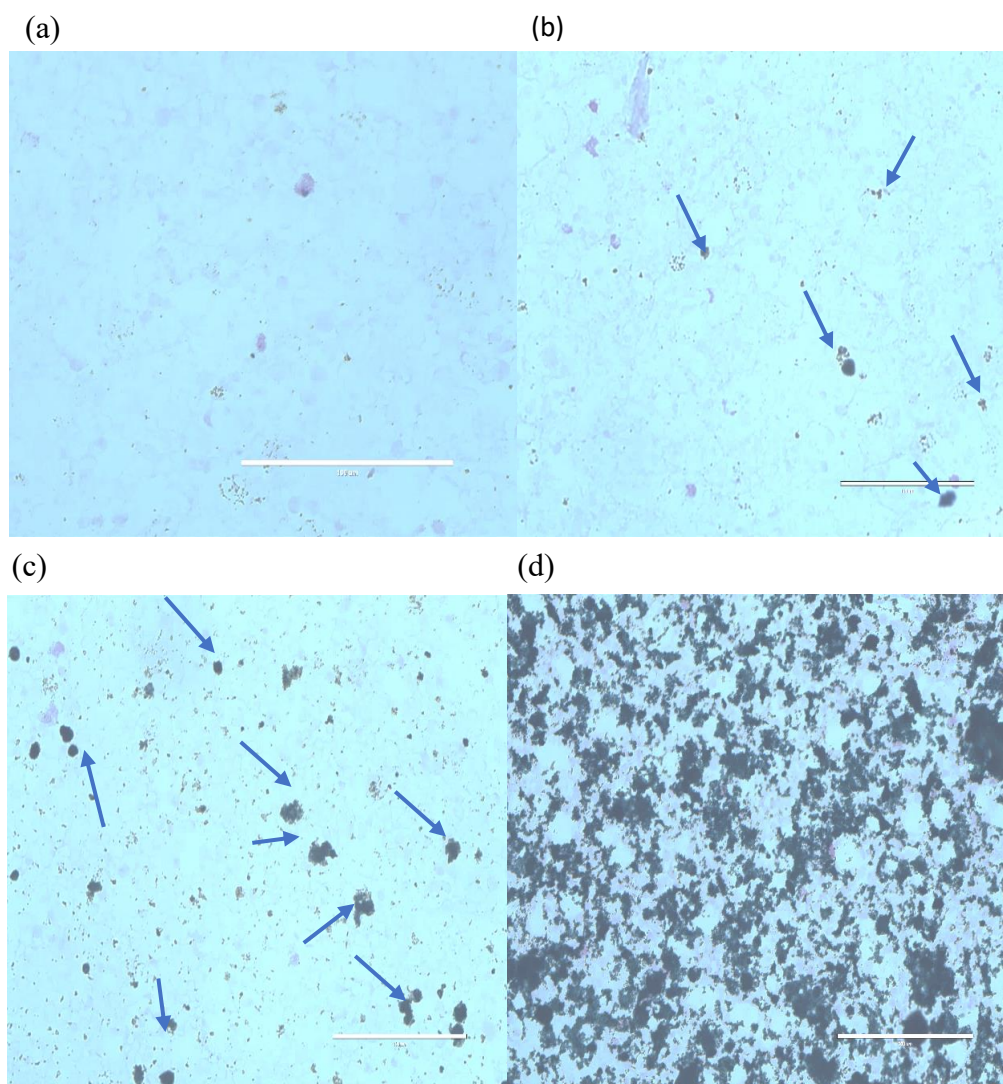
Figure 5:9: Prussian blue staining showed SPION distribution within WBCs. (a) Control WBCs (pink). (b-d) SPIONs of 0.1, 1 and 10 mg/ml (dark) were distributed within WBCs. SPIONs of different concentrations were incubated with WBCs for 24 hours, then 500,000 cells of 1 ml were centrifuged using the Cytospin technique. After applying Prussian blue staining, the slides were ready for analysis using light microscopy, Leica DM1000.

Flow cytometry was used to assess the cell viability. In flow cytometry, cells can be morphologically described by two main axes; forward scatter (FSC) and side scatter (SSC). The forward scatter represents the cell size and the side scatter represents the quality and condition of the cells. 2 μl of a 50 mg/ml stock of the viability dye propidium iodide (PI) was added to each sample immediately before analysing on a BD FACS

Calibur. PI is a membrane impermeant dye that is generally excluded from viable cells. It binds to double stranded DNA by intercalating between base pairs of dead cells [160].

The viability of WBCs with and without SPIONs is illustrated in **Figure 5.10** (a) below. The gated area (R1) presents the population of live cells and highlights that the different WBC populations can be distinguished based on the scatter profile i.e. lymphocytes, monocytes and granulocytes. All debris was removed by applying a gating strategy so that the analysis was only performed on cells. On the right is the gated area (R2), which represents the dead cells that have been stained with PI. The uptake of SPIONs at different concentrations was evaluated by flow cytometry. **Figure 5.10 b** shows representative fluorescent dot plots of the control cells- where no SPIONs were present, and the lowest and highest SPIONs at 0.1 mg/ml and 1 mg/ml respectively. What is interesting is that the WBCs increase in size in the presence of the SPIONs compared to the untreated cells. This is shown in the change in the side scatter profile of the cells (y-axis). This suggests that cells have taken up the iron. **Figure 5.10 (c)** shows there was no significant effect on WBC viability in response to SPIONs, even at high concentrations i.e. 20 mg/ml.
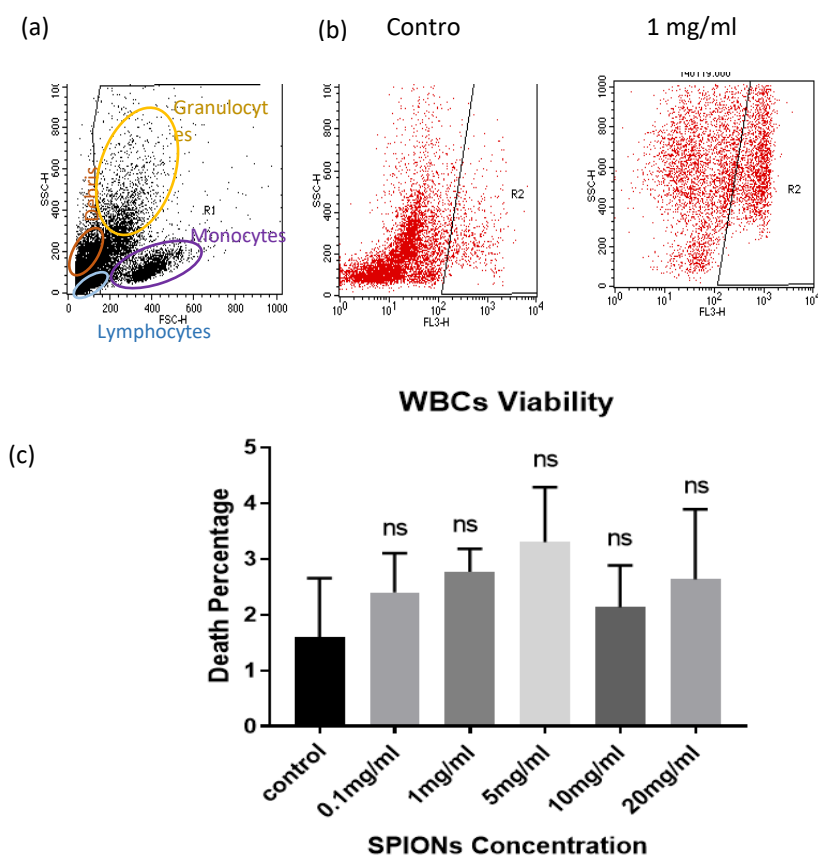
Figure 5.10: WBC take up SPIONs and do not undergo cell death. (a) Representative Flow cytometry dot plot of WBCs in SSC-FSC analysis (R1) which shows all types of WBCs including granulocyte, monocyte and lymphocytes based on their scatter profile. All the cell debris was gated out and a further gate applied to the cells (R2) to detect the dead cells with PI staining in the FL3-H channel. (b) Control sample, cells with 1 mg/ml SPION. (c) WBCs death percentage, where the cells were exposed to different SPIONs concentrations and incubated for 24 h. No toxicity effects were found.

It is also worth investigating the ability of the Halbach magnet array to trap iron in a more complex vasculature model. This will be demonstrated in the section below.

5.4 Halbach array based on Model 2 traps SPIONs in Bio-phantom flow model

In this experiment, a more complex tumour vessel model was developed. A solid homogeneous piece of material with MRI properties close to the average properties of human brain tissue was designed. This is referred to as the bio-phantom tumour. The material has realistic MRI and mechanical properties and is suitable for MR imaging. The tumour used had a complex internal network and had two inlets to be connected to the flow tubes. **Figure 5.11** below.


Figure 5.11: the internal design of bio-tumour where shows the complex network of the 3D tumour.

In order to assess the trapping ability of the Halbach array magnet with a more complex tumour model, the bio-phantom brain tumour model was initially attached to a simple vasculature supply. This was located 5 cm away from the magnet, as illustrated in

Figure 5.12. An iron concentration of 5 mg/ml was used with a flow rate of 150 ml/min. The same trapping procedure as discussed for the previous model was applied in

this experiment. It can be seen that iron particles were mostly trapped in the area close to the magnet (yellow circle). Although the tumour was 5 cm away from the magnet, trapped iron can be seen by naked eye (dark spots in the red circle).
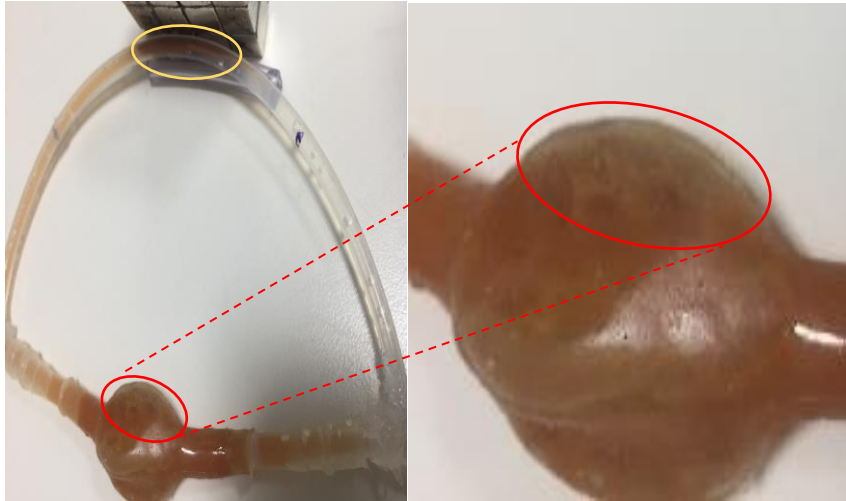
Figure 5.12: A three layer Halbach array magnet was used to trap SPIONs applied at a concentration of 5mg/ml in a bio-phantom tumour model that was attached to a complex vasculature model where the tumour was located 5 cm away from the magnet. The fluid flow was run in a closed loop through a flow system using a peristaltic pump at a rate of 150 ml/min. The magnet was placed in the centre of the main tube parallel to the tumour. The fluid was flowed until most of the SPIONs were trapped and the fluid was clear.

MR images of 9.4 T were also acquired to confirm the trapping (**Figure 5.13**). This showed that SPIONs were trapped at 5 cm distance (dark area). The dark area in the MR images demonstrates the iron particles passing through the tumour. When the magnet was in place, however the iron particles were trapped more effectively and created a dark area, as shown on the RHS**.** This confirmed the ability of the magnet array to trap iron particles in a complex model at a distance as high as 5 cm.

(a)   (b)
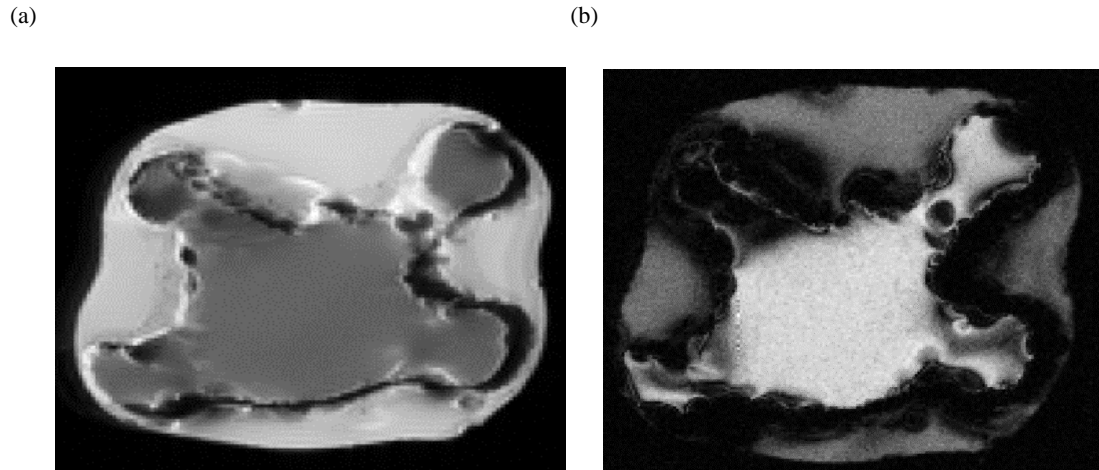
Figure 5.13: 9T MRI scans show the trapped SPIONS in the bio-phantom tumour model. (a) SPIONs where no magnet was applied, (b) SPIONs with applied magnet. A three-layer Halbach array. SPIONs were used at a concentration of 5mg/ml in a bio-phantom tumour model that was attached to a complex vasculature model where the tumour was located 5 cm away from the magnet. When the trapping procedure was completed, the tumour was removed from the vasculature model and the edges were sealed ready for MRI.

For further investigation, a more complex model was designed to assess the trapping ability of the array magnet and this is discussed in the section below.

5.5   Halbach array based on Model 2 traps SPIONs in a complex vasculature flow model

In this experiment, a complex vasculature model was developed in attempt to come closely mimic real human blood vessels. This model had multiple channels with four branches, each with an internal diameter of 2 mm, branched from a main supply vessel (tube) with a 3 mm internal diameter at different distances i.e. 3 cm, 5 cm, 8 cm and 10 cm, as shown in **Figure 5.14.** The main tube had an open inlet and outlet, which were connected to the 50 ml tube, allowing the flow of the iron fluid in a closed loop. This was to assess the magnet's trapping ability in a more complex model. The Halbach array was placed on top of the model until all the SPIONs were trapped and this helped to investigate how long the magnet should be kept in place before removing it.
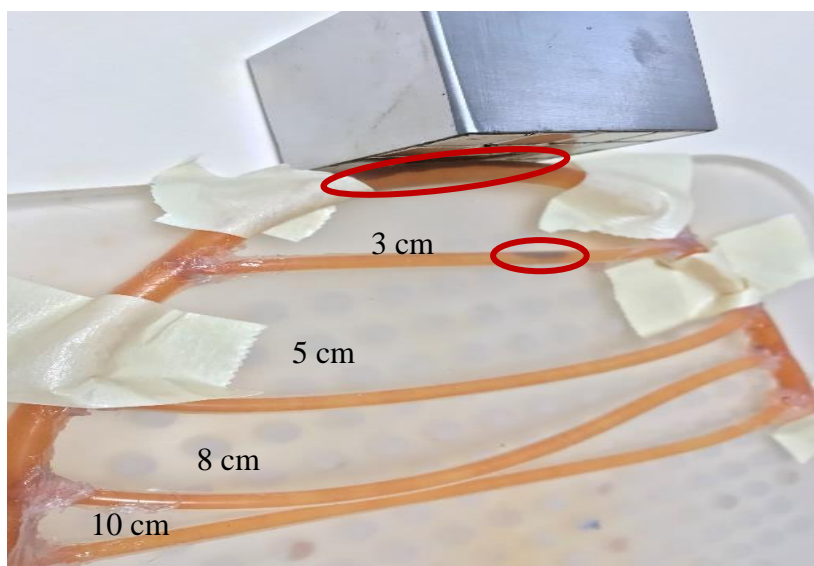
Figure 5.14: A three-layer Halbach array was used to trap SPIONs at a concentration of 5 mg/ml in a complex vasculature model. This consisted of four channels attached to the main vessel supply at different distances i.e. 3, 5, 8, 10 cm away from the magnet. The fluid flow was run in a closed loop through a flow system using a peristaltic pump at a rate of 150 ml/min. The magnet was placed in the centre of the main tube. The fluid was flowed until most of the SPIONs were trapped and the fluid was clear.

The second objective of this experiment was to investigate the time that was required to trap all the iron particles in the initial 5 mg/ml solution in a 50 ml tube, as well as the length of time that the iron particles would remain in place after removing the magnet. This experiment was conducted at two different flow speeds; 150 ml/min and 300 ml/min. The results are discussed below.

The trapped iron particles were observed in the main vessels as well as in the first main branched tube- 3 cm away (**Figure 5.15**). At distances from 5 cm and upwards, however, it was hard to visualise the trapping of the iron particles.

MNP trapping over time can be seen in **Figure 5.15**, where MNPs accumulated over time. It is evident that MNPs were trapped more effectively in the tube close to the magnet than in the tube that was 3 cm away from the magnet.

10 sec   40 sec   80 sec   180 sec
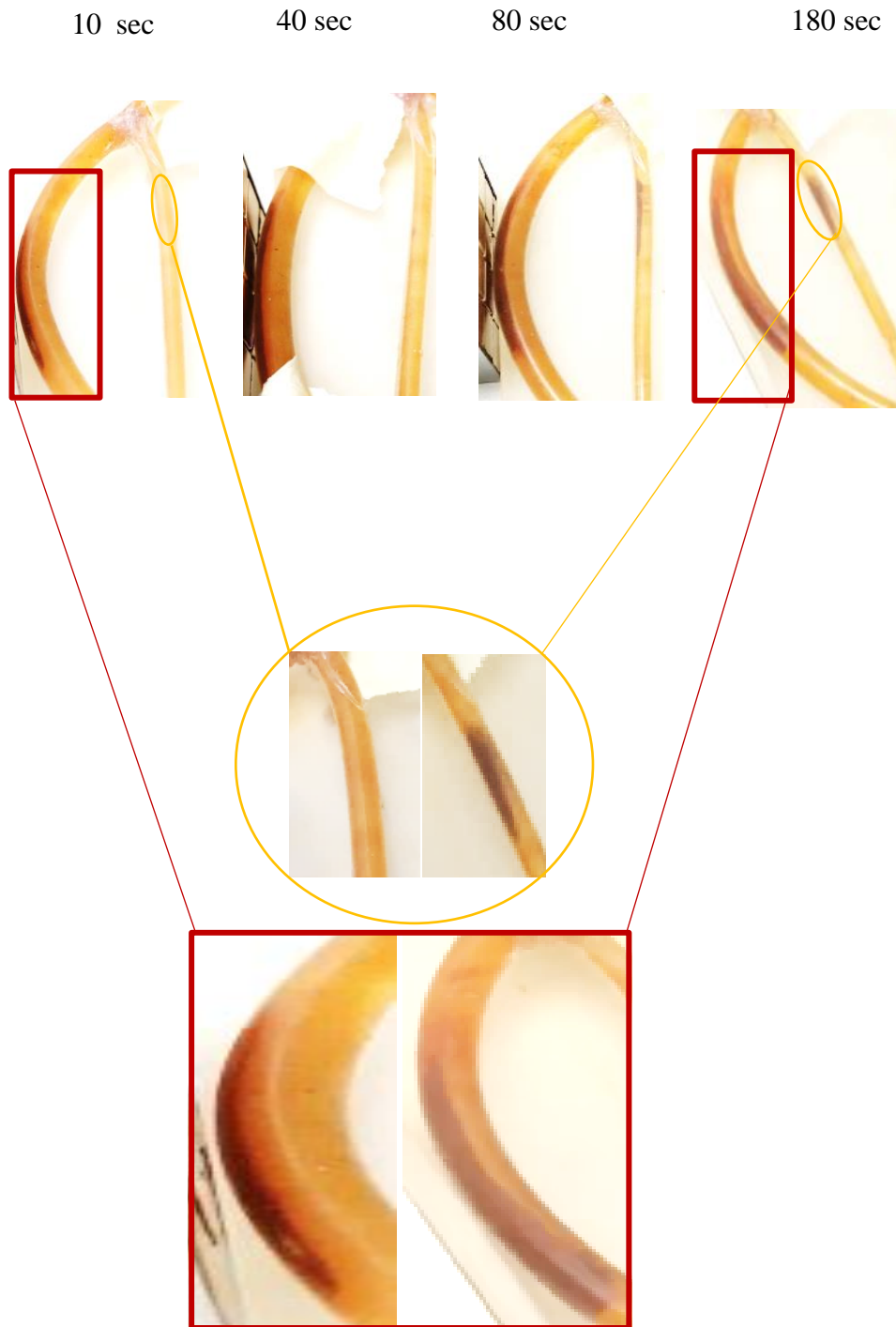
Figure 5.15: Trapped SPIONs in the complex vasculature model at two different distances with different flow rates. Photographs showing 0 cm and 3 cm away from the magnet - black and red circles respectively, at two different flow speeds; (a) 300 ml/min and (b) 150 ml/min. A three-layer Halbach array magnet was used to trap SPIONs applied at a concentration of 5 mg/ml in a complex vasculature model. The fluid flow was run in a closed loop through a flow system using a peristaltic pump at the two flow rates above. The magnet was placed in the centre of the main tube. The fluid was flown until most of the SPIONs were trapped and the fluid was clear. The results showed that the lower the flow rate the more effective the trapping of the SPIONs.

It can be seen from the above Figure that the volume of MNPs was increased over time. It was difficult to quantify the volume of trapped MNPs inside the tube, however, the pixel signal of MNPs (intensity) was considered. To do this, a video of the trapping experiment was taken with clips captured at different times. Each clip was then imported to ImageJ software for iron particle analysis (see Appendix IX). The mean intensity of the iron particles was calculated at different times for each tube as illustrated in Figure 5.16 below.

a

b
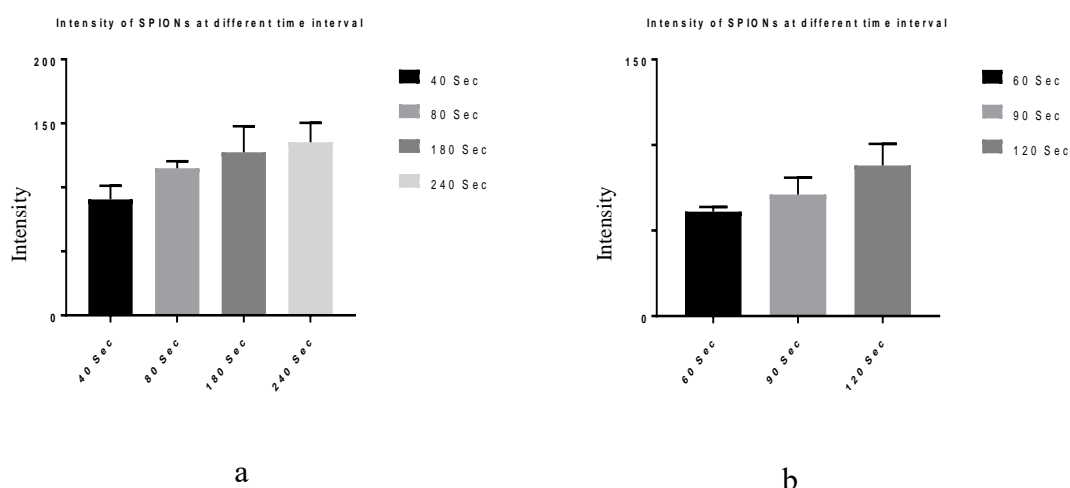
Figure 5.16: Intensity of trapped SPIONs of 150ml/min flow rate at different time interval for (a) the tube close to the magnet (0 cm), (b) 3 cm way from the magnet

Since the flow rate in human capillaries is very high, it would be interesting to see whether or not the magnet was able to trap the iron at higher flow rates. The maximum flow rate that our vasculature model could tolerate was 300 ml/min, anything more than this resulted in the branch tubes being damaged. The experiment was therefore run again at

300 ml/min and the magnet placed on top of the tube model until all the magnetic particles were fully trapped. The mean of intensity signals (volume) of the iron particles was calculated at different times for each tube as illustrated in Figure 5.17.

<div align="center">a   b</div>
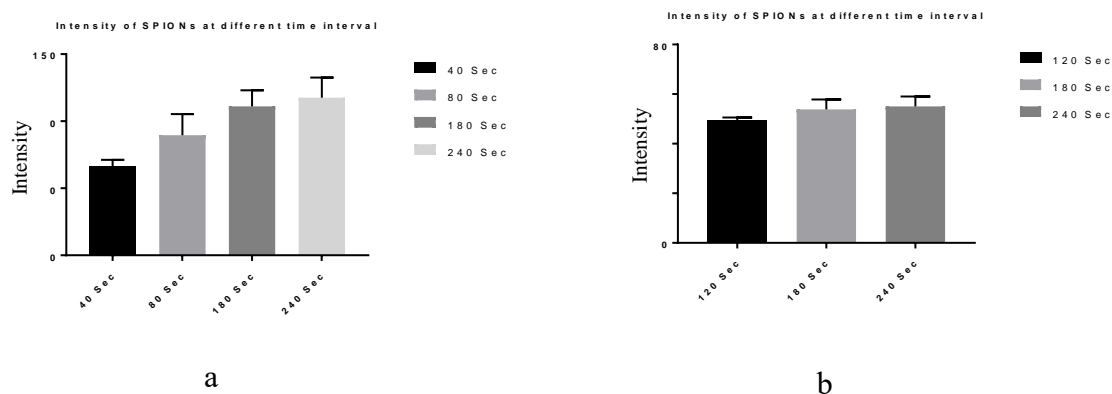
Figure 5.17: Intensity (volume) of trapped SPIONs at 300ml/min flow rate at different time interval for (a) the tube close to the magnet (0 cm), (b) 3 cm way from the magnet.

5.6 Discussion & Conclusion

This chapter has focused on assessing the ability of the Halbach array to trap iron particles in two different phantom models as well as two different vasculature models.

It was mentioned earlier that a strong magnetic field strength plays a major role in effective MDT. Besides that, both the hydrodynamic and physiological parameters play a major role in determining the success of MDT when SPIONs (ferrofluids) are administered intravenously or intra-arterially. Hydrodynamic parameters include blood flow rate, viscosity of the fluid, ferrofluid concentration, infusion route and circulation time. Physiological parameters include tissue depth to the target site (i.e. distance from the magnetic field source), reversibility and strength of the drug/carrier binding, and tumour volume [195].

The hydrodynamics of drug targeting in MDT has been studied and preliminary investigations have suggested that for most magnetite-based carriers, including SPIONs, flux densities at the target site must be of the order of 0.2 T with field gradients of approximately 8 Tm^{-1} for femoral arteries and greater than 100 Tm^{-1} for carotid arteries [185]. This suggests that targeting is likely to be most effective in regions of slower blood flow, particularly if the target site is closer to the magnet source.

To understand the trapping procedure, forces that are applied on SPIONs in order to trap them in a fluid flow model are as follows (Figure 5.18):
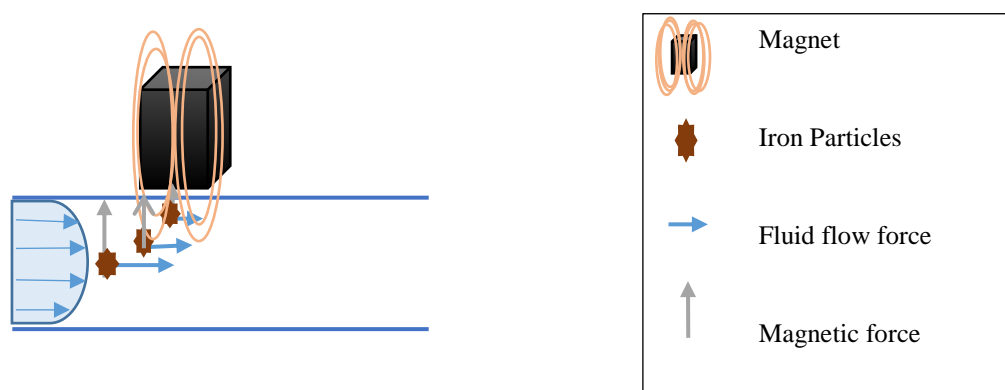
Figure 5.18: A hypothetical magnetic drug delivery system in a simple fluid flow model. The Halbach array is placed outside the tube so that its magnetic field gradient might capture SPIONs flowing in the circulatory system.

Several forces need to be considered in MDT, i.e. magnetic force, fluid (drag) force as well as gravity force. Once the SPIONs reach the magnetic field area, they start to accumulate and form an aggregate. In this case, the magnetic forces that affect the SPIONs are stronger than the force of the flow, and therefore the SPIONs stop moving and stick to the side near the magnet until the size of the aggregate increases so that the flow force again exceeds the magnetic force and they are released. Hence, to achieve a successful magnetic trap in a flow model the magnetic force must exceed all the other forces.

In this project, MRI scans confirmed the ability of a specially designed Halbach array to trap iron particles at different concentrations i.e. 1 mg/ml, 5 mg/ml and 10 mg/ml. It was observed that the main challenge with the 3D printed tumour model was that the plastic material itself had short lived signals (T2) [196] which led to the creation of dark areas in the control tumour even where no iron was present (**Figure 5.3**). Calculation of T2* showed that the tumours that had more iron particles in them, had shorter T2* (**Figure 5.4**) as expected.

ICP data showed that the trapping of iron particles in the presence of the Halbach array increased as the initial concentration of particles was increased. This phenomenon was observed at different distances; that is, the trapping of particles increased with increasing concentration at 0, 5 and 10 cm away from the magnet. The quantity of trapped particles decreased with increasing distance from the magnet, as shown in. The same result was observed when the iron particles were incubated with WBCs. When a cell is loaded with MNPs and an aggregation of magnetic particles forms, the particles will typically act as a single magnetic particle which led them to be trapped under the effect of the magnetic field [197]. Overall, these results suggest that MDT is a promising technique for brain tumour therapy.

In order to improve the visualisation of iron particles, an alternative to the 3D printed tumour model was developed. This was named the bio-tumour phantom and was fabricated to mimic the T2* of brain tissue and hence obtain clearer MRI images. Another more complex model, the vasculature model was also developed. All these were developed in search of a model that would mimic brain tumours *in vitro*.

Both models were developed to illustrate how the flow is divided into multiple paths instead of a simple tube with one path. The MR images showed the ability of the

Halbach array magnet to trap iron particles at a depth of 5 cm. Here, it was observed that a small aggregation was formed in the more distant tube, i.e. 3 cm compared with the tube closer to the magnet at 0 cm. The drag force in the far tube was stronger than the magnetic force due to the increased distance, meaning a weaker trapping force. Since the flow force is proportional to the total volume of particles (aggregation), smaller aggregated particles will experience greater drag due to flow than larger particles [197] . The following simplified diagram in **Figure 5.19** shows how the trapping procedure was performed in the more complex vasculature model.
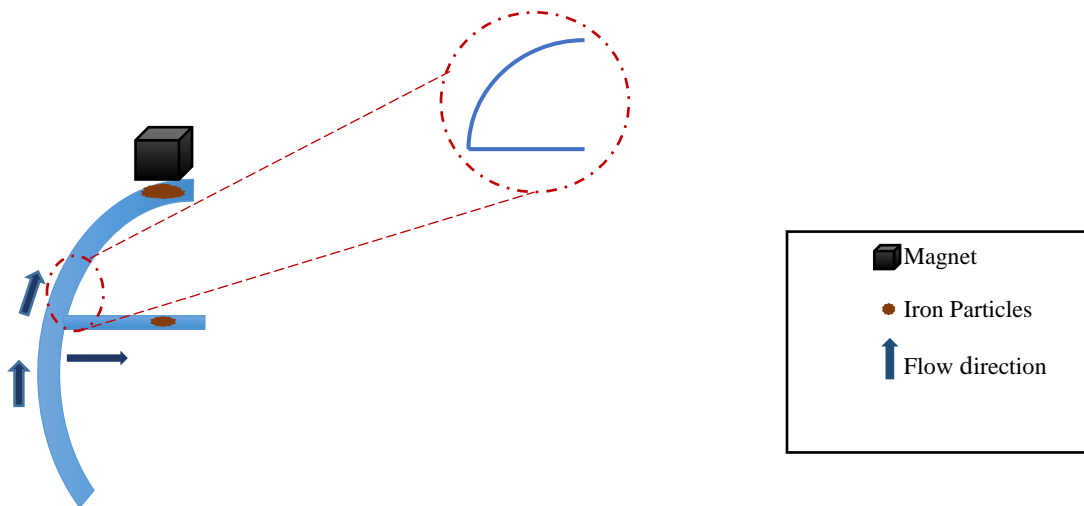
Figure 5.19: The trapping of SPIONs in the complex vasculature model. Fluid with SPIONs divided into two ways crossing the Y channel. More SPIONs were trapped in the tube that was closer to the magnet

The flow rates that were used in the models included 10, 150 and 300 ml/min, and this is lower than the average human brain flow rate of about 800 ml/min [198]. It was difficult to use flow rates above 300ml/min because this resulted in the bursting of the tumour and vasculature models.

Trapping iron particles at further depth, i.e. 10 cm, was also investigated. It was not possible to confirm the data via MRI because the vasculature model was too large to fit in the available scanners.

The experimental results indicate that flow rate influenced the trapping of the iron particles. For instance, the higher the flow rate, the less the amount of iron particles trapped in the tubes and this agrees with results from other studies. For instance, in a dynamic flow experiment, Riegler et al. constructed an *in vitro* model to assess the feasibility of magnetic cell targeting approaches using SPIONs that travelled in a vascular bifurcation (a small artery flow, Y-shaped) phantom at different flow rates; 1, 2, 4 and 6 cm/s [199]. The diameter of the bifurcation tube was 0.8 mm, with a bifurcation angle of 30°. In their study they used MRI with a field gradient of 0.5 T/m to guide the magnetically labelled-cells to the desired location. The phantom was connected to an infusion pump and placed into the centre of the MRI system. They showed that at all the different flow rates, 75% of all magnetised cells were directed to the target but that the rate of trapping decreased as flow rates increased: 49%, 31%, 13%, 0.5% for 1, 2, 4 and 6 cm/s respectively.

It was interesting to see that MNPs accumulated over time when the magnet was applied. It was clear that the volume of accumulated trapped MNPs increased over time. Also, it was shown that the closer MNPs were to the magnet, the more trapping occurred, as expected. The volume of trapped MNPs depends on the exposure time to the magnet. It was observed from the video clips that the time that was needed for MNPs to be trapped completely was about 3 min and 4 min for the tubes that were 0 cm and 3 cm away from the magnet, respectively.

In MDT, it would be interesting to know for how long MNPs and hence the drug would remain in place when the magnet was removed. In this project, it was noticed that when the magnet was removed (after completing the experiment of Figure 5.14), the volume of accumulated trapped MNPs initially flushed away quickly. MNPs in the tube that were 3 cm away from the magnet were released in less than 1 min. while it took

around 10 min for the MNPs close to the magnet (0 cm) to be released. The SPIONs lasted longer in the tube that was closer to the magnet because of the large size of aggregated SPIONs which created stronger magnetised force between the particles capable of resisting the fluid flow force [194].

In general, in order to apply the Halbach array magnet for MDT for brain tumours, several issues should be considered and this include, amongst others, the depth of the tumour, the vasculature network as well as the blood component, i.e. the white blood cells (WBCs) that will carry the SPIONs to the brain. A consideration of the aforementioned issues in this project was essential in order to get a realistic model that closely mimics brain tumour conditions found in humans.

Flow cytometry analysis in this study showed that although a range of SPION concentrations were taken up in WBCs, up to 20 mg/ml, the SPIONs' toxicity was low. In a separate study, it has also been proved that SPION MNPs at concentrations of ≤100 μg/mL are non-toxic to cultures of murine macrophage cells (J774) [200]. Although higher concentrations were being used in this study, SPIONs did not exhibit any toxic effect on WBCs [201] [202].

Overall, the *in vitro* experiments showed that Halbach arrays could trap SPIONs with/without WBCs inside the tumour at distances up to 10 cm. This suggests that the Halbach arrays have the potential to trap therapeutic drugs labelled with iron particles at distances up to 10 cm and we believe this would be useful for targeting of anti-cancer therapies to brain tumours.

Given that the iron particles will be applied inside the patient's body, testing the iron toxicity to human cells is clearly imperative. The testing of iron toxicity in human brain cells constitutes the main focus of the next chapter.

Limitations;

This study was carried out with an *in vitro* 3D flow phantom model, which does not have the complex vasculature and BBB found in humans. This model therefore needs to be replaced with an animal model, such as pig, in order to mimic the brain vasculature networks, the brain flow rate, and the distance between the target site (brain tumour) and the magnet.

In addition, the aggregation caused by accumulating SPIONs, due to the attraction force in the tube was not investigated in this study. This may lead to embolization of the blood vessels in the target area [195]. Further investigations are required to overcome this issue and this could include the coating of SPIONs with appropriate materials to prevent aggregation.

Uncoated SPIONs were used in this study, however, despite being non-toxic at high concentrations if these SPIONs are to be used in biomedical therapy suitable coating materials should be considered. Coating helps to reduce toxicity and the half-life of the particles in circulation and also plays an important role in the conjugation of the SPIONs with therapeutic drugs [116].

The other limitation of this study is that no anticancer drugs were used since the model that was used is just a 3D printed flow phantom. This will need to be the focus of further studies in an animal model.

Chapter 6

Uptake of SPIONs and their viability in brain cells

6.1   Introduction

In MDT to brain tumours, SPIONs are loaded with anticancer drugs and are injected intravenously into the body. An external Halbach array is placed on the patient's head in order to steer and trap all the magnetised drugs to the brain tumour. Injecting SPIONs into a biological system results in their interaction with cellular structures, for instance, cells within the blood stream, endothelial cells lining the blood vessels, and/or epithelial cells in underlying tissues [203]. In chapter 5, it was found that at even high concentrations of SPION, human WBCs were not susceptible to cell death following incubation with high concentrations of SPIONs. It is, therefore, significantly important to investigate the level of toxicity on the cellular structures in biological systems.

Although SPIONs have been used for several biomedical applications, including as a contrast agent for MRI, and are generally considered to be safe, it is also acknowledged that SPIONs can be harmful to cells and tissues in some circumstances [204]. The toxic effect on cells as a result of contact with SPIONs depends on several parameters such as the type of cell and their sensitivity to the iron, the size of the SPIONs, their concentration and incubation time. In addition, other factors such as the type of coating, the nature of the cell-medium (its chemical composition), the charge of the iron (oxidation state) and the way in which the SPION interacts with protein all contribute to SPION toxicity in cells [205]–[207] [208]–[210]. Singh et al., have reported that exposure to SPIONs for a period of time is linked to substantial harmful effects such as inflamed neural cells; mitochondrial dysfunction, the development of apoptotic bodies and a noticeable increase in chromosomal damage, such as the leakage of lactate dehydrogenase through the cell membrane, the condensation of chromosomes and an increase in the number of micronuclei as well as the condensation of chromosomes [211].

A number of studies have been conducted to investigate the toxicity of different types of SPIONs with different coating materials, with the results showing that, in general, the toxicity level is either low or negligible, that is, no toxicity at all in the cells with low SPIONs concentration (<100 µg/ml). The cells investigated include fibroblasts in vitro [206], human dermal fibroblasts in culture [207] and mouse fibroblast cells [208]. It was observed, however, that the level of toxicity increased as the concentration of SPIONs increased (>100 µg/ml) [211].

Conjugating cells with SPIONs make the cells sensitive to an external magnetic field. In an *in vitro* study conducted by Sruthi et al. it was found that more than 85% of magnetised oligodendricyte cell line 158N (with PEG coated SPIONs) were retained when an external magnet was applied and this was verified using Prussian blue staining. The incubation time in their study was 24h at a concentration of 50 µg/ml [203].

Matuszak et al. investigated the toxicity of SPIONs at concentrations between 0 and 60 mg/mL in human umbilical vein endothelial cells (HUVECs), so as to evaluate the effect of SPIONs on the vasculature. Flow cytometry data confirmed that the proportion of necrotic cells was not significantly different between untreated control and SPION-treated samples. In addition, the effect of SPIONs on endothelial growth in a fluid flow model was evaluated using an arterial bifurcation *in vitro* model-Y shaped micro slide. SPIONs were circulated in the model, where 7×10^5 endothelial cells were seeded on to the microslides, at a 9.6 mL/min flow rate for 18 hours. An external 37 mT magnet was placed on the outer wall of the model. The uptake of SPIONs and their effect on endothelial cells were assessed using two methods: real-time cell analysis and live-cell microscopy. The cell index measurement showed that there were no significant differences between the control and SPION treated sample. The live-cell microscopy data indicated that there was also no significant effect on cell morphology in treated cells compared with untreated cells. It was

concluded that SPIONs are safe technique to be used as a drug carrier i.e. for chemotherapy for MDT.

In another study, an *in vitro* BBB Model in Transwell Membrane Plates was used to investigate the ability of fluorescence starch-coated iron oxide nanoparticles (IONPs), with an average diameter of 117.4 nm and with a range of concentrations (35, 70, and 140 µg/ mL) to cross the model and enter into a monolayer of cultured brain capillary endothelial cells (BCECs). An external magnet was applied to investigate the ability of the magnetic force to trap IONPs to the bottom of the plate where the astrocyte cells were located. The IONPs were incubated with BCECs for 24 hours with no magnet present, and for 5 hours with the magnet present. Cell viability was evaluated using a live−dead viability assay, which showed that there were no signs of reduced cell viability either with or without the magnet. In addition, fluorescence microscopy showed that the SPIONs were distributed within the cell boundaries of the BCEC monolayer as well as trapped in astrocytes as a consequence of the magnetic force [212].

Coccini et al., meanwhile, assessed the toxic effect of uncoated-IONP-Fe_2O_4 in cerebral cell lines, including neurovascular cells of the brain, namely astrocytes (D384) and neuronal (SH-SY5Y) cells [213]. The IONPs were ~20 nm diameter and various concentrations, between 1–100 µg/ml, were added to the cells. The incubation time was two days and the toxicity was evaluated by MTT assay. It was found that in the first 4 hours, starting from a concentration of 25 µg/ml, cell viability decreased by between 25 and 30%. It was also observed that cytotoxicity increased significantly with increasing incubation time. The following results were observed:

- After 24 h, the rate of cell death was between 35–55% and the effect was noticed at concentrations of 10 µg/ml.

- After 48 h, 25–75% of significant cell death had taken place and this was evident from concentrations as low as 1 μg/ml.

The results indicated that SH-SY5Y cells were less prone to Fe3O4 toxicity than D384 cells. It was noticed that the function of the mitochondrial cells was affected after only 48 h and there was significant death of the cells of between 35–45%, starting from 10 to 100 μg/ml [213]. In conclusion, IONPs had a more harmful effect in D384 than in SH-SY5Y [213]. This was important since the authors wanted to investigate the relationship between accumulated IONPs in central nervous system (CNS) cells that may lead to neurodegenerative disorders.

A recent study was conducted to assess that the biocompatibility of BSA-coated SPIONs with a range of hydrodynamic diameter sizes, including 85 ± 10 nm (BSA-IONP-80), 36 ± 6 nm (BSA-IONP-40) and 38 ± 6 nm (BSA-IONP-PEG) on brain tumour (U251) glioblastoma cells [214]. Of all the different materials, it was found that MNPs coated with albumin gave the desirable results, that is, a stable and biocompatible shell that prevents cytotoxicity caused by the magnetite core. It was also observed that after a long exposure time (48h), due to free radical production, the iron oxide nanoparticles become more cytotoxic, although this was considered to be at a low level.

For magnetic drug targeting to the brain, the accumulation of SPIONs in and around the BBB may result in toxicity. This needs to be considered since changes in brain iron concentrations are strongly correlated with human neurodegenerative diseases [212]. Given that SPIONs are able to enter the brain cells, potential negative effects arising from the exposure of brain cells to SPIONs have to be taken into consideration [215]. In this

chapter we have used compared concentrations of SPIONs at 0.1 mg/ml and 1 mg/ml on cell toxicity. The cells investigated were originated from the brain.

6.2   Aims and objectives

Hypothesis

Guiding magnetised drugs to brain tumours with the help of an external magnetic field requires the use of MNPs. The size, coating and concentration of these iron particles needs to be taken into consideration in a therapeutic setting. We hypothesise that our SPIONs of <50 nm in diameter are taken up by cells of the brain and result in minimal cell toxicity.

Aims

The aim was to evaluate the uptake of SPIONs and the viability of brain cells and brain tumour cells. The permeability of the BBB is controlled by brain microvasculature endothelial cells (BMVEC) which are supported by the neurovascular unit (NVU), i.e. the microglia, astrocytes, pericytes and neurons that together form the so-called neurodegenerative unit [216]. Therefore, human brain endothelial cells (hBMEC-D3), as well as one of the NVU, i.e. human astrocyte cells (HA), were chosen in order to assess their uptake and viability as they are the main components of the BBB. In addition, a human glioblastoma cell line (U138) was investigated given that glioblastoma is the most common brain tumour in adults [217].

Specific objectives

1. To use transmission electron microscopy (TEM) to assess the SPION size and evaluate the intracellular uptake of SPIONs in the cells.

2. To assess cell viability following incubation of the different cell types with SPIONs for 24h. Flow cytometry was used to measure cell death using Propidium iodide (PI).

6.3   Uncoated SPIONs are not uniform in size or shape

The SPIONs used in this study were prepared for imaging with TEM as described in chapter 2 section 5.1.2. A concentration of 0.1 mg/ml was diluted in PBS and a final volume of 300 µL was prepared for TEM imaging.

As shown in **Figure 6.1a** the SPIONs were surprisingly very different in both size and shape (octagonal and heptagonal) these appeared to aggregate in large clumps, which is typical due to the attraction forces between SPIONs. The average diameter of the SPIONs was measured using ImageJ software from the TEM images. Although the commercial SPIONs were labelled as having a specific diameter of less than 50 nm, our measurement showed that a 60 nm particle was identified (**Figure 6.1 b)** The average size of 23 particles was calculated to be 30 nm, however. This could have significant impact on drug delivery and access to the BBB.

(a)

(b)
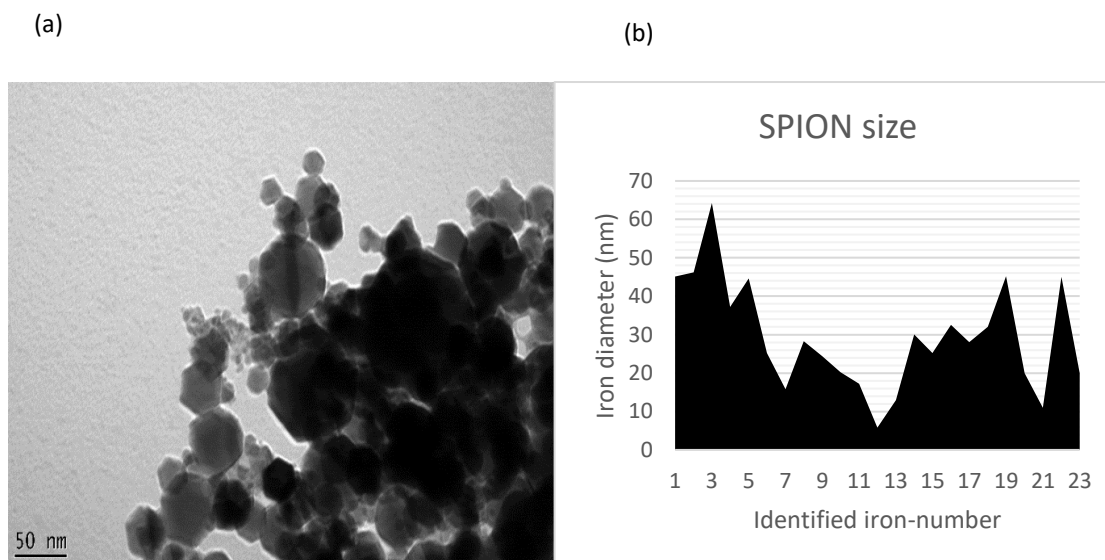
Figure 6.1: SPION identified using TEM are not uniform in size or shape. (a) TEM images of SPIONs at a concentration of 0.1 mg/ml. The size and shape of the particles varied. Images were taken with FEI Tecnai Biotwin operated at 120kV with an Orius 1000 camera using 100-200nm magnification scales. (b) Calculated average SPION size was measured using ImageJ software. The sizes were measured from TEM images, different sizes were found, up to 60 nm in diameter.

6.4 Cell uptake and viability following incubation with SPIONs

All the cells were incubated with SPIONs at a different range of concentrations for 24 hours. Endothelial cells, astrocyte cells and brain tumour cells were seeded at a density of 300,000 cells/well in 2 ml of medium, and 24 h later incubated with 0.1 and 1 mg/ml of iron.

Flow cytometry was used to assess cell viability. In flow cytometry, cells can be morphologically described by two main axis; forward scatter (FSC) and side scatter (SSC). The forward scatter represents the cell size and the side scatter represents the quality and condition of the cells. A 2 µl of a 50 mg/ml stock of the viability dye propidium iodide (PI) was added to each sample immediately before analysing on a flow cytometer (BD FACS

Calibur). PI is a membrane impermeant dye that is generally excluded from viable cells. It binds to double stranded DNA by intercalating between base pairs of dead cells [160]. Transmission electron microscopy (TEM) was used to investigate the intracellular localization of SPIONs in the cells.

The viability of endothelial, astrocytes and glioblastoma cells with and without SPIONs is illustrated in **Figure 6.2**, **6.3** and **6.4** respectively. In each case, the gated area-black dots in (R1) in part (a) of each figure presents the population of live cells while the gated area- red dots (R2) in part (b) represents the dead cells of control (no SPIONs), cells with 0.1mg/ml and 1mg/ml of SPIONS respectively.

The cell viability was visualised by calculating the percentage of live cells that remained after exposing SPIONs to the cells. The reason for calculating the live cells instead of dead cells is that there were many dead cells that were not PI positive (most likely typical cellular debris), as a result, plotting the percentage of live cells was considered more accurate than plotting the percentage of dead cells.

In endothelial cells, it was found out that these concentrations had a significant effect, although still very low, but that it increased with increasing SPION toxicity, **Figure 6.2(c)**.
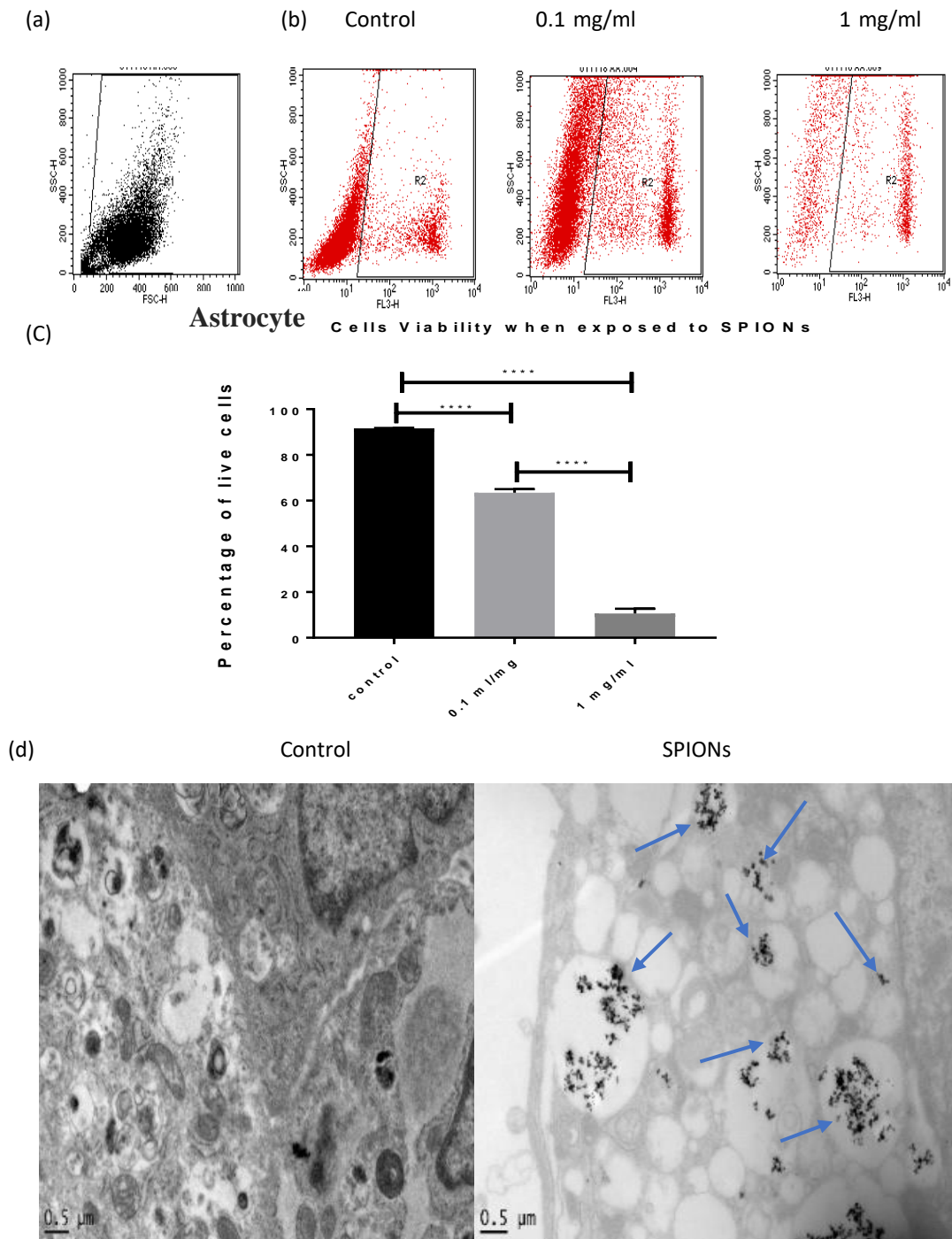
In astrocytes, cell viability results were significant, in that it was found that SPIONs at a concentration of 0.1 mg/ml had a small toxicity effect, while a 1 mg/ml concentration had a high toxicity effect, **Figure 6.3 (c)**. This means that astrocyte cells are sensitive to SPIONs.

In glioblastoma cells, it was found that the toxicity of the 0.1 mg/ml was slightly significant but the effect increased with increasing concentration, i.e. 1 mg/ml, **Figure 6.4 (c).**
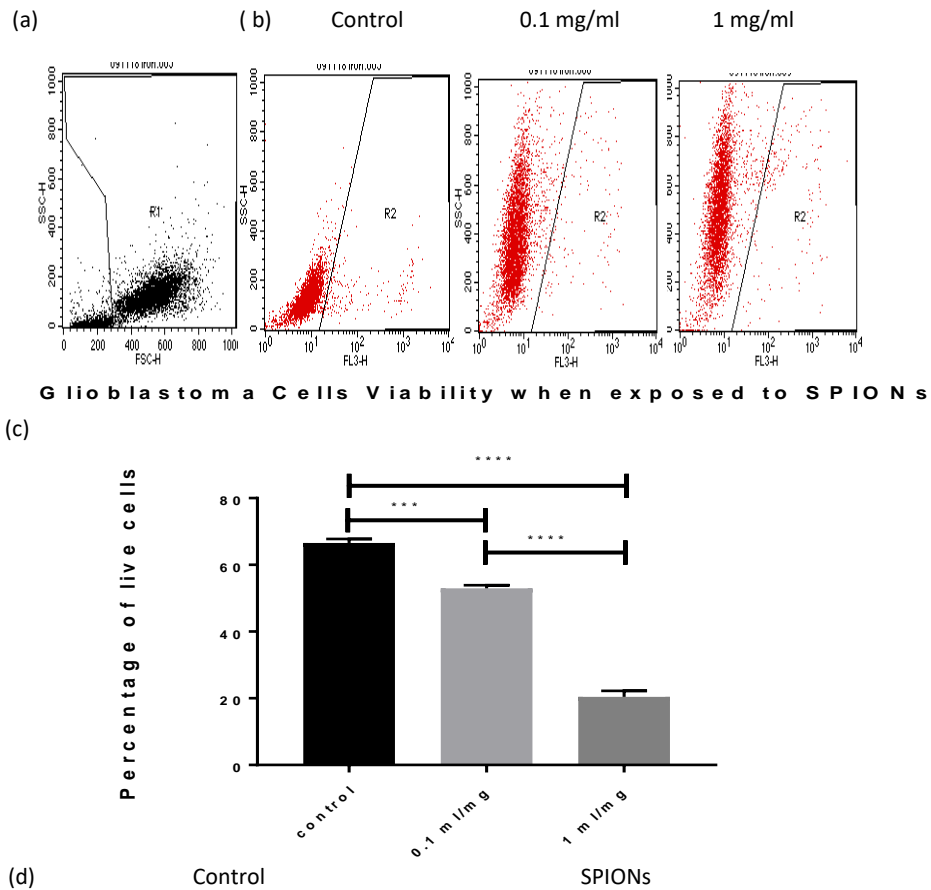
In order to visualise the SPIONs within the cells, TEM images were taken, as illustrated in **Figure 6.2 (d)**, **6.3 (d)** and **6.4 (d)**. On the left hand side are the control cells, in which no SPIONS were present, whereas SPIONs are clearly visualised accumulated in the cytoplasm area on the right hand side image (see blue arrows).

Endothelial Cells Viability when exposed to SPIONs

(c)

(d)
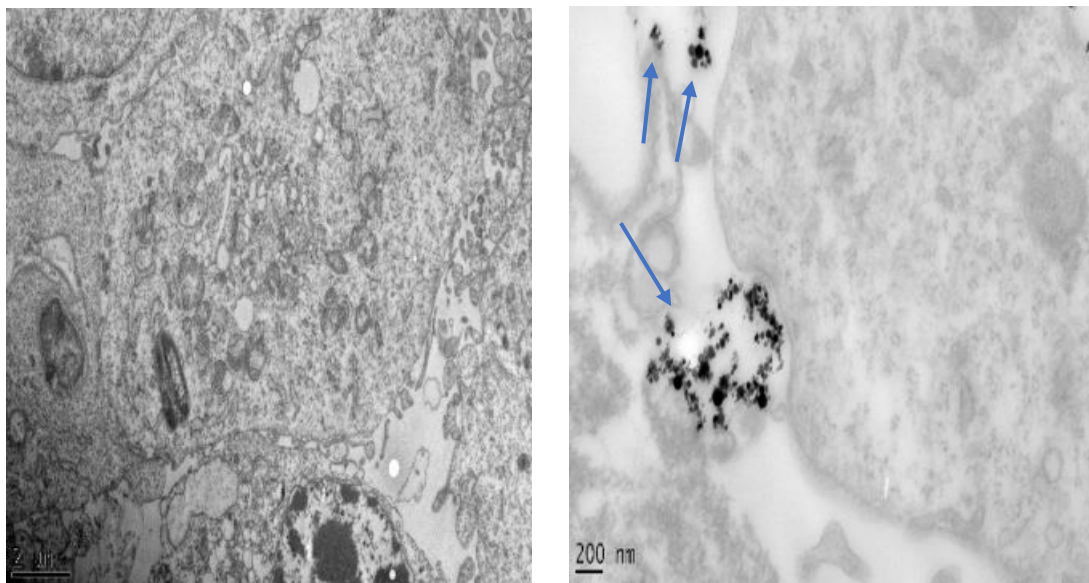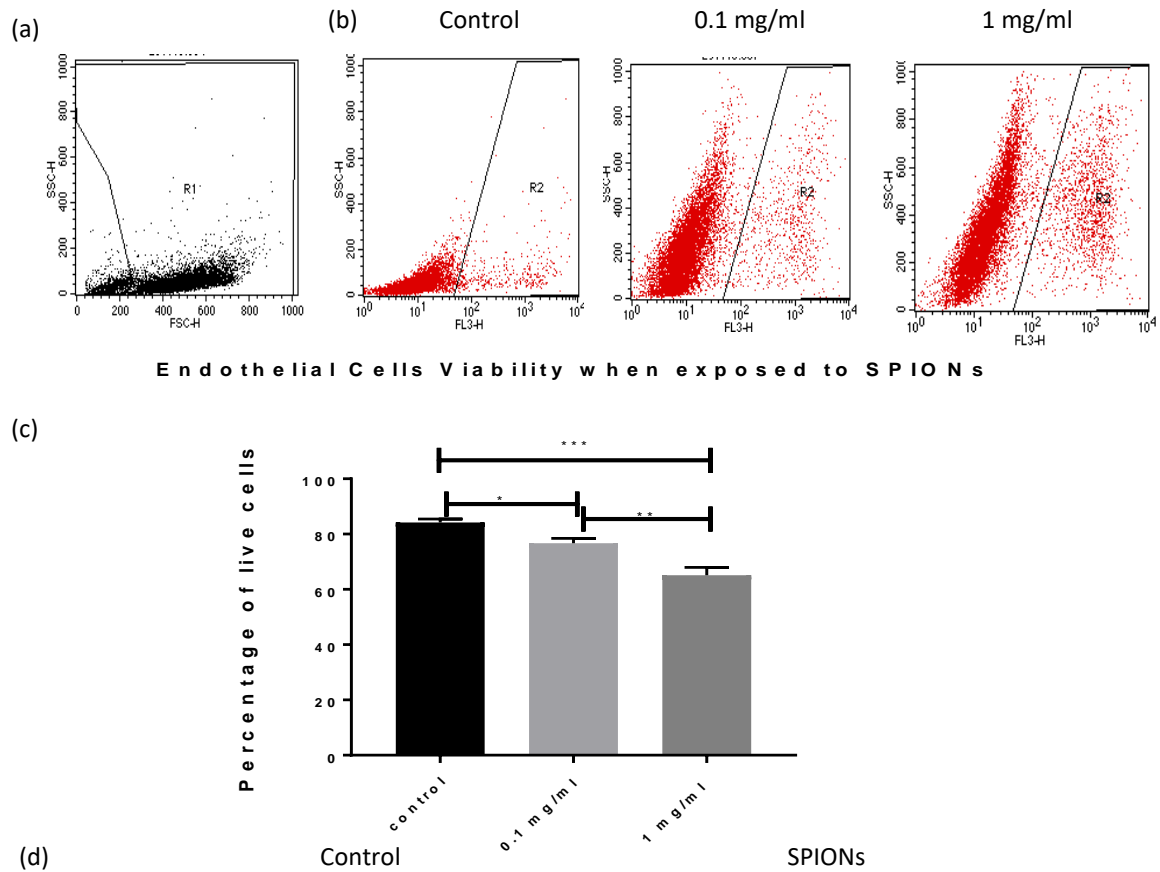
Figure 6.2: Endothelial cells take up SPIONs and undergo cell death: (a) Representative flow cytometry dot plot of endothelial cells in SSC-FSC analysis (R1), based on their scatter profile. (b) All the cell debris was gated out and a further gate applied to the cells (R2) to detect the dead cells with PI staining in the FL3. (c) The percentage of live cells presented and a multiple comparisons test was performed and slight toxicity effects were found with the 0.1 mg group compared with the control, while a more significant effect was found with the 1 mg group compared with control. Data are the mean and SD of N=3 experiments. All data was analysed using one- way ANOVA-PRISM.*p <0.01,**p =0.001 and ***p <0.001. (d) TEM images of endothelial cells; control-LHS and 0.1 mg/l SPIONs within the cells-RHS (blue arrows).

(a)

(b) Control   0.1 mg/ml   1 mg/ml

Astrocyte   **Cells Viability when exposed to SPIONs**

(C)

(d)   Control   SPIONs

Figure 6.3: Astrocyte cells take up SPIONs and seems to be sensitive to SPIONs: (a) Representative Flow cytometry dot plot of WBCs in SSC-FSC analysis (R1) which shows all types of WBCs, including granulocytes, monocytes and lymphocytes based on their scatter profile. (b) All the cell debris was gated out and a further gate applied to the cells (R2) to detect the dead cells with PI staining in the FL3-H channel. Top- control sample, middle- cells with 0.1 mg/ml SPIONs and bottom- cells with 1 mg/ml SPIONs. (c) WBCs death percentage, where the cells were exposed to different SPION concentrations and incubated for 24h. A multiple comparisons test was performed and significant toxicity effects were found. Data are the mean and SD of N=3 experiments. All data was analysed using one way ANOVA-PRISM.****p <0.0001. (d) TEM images of endothelial cells; control-LHS and 0.1 mg/l SPIONs within the cells-RHS (blue arrows).

Figure elements (a), (b) Control, 0.1 mg/ml, 1 mg/ml

G l i o b l a s t o m a   C e l l s   V i a b i l i t y   w h e n   e x p o s e d   t o   S P I O N s

(c)

(d)   Control   SPIONs

Figure 6.4: Glioblastoma cells take up SPIONs and do undergo cell death at high SPIONs concentrations

(a) FACs- flow cytometry of brain tumour cells in SSC-FSC analysis (R1) -control- shows both live and dead cells. SSC-FL3 (R2) plot shows the dead cells with PI staining. (b) cells with 0.1 mg/ml, 1 mg/ml SPION, respectivly. (c) Cell viability when exposed to different SPIONs concentrations and incubated for 24h. A multiple comparisons test was performed and no toxicity effects were found. Data are the mean and SD of N=3 experiments. All data was analysed using one way ANOVA-PRISM.***p =0.0007, ****p <0.0001. No toxicity effects were found with 0.1 mg/ml, however, low toxicity were found with 1 mg/ml SPIONs for 24h. (d) TEM images of brain tumour cells; control-LHS and 0.1 mg/ml SPIONs within the cells-RHS (blue arrows).

6.5   Discussion & Conclusion

In this experiment, SPION uptake and cell toxicity were investigated using some BBB cells including endothelial cells (hBMEC-D3) and astrocyte cells. Brain tumour, i.e. human glioblastoma cells (U138) were also used.

Shape and size are crucial parameters of SPIONs that should be considered for MDT. An ultra-small SPION i.e. < 9 nm diameter is rapidly cleared from the circulation [218]. It also would be difficult for them to be trapped by external magnetic field due to the large flow force, which would exceed the magnetic force. Larger SPIONs of 50 – 100 nm diameter have been found to be better than ultra-small SPIONs but they carry the risk of thrombosis due to their attachment to the blood vascular system. Although the ultra-small SPION are difficult to trap due to their small size, it has been suggested that they are ideal for use in MDT as they help to prevent the formation of large aggregates. In addition, particles whose surfaces are mainly hydrophobic are coated with plasma components and, therefore, can be removed rapidly from the circulation. In contrast, particles whose surfaces are mainly hydrophilic are resistant to this coating process, hence they can be cleared from the circulation more slowly [218].

In this chapter, it has been shown that 0.1 mg/ml of SPIONs has less effect on cell toxicity on endothelial and glioblastoma cells, however, the results showed that astrocyte cells were more sensitive to SPIONs even at their low concentration of iron. These results are consistent with observations made in previous studies. For instance, it has been shown that SPION concentrations which are used as MRI contrast agent applications have no toxic effect on endothelial cells *in vitro* and *in vivo* [219] [220]. Here, it was also demonstrated that at 1 mg/ml there is toxicity in all the cell lines investigated but this was more pronounced in astrocytes, where hardly any cells survived. As a result, it was

concluded that astrocyte cells are more sensitive to SPIONs than endothelial cells. Glioblastoma cells seemed to be more resistant to SPIONs and this might be explained by the overexpression of antioxidant enzymes, for example, superoxide dismutase, catalase, glutathione peroxidase, and glutathione reductase. These enzymes help to decrease toxicity on cell growth by participating in ROS neutralisation [214]. It was not possible to measure these enzymes in this study due to time constraints but this is something that could be considered in future work. Also, a study into the mechanisms of cell death is warranted. Markers for apoptosis, autophagy and ferroptosis should also be investigated. The latter is a form of non-apoptotic programmed cell death characterised by iron dependent build-up of lipid hydroperoxides. An increased number of studies have linked ferroptosis and nanomedicine as reviewed in [221].

Previous research has shown that SPIONs do not cause cytotoxicity in nerve cells up to a concentration of 100 μgFe/ml. This concentration range is considered as safe with regard to cell viability [200]. Naqvi et al. cultured murine macrophages with SPIONs of mean diameter 30 nm which were coated with Tween 80. They then used the H$_2$DCFDDA assay to quantify the generation of intracellular reactive oxygen species (ROS), finding that at concentrations higher than 100 μg/mL, SPIONs result in oxidative stress in murine macrophage (J774) cells [200]. It was concluded that exposure of cells to a higher concentration of nanoparticles resulted in enhanced ROS which causes cellular damage. The same study also investigated cell viability using the MTT assay, reporting >95% viability with lower SPION concentrations (25-200 μg/mL) and up to three hours of exposure, whereas at higher concentrations (300-500 μg/mL) and prolonged (six hours) exposure viability was reduced to 55%-65%. The cytotoxicity could depend on the type of brain cells, however: indeed, no relevant toxicity was obtained for neurons and astrocytes [222], whereas a toxic effect was observed for microglial cells [223].

Since SPIONs would be used for MDT for brain tumours, it is worth investigating the interaction of SPIONs with different brain cells [203]. In an *in vitro* study, the interaction of SPIONs (8.9 nm) with murine oligodendrocytes 158N was investigated. The SPIONs of 1, 5, 10, 50 and 100 μg/mL were functionalized using the polymer, PolyEthylene Glycol (PEG) and a fluorophore (Rhodamine). After 6 hours of incubating time it was found that SPIONs were taken up by the cells via endocytosis, which was verified using flow cytometry, transmission electron microscopy and confocal microscopy. It was found that SPIONs had no toxicological responses, including morphological changes, loss of viability, oxidative stress or inflammatory response, which means that SPIONs have good biocompatibility. It was concluded that SPIONs have no side effects on 158N cells, and constitute interesting tools for biomedical applications across the brain, including cellular imaging and targeting. Our study demonstrated similar results, however, the SPIONs were uncoated and the incubation time was 24 hours. In this case, uptake of SPIONs in brain cells takes place whether the SPIONs are coated or uncoated.

In this chapter, TEM images helped to show the distribution of SPIONs in each of the cells under investigation. SPION uptake depends on the properties and function of the cells. For example, it seems that the SPIONs were taken up by cytoplasm, i.e. by the lysosome of the cells, this is consistent with previous studies that demonstrated the uptake and metabolism of iron oxides nanoparticles in brain cells [217].

A 24 h time point was used in this study; it would be interesting to carry out further investigations to see whether SPIONs would be transported to other parts of the cells over a longer incubation time, i.e. 48 h and more. Co-localisation of the SPIONs with other markers of the cell using fluorescent microscopy would also be interesting. Using markers for endosomes or lysosomes in combination with fluorescent labelled iron particles would provide information on the position of the SPIONs in the cells over time.

In general, SPIONs at the specific concentrations that were investigated in this study were toxic to the cell but at the low concentration this was minimal. Future studies could also include much lower concentrations of SPIONs. These findings indicate that using SPIONs for magnetic targeting applications could be a promising and safe technique for the delivery of drugs to brain tumours.

It is worth noting that certain concentrations have to be used to ensure the safe delivery of drugs. For instance, 1mg/mL of SPIONs is considered safe for the *in vitro* experiment in this PhD research project. However, more *in vivo* research needs to be conducted to confirm the safe dose for human beings. From clinical research, Lubbe [95] suggested that for MDT, SPIONs in fluid should be no more than 0.5% of the estimated blood volume whereas the drugs such as epirubicin should be 1mg/mL of the body weight.

Limitations;

There were some limitations in this study due to the timeframe of this project. Quantification of SPIONs in brain cells was not conducted. The quantification of SPIONs could have been assessed using either ICP (as in the previous chapter), Prussian blue staining or SQUID [203]. Fluorescence can also be used to label the SPIONs for quantification purposes. Many different types of fluorescent labels are available and have been used in the past including green fluorescent protein that was used to label SPIONs [92].

Naked SPIONs are cleared rapidly from circulation, therefore, it would not be appropriate to use them for MDT, hence, it would be interesting to consider SPIONs coated with different materials. The toxicity assessments here were conducted on cultured cells and it would be worthwhile to investigate toxicity in an *in vivo* model of brain cancer.

Also, the toxicity of SPIONs in this experiment was conducted without using an external Halbach array magnet. It would be interesting to investigate in future studies how the SPIONs affect cell viability in the presence of an external magnetic field. Does this increase the accumulation of the iron in the cells? Could this lead to an increase in the temperature of the cells, its metabolic properties etc., this is worth investigating in the future. It would also be interesting if oxidative stress could be measured; this can be evaluated by measuring the intracellular ROS production by H_2DCF-DA assay [203]. Inflammatory response measurement would also be worth investigating, and inflammatory cytokine secretion under treatment with SPIONs, which can be carried out using an ELISA assay. Importantly, conjugating of the SPIONs with an appropriate drug to target brain tumour *in vivo* and is currently being investigated by a post-doctoral researcher in our research group. Drugs including Temozolomide and Lomoustine are currently being investigated and have been conjugated to SPIONs like those used in this study. Both these drugs are administered to patients with brain tumours.

Chapter 7

Conclusion and Recommendations

7.1   Summary and outlook

7.1.1   Summary of major findings

This study helped to demonstrate that it is possible to use FEMM software to design and model different Halbach arrays and to identify the most effective model for use in MDT of brain tumours. In chapter 3, the study findings revealed that in order to use the Halbach array for brain tumour treatment, a number of factors should be considered including the size of the magnet, the orientation of magnetisation of each magnet element and the choice of SPION for MDT. For the latter, Lua scripting modelling of different sizes of SPIONs showed that smaller sizes of SPIONs require less magnetic force to move them towards the target site. As discussed in chapter 3.6, this result resonates with observations made by others [168] where it was shown that the amount of magnetic force required to move SPIONs to the target site is directly proportional to the volume of the SPIONs. It is therefore an advantage to use small size SPIONs (nano) as they require less magnetic force to be moved to the target area. In addition, the use of small sized MNPs has the advantage of preventing aggregation and subsequent clotting inside the blood vessels [116].

The size of the magnet device and the orientation of magnetisation also play an important role in generating strong magnetic field strength. It was established that increasing the layers of magnets (size of the magnet device) resulted in increased magnetic field/gradient and magnetic force. This echoes findings from previous study, for instance, a study by Sarwar et al. revealed that the more layers of magnet resulted in a stronger magnetic field strength [61]. In general, by increasing the number of layers of the magnets, the volume of the device is increased and can be inconvenient for use with brain tumour patients, however, our model consists of small magnetic elements (1cm ×1cm × 1 cm) which make it possible to increase the number of layers without increasing the volume of the magnet device massively (4000g of

$3 \times 3 \times 3$cm). The other benefit of using small size magnetic elements was that it was easy to change the orientation of magnetisation when creating the model to facilitate the generation of stronger magnetic field.

Several simulation studies of Halbach array models have been conducted to reach higher depth, for example, 30mm [165], 50mm [116] with magnetic field strength of 1.5T and 0.8T, respectively. These models cannot be adapted for application in the treatment of brain tumours for various reasons including their weak magnetic field strength, short penetration distance and the overall volume of the magnet devices. Our Halbach array magnet of model 2 successfully achieved the highest magnetic field strength of 1.2T with a smaller overall size ($6cm^3$) and greater penetration depth of 6cm. Due to the boundary of the model, we were unable to measure penetration depth at more than 6cm, however, this was achieved *in vitro* as will be discussed in the subsequent paragraphs.

In order to focus the magnetic field strength and to enhance the guidance of the MNPs to the target site, iron-loaded epoxy resin was modelled to fill the gaps between the head surface and the magnet. This was confirmed to be effective in our FEEM Model (Figure 3.10). Use of iron-loaded epoxy resin enables the magnetic field strength to penetrate greater depth. This interesting result needs to be pursued in further studies in this area and should be considered when designing a helmet to host the magnetic device.

There were slight differences observed between the FEMM model and the assembled Halbach array magnets in terms of the magnetic field strength, field gradient and magnetic force and this confirmed observation made previously [183]. Bashyam et al., showed minor difference between the magnetic strength of the assembled and simulated magnet and this is due to assembling imperfections, for example, use of adhesive glue to stick the magnet

elements together created slight gaps that might have contributed to the reduction of the magnetic field strength.

When assembling the Halbach array magnets the major challenge was to overcome the repulsive forces caused by the magnetisation orientation of each magnet element. This was achieved by using small magnet elements of $1cm^3$ attached to each other using adhesive glue and supported by the ferritic stainless steel sheets and blocks. However, when the Halbach array magnet was optimised to have a square shape it was difficult to attach a second layer due to the strength of the repulsive forces between the magnets, hence, expert help was sought from the Magnet Expert Company, UK. In future, it is important to consider having such manufacturing abilities in house or in collaboration with industrial partners when developing our complex Halbach arrays.

As observed in the *in silico* model, an increase in the size of the magnet leads to increased strength of the magnetic field and this was also confirmed when the magnetic field strength was measured using the Gaussmeter. Although an increase in the size of the magnet can be viewed positively given that it produces stronger magnetic field that can reach further depth in the body, the downside is that the large volume of Halbach array. The device then becomes heavy and uncomfortable for use with brain tumour patients. In this case, use of a bigger magnet would require consideration regarding how to hold the magnet on top of the patient's head without discomfort. The unique feature of our Halbach array (Model 2) is the configuration of magnetisation orientation which helped to generate a strong magnetic field capable of reaching further depth ($6cm^3$) and weighing 400g. The optimised Halbach array magnet of model 2 would be beneficial in MDT in patients with deep brain tumours while Halbach array model 1 would be more appropriate for use in the treatment of superficial brain tumours due to its focused magnetic field strength at the surface of the magnet.

In vitro experimental data demonstrated the ability of the Halbach array to trap SPIONs at different distances in a 3D flow phantom model. It emerged from the experiments that there are some key factors that should be considered for the effective targeting. For example, the magnetic field strength should be strong enough to overcome the hydrodynamic parameters which include the blood flow rate, viscosity of the fluid and ferrofluid concentration. In addition, the magnetic field strength should also overcome physiological parameters such as the tissue depth to the target site and for brain tumour the resistance of the BBB. Riegler et al., showed that the flow rate plays a pivotal role in the trapping of SPIONs, and increasing the flow rate leads to a decrease in the trapping of the SPIONs [224]. In addition, the study indicated that increasing the distance between the target and the magnet results in a decrease in the trapping of the SPIONs. As a result, the aggregated SPIONs at a further distance are cleared away quickly when the external magnet is removed. The observations made by Riegler et al. were confirmed in our study where it was found that increasing the flow rate and the distance between the magnet and the target leads to a decrease in the trapping of the SPIONs. Given the findings by Riegler et al., future studies should compare different flow rates and using reagents of different viscosity, for example, use of blood instead of water in the pump.

This study showed that SPIONs of average size of 30 nm in diameter are taken up by WBC with no significant toxic effect. The study also revealed that WBCs are able to take up SPIONs of different concentrations up to 20mg/ml with little toxicity. Within that range of SPION concentration, 0.1mg/ml and 1.0mg/ml were selected to assess the toxicity and uptake on brain cells as well as brain tumour cells as any concentration higher than this would be harmful to the brain cells [211], [213]. It was concluded that the SPIONs have concentration-dependent toxicity on brain cells, i.e. an increase in concentration results in an increase in

toxicity. Our results resonate with findings from other studies, for example, [219], [220]. On the other hand, the results indicated that glioblastomas are less susceptible to SPION toxicity.

As discussed above, the findings from this study help to confirm the overall hypothesis that it is possible to model, design and build an inexpensive, portable and powerful Halbach array that could be used for MDT in brain tumour treatment.

7.1.2 Limitations of the study and future work

The modelling in this study made use of FEMM software because it was freely accessible, however, this software only allowed us to design 2D models. 2D models were limited given that they could not give us a full picture of the actual device in 3D. As a result, it was difficult to achieve precise measurements of the magnetic field strength of the actual magnet. Other software is available commercially such as COMSOL [181], however, this was expensive and required specific training that was not available locally. This is something that has been discussed with colleagues and will be considered in the future.

The modelling procedures conducted in this study were in magnetostatic state and future studies could explore similar modelling procedures but in a dynamic state to include all the aspects of MDT in brain tumour treatment. For instance, modelling the magnet with iron-loaded epoxy resin and everything fixed to the holder (helmet) attached to the head containing the brain tumour and the BBB, to mimic the real situation of the treatment of the brain tumour; that is, from the time of the introduction of the magnetised therapeutic agent intravenously to the trapping of the MNPs at the desired site. It is anticipated that this would provide a clear and comprehensive *in silico* model which would facilitate the observation of the behaviour of MNPs under the effect of our Halbach array in a flow model.

The assembling of the Halbach array could benefit from an exploration of new techniques to assemble the device. This is necessary in order to overcome the existing

challenges of assembling the device including how to overcome the repulsive forces and the use of adhesive glue. It is important to find an effective way to design a Halbach array model for personalised treatment for brain tumour patients. Using a 3D printer to print the complete model of Halbach array for individual patient needs based on MRI scan data. Alternatively, the 3D printer can be used to print out the design or holder where different magnet elements of multiple layers can be placed in the right positions based on the *in silico* model. Another less costly technique involves the use of iron-loaded epoxy resin instead of adhesive glue. This helps to overcome the downside of adhesive glue which creates slight gaps between the magnets in the device.

This study made use of the 3D flow phantom model which is not ideal for mimicking the human brain, i.e. the actual brain vasculature, the brain blood flow rate and the BBB. In addition, the use of an external magnetic field resulted in the aggregation of SPIONs which may result in the creation of aggregate whilst in circulation [98]. This aspect has not been investigated in the current study, hence, there is potential for further studies to explore ways of preventing aggregation of SPIONs in the blood vessels. One consideration is coating the SPIONs to weaken the aggregates.

In the experimental work aimed at assessing the uptake of SPIONs and viability of cells, the experiment was not conducted in a flow model with exposure to the magnetic field. As a result, future studies should be conducted using a sophisticated flow model and should also include the use of Halbach array magnet. Furthermore, in order to mimic the real brain blood flow rate which is approximately 800ml/min, future studies should consider the use of high quality material of the 3D flow phantom model capable of with standing such high blood flow rates such as SynBBB 3D Blood Brain Barrier model [225]. The materials used in this study could only withstand up to 300ml/min.

On the other hand, further studies should explore the application of this magnet, in particular, its effectiveness in *in vivo* models such as rodents and pigs. This could be done with existing brain cancer drugs like Temozolomide or with drugs that are not as effective at crossing the BBB. MDT opens up the possibility of using drugs that would be deemed unsuitable for brain tumours and therefore has the potential to improve patient outcome for a disease that is incurable and has such poor prognosis. In the same vein, future studies can investigate the effectiveness of using a range of anticancer drugs conjugated with a range of SPIONs coated with different materials to help identify the best combination to target the brain tumours. Furthermore, it will be interesting if future studies can also focus on the investigation of the transportation of SPIONs within the cells for periods of more than 24 hours. This study indicated that the SPIONs are distributed in the lysosomes after 24 hours of incubation time. In the same vein, further studies can also explore the quantification of SPIONs in the brain tumour cells as well as in other healthy cells, something that has not been explored in this study.

Indeed, a preliminary study carried out by Dr Priya Patel in our research group carried out an *in vivo* study using a miniaturised magnetic device. The device was designed and modelled in FEMM and built using small magnets of 3mm. The magnetic strength of the device was 0.7 T and this was able to trap iron in a phantom flow model at distances up to 1.8 cm. For the *in vivo* study, Priya implanted luciferase labelled CT2A murine glioblastoma cells intracranially into male C57BL/6 mice. Once tumours were visible by bioluminescence imaging, 5 mg/kg of SPIONs was administered intravenously into tumour bearing mice in the presence of the Halbach array that was secured to the head of the mouse for 30 min. From these unpublished observations it was clear by both MRI and histology that the presence of the Halbach array resulted in successful transfer of the SPIONs across the BBB into the tumour without any harm to the animal (**Figure 7.1**). These results are very encouraging and

further studies are now investigating drug delivery into the tumour using this approach to determine anti-tumour responses.
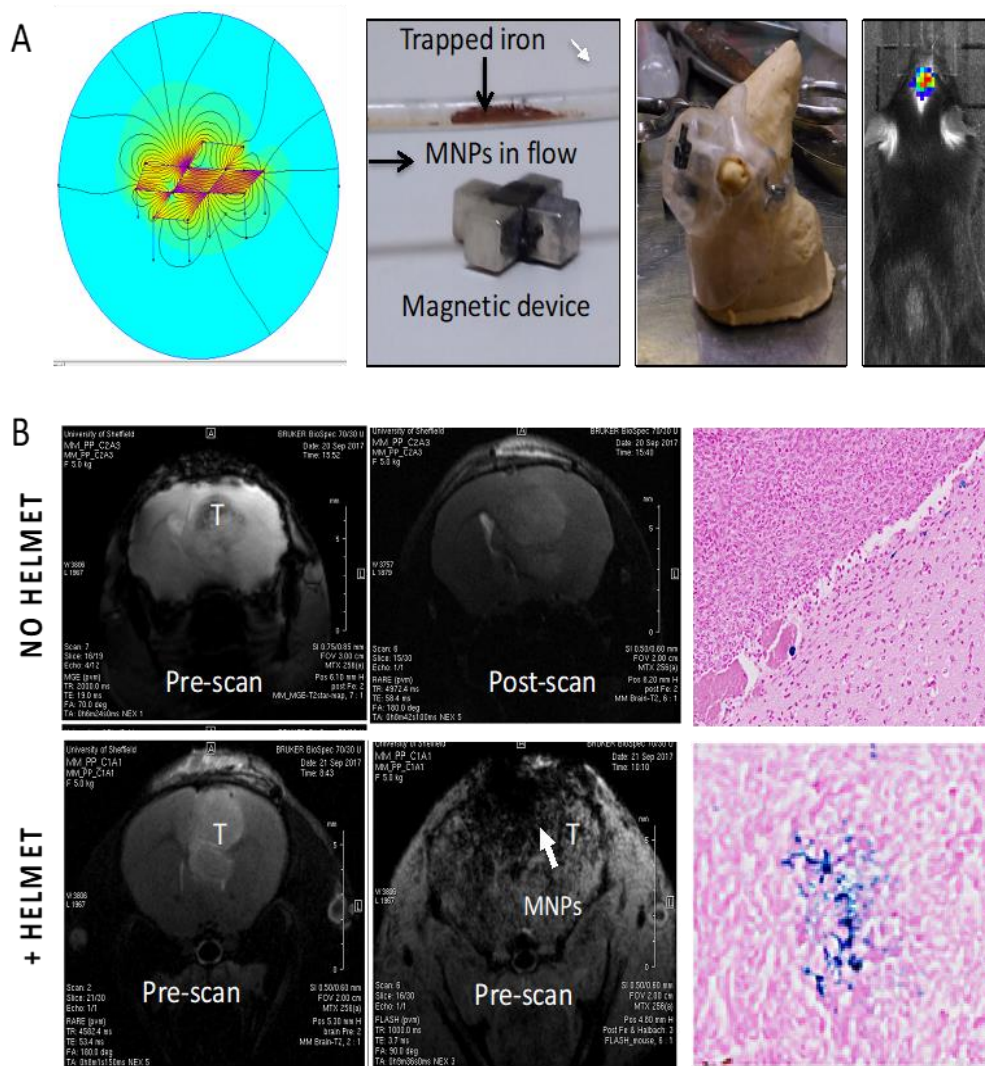
Figure 7.1: MDT of SPIONs in mice. (A) Left: *In vitro* Magnetic SPIONs trapping in presence of 0.7T magnetic device. SPIONs were added to water (1mg/15ml) and pumped around clear plastic tubing using a peristaltic pump. The magnetic device was placed underneath the plastic tubing at different distances and trapping was achieved up to a maximum distance of 1.8 cm. Middle: A custom-made helmet made from 3D printed material designed to fit securely on a mouse head. The magnetic array fit into the helmet to create a magnetic helmet and was positioned on top of the head. Right: Representative image from IVIS-bioluminescence imaging system showing a brain tumour in a mouse. CT2A luciferase labelled glioma cells were implanted via the intracranial route into C57Bl/6 mice. Bioluminescence imaging was used to monitor tumour growth over time. (B) SPIONs infiltrate brain tumours in the presence of the magnetic helmet. Once tumours were visible via IVIS mice to be imaged received an intravenous injection of (5mg/kg) SPIONs in water (100ul) in the presence/absence of the magnetic helmet. MRI scans were taken on a 7 Tesla MR imaging system. All mice underwent a pre-scan before the SPIONs were injected to determine the tumour location (T). The post-scan was taken 30 min after i.v. injection of SPIONs in both the no helmet and magnetic helmet group.

Finally, in order to develop this magnetic device for patient use it is important to consider how it would be fitted to a patient's head. This work is ongoing in our laboratory and discussions around the type of housing and material required to develop this have been initiated. So far, a helmet that allows the device to be positioned in multiple locations depending on where the tumour is located and that is made of comfortable materials has been suggested. These discussions have evolved as a result of this PhD study and have involved patient and public involvement groups, neuro-oncologists, physicists and material engineers. The next steps are to design and engineer the helmet with comfort for patients in mind. Furthermore, studies using larger animals are warranted. Pigs have similar brain physiology to humans and it is necessary to see how MDT affects the brain physiology prior to clinical studies in human.

It is worth mentioning that Halbach arrays of Model 2 was filed on 22nd October 2018 in order to obtain a patent for the device to be used for delivering anticancer drugs for targeting brain tumours (Appendices X).

References

[1]   D. Hambardzumyan, D. H. Gutmann, and H. Kettenmann, "The role of microglia and macrophages in glioma maintenance and progression," *Nature Neuroscience*. 2015.

[2]   J. Kipnis, "Multifaceted interactions between adaptive immunity and the central nervous system," *Science*. 2016.

[3]   B. Obermeier, R. Daneman, and R. M. Ransohoff, "Development, maintenance and disruption of the blood-brain barrier," *Nature Medicine*. 2013.

[4]   N. J. Abbott, L. Rönnbäck, and E. Hansson, "Astrocyte-endothelial interactions at the blood-brain barrier," *Nature Reviews Neuroscience*. 2006.

[5]   J. I. Alvarez, T. Katayama, and A. Prat, "Glial influence on the blood brain barrier," *GLIA*. 2013.

[6]   G. P. Cardona-Gomez, M. Ã• vila, R. Cabezas, R. S. El-BachÃ¡, J. C. Jurado Coronel, J. Gonzalez, E. BÃ¡ez, L. M. GarcÃa-Segura, G. E. Barreto, and F. Capani, "Astrocytic modulation of blood brain barrier: perspectives on Parkinsonâ€™s disease," *Front. Cell. Neurosci.*, 2014.

[7]   R. Daneman, L. Zhou, A. A. Kebede, and B. A. Barres, "Pericytes are required for bloodâ€"brain barrier integrity during embryogenesis," *Nature*, 2010.

[8]   P. A. McKinney, "Brain tumours: incidence, survival, and aetiology," *J. Neurol. Neurosurg. Psychiatry*, 2004.

[9]   N. Howlader, A. Noone, M. Krapcho, D. Miller, K. Bishop, S. Altekruse, C. Kosary, M. Yu, J. Ruhl, Z. Tatalovich, A. Mariotto, D. Lewis, H. Chen, E. Feuer,

and K. Cronin, "SEER Cancer Statistics Review 1975-2013," *Natl. Cancer Inst.*, 2013.

[10] J. Gould, "Breaking down the epidemiology of brain cancer," *Nature*. 2018.

[11] Q. T. Ostrom, H. Gittleman, P. Liao, T. Vecchione-Koval, Y. Wolinsky, C. Kruchko, and J. S. Barnholtz-Sloan, "CBTRUS Statistical Report: Primary brain and other central nervous system tumors diagnosed in the United States in 2010-2014," *Neuro. Oncol.*, 2017.

[12] L. Nayak, E. Q. Lee, and P. Y. Wen, "Epidemiology of brain metastases," *Curr. Oncol. Rep.*, 2012.

[13] J. S. Barnholtz-Sloan, A. E. Sloan, F. G. Davis, F. D. Vigneau, P. Lai, and R. E. Sawaya, "Incidence proportions of brain metastases in patients diagnosed (1973 to 2001) in the Metropolitan Detroit Cancer Surveillance System," *J. Clin. Oncol.*, 2004.

[14] P. W. Sperduto, S. T. Chao, P. K. Sneed, X. Luo, J. Suh, D. Roberge, A. Bhatt, A. W. Jensen, P. D. Brown, H. Shih, J. Kirkpatrick, A. Schwer, L. E. Gaspar, J. B. Fiveash, V. Chiang, J. Knisely, C. M. Sperduto, and M. Mehta, "Diagnosis-Specific Prognostic Factors, Indexes, and Treatment Outcomes for Patients With Newly Diagnosed Brain Metastases: A Multi-Institutional Analysis of 4,259 Patients," *Int. J. Radiat. Oncol. Biol. Phys.*, 2010.

[15] A. S. Berghoff and M. Preusser, "The inflammatory microenvironment in brain metastases : potential treatment target ?," *Chinese Clin. Oncol.*, 2015.

[16] S. Lapointe, A. Perry, and N. A. Butowski, "Primary brain tumours in adults," *The Lancet*. 2018.

[17] D. N. Louis, H. Ohgaki, O. D. Wiestler, W. K. Cavenee, P. C. Burger, A. Jouvet, B. W. Scheithauer, and P. Kleihues, "The 2007 WHO classification of tumours of the central nervous system," *Acta Neuropathologica*. 2007.

[18] D. N. Louis, "MOLECULAR PATHOLOGY OF MALIGNANT GLIOMAS," *Annu. Rev. Pathol. Mech. Dis.*, 2006.

[19] F. B. Furnari, T. Fenton, R. M. Bachoo, A. Mukasa, J. M. Stommel, A. Stegh, W. C. Hahn, K. L. Ligon, D. N. Louis, C. Brennan, L. Chin, R. A. DePinho, and W. K. Cavenee, "Malignant astrocytic glioma: Genetics, biology, and paths to treatment," *Genes and Development*. 2007.

[20] H. Ohgaki and P. Kleihues, "Genetic pathways to primary and secondary glioblastoma," *American Journal of Pathology*. 2007.

[21] W. A. Hall, H. R. Djalilian, E. S. Nussbaum, and K. H. Cho, "Long-term survival with metastatic cancer to the brain," *Med. Oncol.*, 2000.

[22] A. C. Bellail, S. B. Hunter, D. J. Brat, C. Tan, and E. G. Van Meir, "Microregional extracellular matrix heterogeneity in brain modulates glioma cell invasion," *International Journal of Biochemistry and Cell Biology*. 2004.

[23] A. A. Aizer and E. Q. Lee, "Brain Metastases," *Neurol. Clin.*, vol. 36, no. 3, pp. 557–577, 2018.

[24] L. Burt Nabors, M. Ammirati, P. J. Bierman, H. Brem, N. Butowski, M. C. Chamberlain, L. M. DeAngelis, R. A. Fenstermaker, A. Friedman, M. R. Gilbert, D. Hesser, M. Holdhoff, L. Junck, R. Lawson, J. S. Loeffler, M. H. Maor, P. L. Moots, T. Morrison, M. M. Mrugala, H. B. Newton, J. Portnow, J. J. Raizer, L. Recht, D. C. Shrieve, A. K. Sills, D. Tran, N. Tran, F. D. Vrionis, P. Y. Wen, and M. Ho,

"Central nervous system cancers," *JNCCN Journal of the National Comprehensive Cancer Network*. 2013.

[25] M. Back, D. Jayamanne, D. Brazier, D. Bailey, E. Hsiao, L. Guo, and H. Wheeler, "Tumour volume reduction following PET guided intensity modulated radiation therapy and temozolomide in IDH mutated anaplastic glioma," *J. Clin. Neurosci.*, 2019.

[26] A. Dutz, A. Lühr, L. Agolli, E. G. C. Troost, M. Krause, M. Baumann, X. Vermeren, D. Geismar, E. F. Schapira, M. Bussière, J. E. Daly, M. R. Bussière, B. Timmermann, H. A. Shih, and S. Löck, "Development and validation of NTCP models for acute side-effects resulting from proton beam therapy of brain tumours," *Radiother. Oncol.*, 2019.

[27] R. J. KOMOTAR, D. A. WILSON, and E. S. CONNOLLY, "Radiotherapy plus Concomitant and Adjuvant Temozolomide for Glioblastoma," *Neurosurgery*, 2017.

[28] K. L. Pitter, I. Tamagno, K. Alikhanyan, A. Hosni-Ahmed, S. S. Pattwell, S. Donnola, C. Dai, T. Ozawa, M. Chang, T. A. Chan, K. Beal, A. J. Bishop, C. A. Barker, T. S. Jones, B. Hentschel, T. Gorlia, U. Schlegel, R. Stupp, M. Weller, E. C. Holland, and D. Hambardzumyan, "Corticosteroids compromise survival in glioblastoma," *Brain*, 2016.

[29] R. L. Sabado and N. Bhardwaj, "Cancer immunotherapy: Dendritic-cell vaccines on the move," *Nature*. 2015.

[30] A. C. Filley and M. Dey, "Dendritic cell based vaccination strategy: an evolving paradigm," *Journal of Neuro-Oncology*. 2017.

[31] M. Weller, P. Roth, M. Preusser, W. Wick, D. A. Reardon, M. Platten, and J. H.

Sampson, "Vaccine-based immunotherapeutic approaches to gliomas and beyond," *Nature Reviews Neurology*. 2017.

[32] S. J. Bagley, A. S. Desai, G. P. Linette, C. H. June, and D. M. O'Rourke, "CAR T-cell therapy for glioblastoma: Recent clinical advances and future challenges," *Neuro. Oncol.*, 2018.

[33] L. M. Liau, K. L. Black, N. A. Martin, S. N. Sykes, J. M. Bronstein, L. Jouben-Steele, P. S. Mischel, A. Belldegrun, and T. F. Cloughesy, "Treatment of a glioblastoma patient by vaccination with autologous dendritic cells pulsed with allogeneic major histocompatibility complex class I–matched tumor peptides," *Neurosurg. Focus*, 2008.

[34] K. Bielamowicz, S. Khawja, and N. Ahmed, "Adoptive Cell Therapies for Glioblastoma," *Front. Oncol.*, 2013.

[35] J. H. Sampson, M. V. Maus, and C. H. June, "Immunotherapy for brain tumors," *Journal of Clinical Oncology*. 2017.

[36] Y. Lin and H. Okada, "Cellular immunotherapy for malignant gliomas," *Expert Opinion on Biological Therapy*. 2016.

[37] C. E. Brown, B. Aguilar, R. Starr, X. Yang, W. C. Chang, L. Weng, B. Chang, A. Sarkissian, A. Brito, J. F. Sanchez, J. R. Ostberg, M. D'Apuzzo, B. Badie, M. E. Barish, and S. J. Forman, "Optimization of IL13Rα2-Targeted Chimeric Antigen Receptor T Cells for Improved Anti-tumor Efficacy against Glioblastoma," *Mol. Ther.*, vol. 26, no. 1, pp. 31–44, Jan. 2018.

[38] D. Zamarin and M. A. Postow, "Immune checkpoint modulation: Rational design of combination strategies," *Pharmacology and Therapeutics*. 2015.

[39] J. D. Wolchok, H. Kluger, M. K. Callahan, M. A. Postow, N. A. Rizvi, A. M. Lesokhin, N. H. Segal, C. E. Ariyan, R.-A. Gordon, K. Reed, M. M. Burke, A. Caldwell, S. A. Kronenberg, B. U. Agunwamba, X. Zhang, I. Lowy, H. D. Inzunza, W. Feely, C. E. Horak, Q. Hong, A. J. Korman, J. M. Wigginton, A. Gupta, and M. Sznol, "Nivolumab plus Ipilimumab in Advanced Melanoma," *N. Engl. J. Med.*, 2013.

[40] J. D. Wolchok, V. Chiarion-Sileni, R. Gonzalez, P. Rutkowski, J.-J. Grob, C. L. Cowey, C. D. Lao, J. Wagstaff, D. Schadendorf, P. F. Ferrucci, M. Smylie, R. Dummer, A. Hill, D. Hogg, J. Haanen, M. S. Carlino, O. Bechter, M. Maio, I. Marquez-Rodas, M. Guidoboni, G. McArthur, C. Lebbé, P. A. Ascierto, G. V. Long, J. Cebon, J. Sosman, M. A. Postow, M. K. Callahan, D. Walker, L. Rollin, R. Bhore, F. S. Hodi, and J. Larkin, "Overall Survival with Combined Nivolumab and Ipilimumab in Advanced Melanoma," *N. Engl. J. Med.*, 2017.

[41] J. Huang, F. Liu, Z. Liu, H. Tang, H. Wu, Q. Gong, and J. Chen, "Immune checkpoint in glioblastoma: Promising and challenging," *Frontiers in Pharmacology*. 2017.

[42] G. Wollmann, K. Ozduman, and A. N. Van Den Pol, "Oncolytic virus therapy for glioblastoma multiforme: Concepts and candidates," *Cancer Journal*. 2012.

[43] J. V. Cockle, A. Brüning-Richardson, K. J. Scott, J. Thompson, T. Kottke, E. Morrison, A. Ismail, A. M. Carcaboso, A. Rose, P. Selby, J. Conner, S. Picton, S. Short, R. Vile, A. Melcher, and E. Ilett, "Oncolytic Herpes Simplex Virus Inhibits Pediatric Brain Tumor Migration and Invasion," *Mol. Ther. - Oncolytics*, 2017.

[44] K. A. Streby, J. I. Geller, M. A. Currier, P. S. Warren, J. M. Racadio, A. J. Towbin, M. R. Vaughan, M. Triplet, K. Ott-Napier, D. J. Dishman, L. R. Backus, B.

Stockman, M. Brunner, K. Simpson, R. Spavin, J. Conner, and T. P. Cripe, "Intratumoral injection of HSV1716, an oncolytic herpes virus, is safe and shows evidence of immune response and viral replication in young cancer patients," *Clin. Cancer Res.*, 2017.

[45] W. M. Pardridge, W. H. Oldendorf, P. Cancilla, and H. J. L. Frank, "Blood-brain barrier: Interface between internal medicine and the brain," *Annals of Internal Medicine*. 1986.

[46] D. Beier, S. Röhrl, D. R. Pillai, S. Schwarz, L. A. Kunz-Schughart, P. Leukel, M. Proescholdt, A. Brawanski, U. Bogdahn, A. Trampe-Kieslich, B. Giebel, J. Wischhusen, G. Reifenberger, P. Hau, and C. P. Beier, "Temozolomide preferentially depletes cancer stem cells in glioblastoma," *Cancer Res.*, 2008.

[47] J. Blakeley, "Drug delivery to brain tumors," *Current Neurology and Neuroscience Reports*. 2008.

[48] O. Van Tellingen, B. Yetkin-Arik, M. C. De Gooijer, P. Wesseling, T. Wurdinger, and H. E. De Vries, "Overcoming the blood-brain tumor barrier for effective glioblastoma treatment," *Drug Resistance Updates*. 2015.

[49] S. Watkins, S. Robel, I. F. Kimbrough, S. M. Robert, G. Ellis-Davies, and H. Sontheimer, "Disruption of astrocyte-vascular coupling and the blood-brain barrier by invading glioma cells," *Nat. Commun.*, 2014.

[50] A. Korfel and E. Thiel, "Targeted therapy and blood-brain," *Recent results in cancer research. Fortschritte der Krebsforschung. Progrès dans les recherches sur le cancer*. 2007.

[51] C. La Fougère, B. Suchorska, P. Bartenstein, F. W. Kreth, and J. C. Tonn,

References

"Molecular imaging of gliomas with PET: Opportunities and limitations," *Neuro-Oncology*. 2011.

[52] a S. Lübbe, C. Alexiou, C. Bergemann, and A. S. Lubbe, "Clinical applications of magnetic drug targeting," *J. Surg. Res.*, vol. 95, no. 2, pp. 200–206, 2001.

[53] A. Carpentier, M. Canney, A. Vignot, V. Reina, K. Beccaria, C. Horodyckid, C. Karachi, D. Leclercq, C. Lafon, J. Y. Chapelon, L. Capelle, P. Cornu, M. Sanson, K. Hoang-Xuan, J. Y. Delattre, and A. Idbaih, "Clinical trial of blood-brain barrier disruption by pulsed ultrasound," *Sci. Transl. Med.*, 2016.

[54] D. Ye, X. Zhang, Y. Yue, R. Raliya, P. Biswas, S. Taylor, Y. chuan Tai, J. B. Rubin, Y. Liu, and H. Chen, "Focused ultrasound combined with microbubble-mediated intranasal delivery of gold nanoclusters to the brain," *J. Control. Release*, 2018.

[55] S. Alli, C. A. Figueiredo, B. Golbourn, N. Sabha, M. Y. Wu, A. Bondoc, A. Luck, D. Coluccia, C. Maslink, C. Smith, H. Wurdak, K. Hynynen, M. O'Reilly, and J. T. Rutka, "Brainstem blood brain barrier disruption using focused ultrasound: A demonstration of feasibility and enhanced doxorubicin delivery," *J. Control. Release*, 2018.

[56] T. Maruyama, Y. Muragaki, M. Nitta, S. Tsuzuki, T. Yasuda, S. Ikuta, and T. Kawamata, "Photodynamic therapy for malignant brain tumors," *Japanese J. Neurosurg.*, 2016.

[57] D. Kyurkchiev, E. G. Borisova, I. Angelov, O. Semyachkina-Glushkovskaya, T. Genova-Hristova, K. Minkin, and K. Tumangelova-Yuzeir, "Evaluation of photodynamic treatment efficiency on glioblastoma cells received from malignant lesions: initial studies," 2018.

[58] A. P. Castano, T. N. Demidova, and M. R. Hamblin, "Mechanisms in photodynamic therapy: Part one - Photosensitizers, photochemistry and cellular localization," *Photodiagnosis and Photodynamic Therapy*. 2004.

[59] A. P. Castano, T. N. Demidova, and M. R. Hamblin, "Mechanisms in photodynamic therapy: Part two - Cellular signaling, cell metabolism and modes of cell death," *Photodiagnosis and Photodynamic Therapy*. 2005.

[60] B. Chertok, A. E. David, and V. C. Yang, "Magnetically-enabled and MR-monitored selective brain tumor protein delivery in rats via magnetic nanocarriers.," *Biomaterials*, vol. 32, no. 26, pp. 6245–53, Sep. 2011.

[61] A. Sarwar, A. Nemirovski, and B. Shapiro, "Optimal Halbach Permanent Magnet Designs for Maximally Pulling and Pushing Nanoparticles.," *J. Magn. Magn. Mater.*, vol. 324, no. 5, pp. 742–754, Mar. 2012.

[62] L. Cheng, C. Wang, X. Ma, Q. Wang, Y. Cheng, H. Wang, Y. Li, and Z. Liu, "Multifunctional upconversion nanoparticles for dual-modal imaging-guided stem cell therapy under remote magnetic control," *Adv. Funct. Mater.*, vol. 23, no. 3, pp. 272–280, 2013.

[63] V. Vaněček, V. Zablotskii, S. Forostyak, J. Růžička, V. Herynek, M. Babič, P. Jendelová, Š. Kubinová, A. Dejneka, and E. Syková, "Highly efficient magnetic targeting of mesenchymal stem cells in spinal cord injury," *Int. J. Nanomedicine*, vol. 7, pp. 3719–3730, 2012.

[64] L. A. Tran, M. Hernández-Rivera, A. N. Berlin, Y. Zheng, L. Sampaio, C. Bové, M. da G. Cabreira-Hansen, J. T. Willerson, E. C. Perin, and L. J. Wilson, "The use of gadolinium-carbon nanostructures to magnetically enhance stem cell retention for cellular cardiomyoplasty," *Biomaterials*, vol. 35, no. 2, pp. 720–726, 2014.

References

[65] J. J. Connell, P. S. Patrick, Y. Yu, M. F. Lythgoe, and T. L. Kalber, "Advanced cell therapies: targeting, tracking and actuation of cells with magnetic particles.," *Regen. Med.*, vol. 10, no. 6, pp. 757–772, 2015.

[66] K. Lee, A. E. David, J. Zhang, M. C. Shin, and V. C. Yang, "Enhanced accumulation of theranostic nanoparticles in brain tumor by external magnetic field mediated in situ clustering of magnetic nanoparticles," *J. Ind. Eng. Chem.*, 2017.

[67] M. Fernández, F. Javaid, and V. Chudasama, "Advances in targeting the folate receptor in the treatment/imaging of cancers," *Chemical Science*. 2018.

[68] W. Sun, J. Fan, S. Wang, Y. Kang, J. Du, and X. Peng, "Biodegradable Drug-Loaded Hydroxyapatite Nanotherapeutic Agent for Targeted Drug Release in Tumors," *ACS Appl. Mater. Interfaces*, 2018.

[69] C. Alexiou, W. Arnold, R. J. Klein, F. G. Parak, P. Hulin, C. Bergemann, W. Erhardt, S. Wagenpfeil, and A. S. Lubbe, "Locoregional cancer treatment with magnetic drug targeting," *Cancer Res.*, 2000.

[70] J. L. Gaglia, M. Harisinghani, I. Aganj, G. R. Wojtkiewicz, S. Hedgire, C. Benoist, D. Mathis, and R. Weissleder, "Noninvasive mapping of pancreatic inflammation in recent-onset type-1 diabetes patients," *Proc. Natl. Acad. Sci.*, 2015.

[71] R. Tietze, R. Jurgons, S. Lyer, E. Schreiber, F. Wiekhorst, D. Eberbeck, H. Richter, U. Steinhoff, L. Trahms, and C. Alexiou, "Quantification of drug-loaded magnetic nanoparticles in rabbit liver and tumor after in vivo administration," *J. Magn. Magn. Mater.*, 2009.

[72] M. Arruebo, R. Fernández-Pacheco, M. R. Ibarra, and J. Santamaría, "Magnetic nanoparticles for drug delivery," *JUNE*, vol. 2, no. 3, 2007.

[73] Y. H. Ma, Y. W. Hsu, Y. J. Chang, M. Y. Hua, J. P. Chen, and T. Wu, "Intra-arterial application of magnetic nanoparticles for targeted thrombolytic therapy: A rat embolic model," *J. Magn. Magn. Mater.*, 2007.

[74] S. C. Goodwin, C. A. Bittner, C. L. Peterson, and G. Wong, "Single-dose toxicity study of hepatic intra-arterial infusion of doxorubicin coupled to a novel magnetically targeted drug carrier," *Toxicol. Sci.*, 2001.

[75] A. S. Lübbe, C. Bergemann, H. Riess, F. Schriever, P. Reichardt, K. Possinger, M. Matthias, B. Dörken, F. Herrmann, R. Gürtler, P. Hohenberger, N. Haas, R. Sohr, B. Sander, A. J. Lemke, D. Ohlendorf, W. Huhnt, and D. Huhn, "Clinical experiences with magnetic drug targeting: A phase I study with 4'-epidoxorubicin in 14 patients with advanced solid tumors," *Cancer Res.*, 1996.

[76] C. Alexiou, R. Jurgons, C. Seliger, S. Kolb, B. Heubeck, and H. Iro, "Distribution of mitoxantrone after magnetic drug targeting: Fluorescence microscopic investigations on VX2 squamous cell carcinoma cells," in *Zeitschrift fur Physikalische Chemie*, 2006.

[77] A. Sarwar, R. Lee, D. A. Depireux, and B. Shapiro, "Magnetic Injection of Nanoparticles Into Rat Inner Ears <newline/>at a Human Head Working Distance," *IEEE Trans. Magn.*, vol. 49, no. 1, pp. 440–452, Jan. 2013.

[78] L. Danielyan, R. Schäfer, A. von Ameln-Mayerhofer, M. Buadze, J. Geisler, T. Klopfer, U. Burkhardt, B. Proksch, S. Verleysdonk, M. Ayturan, G. H. Buniatian, C. H. Gleiter, and W. H. Frey, "Intranasal delivery of cells to the brain," *Eur. J. Cell Biol.*, 2009.

[79] R. K. Gilchrist, R. Medal, W. D. Shorey, R. C. Hanselman, J. C. Parrott, and C. B. Taylor, "Selective Inductive Heating of Lymph Nodes *," *Ann. Surg.*, vol. 146, no.

4, pp. 596–606, 1957.

[80] R. D. Turner, R. W. Rand, J. R. Bentson, and J. A. Mosso, "Ferromagnetic silicone necrosis of hypernephromas by selective vascular occlusion to the tumor: a new technique.," *J. Urol.*, vol. 113, no. 4, pp. 455–459, 1975.

[81] U. O. Häfeli, "Magnetically modulated therapeutic systems.," *Int. J. Pharm.*, vol. 277, no. 1–2, pp. 19–24, Jun. 2004.

[82] S. K. Hilal, W. J. Michelsen, J. Driller, and E. Leonard, "Magnetically guided devices for vascular exploration and treatment.," *Radiology*, vol. 113, no. 3, pp. 529–540, 1974.

[83] K. J. Widder, A. E. Senyei, and D. F. Ranney, "Magnetically Responsive Microspheres and Other Carriers for the Biophysical Targeting of Antitumor Agents," *Adv. Pharmacol.*, vol. 16, no. C, pp. 213–271, 1979.

[84] S. K. Jones and J. G. Winter, "Experimental examination of a targeted hyperthermia system using inductively heated ferromagnetic microspheres in rabbit kidney," *Phys. Med. Biol.*, vol. 46, no. 2, pp. 385–398, 2001.

[85] D. N. Price, L. R. Stromberg, N. K. Kunda, and P. Muttil, "In Vivo Pulmonary Delivery and Magnetic-Targeting of Dry Powder Nano-in-Microparticles," *Mol. Pharm.*, 2017.

[86] B. Hu, Y. Y. Tu, G. P. Yan, R. X. Zhuo, S. E. Bottle, Y. Wu, C. L. Fan, and Y. J. Duan, "Polycarbonate microspheres containing mitomycin C and magnetic powders as potential hepatic carcinoma therapeutics," *Colloids Surfaces B Biointerfaces*, vol. 84, no. 2, pp. 550–555, 2011.

[87] G. Wunderlich, E. Schiller, R. Bergmann, and H. J. Pietzsch, "Comparison of the

stability of Y-90-, Lu-177- and Ga-68- labeled human serum albumin microspheres (DOTA-HSAM)," *Nucl. Med. Biol.*, vol. 37, no. 8, pp. 861–867, 2010.

[88] Y. Sun, L. Chen, J. Yu, X. Zhi, S. Tang, P. Zhou, and C. Wang, "Folate-bearing doxorubicin-loaded magnetic poly(N-isopropylacrylamide) microspheres as a new strategy for cancer therapy," *Anticancer Drugs*, vol. 20, no. 7, pp. 607–615, 2009.

[89] E. E. Hassan, R. C. Parish, and J. M. Gallo, "Optimized Formulation of Magnetic Chitosan Microspheres Containing the Anticancer Agent, Oxantrazole," *Pharm. Res. An Off. J. Am. Assoc. Pharm. Sci.*, vol. 9, no. 3, pp. 390–397, 1992.

[90] T. A. O. K. I, "Preparation of Adriamycin Magnetic Albumin Microspheres and Their Experimental Antitumor Effects in vitro and in vivo *," vol. 19, no. 4, pp. 295–299, 1999.

[91] A. M. Grumezescu, A. Ficai, D. Ficai, G. Predan, and M. C. Chifiriuc, "Polymeric magnetic silica microspheres as a drug loader for antimicrobial delivery substances," *Dig. J. Nanomater. Biostructures*, vol. 7, no. 4, pp. 1891–1896, 2012.

[92] M. Muthana, S. D. Scott, N. Farrow, F. Morrow, C. Murdoch, S. Grubb, N. Brown, J. Dobson, and C. E. Lewis, "A novel magnetic approach to enhance the efficacy of cell-based gene therapies.," *Gene Ther.*, vol. 15, no. 12, pp. 902–10, 2008.

[93] M. Muthana, A. J. Kennerley, R. Hughes, E. Fagnano, J. Richardson, M. Paul, C. Murdoch, F. Wright, C. Payne, M. F. Lythgoe, N. Farrow, J. Dobson, J. Conner, J. M. Wild, and C. Lewis, "Directing cell therapy to anatomic target sites in vivo with magnetic resonance targeting.," *Nat. Commun.*, vol. 6, p. 8009, Jan. 2015.

[94] J. B. Mathieu and S. Martel, "Magnetic microparticle steering within the constraints of an MRI system: Proof of concept of a novel targeting approach," *Biomed.*

Microdevices, 2007.

[95] P. Pouponneau, G. Bringout, and S. Martel, "Therapeutic Magnetic Microcarriers Guided by Magnetic Resonance Navigation for Enhanced Liver Chemoembilization: A Design Review," *Annals of Biomedical Engineering*, vol. 42, no. 5. pp. 929–939, 2014.

[96] N. J. Darton, A. J. Sederman, A. Ionescu, C. Ducati, R. C. Darton, L. F. Gladden, and N. K. H. Slater, "Manipulation and tracking of superparamagnetic nanoparticles using MRI.," *Nanotechnology*, vol. 19, no. 39, p. 395102, 2008.

[97] J. L. Arias, L. H. Reddy, and P. Couvreur, "Fe 3O 4/chitosan nanocomposite for magnetic drug targeting to cancer," *J. Mater. Chem.*, 2012.

[98] a S. Lübbe, C. Bergemann, H. Riess, F. Schriever, P. Reichardt, K. Possinger, M. Matthias, B. Dörken, F. Herrmann, R. Gürtler, P. Hohenberger, N. Haas, R. Sohr, B. Sander, a J. Lemke, D. Ohlendorf, W. Huhnt, and D. Huhn, "Clinical experiences with magnetic drug targeting: a phase I study with 4'-epidoxorubicin in 14 patients with advanced solid tumors.," *Cancer Res.*, vol. 56, no. 20, pp. 4686–4693, 1996.

[99] J. Riegler, A. Liew, S. O. Hynes, D. Ortega, T. O'Brien, R. M. Day, T. Richards, F. Sharif, Q. A. Pankhurst, and M. F. Lythgoe, "Superparamagnetic iron oxide nanoparticle targeting of MSCs in vascular injury," *Biomaterials*, vol. 34, no. 8, pp. 1987–1994, 2013.

[100] A. Yanai, U. O. Häfeli, A. L. Metcalfe, P. Soema, L. Addo, C. Y. Gregory-Evans, K. Po, X. Shan, O. L. Moritz, and K. Gregory-Evans, "Focused Magnetic Stem Cell Targeting to the Retina Using Superparamagnetic Iron Oxide Nanoparticles," *Cell Transplant.*, 2012.

References

[101] H.-L. Liu, M.-Y. Hua, H.-W. Yang, C.-Y. Huang, P.-C. Chu, J.-S. Wu, I.-C. Tseng, J.-J. Wang, T.-C. Yen, P.-Y. Chen, and K.-C. Wei, "Magnetic resonance monitoring of focused ultrasound/magnetic nanoparticle targeting delivery of therapeutic agents to the brain," *Proc. Natl. Acad. Sci.*, 2010.

[102] M. Johannsen, U. Gneveckow, B. Thiesen, K. Taymoorian, C. H. Cho, N. Waldöfner, R. Scholz, A. Jordan, S. A. Loening, and P. Wust, "Thermotherapy of Prostate Cancer Using Magnetic Nanoparticles: Feasibility, Imaging, and Three-Dimensional Temperature Distribution," *Eur. Urol.*, 2007.

[103] M. Johannsen, B. Thiesen, P. Wust, and A. Jordan, "Magnetic nanoparticle hyperthermia for prostate cancer," *Int. J. Hyperth.*, 2010.

[104] M. Taupitz, S. Wagner, B. Hamm, D. Dienemann, R. Lawaczeck, and K. J. Wolf, "Mr lymphography using iron oxide particles: Detection of lymph node metastases in the VX2 rabbit tumor model," *Acta radiol.*, 1993.

[105] A. Senyei, K. Widder, and G. Czerlinski, "Magnetic guidance of drug-carrying microspheres," *J. Appl. Phys.*, vol. 49, no. 6, pp. 3578–3583, 1978.

[106] S. Laurent, A. A. Saei, S. Behzadi, A. Panahifar, and M. Mahmoudi, "Superparamagnetic iron oxide nanoparticles for delivery of therapeutic agents: opportunities and challenges," *Expert Opin. Drug Deliv.*, 2014.

[107] S. C. McBain, H. H. P. Yiu, and J. Dobson, "Magnetic nanoparticles for gene and drug delivery," *International Journal of Nanomedicine*. 2008.

[108] W. Wu, Z. Wu, T. Yu, C. Jiang, and W. S. Kim, "Recent progress on magnetic iron oxide nanoparticles: Synthesis, surface functional strategies and biomedical applications," *Science and Technology of Advanced Materials*. 2015.

References

[109] A. Singh and S. K. Sahoo, "Magnetic nanoparticles: A novel platform for cancer theranostics," *Drug Discovery Today*. 2014.

[110] M. K. Lima-Tenório, E. A. Gómez Pineda, N. M. Ahmad, H. Fessi, and A. Elaissari, "Magnetic nanoparticles: In vivo cancer diagnosis and therapy," *Int. J. Pharm.*, 2015.

[111] L. L. Vatta, R. D. Sanderson, and K. R. Koch, "Magnetic nanoparticles : Properties and potential applications," *Adv. Mater.*, vol. 78, no. 9, pp. 1793–1801, 2006.

[112] R. V. Ramanujan, "Magnetic particles for biomedical applications," in *Biomedical Materials*, Springer US, 2009, pp. 477–491.

[113] I. Brigger, C. Dubernet, and P. Couvreur, "Nanoparticles in cancer therapy and diagnosis," *Advanced Drug Delivery Reviews*, vol. 64, no. SUPPL. pp. 24–36, 2012.

[114] I. K. Puri and R. Ganguly, "Particle Transport in Therapeutic Magnetic Fields," *Annu. Rev. Fluid Mech*, vol. 46, pp. 407–40, 2014.

[115] P. Vartholomeos and C. Mavroidis, "In silico studies of magnetic microparticle aggregations in fluid environments for MRI-guided drug delivery," *IEEE Trans. Biomed. Eng.*, vol. 59, no. 11 PART1, pp. 3028–3038, 2012.

[116] L. C. Barnsley, D. Carugo, J. Owen, and E. Stride, "Halbach arrays consisting of cubic elements optimised for high field gradients in magnetic drug targeting applications.," *Phys. Med. Biol.*, vol. 60, no. 21, pp. 8303–27, Nov. 2015.

[117] M. Hu, J. Chen, Z. Y. Li, L. Au, G. V. Hartland, X. Li, M. Marquez, and Y. Xia, "Gold nanostructures: Engineering their plasmonic properties for biomedical applications," *Chemical Society Reviews*. 2006.

[118] Y. S. Wang, L. R. Liu, Q. Jiang, and Q. Q. Zhang, "Self-aggregated nanoparticles of

cholesterol-modified chitosan conjugate as a novel carrier of epirubicin," *Eur. Polym. J.*, 2007.

[119] K. Schulze, A. Koch, B. Schöpf, A. Petri, B. Steitz, M. Chastellain, M. Hofmann, H. Hofmann, and B. Von Rechenberg, "Intraarticular application of superparamagnetic nanoparticles and their uptake by synovial membrane - An experimental study in sheep," in *Journal of Magnetism and Magnetic Materials*, 2005.

[120] A. O. Elzoghby, W. M. Samy, and N. A. Elgindy, "Albumin-based nanoparticles as potential controlled release drug delivery systems," *Journal of Controlled Release*. 2012.

[121] T. Matsunaga and H. Takeyama, "Biomagnetic nanoparticle formation and application," *Supramol. Sci.*, 1998.

[122] M. Shinkai, "Functional magnetic particles for medical application," *Journal of Bioscience and Bioengineering*, vol. 94, no. 6. pp. 606–613, 2002.

[123] L. L. Horstman, W. Jy, Y. S. Ahn, R. Zivadinov, A. H. Maghzi, M. Etemadifar, J. Steven Alexander, and A. Minagar, "Role of platelets in neuroinflammation: A wide-angle perspective," *Journal of Neuroinflammation*. 2010.

[124] S. Sarkar, M. A. Alam, J. Shaw, and A. K. Dasgupta, "Drug delivery using platelet cancer cell interaction," *Pharm. Res.*, 2013.

[125] P. Xu, R. Wang, X. Wang, and J. Ouyang, "Recent advancements in erythrocytes, platelets, and albumin as delivery systems," *OncoTargets and Therapy*. 2016.

[126] P. Krůpa, S. Řehák, D. Diaz-Garcia, and S. Filip, "NANOTECHNOLOGY – NEW TRENDS IN THE TREATMENT OF BRAIN TUMOURS," *Acta Medica (Hradec*

Kral. Czech Republic), 2015.

[127] H. Kato, Y. Kanazawa, M. Okumura, A. Taninaka, T. Yokawa, and H. Shinohara, "Lanthanoid endohedral metallofullerenols for MRI contrast agents," *J. Am. Chem. Soc.*, 2003.

[128] N. Nitin, L. E. W. LaConte, O. Zurkiya, X. Hu, and G. Bao, "Functionalization and peptide-based delivery of magnetic nanoparticles as an intracellular MRI contrast agent," *J. Biol. Inorg. Chem.*, 2004.

[129] W. S. M. Wold and K. Toth, "Adenovirus vectors for gene therapy, vaccination and cancer gene therapy.," *Curr. Gene Ther.*, 2013.

[130] J. W. Choi, J. W. Park, Y. Na, S. J. Jung, J. K. Hwang, D. Choi, K. G. Lee, and C. O. Yun, "Using a magnetic field to redirect an oncolytic adenovirus complexed with iron oxide augments gene therapy efficacy," *Biomaterials*, 2015.

[131] C. Sapet, C. Pellegrino, N. Laurent, F. Sicard, and O. Zelphati, "Magnetic nanoparticles enhance adenovirus transduction in vitro and in vivo," *Pharm. Res.*, 2012.

[132] D. Singh, J. M. McMillan, X. M. Liu, H. M. Vishwasrao, A. V. Kabanov, M. Sokolsky-Papkov, and H. E. Gendelman, "Formulation design facilitates magnetic nanoparticle delivery to diseased cells and tissues," *Nanomedicine*. 2014.

[133] J. Carrey, B. Mehdaoui, and M. Respaud, "Simple models for dynamic hysteresis loop calculations of magnetic single-domain nanoparticles: Application to magnetic hyperthermia optimization," *J. Appl. Phys.*, 2011.

[134] I. Hilger, K. Frühauf, W. Andrä, R. Hiergeist, R. Hergt, and W. A. Kaiser, "Heating potential of iron oxides for therapeutic purposes in interventional radiology," *Acad.*

Radiol., 2002.

[135] S. K. Jones, J. G. Winter, and B. N. Gray, "Treatment of experimental rabbit liver tumours by selectively targeted hyperthermia," *Int. J. Hyperth.*, 2002.

[136] P. Moroz, S. K. Jones, J. Winter, and B. N. Gray, "Targeting liver tumors with hyperthermia: Ferromagnetic embolization in a rabbit liver tumor model," *J. Surg. Oncol.*, 2001.

[137] Q. A. Pankhurst, J. Connolly, S. K. Jones, and J. Dobson, "Applications of magnetic nanoparticles in biomedicine," *Journal of Physics D: Applied Physics*. 2003.

[138] C. Bárcena, A. K. Sra, and J. Gao, "Applications of magnetic nanoparticles in biomedicine," in *Nanoscale Magnetic Materials and Applications*, 2009.

[139] A. . Zettlemoyer, "Colloid and interface science," *J. Colloid Interface Sci.*, 2004.

[140] W. S.-Y., A. C., S. C.J.S., G. J., Z. W., F. V., and K. E.E., "Computer-aided transcranial ultrasound for time-efficient blood-brain barrier opening in primates," *J. Ther. Ultrasound*, 2018.

[141] D. C.F. Chan, D. B. Kirpotin, and P. A. Bunn Jr., "Synthesis and evaluation of colloidal magnetic iron oxides for the site-specific radiofrequency-induced hyperthermia of cancer," *J. Magn. Magn. Mater.*, 1993.

[142] K. Halbach, "Design of permanent multipole magnets with oriented rare earth cobalt material," *Nucl. Instruments Methods*, 1980.

[143] S. T. Sonawane and M. Meribout, "Halbach array design targeting nuclear magnetic resonance," in *International Conference on Electronic Devices, Systems, and Applications*, 2017.

[144] P. Babinec, A. Krafčík, M. Babincová, and J. Rosenecker, "Dynamics of magnetic particles in cylindrical Halbach array: implications for magnetic cell separation and drug targeting.," *Med. Biol. Eng. Comput.*, vol. 48, no. 8, pp. 745–53, Aug. 2010.

[145] J. Suo, S. Tong, M. McDaniel, H. Samady, R. W. Taylor, G. Bao, and D. Giddens, "Numerical Simulation of Magnetic Nanoparticles Targeted at an Atherosclerotic Lesion in the Left Coronary Artery of Patient," 2013.

[146] S. Bose, A. Datta, R. Ganguly, and M. Banerjee, "Lagrangian Magnetic Particle Tracking Through Stenosed Artery Under Pulsatile Flow Condition," *J. Nanotechnol. Eng. Med.*, 2014.

[147] O. Baun and P. Blümler, "Permanent magnet system to guide superparamagnetic particles," *J. Magn. Magn. Mater.*, 2017.

[148] L. C. Barnsley, D. Carugo, M. Aron, and E. Stride, "Understanding the dynamics of superparamagnetic particles under the influence of high field gradient arrays," *Phys. Med. Biol.*, 2017.

[149] S. Odenbach, "Fluid mechanics aspects of magnetic drug targeting," *Biomed. Tech.*, 2015.

[150] P. Kopcansky, M. Timko, M. Hnatic, M. Vala, G. M. Arzumanyan, E. A. Hayryan, L. Jancurova, and J. Jadlovsky, "Numerical modeling of magnetic drug targeting," *Phys. Part. Nucl. Lett.*, 2011.

[151] W. He, Y. Ji, C. Luo, and Z. Xu, "Development of single-side magnet array for super paramagnetic nano-particle targeting," *Res. J. Appl. Sci. Eng. Technol.*, 2014.

[152] M. Babincová, V. Altanerová, M. Lampert, Č. Altaner, E. Machová, M. Šrámka, and P. Babinec, "Site-specific in vivo targeting of magnetoliposomes using

externally applied magnetic field," *Zeitschrift fur Naturforsch. - Sect. C J. Biosci.*, 2000.

[153] I. Neuner, J. B. Kaffanke, K. J. Langen, E. R. Kops, L. Tellmann, G. Stoffels, C. Weirich, C. Filss, J. Scheins, H. Herzog, and N. J. Shah, "Multimodal imaging utilising integrated MR-PET for human brain tumour assessment," *Eur. Radiol.*, 2012.

[154] G. B. Chavhan, P. S. Babyn, B. Thomas, M. M. Shroff, and E. Mark Haacke, "Principles, techniques, and applications of T2*-based MR imaging and its special applications," *Radiographics*, 2009.

[155] L. J. Anderson, S. Holden, B. Davis, E. Prescott, C. C. Charrier, N. H. Bunce, D. N. Firmin, B. Wonke, J. Porter, J. M. Walker, and D. J. Pennell, "Cardiovascular T2-star (T2*) magnetic resonance for the early diagnosis of myocardial iron overload," *Eur. Heart J.*, 2001.

[156] C. Moor, T. Lymberopoulou, and V. J. Dietrich, "Determination of heavy metals in soils, sediments and geological materials by ICP-AES and ICP-MS," *Mikrochim. Acta*, vol. 136, no. 3–4, pp. 123–128, 2001.

[157] M. Muthana, J. Richardson, S. Rodrigues, and C. Lewis, "Construction of Human Monocyte Derived Macrophages Armed with Oncolytic Viruses," vol. 3, pp. 2–6, 2013.

[158] Y. Takeshita, B. Obermeier, A. Cotleur, Y. Sano, T. Kanda, and R. M. Ransohoff, "An in vitro blood-brain barrier model combining shear stress and endothelial cell/astrocyte co-culture," *J. Neurosci. Methods*, vol. 232, pp. 165–172, 2014.

[159] S. Warrier, P. Pavanram, D. Raina, and M. Arvind, "Study of chemoresistant

CD133+ cancer stem cells from human glioblastoma cell line U138MG using multiple assays," *Cell Biol. Int.*, vol. 36, no. 12, pp. 1137–1143, 2012.

[160] L. C. Crowley, A. P. Scott, B. J. Marfell, J. A. Boughaba, G. Chojnowski, and N. J. Waterhouse, "Measuring cell death by propidium iodide uptake and flow cytometry," *Cold Spring Harb. Protoc.*, 2016.

[161] A. Heymer, D. Haddad, M. Weber, U. Gbureck, P. M. Jakob, J. Eulert, and U. Nöth, "Iron oxide labelling of human mesenchymal stem cells in collagen hydrogels for articular cartilage repair," *Biomaterials*, vol. 29, no. 10, pp. 1473–1483, 2008.

[162] L. C. Barnsley, D. Carugo, and E. Stride, "Optimized shapes of magnetic arrays for drug targeting applications," *J. Phys. D. Appl. Phys.*, vol. 49, no. 22, p. 225501, Jun. 2016.

[163] S. Goodwin, C. Peterson, C. Hoh, and C. Bittner, "Targeting and retention of magnetic targeted carriers (MTCs) enhancing intra-arterial chemotherapy," *J. Magn. Magn. Mater.*, 1999.

[164] P. Dames, B. Gleich, A. Flemmer, K. Hajek, N. Seidl, F. Wiekhorst, D. Eberbeck, I. Bittmann, C. Bergemann, T. Weyh, L. Trahms, J. Rosenecker, and C. Rudolph, "Targeted delivery of magnetic aerosol droplets to the lung," *Nat. Nanotechnol.*, 2007.

[165] J. H. Kang, H. Driscoll, M. Super, and D. E. Ingber, "Application of a Halbach magnetic array for long-range cell and particle separations in biological samples," *Appl. Phys. Lett.*, 2016.

[166] L. C. Barnsley, D. Carugo, J. Owen, and E. Stride, "Halbach arrays consisting of cubic elements optimised for high field gradients in magnetic drug targeting

applications," *Phys. Med. Biol.*, vol. 60, no. 21, pp. 8303–8327, 2015.

[167] U. O. Häfeli, K. Gilmour, A. Zhou, S. Lee, and M. E. Hayden, "Modeling of magnetic bandages for drug targeting: Button vs. Halbach arrays," *J. Magn. Magn. Mater.*, vol. 311, no. 1, pp. 323–329, Apr. 2007.

[168] A.-L. Gassner, M. Abonnenc, H.-X. Chen, J. Morandini, J. Josserand, J. S. Rossier, J.-M. Busnel, and H. H. Girault, "Magnetic forces produced by rectangular permanent magnets in static microsystems.," *Lab Chip*, vol. 9, no. 16, pp. 2356–2363, 2009.

[169] K. B. Baltzis, "ON THE USAGE AND POTENTIAL APPLICATIONS OF THE FINITE ELEMENT METHOD MAGNETICS (FEMM) PACKAGE IN THE TEACHING OF ELECTROMAGNETICS IN HIGHER EDUCATION," pp. 408–420.

[170] O. Rotariu and N. J. C. Strachan, "Modelling magnetic carrier particle targeting in the tumor microvasculature for cancer treatment," in *Journal of Magnetism and Magnetic Materials*, 2005.

[171] S. H. Mohades Kasaei, S. M. Mohades Kasaei, and S. A. Mohades Kasaei, "Design and implementation solenoid based kicking mechanism for soccer robot applied in robocup-MSL," *Int. J. Adv. Robot. Syst.*, 2010.

[172] N. Pamme, "Magnetism and microfluidics," *Lab on a Chip*. 2006.

[173] C. B. Fu, T. R. Gentile, G. L. Jones, W. C. Chen, R. Erwin, S. Watson, C. Broholm, J. A. Rodriguez-Rivera, and J. Scherschligt, "A wide angle neutron spin filter system using polarized 3He," in *Physica B: Condensed Matter*, 2011.

[174] K. B. Baltzis, "The finite element method magnetics (FEMM) freeware package:

May it serve as an educational tool in teaching electromagnetics?," *Educ. Inf. Technol.*, 2010.

[175] T. A. Voronina, G. M. Molodavkin, S. A. Sergeeva, and O. I. Epstein, "Anxiolytic Effect of Proproten under Conditions of Punished and Unpunished Behavior," *Bull. Exp. Biol. Med.*, vol. 135–136, no. SUPPL. 1, pp. 120–122, 2003.

[176] F. Zhai, A. Sun, D. Yuan, J. Wang, S. Wu, A. A. Volinsky, and Z. Wang, "Epoxy resin effect on anisotropic Nd-Fe-B rubber-bonded magnets performance," *Journal of Alloys and Compounds*. 2011.

[177] S. Yin, D. Arbelaez, J. H. Swanson, and T. Shen, "Epoxy resins for vacuum impregnating superconducting magnets: A review and tests of key properties," *IEEE Trans. Appl. Supercond.*, 2019.

[178] D. Zhu, S. Beeby, J. Tudor, and N. Harris, "Increasing output power of electromagnetic vibration energy harvesters using improved Halbach arrays," *Sensors Actuators, A Phys.*, 2013.

[179] W. Mao, M. B. Smith, and C. M. Collins, "Exploring the limits of RF shimming for high-field MRI of the human head," *Magn. Reson. Med.*, 2006.

[180] P. Campbell and A. Nafisi, "The effect of iron powders on the utilization of permanent magnet materials in advanced motors," *IEEE Trans. Magn.*, 1980.

[181] C. Multiphysics and C. Multiphysics, "COMSOL Multiphysics ® 4.3a," *COMSOL Multiphysics ® 4.3a*, 2013.

[182] M. C. D. Tayler and D. Sakellariou, "Low-cost, pseudo-Halbach dipole magnets for NMR," *J. Magn. Reson.*, 2017.

[183] A. Bashyam, M. Li, and M. J. Cima, "Design and experimental validation of

Unilateral Linear Halbach magnet arrays for single-sided magnetic resonance," *J. Magn. Reson.*, 2018.

[184] L. C. Barnsley, D. Carugo, J. Owen, and E. Stride, "Halbach arrays consisting of cubic elements optimised for high field gradients in magnetic drug targeting applications."

[185] P. A. Voltairas, D. I. Fotiadis, and L. K. Michalis, "Hydrodynamics of magnetic drug targeting," *J. Biomech.*, 2002.

[186] E. K. Ruuge and A. N. Rusetski, "Magnetic fluids as drug carriers: Targeted transport of drugs by a magnetic field," *J. Magn. Magn. Mater.*, 1993.

[187] S. ichi Takeda, F. Mishima, S. Fujimoto, Y. Izumi, and S. Nishijima, "Development of magnetically targeted drug delivery system using superconducting magnet," *J. Magn. Magn. Mater.*, 2007.

[188] A. Nacev, C. Beni, O. Bruno, and B. Shapiro, "Magnetic nanoparticle transport within flowing blood and into surrounding tissue," *Nanomedicine*, 2010.

[189] A. Nacev, C. Beni, O. Bruno, and B. Shapiro, "The behaviors of ferromagnetic nano-particles in and around blood vessels under applied magnetic fields," *J. Magn. Magn. Mater.*, 2011.

[190] L. Agiotis, I. Theodorakos, S. Samothrakitis, S. Papazoglou, I. Zergioti, and Y. S. Raptis, "Magnetic manipulation of superparamagnetic nanoparticles in a microfluidic system for drug delivery applications," *Journal of Magnetism and Magnetic Materials*. 2016.

[191] Z. Huang, N. Pei, Y. Wang, X. Xie, A. Sun, L. Shen, S. Zhang, X. Liu, Y. Zou, J. Qian, and J. Ge, "Biomaterials Deep magnetic capture of magnetically loaded cells

for spatially targeted therapeutics," *Biomaterials*, vol. 31, no. 8, pp. 2130–2140, 2010.

[192] A. Hajiaghajani, S. Hashemi, and A. Abdolali, "Adaptable setups for magnetic drug targeting in human muscular arteries: Design and implementation," *J. Magn. Magn. Mater.*, 2017.

[193] K. Gitter and S. Odenbach, "Quantitative targeting maps based on experimental investigations for a branched tube model in magnetic drug targeting," *Journal of Magnetism and Magnetic Materials*. 2011.

[194] A. Munir, Z. Zhu, J. Wang, and H. S. Zhou, "Experimental investigation of magnetically actuated separation using tangential microfluidic channels and magnetic nanoparticles," *IET nanobiotechnology*, 2014.

[195] A. S. Lübbe, C. Bergemann, J. Brock, and D. G. McClure, "Physiological aspects in magnetic drug-targeting," *J. Magn. Magn. Mater.*, 1999.

[196] R. A. Horch, K. Wilkens, D. F. Gochberg, and M. D. Does, "RF coil considerations for short-T2MRI," *Magn. Reson. Med.*, 2010.

[197] J. W. M. Bulte and M. M. J. Modo, "Design and applications of nanoparticles in biomedical imaging," *Des. Appl. Nanoparticles Biomed. Imaging*, pp. 1–469, 2016.

[198] S. S. Kety and C. F. Schmidt, "THE NITROUS OXIDE METHOD FOR THE QUANTITATIVE DETERMINATION OF CEREBRAL BLOOD FLOW IN MAN: THEORY, PROCEDURE AND NORMAL VALUES," *J. Clin. Invest.*, 1948.

[199] J. Riegler, J. A. Wells, P. G. Kyrtatos, A. N. Price, Q. A. Pankhurst, and M. F. Lythgoe, "Targeted magnetic delivery and tracking of cells using a magnetic

resonance imaging system," *Biomaterials*, vol. 31, no. 20, pp. 5366–5371, Jul. 2010.

[200] S. Naqvi, M. Samim, M. Z. Abdin, F. J. Ahmed, A. N. Maitra, C. K. Prashant, and A. K. Dinda, "Concentration-dependent toxicity of iron oxide nanoparticles mediated by increased oxidative stress," *Int. J. Nanomedicine*, 2010.

[201] S. Laurent, C. Burtea, C. Thirifays, U. O. Häfeli, and M. Mahmoudi, "Crucial ignored parameters on nanotoxicology: The importance of toxicity assay modifications and 'cell vision,'" *PLoS One*, 2012.

[202] M. Mahmoudi, S. Sant, B. Wang, S. Laurent, and T. Sen, "Superparamagnetic iron oxide nanoparticles (SPIONs): Development, surface modification and applications in chemotherapy," *Adv. Drug Deliv. Rev.*, vol. 63, no. 1–2, pp. 24–46, 2011.

[203] S. Sruthi, L. Maurizi, T. Nury, F. Sallem, J. Boudon, J. M. Riedinger, N. Millot, F. Bouyer, and G. Lizard, "Cellular interactions of functionalized superparamagnetic iron oxide nanoparticles on oligodendrocytes without detrimental side effects: Cell death induction, oxidative stress and inflammation," *Colloids Surfaces B Biointerfaces*, 2018.

[204] C. Petters and R. Dringen, "Accumulation of iron oxide nanoparticles by cultured primary neurons," *Neurochem. Int.*, 2015.

[205] C. C. Berry and A. S. G. Curtis, "Functionalisation of magnetic nanoparticles for applications in biomedicine," *J. Phys. D. Appl. Phys.*, vol. 36, no. 13, pp. R198–R206, 2003.

[206] C. C. Berry, S. Wells, S. Charles, and A. S. G. Curtis, "Dextran and albumin derivatised iron oxide nanoparticles: Influence on fibroblasts in vitro," *Biomaterials*,

2003.

[207] C. C. Berry, S. Wells, S. Charles, G. Aitchison, and A. S. G. Curtis, "Cell response to dextran-derivatised iron oxide nanoparticles post internalisation," *Biomaterials*, 2004.

[208] M. Mahmoudi, A. Simchi, M. Imani, M. A. Shokrgozar, A. S. Milani, U. O. Häfeli, and P. Stroeve, "A new approach for the in vitro identification of the cytotoxicity of superparamagnetic iron oxide nanoparticles," *Colloids Surfaces B Biointerfaces*, 2010.

[209] M. Morteza, S. Abdolreza, I. Mohammad, S. M. Abbas, S. Pieter, M. Mahmoudi, A. Simchi, M. Imani, A. S. Milani, and P. Stroeve, "An in vitro study of bare and poly(ethylene glycol)-co-fumarate-coated superparamagnetic iron oxide nanoparticles: a new toxicity identification procedure," *Nanotechnology*, 2009.

[210] M. Mahmoudi, S. Sant, B. Wang, S. Laurent, and T. Sen, "Superparamagnetic iron oxide nanoparticles (SPIONs): Development, surface modification and applications in chemotherapy," *Advanced Drug Delivery Reviews*, vol. 63, no. 1–2. pp. 24–46, 2011.

[211] N. Singh, G. J. S. Jenkins, R. Asadi, and S. H. Doak, "Potential toxicity of superparamagnetic iron oxide nanoparticles (SPION)," *Nano Rev.*, vol. 1, no. 1, p. 5358, 2010.

[212] L. B. Thomsen, T. Linemann, K. M. Pondman, J. Lichota, K. S. Kim, R. J. Pieters, G. M. Visser, and T. Moos, "Uptake and transport of superparamagnetic iron oxide nanoparticles through human brain capillary endothelial cells," *ACS Chem. Neurosci.*, 2013.

[213] T. Coccini, F. Caloni, L. J. Ramírez Cando, and U. De Simone, "Cytotoxicity and proliferative capacity impairment induced on human brain cell cultures after short- and long-term exposure to magnetite nanoparticles," *J. Appl. Toxicol.*, 2017.

[214] M. A. Abakumov, A. S. Semkina, A. S. Skorikov, D. A. Vishnevskiy, A. V. Ivanova, E. Mironova, G. A. Davydova, A. G. Majouga, and V. P. Chekhonin, "Toxicity of iron oxide nanoparticles: Size and coating effects," *J. Biochem. Mol. Toxicol.*, no. July, pp. 1–6, 2018.

[215] C. Petters, K. Thiel, and R. Dringen, "Lysosomal iron liberation is responsible for the vulnerability of brain microglial cells to iron oxide nanoparticles: Comparison with neurons and astrocytes," *Nanotoxicology*, vol. 10, no. 3, pp. 332–342, 2016.

[216] F. L. Cardoso, D. Brites, and M. A. Brito, "Looking at the blood-brain barrier: Molecular anatomy and possible investigation approaches," *Brain Research Reviews*. 2010.

[217] C. Petters, E. Irrsack, M. Koch, and R. Dringen, "Uptake and Metabolism of Iron Oxide Nanoparticles in Brain Cells," *Neurochemical Research*, vol. 39, no. 9. pp. 1648–1660, 2014.

[218] M. W. Brightman, "The distribution within the brain of ferritin injected into cerebrospinal fluid compartments. II. Parenchymal distribution," *Am. J. Anat.*, 1965.

[219] E. Pollert, P. Veverka, M. Veverka, O. Kaman, K. Závěta, S. Vasseur, R. Epherre, G. Goglio, and E. Duguet, "Search of new core materials for magnetic fluid hyperthermia: Preliminary chemical and physical issues," *Progress in Solid State Chemistry*. 2009.

[220] R. A. Revia and M. Zhang, "Magnetite nanoparticles for cancer diagnosis,

treatment, and treatment monitoring: Recent advances," *Mater. Today*, 2016.

[221] M. Liu, B. Liu, Q. Liu, K. Du, Z. Wang, and N. He, "Nanomaterial-induced ferroptosis for cancer specific therapy," *Coordination Chemistry Reviews*. 2019.

[222] M. C. Lamkowsky, M. Geppert, M. M. Schmidt, and R. Dringen, "Magnetic field-induced acceleration of the accumulation of magnetic iron oxide nanoparticles by cultured brain astrocytes," *J. Biomed. Mater. Res. - Part A*, 2012.

[223] E. M. Luther, C. Petters, F. Bulcke, A. Kaltz, K. Thiel, U. Bickmeyer, and R. Dringen, "Endocytotic uptake of iron oxide nanoparticles by cultured brain microglial cells," *Acta Biomater.*, 2013.

[224] J. Riegler, J. A. Wells, P. G. Kyrtatos, A. N. Price, Q. A. Pankhurst, and M. F. Lythgoe, "Targeted magnetic delivery and tracking of cells using a magnetic resonance imaging system," *Biomaterials*, vol. 31, no. 20, pp. 5366–5371, 2010.

[225] B. Prabhakarpandian, M. C. Shen, J. B. Nichols, I. R. Mills, M. Sidoryk-Wegrzynowicz, M. Aschner, and K. Pant, "SyM-BBB: A microfluidic blood brain barrier model," *Lab Chip*, 2013.

Appendices

Appendix I. Developing Halbach array-Model 3

Model 3 consists of a hundred of cube shaped magnets with a volume of 1 cm^3 each. The model contains of ten layers and each layer has a set of magnets in different magnetisation.
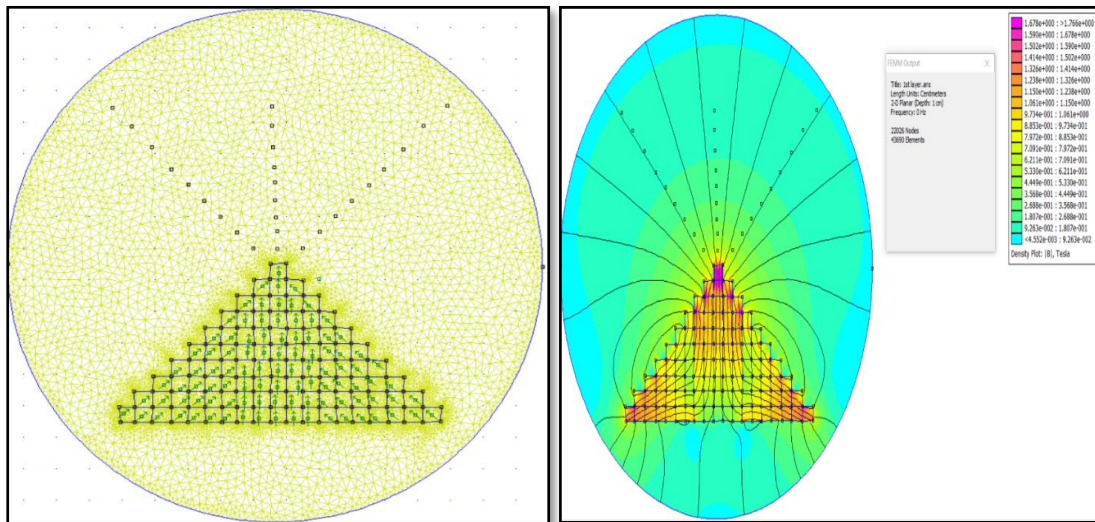
Appendix II. The strength and the shape of magnetic field of Model 3 at different distances (FEMM)

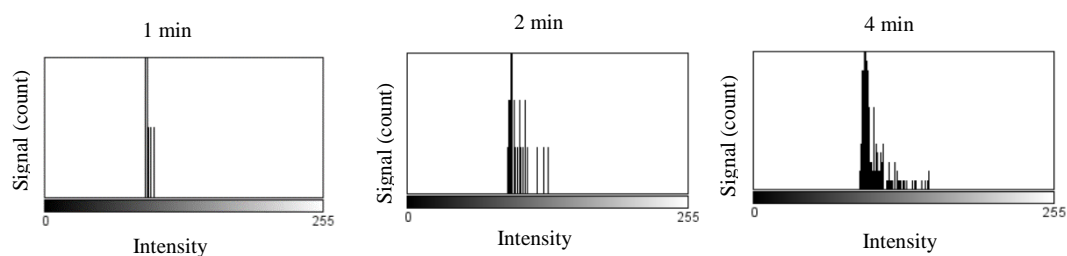| Distance (cm)	Magnetic field (T)	Graph/peak shape
0.5	0.65	
1.5	0.44	
2	0.34	
2.5	0.28	
3.5	0.24	

4	0.2	
5	0.17	
6	0.15	
7	0.13	
20	0.02	
25	0.016	

Appendix III. Developing Halbach array-Model 4

Model 4 consists of a 12 of cube shaped magnets of 2 sets of orthogonal and horizontal sets (connected from the corner) with a volume of 1 cm^3 each. The model contains of 2 layers and each layer has a set of magnets in different magnetisation.
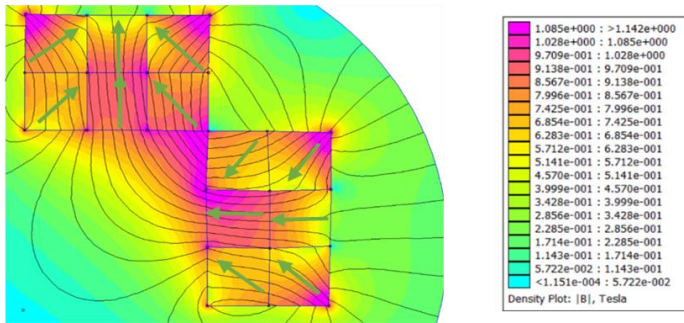
Appendix IV. The strength and the shape of magnetic field of Model 4 at different distances (FEMM)

Distance (cm)	Magnetic field (T)	Graph/peak shape
0.5	1.3	
1.5	1.2	
2	0.2	
2.5	0.1	
3	0.055	

Appendix V. Developing Halbach array-Model 5

Model 5 consists of a 12 of cube shaped magnets of 2 sets of orthogonal and horizontal sets (connected from the corner) with a volume of 1 cm^3 each. The model contains of 2 layers and each layer has a set of magnets in different magnetisation.
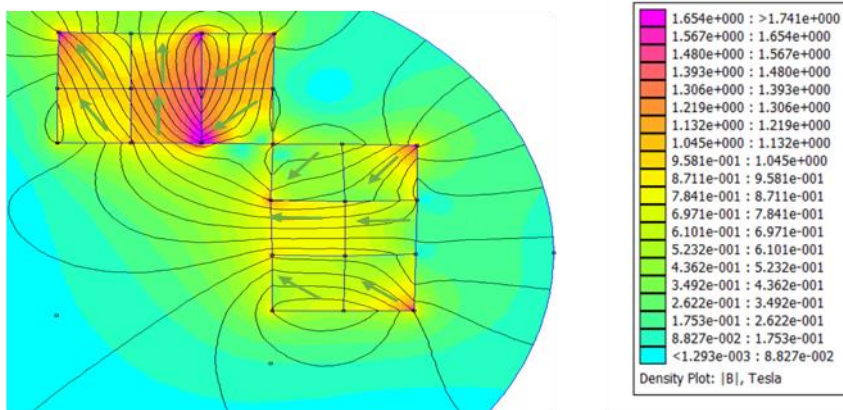
Appendix VI. The strength and the shape of magnetic field of Model 5 at different distances (FEMM)

Magnetic field strength at 0 cm
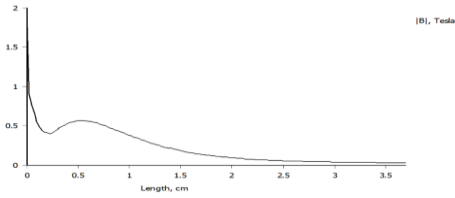
Distance (cm)	Magnetic field (T)	Graph/peak shape
0.5	1.4	
1	1.3	
1.5	1.1	
2	0.25	
2.5	0.15	

3	0.09	
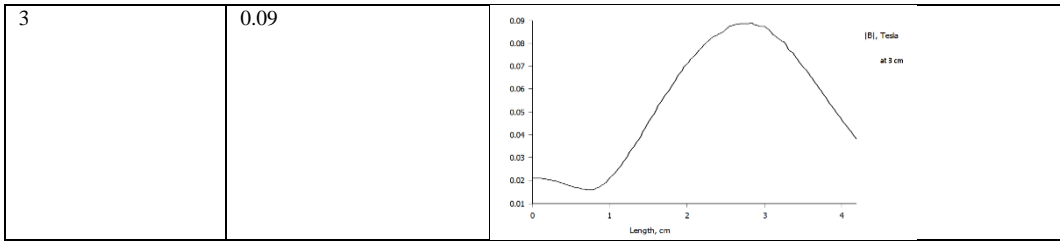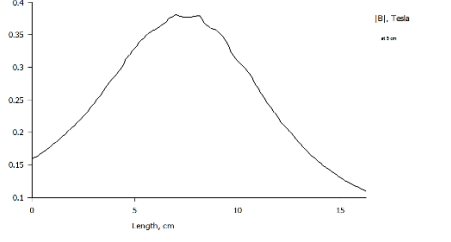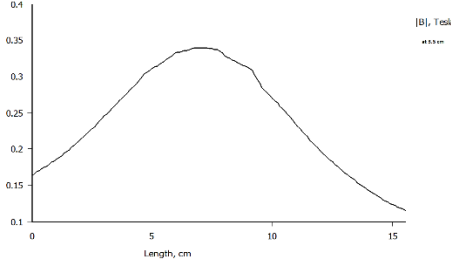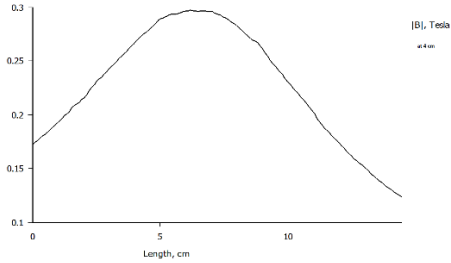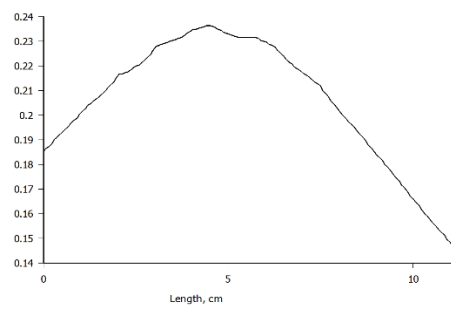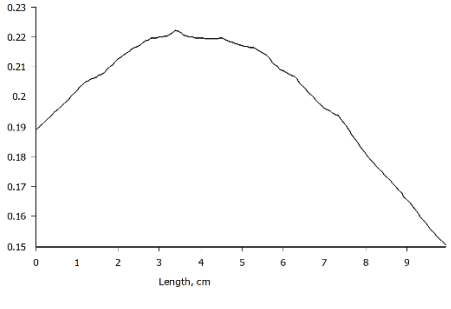
Appendix VII. Developing Halbach array-Model 6

Model 6 was modeled to be a rectangular shape, which consists of two main blocks with different magnetisation orientation. The top block has five layers and each layer has eight magnets giving fourteen magnets in total.
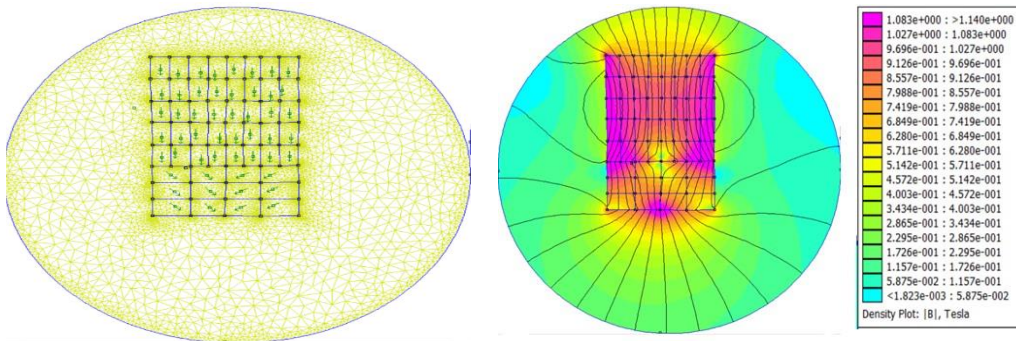
Appendix VIII. The strength and the shape of magnetic field of Model 6 at different distances (FEMM)

Distance (cm)	Magnetic field (T)	Graph/peak shape
0.5	1	
1	0.7	
1.5	0.6	
2	0.5	
2.5	0.42	

3	0.37	
3.5	0.34	
4	0.3	
4.5	0.23	
6	0.22	

Appendix IX. An intensity histogram of detected SPIONs at different distance and time intervals in the vessels
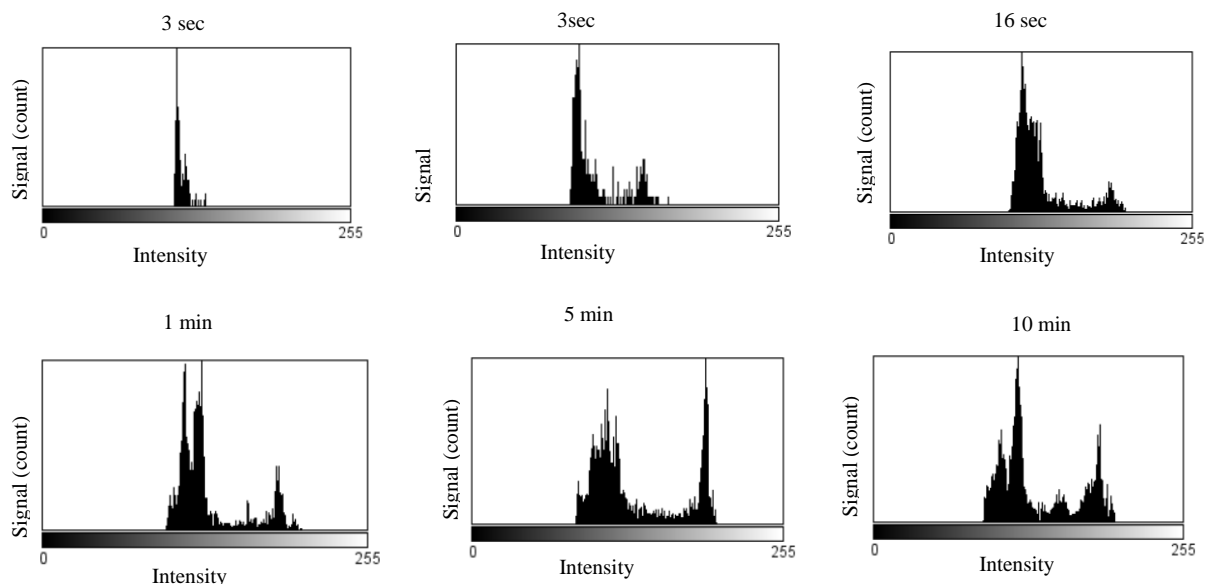
An intensity histogram of detected SPIONs at different time intervals in the vessels that were closest to the magnet with a 150 ml/min flow rate. Video was taken for the trapping experiment where the three-layer Halbach array was applied to trap SPIONs in the complex vasculature model. Several video clips were taken at different time intervals, and then imported to ImageJ software to generate the intensity histogram.
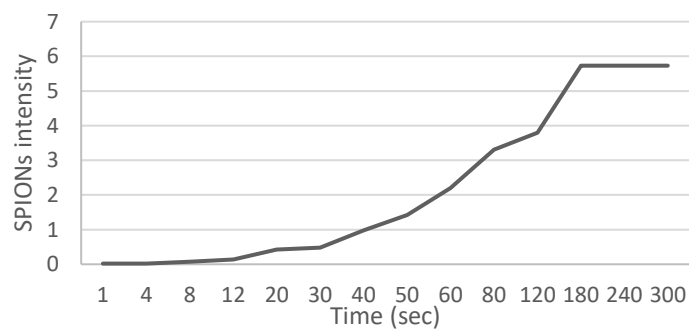

An intensity histogram of detected SPIONs at different time intervals in the vessels that were 3cm to the magnet with a 150 ml/min flow rate. Video was taken for the trapping experiment where the three-layer Halbach array was applied to trap SPIONs in the complex vasculature model. Several video clips were taken at different time intervals, and then imported to ImageJ software to generate the intensity histogram.

(a)

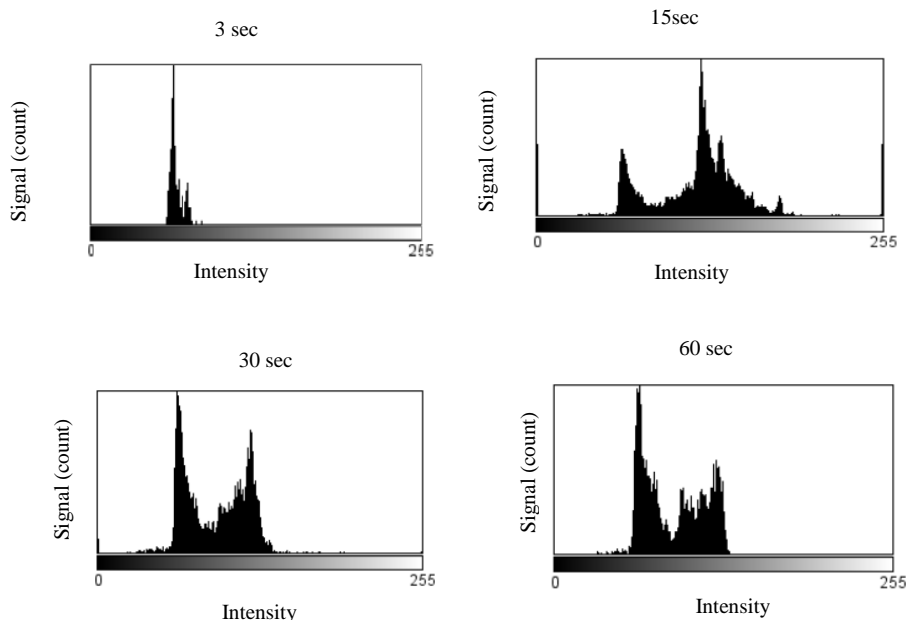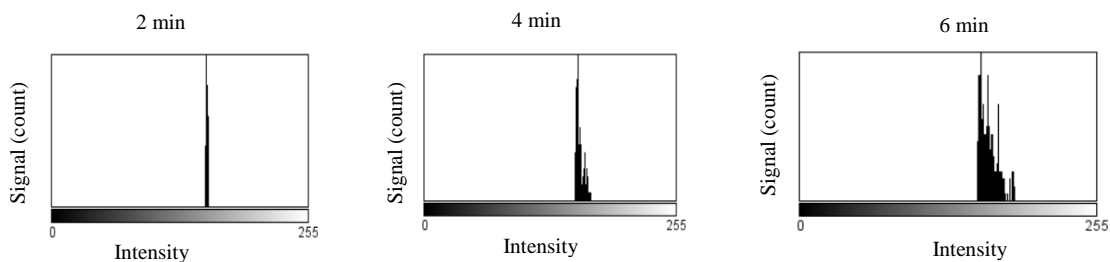## Time required to trap SPIONs at 0 cm (150ml/min)
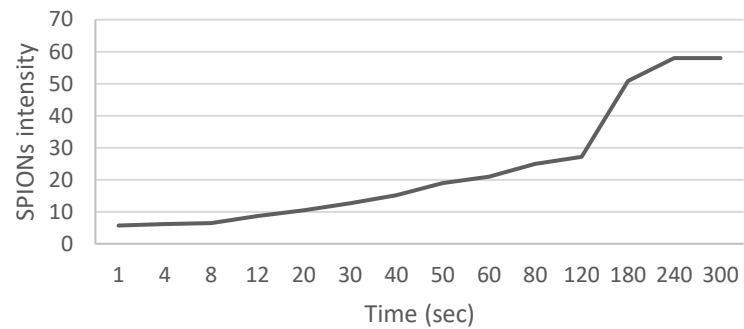
(b)

Time required to trap SPIONs at 3cm (150ml/min)

Time required for SPIONs to be trapped using a Halbach array magnet in the complex vasculature model at two different distances. (a) 0 cm and (b) 3 cm away from the magnet, at a flow rate of 150 ml/min.

An intensity histogram of SPIONs detected at different time intervals in the vessels that were closest to the magnet with a 300 ml/min flow rate. Video was taken for the trapping experiment where the three-layer Halbach array magnet was applied to trap SPIONs in the complex vasculature model. Several video clips were taken at different time intervals and then imported into ImageJ software to generate the intensity histogram.

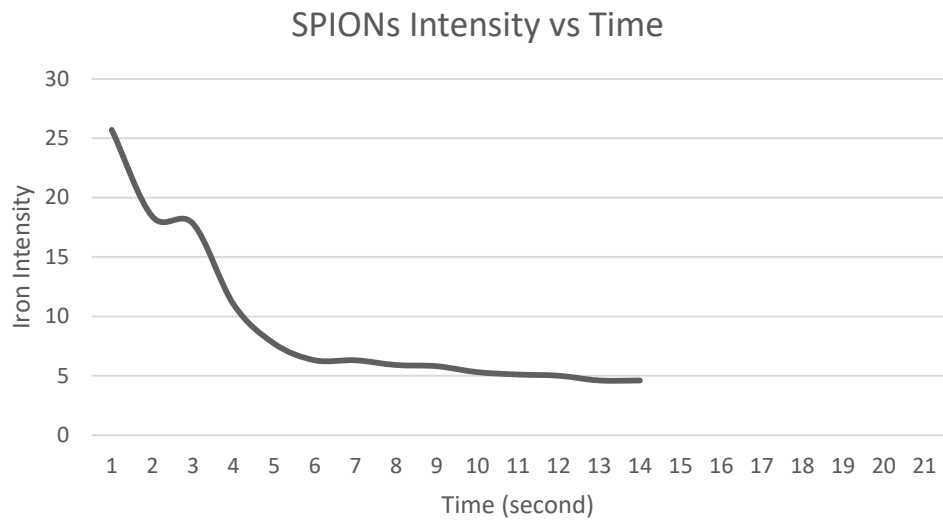Intensity **am of dete** Intensity **time vals in the vessels that were 3 the nl/min flo for the ping experiment where the t ayer Halbach array was applied to trap SPIONs in the complex lature model. Several video ere taken at different time intervals, and then imported to J software to generate the sity histogram.**

(a)

SPIONs Intensity vs Time

(b)

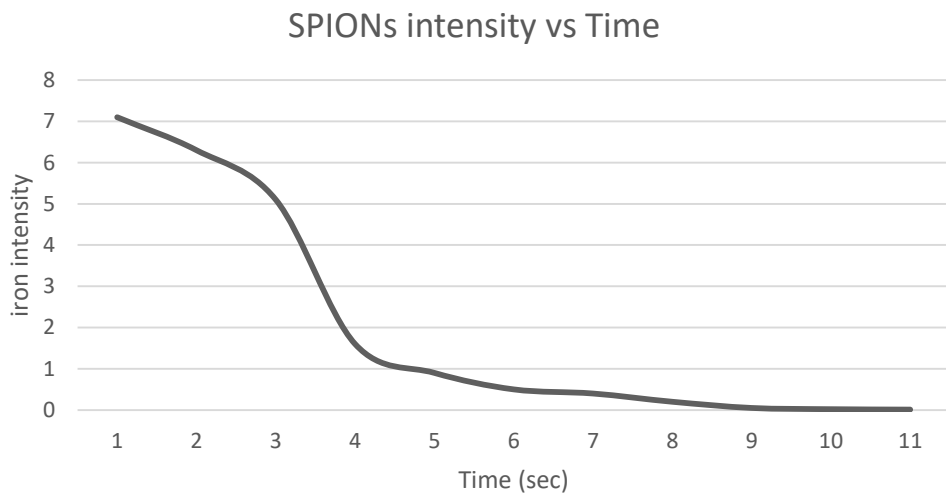**SPIONs intensity vs Time**

Time required for the SPIONs to be released completely from the complex vasculature model after being trapped using a Halbach array magnet. The SPIONs was trapped at two different distances- (a) 0 cm and (b) 3 cm away from the magnet, at a flow rate 150 ml/min.

Appendices X. Filing receipt of Halbach array of model 2

The patent application of Halbach array (Mosel 2) was filed on the 22nd October 2018. The number of the application is GB1817176.9

Concept House
Cardiff Road, Newport
South Wales
NP10 8QQ
United Kingdom

Telephone +44 (0)1633 814000

Website https://www.gov.uk/ipo

Intellectual Property Office

Electronic Filing Receipt

HGF Limited
Document Handling - HGF (Manchester)
1 City Walk
LEEDS
United Kingdom
LS11 9DX

Your Ref: P249888GB/CAB   22 October 2018

PATENT APPLICATION NUMBER 1817176.9

We have received your request for grant of a patent and recorded its details as follows:

Filing date(*)	22 October 2018
Earliest priority date (if any)	
Applicant(s) / contact point	THE UNIVERSITY OF SHEFFIELD
Application fee paid	Yes
Description (number of pages or reference)	12
Certified copy of referenced application	Not applicable
If description not filed	Not applicable
Claims (number of pages)	5
Drawings (number of pages)	10
Abstract (number of pages)	No, file by 22 October 2019
Statement of inventorship (Form 7)	No, file by 24 February 2020
Request for search (Form 9A)	Yes
Request for examination (Form 10)	Yes
Priority Documents	None
Other Attachments Received	PDAS Registration Form PDASRegistration.pdf
	Fee Sheet FeeSheet.pdf
	Validation Log ValidLog.pdf

Intellectual Property Office is an operating name of the Patent Office   https://www.gov.uk/ipo

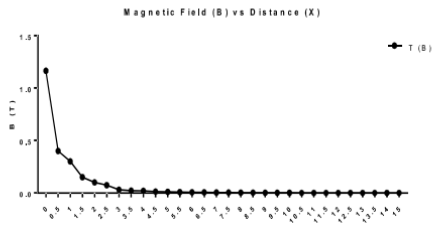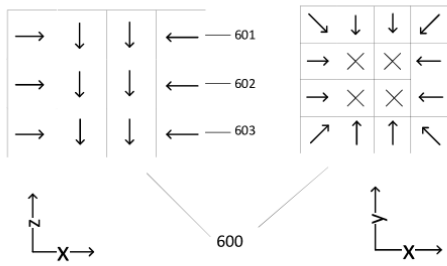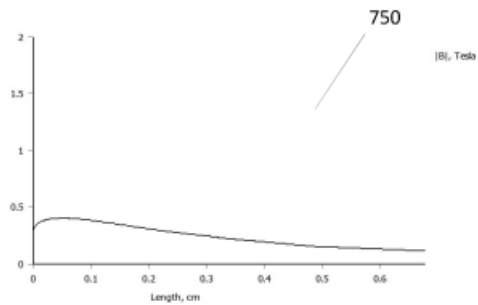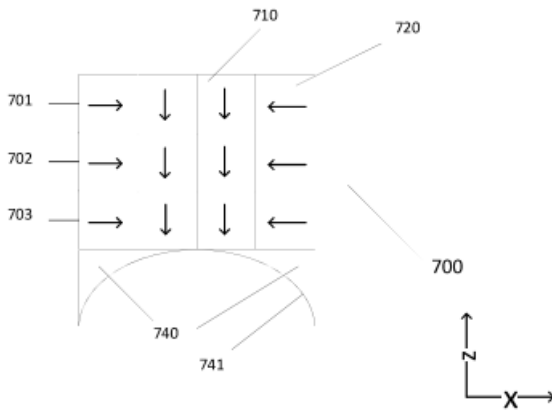## Appendix XI. Description of Halbach array of Model 2

Figure 6

Figure 7

Appendix XII. Suggested helmet for Halbach array of Model 2

Figure 8